Drops on Liquid-Infused Solids

Saurabh Nath

PSL UNIVERSITÉ PARIS

THÈSE DE DOCTORAT

DE L'UNIVERSITÉ PSL

Préparée à **École supérieure de physique et de chimie industrielles de la Ville de Paris**

DROPS ON LIQUID–INFUSED SOLIDS

GOUTTES SUR DES SOLIDES IMPRÉGNÉS

Soutenue par

Saurabh NATH

Le 5 Juillet 2021

Ecole doctorale n° 564

Physique en Île-de-France

Spécialité

Physique des Liquides

Composition du jury :

Lydéric, BOCQUET Directeur de recherche, École normale supérieure	*Président du Jury*
Cecile, COTTIN-BIZONNE Directeur de recherche, University of Lyon	*Rapporteur*
Isabelle, CANTAT Professeur, Université Rennes 1	*Rapporteur*
Howard, STONE Professeur, Princeton University	*Examinateur*
Jacco, SNOEIJER Professeur, University of Twente	*Examinateur*
David, QUÉRÉ Directeur de Recherche, ESPCI Paris	*Directeur de thèse*

ESPCI PARIS | PSL

তরলার্দ্র ঘন পদার্থ ও জলবিন্দু বিষয়ক

সৌরভ নাথ

DROPS ON LIQUID-INFUSED SOLIDS

SAURABH NATH

GOUTTES SUR DES SOLIDES IMPRÉGNÉS

SAURABH NATH

ABSTRACT

A textured solid infused with a liquid comprises a class of materials in between a liquid and a solid. Unlike classical solids, these materials typically exhibit extraordinarily little adhesion, due to the marginal role of pinning sites. Their liquid-like nature, owing to the trapped infusion, also makes them exceptionally slippery to drops of other non-miscible liquids. In this thesis, we experimentally investigate the original spreading, adhesion and frictional behaviour of these special materials, the physics of which we capture with the construction of scaling laws, wherever possible. In the first section, we show that infused solids, despite their celebrated slipperiness, slow down the spreading of a water drop in comparison to classical solids. The situation, however, is opposite for viscous drops, where spreading can be substantially enhanced by slip at the oil/drop interface. In both cases, we find that the laws of spreading on infused solids preserve the structure of the laws established on bare solids, even if the speed can be tuned by the viscosity ratio of the drop and infused oil. In the second section, we demonstrate that contrary to the vanishing lateral adhesion of these materials, their vertical adhesion is remarkably high. The dynamical adhesion of these solids can be utilized to create a viscous tweezer for water droplets. Finally in the third section, we discuss the friction properties of liquid-infused solids towards solid beads, and describe in particular how these rolling spheres drag a tail behind them.

RÉSUMÉ

Un solide texturé infusé est un matériau ambigu, sa surface étant mi-solide, mi-liquide. En conséquence, ces matériaux présentent généralement une adhérence extraordinairement faible qui les rend spécialement glissants pour des gouttes (d'un autre liquide) qu'on y dépose. Nous étudions dans cette thèse quelques comportements originaux de ces surfaces en termes de mouillage, d'adhésion et de friction – à la fois d'un point de vue expérimental et en loi d'échelle, quand c'est possible. Chaque fois que c'est possible. Dans la première section, nous montrons que les solides infusés, supposés ultra-glissants, ralentissent pourtant l'étalement d'une goutte d'eau par rapport aux solides classiques. La situation est opposée pour des gouttes visqueuses, dont l'étalement peut être nettement accéléré par le glissement à l'interface huile/goutte. Dans les deux cas, nous constatons que les lois d'étalement sur les solides infusés conservent la structure des lois établies sur les solides nus, avec des aménagements fonctions des viscosités des deux liquides en jeu. Dans la deuxième section, nous montrons que, contrastant avec l'adhésion horizontale ultra-faible de ces matériaux, leur adhérence verticale peut être élevèe et servir à capturer un liquide par viscosité (pince visqueuse). Dans la troisième section enfin, nous discutons des propriétés de friction de billes solides dévalant sur des surfaces infusées et décrivons en particulier comment ces sphéres roulantes engendrent une traînée visqueuse derrière elles.

Dedicated to Yash

On a Night with no end
In the dying Light of the Stars
He bathed in the Sorrows of the Seine -
And he bathed in the Sorrows of the Seine
On a Night with no end
In the dying Light
Of the Stars

1994 – 2020

Thanks to *Marie Curie Fellowship*

'C'est la lutte finale...'

- L'Internationale,
Eugène Pottier

CONTENTS

PROLOGUE

1

RUNAWAY CYCLONE

Calcutta, 1896.
The capital of the British colonial empire in the East - 'The City of Dreadful Night' to Rudyard Kipling, the scribe of the British Empire, 'La Cité de la Joie ' to French author Dominique Lapierre - inhabited by the European imperialists - the British, the French, the Dutch, with Afghan fruit-sellers, Cantonese carpenters, opium traders, Armenian businessmen, Polish priests, and the Bengalis - a native bourgeois intelligentsia igniting a Renaissance in Bengal influenced by European ideas of liberalism and the Bengali proletariat dying of the Plague of 1896 and bullets of the Europeans, resurrecting in class-consciousness - a city brewing with political unrest about to witness a series of bombings by young radicals, to be hanged, shot and killed during the partitioning of Bengal - a city at the crossroads of tectonic political and cultural revolutions, breaking colonial myths of Orientalism - where Bengali Shakespearean theater artists had taken to streets after the burning of the *Chowringhee Theater*, where the Bengali working class had exploded on the streets in the Jute Mill Strikes of 1896 - to that city of 1896, returns home a young Bengali, finishing his doctoral studies in London [1–3].

He writes in Bengali what would be the first piece of science fiction in India - *'Polatok Toophan'* that translates to 'Runaway Cyclone' in English and 'Cyclone en Fuite' in French. First published in 1896, this colonial-era science fiction by a non-western author is set in colonial Calcutta and told from the perspective of a local Calcuttan.

The story begins with the meteorological office warning the people of Bengal about an imminent cyclone threatening to devastate the city of Calcutta. However, on the fateful night, as the petrified populace of Bengal awaits with bated breath, the cyclone vanishes. The meteorologists and physicists worldwide - all stand stupefied, struggling to find a scientific rationale to explain the mysterious disappearance of the foretold cyclone. Soon, the European and American physicists start heatedly debating on the mysterious disappearance. An unnamed scientist who 'once published an article in *Nature*' proposes that 'the cyclone must have been whisked away by the attraction of an invisible passing asteroid'. A German professor presents 'a theoretically dense article on the *Runaway cyclone* phenomenon' at the British Association convention at Oxford that in truth does little to explain why the cyclone disappeared at all.

The story now goes back in time to two different points - one, moments before the cyclone hits, where a ship is asail on the Bay of

Bengal and a balding man standing on its deck, and the other an indefinite time before the cyclone, when an English man boards a ship with a lion, to reach the shores of India and start his own circus. The English man arrives in India only to find his woes know no end as the star of his circus - the lion has lost all its mane during the voyage, courtesy an unknown 'microbial disease'. The lion, he laments, now looks no different from a 'hairless street dog'. Desperate and devastated, the English man tries everything and when all else fails, he visits an Indian holy man, where the English man's unending antics to prove his devotion earns him a bottle of hair oil from the monk for his lion. The hair oil incidentally not only grows back the lion's mane and saves the English man's circus, it then finds its way onto the shelves of shops and in advertisements in print describing its miraculous hair-recovery properties. A young girl buys this hair-oil and packs it in the bag of her balding father, about to go travelling on a ship - as recommended by his doctor for a change of air.

This brings us to moments before the cyclone hits, when the balding man stands on the deck of the ship. Holding the bottle of hair oil in his hand, he suddenly remembers having read somewhere in some scientific article that oil can calm waves on the surface of water. As the waves bellowed, he throws the bottle of hair oil - which from the Indian monk to the English man to the hairless lion to the young girl to the balding man now falls on the waves of the sea. As the first drop of oil touches the waters, it spread across almost instantaneously, almost like a miracle - stilling all the waves of the ocean - creating the calm of a storm that was to be, but never was.

The story ends with the line -

'Who would know how many millions of lives
were saved by a mere bottle of hair oil!'

Not aliens or time machines or extraordinary voyages or the modern Prometheus[1], what marks the beginning of science fiction in India is a bottle of hair oil. However, it is not just a bottle of hair oil, the short story also has hidden within it the idea of sensitivity to initial conditions - the idea that characters in a complex system may not know how small changes at their end may affect someone else somewhere or trigger a series of events that may drastically alter the global outcome, influencing everyone's lives - what lies at the heart of Edward Lorenz's celebrated talk, eighty years later - 'Does the flapping of a butterfly's wing in Brazil set off a tornado in Texas?'[2]

1 To give a timeline, H. G. Wells published 'The Time Machine' in 1895, and 'The War of the Worlds' in 1898, Jules Verne published 'Voyage au centre de la Terre' in 1864, and Mary Shelley's 'Frankenstein' is in 1818.

2 Interestingly, Lorenz had previously used seagulls instead of butterflies in his discussions on sensitivity. Nevertheless, in science fiction, the 'Butterfly Effect' is typically

Coming back to the hair oil, sadly a bottle of hair oil cannot stop a cyclone. It can, however, calm the ripples on a water surface, spreading molecularly thin on it - a real physical phenomenon that inspired this story. In the spirit of the chain of causal links from the story, we can now go back in time to trace the origins of *this* phenomenon - to London in early 1890-s where the author was a student of Lord Rayleigh, who was then experimenting on the effect of oil spreading on water, even performing public demonstrations of the same, developing his famous 1892 lecture series[3] inspired by Thomas Young's *Course of Lectures on Natural Philosophy* of 1807, from where this effect can be traced back to a fleet of 96 ships sailing across the Atlantic in 1757. And, in one of those ships was Benjamin Franklin, who noticed that the cooks had been emptying greasy water onto the sea and this had stilled the waves in the water between adjacent ships[4] [5]. Franklin verified this effect in an experiment at the Clapham pond in the 1770-s, and in one of his letters to William Brownrigg, dated November 7, 1773, he wrote

'But (oil) when put on water it spreads instantly many feet around, becoming so thin as to produce the prismatic colors, for a considerable space, and beyond them so much thinner as to be invisible, except in its effect of smoothing the waves.'

From Franklin to Young to Rayleigh, across a hundred years and ten thousand miles, the story of *the calming of waves by the pouring of oil* reached Calcutta in 1896 - with *Sir Jagadis Chandra Bose*, who alongside being a remarkable physicist, botanist and thinker, was also an exceptional storyteller and the writer of the first science fiction in India, *'Polatok Toophan'*.

We would not be stilling any waves in this work, but we will see how oil, water and solids can come together to exhibit some original phenomena. This thesis is written in the spirit of Bose - the remarkable experimentalist and author that he was - who did not merely still the waves, who annihilated cyclones.

---

attributed to Ray Bradbury's 1952 short story, 'A Sound of Thunder' where the death of a butterfly alters timelines and brings fascism. *'Polatok Toophan'* predates 'A Sound of Thunder' by 56 years [4].

3 We would be remiss here if we do not mention the contribution of Agnes Pockels, a German woman who had been denied schooling and yet had been experimenting all by herself with oil films since 1881. She made her first observations while washing dishes in her kitchen and wrote a letter to Lord Rayleigh with her observations in 1891, which he subsequently published in *Nature*.

4 Franklin is only a thousand years too late to be the first one to make this observation, the first recorded observation being that of *Pliny the Elder*, a Naturalist who died in the eruption of Mount Vesuvius in 79 AD.

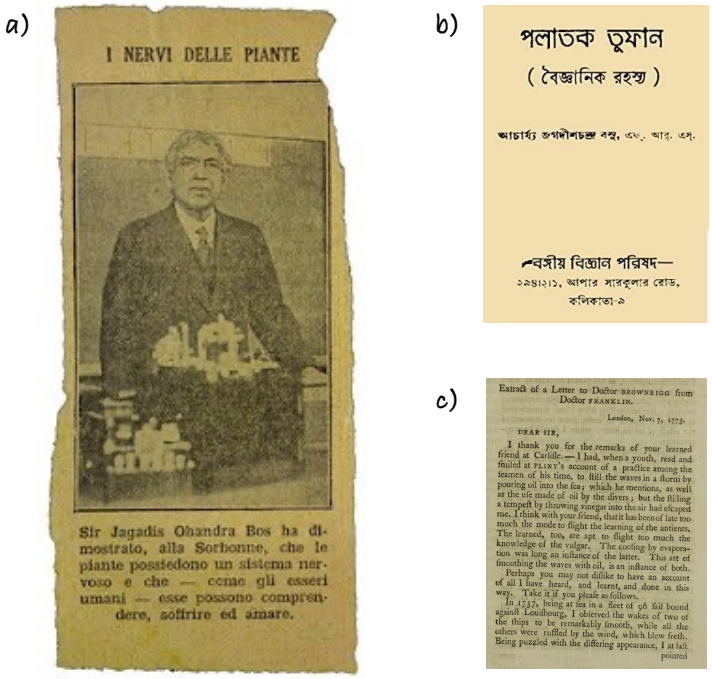

Figure 1: **He who annihilated cyclones.** a) Sir Jagadis Chandra Bose at the Sorbonne University in 1926, giving a series of lectures on *the nervous system* of plants. b) Cover of the original print of *Runaway Cyclone* in Bengali, first written in 1896, as published by *Bangiya Bigyan Porishad*. The heading reads *Polatok Toophan* phonetically in Bengali. c) The original letter of Benjamin Franklin to his friend William Brownrigg dated November 7, 1773, in which he mentions his observation of the stilling of the ocean waves by greasy water.

Part I

HEMI-SOLID, HEMI-LIQUID

2

A CLASS OF NEW MATERIALS

In this chapter, we describe what is a liquid-infused solid - its historical development and properties. In the process, we also touch upon various discoveries in the field of capillarity and how that helps us understand these special materials.[1]

Sketched maps of Calcutta and Paris circa 1890 *with two strips of paper cut out in the shape of the rivers Ganges and Seine, and placed over the sketch. When the two strips are infused with an aqueous solution of red and green dye, we see a liquid-infused Ganges and a liquid-infused Seine running through the cities of Calcutta and Paris.*

1 Acknowledgements to *Aditya Jha* for several pictures, and sugar cubes for *Joachim Delannoy*.

2.1 SOLIDS, LIQUIDS AND LIQUID-INFUSED SOLIDS

For more than half a century, a Korean man in Paris obsessively painted water drops, and water drops alone - drops that were static or in a run, drops that were in a crowd or had been shunned. In January 2021, he passed away. We begin our discussion with two creations of *'the man who painted water drops'* - Kim Tschang-yeul.

Figure 2: **The man who painted water drops.** Two creations of Kim Tschang-yeul (1929-2021), who painted only water drops in different forms and abstractions for fifty-two years. Left: *Waterdrop*, painted with Indian ink and oil on wood. Right: *Five Drops*, painted with tinfix and oil on canvas.

In Fig. 2, we see two of his paintings. On the left, we see a painting of a single drop, set against a red background, its shape, shade and lighting tell us that it is in equilibrium on a wall. On the right, we see dynamics - a painting of five drops, set against an ochre background, the blurriness of each reflective of the quick pace of the race they are engaged in, each one leaving a trail behind with the remains of itself. Both of these configurations are hidden in the myriad everyday observations of ours of water drops interacting with solid surfaces, where we notice that, generally speaking, some drops run while some drops stay where they are 'happy' in their being. The scientific reasoning behind this difference in behavior of drops on solids often lies in their material conditions - the surface of the solid is not 'perfectly flat'.

The backdrop of the painting here serves as an example of a classical solid that is 'rough'. Said differently, any generic solid, even a chemically homogeneous one, is physically heterogeneous - its surface has 'bumps' and 'troughs', which is why even a flat solid is not 'perfectly flat'. The scale of such roughness on typical solids may range from the order of tens of nanometers to hundreds of microns, the smoothest surface discovered till date being freshly cleaved mica

where asperities are of the order of a single nanometer[6]. A consequence of the inescapable existence of roughness on solids is that droplets may get pinned on these asperities, and not move even when driven by a force like gravity, as we see in Kim's painting.

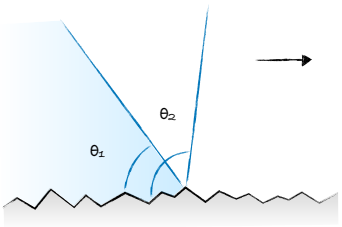

Figure 3: **Pinning**. Sketch of a liquid front moving on a generic solid surface. The physical heterogeneities at the solid surface allow for a multiplicity of angles, denoted here by θ_1 and θ_2 to be exhibited at the contact line, which remains 'pinned' locally at these defects.

A liquid interface on the other hand is atomically smooth. Thus, a drop of oil on an air-water interface has no possibility of being pinned and if pushed, would move 'freely'. There could, of course, be other sources of dissipation as viscosity of the drop and the medium but the onset of motion of the drop would not be inhibited by pinning defects, as is the case on a solid.

To understand the nature of pinning on classical solids and how to minimize them has been one of the most ponderous quests in the field of soft matter. One may even say that a solid with no pinning whatsoever is equivalent to *the holy grail* in the field of surface sciences. To this end, if one were to pour some liquid (say, oil) on a solid, then deposit a drop of an immiscible liquid (water) on it, it could be argued that the drop would not 'feel' any pinning defects, making it seem that achieving the *grail* was apparently quite trivial, after all! Alas! The above solution, although remarkably simple and not without merits, is truly no solution at all, the biggest caveat being that in this case it is not only the drop that is 'free' to move, but the film too, that is free to flow. Furthermore, the deposited drop would be partially submerged in the film, and the situation would be analogous to that of a liquid on a liquid (immiscible), with barely any signature of the solid at all.

Similar other two attempts at the 'grail' have been Leidenfrost surfaces and superhydrophobic surfaces.

However, if we could 'lock' the film or suffuse it into the solid in a microscopically thin layer so that it would be just enough to minimize the pinning defects but not enough to freely flow, to not completely overfill and have liquid over the solid yet allow the possibility of the drop to slip on the solid below, then in principle we could have a material that is truly ambiguous between a solid and a liquid. But,

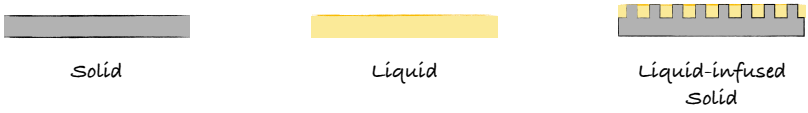

Figure 4: **Three Classes of Materials.** Left to right - a classical solid, a classical liquid, and a liquid-infused solid.

is such a solid possible? How does one even 'lock' a microscopically thin layer of liquid on top of a solid?
It is.
And, the specific process in which a microscopic layer of liquid is preserved on top of a solid is called *hemi-wicking*. In the subsequent sections, we discuss how to make these surfaces, their original properties and historically how they came to be, and also the physics and details of *hemi-wicking*. But, first we give the definition of a liquid-infused surface -

A liquid-infused solid is a class of materials
that are hemi-solid and hemi-liquid
and created by hemi-wicking.

It is imperative that we define *'hemi-wicking'* now, but before that we must meet *wicking* and *wetting* - the *Remus* and *Romulus* of Capillarity.

2.2 WICKING AND WETTING

2.2.1 *Wicking*

We start with a cup of coffee. If we bring a cube of sugar in contact with the coffee, we immediately observe that the coffee invades into the solid, percolating through the porous network of the sugar cube, as seen by the distinctive change of color (Fig. 5). This invasion of the liquid into a solid is called *wicking*.

A necessary condition for imbibition is that the solid must be porous, or must have a network of capillaries within. A second condition is that the liquid must have an affinity for the solid. In other words, if a drop of the liquid were deposited on the surface of a non-porous version of the solid, it makes a contact angle θ that is less than $\pi/2$. The first condition of a network of capillaries also requires the dimension of the capillaries to be necessarily smaller than a critical size κ^{-1}, also called the capillary length.

The capillary length is a threshold length, beyond which gravity becomes dominant. This can be visually observed by placing drops

Figure 5: **Sugar Cubes and Coffee.** A classical example of wicking is a sugar cube brought in contact with coffee. Inset shows snapshots at 0.3 s intervals after contact. The distinctive change in color shows the front of the liquid (coffee) that wicks through the three-dimensional porous medium of the sugar cube.

of different volumes on a flat solid surface, as shown in Fig 6, where drops of volumes 5μL, are placed on a superhydrophobic surface. We observe from the experimental image that as the droplet volume increases, its shape transitions from that of a spherical to a puddle. In other words, the height of the drop increases with volume until a certain size of the drop, where it saturates. This is because there are two antagonistic forces here at play - capillarity, which wants to minimize the surface energy γA of the drop, where γ is the surface tension of the liquid and A is the surface area, and hence favors the drop being spherical (as a sphere has the minimum surface area for a fixed volume), and gravity, which flattens the drop. The capillary length can be estimated by comparing the Laplace pressure γ/κ^{-1}, where γ is the surface tension of the liquid with the hydrostatic pressure $\rho g \kappa^{-1}$, where ρ is the density of the liquid and g is the acceleration due to gravity. A balance of the two yields the threshold length to be

$$\kappa^{-1} = (\gamma/\rho g)^{1/2} \tag{1}$$

For water, $\gamma = 72$ mN/m, and $\rho = 997$ kg/m^3, which gives the capillary length to be $\kappa^{-1} \approx 2.7$ mm. For a drop, it can be shown that beyond a volume $\Omega > \kappa^{-3}$, the height of the puddle becomes a constant at $h \approx \kappa^{-1}\sqrt{2(1-\cos\theta_e)}$, where θ_e is the equilibrium contact angle of the liquid on the solid. The millimetric magnitude of capillary length of water implies that there are six orders of magnitude from the atomic scale to κ^{-1} where surface forces dominate. This has far reaching consequences from dictating the size of rain to the flow in our veins, which have also allowed us to engineer on mi-

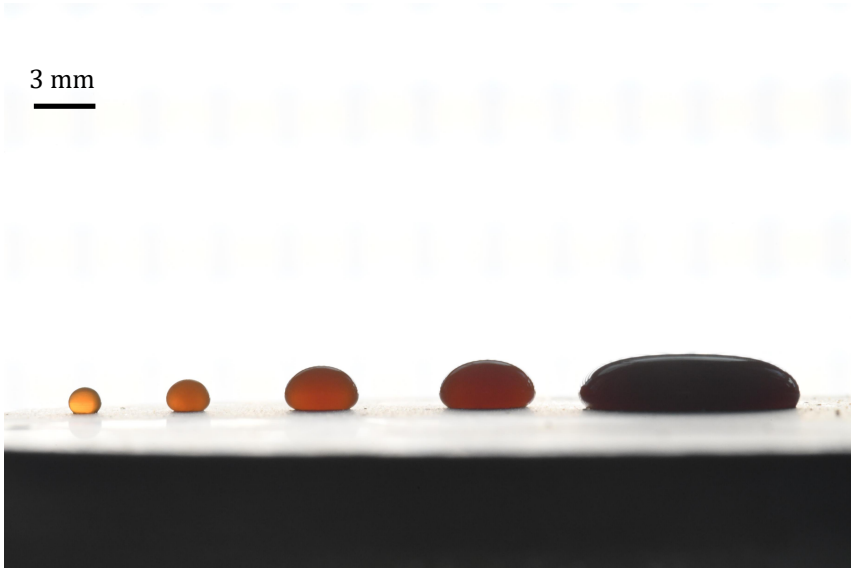

Figure 6: **Capillary Length.** Coffee drops of volumes $\Omega = 5\mu L$, $10\mu L$, $50\mu L$, $100\mu L$ and $500\mu L$ deposited on a superhydrophobic surface. The bigger, the darker, but also the flatter.

croscopic scales such that there are macroscopic manifestations - a liquid-infused solid being one of the many such examples.

Back to the imbibition, we have established that a necessary (not sufficient) criterion for imbibition is that the solid must be porous and the pores must have a dimension less than κ^{-1} that is ≈ 2.7 mm for water. In this sense, a simplified version of *coffee wicking into a sugar cube* is coffee rising up a capillary. In Figure 7, a thin capillary tube of $250\mu m$ is gently brought in contact with a cup of coffee, when we see the coffee quickly invades into the capillary and subsequently slows down to come to an equilibrium at a height of ~ 4 mm.

Now that we stand at the footsteps of the founding experiment of capillarity, we would be remiss if we did not take a short historical detour.

2.2.1.1 *The Age of Enlightenment:*

The phenomenon of wicking has been known to humans, in some shape or form, for millennia - as long as humans have known how to make oil wicks, in lamps, lanterns and torches. This can be traced back to at least the Iron Age $\sim$ 700BC, when the Inuits as well as the Chinese were lighting oil lamps with fibrous wicks to illuminate their parts of the world [7, 8].

However, the distillation of the phenomena of wicking into an experiment of capillary rise in a narrow tube did not happen until Robert Boyle's experiment on capillary rise in 1682 [9]. Although, mentions of the capillary rise appear even in da Vinci's writings (as

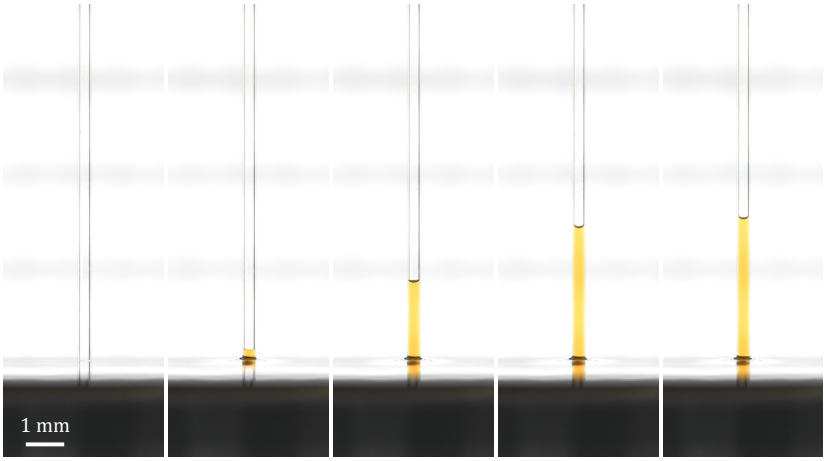

Figure 7: **Capillary Rise of Coffee.** A narrow capillary tube of 250 µm radius gently touches the top of a cup of coffee. We see the coffee quickly rises up the tube and then slows down to finally equilibriate at a height above 3 mm. Successive snapshots are at an interval of 0.2 s.

possible mechanisms of mountain springs), Hardy's account on the history of capillarity distinguishes Boyle's experiment as the starting point on the study of surface energies and short-range forces[10, 11]. Boyle's experiment greatly enthused seventeenth and eighteenth century philosophers as evident in the words of the astronomer Joseph Jérôme Lefrançois de Lalande: [10]

'Many phenomena are regarded as allied to those of capillary tubes ... e.g. the suction of sugar and of sponges, the origin of springs in elevated sites; the secretions in the human body seem to be due to the same cause ... Capillary tubes put into our hands an obvious example of the generality of this law, which is the keystone of physical science.'

By 'law', de Lalande refers here to general attraction of matter, that had been previously debated for long.

Of the many investigators of the time, the person often forgotten who made seminal contributions to the understanding of capillary rise is Francis Hauksbee (1713). He was even forgotten by his colleague of Newton, in the passage of *OpticKs* where he describes capillary rise. [12]. Hauksbee was an experimentalist par excellence who showed through his experiments that the phenomenon of capillary rise in narrow confinements is not specific to a particular solid or a liquid, neither is it driven by the presence of air, as it occurs in a vacuum too. Furthermore, the height of the rise is the same in two tubes of the same diameter, even if one of them has a wall that is ten times thicker - proving that the attraction between liquids and solids is dictated by the area of surfaces.

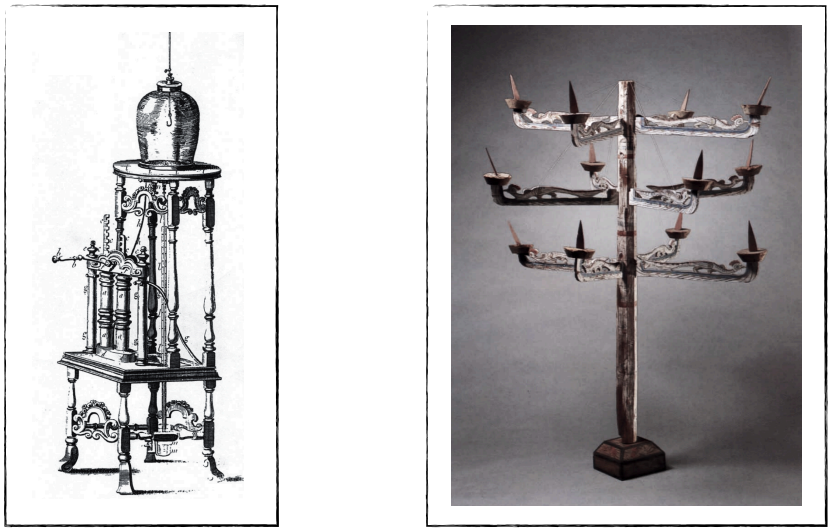

Figure 8: **Hawksbee and Chinese Oil Lamps.** Left: The double-barrelled air pump of Francis Hauksbee (1705) which he used to perform experiments on capillary rise in vacuum. Reproduced from *Francis Hauksbee's Physico-Mechanical Experiments (London, 1719)* [13]. Right: the largest excavated Chinese oil lamp dating back to the *Sixteen Kingdoms, Former Liang dynasty* (314-76 AD). The lamp is four foot high with three tiers and twelve branches. The curved end of each branch has an oil tray with a wooden wick extending from it. Reproduced from *China: Dawn of a Golden Age, 200-750 AD* [7].

However it was not until a century later that a complete understanding was developed with Laplace (1806). We may succinctly describe it here as follows.

If γ, γ_{sv}, and γ_{sl} be the surface energies of the coffee (liquid) with respect to air, solid with respect to air and solid with respect to coffee and R the radius of the capillary, then we may write the energy of the system when the liquid has invaded into the capillary by an extent h as $E = -2\pi r h(\gamma_{sv} - \gamma_{sl}) + (1/2)\pi r^2 h^2 \rho g$, where the first term represents the gain in surface energy and the second term corresponds to the loss in gravitational potential energy, and we have ignored the contributions of the meniscus, which is valid when $h \gg R$. We now substitute $\gamma_{sv} - \gamma_{sl}$ by $\gamma \cos\theta_0$, that we can obtain from a balance of the surface tension forces at the contact line. This relation is also known as the Young's Equation, which we discuss in the next subsection. Minimizing E with respect to h gives us

$$H = 2\gamma \cos\theta_0 / \rho g R, \tag{2}$$

where H is sometimes known as the Jurin's height. Equation 2 reveals that firstly, all of Hawksbee's observations hold - there is no influence of air, pressure, thickness of walls, and the height varies as R^{-1}. We also note that for capillaries of the size of tens of microns, water may rise to $\sim 1\,m$ on perfectly wetting solids ($\theta_0 \approx 0$). In the context of a porous medium the radius would be replaced by the smallest pore radius. Furthermore, the limiting height is only a consequence of vertical capillaries. For a horizontal capillary, the imbibition is unbounded (the limit $g \to 0$ in Equation 2).

2.2.1.2 *Dynamics*

While an understanding of the statics and energetics of wicking developed in 1806, the dynamics would not be laid down until a hundred years later in 1906 by J. M. Bell and F. K. Cameron. Unfortunately, Bell and Cameron's contributions are often forgotten in the light of the works of R. Lucas and E. W. Washburn who independently described the dynamics a decade later [14–16]. The impregnating flow has a Poiseuille nature which leads to a viscous friction that scales as $F \sim \eta V z$, where z is the length of imbibition. The driving force being given by $F \sim \gamma R \cos\theta$, when gravity can be neglected ($z \ll H$) a balance of the two gives us the Washburn's law, rather the Bell-Cameron-Luas-Washburn's Law

$$z \sim (\gamma R \cos\theta/\eta)^{1/2}\ t^{1/2} \tag{3}$$

The law reveals that the dynamics of wicking is 'diffusive' in nature, that is $z \sim t^{1/2}$. The $1/2$ law also tells us that the invasion of the liquid is fast in the beginning and becomes slower and slower as time progresses, as the front moves further and further away from the source. In the case of porous materials, Washburn's law can be used to determine a mean pore size or porosity of the material.

Another observation regarding the Washburn's law is that diverges at short times, as $t \to 0$. This was brought to attention in the 1990-s by David Quéré, where he noted that the singularity can be resolved by considering inertia which becomes dominant at such scales. The inertia of the liquid scales as $\rho R^2 z V$ which when balanced by capillarity we get the inertial law of imbibition at small time as

The divergence was first remarked on by C. H. Bosanquet in 1923 soon after Washburn published the dynamical law of imbibition [17].

$$z \sim (\gamma \cos\theta/\rho R)^{1/2} t, \tag{4}$$

which gives a speed $\sim 10\,cm/s$ for millimetric tubes. Such a law would be dominant up to a time scale $\tau \sim \rho R^2/\eta$, which also can be looked upon as the time required for the flow to form a viscous boundary layer across the tube. Once the boundary layer has invaded the tube, the dynamics crosses over to the Washburnian regime, or comes to rest, depending on the properties of the liquid and the solid used.

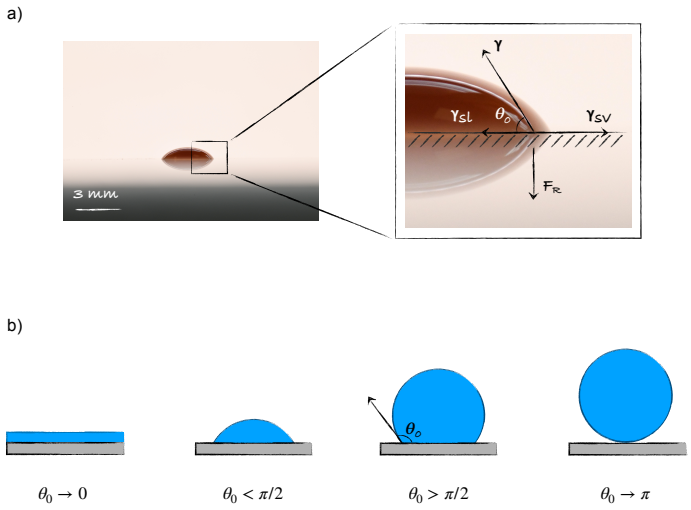

Figure 9: **Wetting.** a) A classical example of wetting: a drop of coffee deposited on a glass plate. Inset shows a zoom-in of the contact line, that exhibits a contact angle θ. The three surface tension forces acting at the contact line are sketched on the experimental image. b) The three cases of wetting categorized by the Young contact angle - *complete wetting*, *partial wetting*, *poor wetting* and *non-wetting* (from left to right).

2.2.2 *Wetting*

If a drop of coffee were to spill onto a glass plate, it would spread out on the surface in the form a spherical cap and come to rest at its equilibrium contact angle θ_0 (Fig. 9). This is called *wetting*, more specifically *partially wetting* as the contact angle θ_0 is less than $\pi/2$.

The key difference between wicking and wetting is that, for wetting, the solid must have the impenetrability condition, that is it must be non-porous. As we will see, classical solids may be non-porous, but they are never 'perfectly flat', which consequently affects the contact angle θ_0 .

In 1805, in one of the series of founding articles that marked the beginning of the field of wetting, Thomas Young proposed a relationship between the contact angle and the surface tension of the three media, now famous as *Young's Equation*, based on which successive ideas on wetting developed [18]. The Young relation can be derived by considering a force balance at the contact line, where the three interfaces - liquid-air, liquid-solid and solid-air meet. Thus, three forces of capillarity γ, the surface tension of liquid with respect to air, γ_{ls}, the surface tension of solid with respect to the liquid and γ_{sv}, the surface tension of solid with respect to vapor, act on this line, parallel to the three interfaces, along with an additional vertical reaction force

Curiously, Young never explicitly wrote the equation in his original article of 1805 [18].

F_R by the solid to maintain equilibrium. A balance of the horizontal components of the force yields

$$\gamma \cos\theta_0 = \gamma_{sv} - \gamma_{sl}. \tag{5}$$

A natural conclusion that follows from Equation 5 is that fixing the three media that meet at a contact line should fix the contact angle too. Sadly that holds only for the academic example of a perfectly flat, physically and chemically homogeneous surface, as was considered by Young. As discussed before real solids are characterized by pinning defects, that allow a drop to exhibit a range of contact angles while remaining in equilibrium. The difference between the maximum and the minimum of these angles, $\Delta\theta = \theta_a - \theta_r$, is called *contact angle hysteresis* and is a measure of the defects on the surface.

The existence of pinning diminishes the applicability of the Young relation for real surfaces. Nevertheless, for the ideal case of a solid with no pinning, important limits can be drawn from Equation 5. First, the surface tension values being independent of each other, it is possible that $(\gamma_{sv} - \gamma_{sl})/\gamma$ is greater than 1. This corresponds to the case of *complete wetting*. In other words, as put by Marangoni, physically the relation $\gamma_{sv} > \gamma + \gamma_{sl}$ means that a high energy solid prefers to lower its surface energy by completely covering itself with a low-energy liquid, a typical example being a drop of silicone oil deposited on a glass plate in air.

The converse case where the two fluids are switched - a bubble of air approaching a glass slide surrounded by a medium of silicone oil, demonstrates *non-wetting*, where in Equation 5, $(\gamma_{sv} - \gamma_{sl})/\gamma$ is lesser than - 1. In both the cases of *perfect wetting* and *non-wetting*, we see the contact line vanishes because Equation 5 does not allow a solution for the equilibrium angle θ_0.

However, the non-wetting limit of $\theta_0 \to \pi$ cannot be achieved for a water drop on a solid in air. The chemical limit of hydrophobicity is $\theta_0 \approx 120°$ (for fluorinated materials such as Teflon), which is far from 180°.

The 1990-s would see a series of breakthroughs in approaching the limit of non-wetting beyond the chemical limit. This in conjunction with the quest to create a solid with no pinning would be become one of the driving forces of the research in the 90-s, and thereafter.

2.2.2.1 *The 'Rough' 90-s.*

Three key events marked a change in the course of wettability research which led to the discovery of superhydrophobicity.

First, in 1996-1997, the Kao Group from Japan showed that if a surface be made sufficiently rough, then the limit of 120° can be broken. In a series of experiments they showed different chemical processes

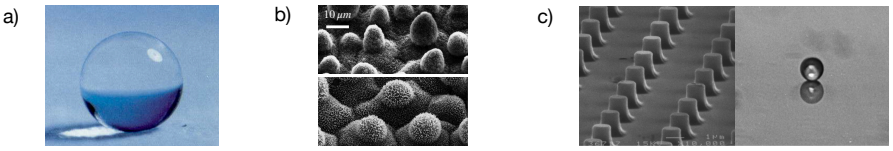

Figure 10: **Foundation of Superhydrophobicity**. a) The 1996 experimental image of a *pearl drop*, as reported by the Kao group - Onda, Shibuichi, Satoh and Tsujii in *Langmuir*. b) The 1997 SEM images of hierarchical structures on lotus and taro leaves by Neinhuis and Barthlott in *Planta*. c) The 1999 image of lab-made patterns leading to pearl drops by Bico and Quéré in *Europhys. Lett.*.

in which this may be achieved, one of which is anode oxidation of an aluminum surface, followed by a chemical vapor deposition with fluorinated silanes. Such a chemical process created fractal-like rough surfaces where deposited water drops looked like pearls with angles as high as 174°.

Second, in 1997 Neinhuis and Barthlott reported that water drops exhibit contact angles larger than 150° on a plethora of natural biological surfaces like lotus and eucalyptus. These surfaces are wax-coated (hence, hydrophobic chemically) and then functionalized by bumps of the scale of $\sim 10\mu m$, which are further decorated with hairs, typically $\sim 1\mu m$ creating a hierarchically rough surface which allows the contact angle to be far beyond the chemical limit. Such functionalized surfaces are not limited to just leaves but are also seen on water strider legs and butterfly wings.

Third, in 1999, José Bico and David Quéré showed that by building micrometric posts on a hydrophobic solid, one can induce superhydrophobicity - jump from a contact angle of 110° on a bare silicon wafer to 160° on the textured surface. By controlling the spacing of the pillars, and pillar dimensions from 100 nm to $100\mu m$, the extent of superhydrophobicity may be tuned as desired. The different limits and physics of obtaining non-wetting may now be studied in detail.

In one word, what these three works brought to the world of wetting is *texture*.

There exists a second state, called the Wenzel state where the drop is stuck inside the texture and exhibits a much larger hysteresis and relatively smaller contact angle than what is observed in the Cassie state.

Physically, the effect of a (hydrophobic) texture may be explained as follows: a drop sitting on top of a hydrophobic surface decorated with texture (known as *Cassie state*) is sitting on part-air (where $\theta \to 180°$), part-solid (where $90° < \theta \leqslant 120°$), which leads to an averaging of the contact angle that allows θ to exceed the chemical limit. Furthermore, the solid-liquid contact becomes minimal because the drop is sitting on pillar tops and is very spherical, leading to a significant decrease in pinning and thus, hysteresis. Said differently, roughness - the very property of classical solids that makes pinning its signature, can be used to minimize pinning itself, if one decorates the defects on the solid appropriately. The effect of texture on contact angle can

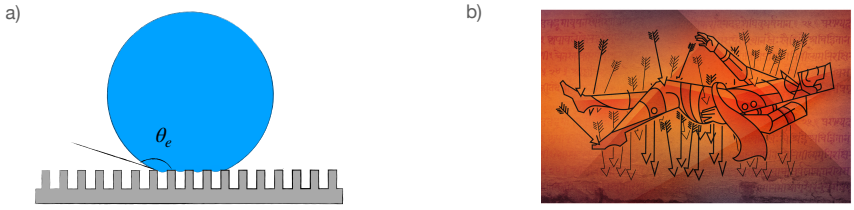

Figure 11: **Cassie and *Bheeshma*.** a) Schematic of a *Cassie* state, where a drop sits on top of the texture of a hydrophobic solid. The *Cassie* state is also reminiscent of the death of the near-immortal character of *Bheeshma* in the Indian epic *Mahabharata*. In his dying moments during the battle of *Kurukshetra*, *Bheeshma* lay on a bed of arrows much like a *Cassie* drop, as we see in this painting by Aniket Mitra in b) [23].

be captured as a function of the roughness and solid fraction by minimizing he surface energy in conjunction with the Young's relation, which was first derived by Cassie and Wenzel in 1930-s and 40-s, in their work on apparent contact angle [19–22].

2.2.3 *Hemi-wicking*

In the last section, we noted that the addition of texture on a hydrophobic solid renders it superhydrophobic. It becomes natural to now ask what would happen if the textured surface is brought in contact with a wetting liquid, like silicone oil which is wets hydrophobic solids. Figure 12 shows a schematic of such a situation where a hydrophobic (that is, oleophilic) solid decorated with texture is brought into contact with an unbounded reservoir of oil.

This leads to the oil invading through the roughness, in a two-dimensional wicking (hence, the name hemi-wicking). This is shown in Figure 13 where a textured solid with 90 μm high pillars is brought in contact with a reservoir of silicone oil of viscosity $\eta = 19$ mPa-s. Successive snapshots reveal how the oil wicks through the texture in such a way that at the end of the filmification, a distinct meniscus can be seen between the texture, as are the pillar tops.

We now discuss the specific conditions for such filmification. Let r be the roughness of the textured surface and ϕ_s the solid fraction. This means r is the ratio of the true surface area over the apparent surface area of the solid, and ϕ_s is the ratio of the surface area of the pillar tops over the apparent solid surface area. Therefore, we have $r > 1$ and $\phi_s < 1$. If we consider the case where only the cavities are filled, but the pillar tops remain emerged in a situation of partial

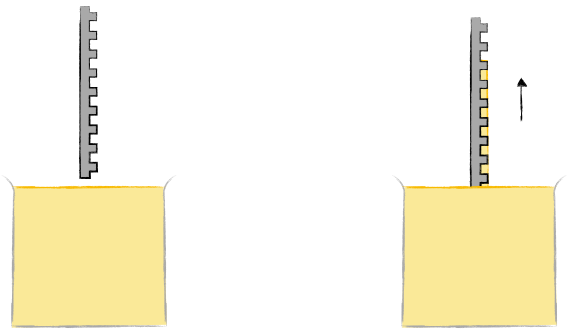

Figure 12: **Hemiwicking** Schematic of *hemiwicking* or *rough wetting*. A textured solid is brought in contact with a reservoir of wetting liquid. The liquid invades into the roughness, in a two-dimensional wicking phenomenon.

wetting, the variation in energy dE (per unit width) corresponding to the progression of the film by a length dx can be expressed as

$$dE = (\gamma_{sl} - \gamma_{sv})(r - \phi_s)dx + \gamma(1 - \phi_s)dx, \tag{6}$$

where we neglect both gravity and the curvature of the film in between the texture, a reasonable assumption given the film and the reservoir have the same curvature as the pressure is constant inside the liquid. The first term on the left hand side corresponds to the filling of the cavities whereas the second term corresponds to creating new liquid-air interfaces. The criterion for hemiwicking would correspond to a lowering of surface energy by the filling of the texture. Using Young's relation, it follows that hemiwicking would occur if $\theta < \theta_c$, where

$$\theta_c = (1 - \phi_s)/(r - \phi_s) \tag{7}$$

We may now test Equation 7 to see if we can recover its different limits. First, for a three-dimensional porous medium, $r \to \infty$. This gives us $\theta_c = \pi/2$, which agrees with the necessary criterion for three dimensional wicking previously discussed: $\theta < \pi/2$. Second, for complete wetting on a flat surface, $\phi_s = 1$, which gives us $\theta_c = 0$. This corresponds to $\cos\theta > 1$, that is $\gamma_{sv} > \gamma_{sl} + \gamma$ which is indeed the Marangoni condition for perfect wetting.

Furthermore, Equation 7 may not only be utilized to design textured surfaces that can be hemi-wicked, we may also probe the question of hemiwicking into a disordered rough surface, where ϕ_s is phenomenological. A sufficient condition for imbibition into a generic

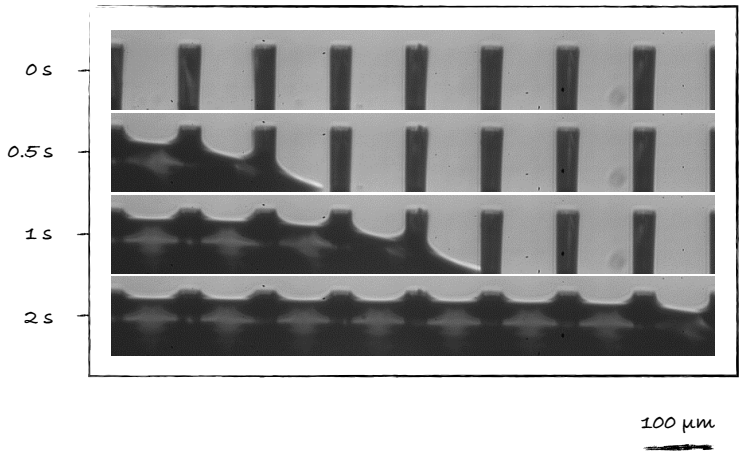

Figure 13: **Timelapse of Hemiwicking.** Successive snapshots of imbibition of silicone oil of viscosity $\eta = 19$ mPa-s, when a textured solid with pillars of height $h = 90\,\mu m$ is brought in contact with a reservoir of the same. At the end of the hemiwicking process, the spaces between the pillars are filled with oil which have a distinct meniscus, and the pillar tops are free. This is the signature of a perfectly infused surface, which is not overfilled. Images by Daniel Beilharz.

rough surface is $\cos\theta > 1/r$. Said differently, the limit $\phi_s \ll 1$ greatly simplifies the case of hemiwicking into disordered rough surface.

The phenomenon of *rough wetting* was first shown by José Bico and David Quéré in 2001, where they laid out these conditions for hemiwicking [24]. The dynamics of hemiwicking can be obtained by balancing capillary forces with viscous dissipation which leads to a Washburnian diffusive law analogous to Equation 3 with an added prefactor of $(\cos\theta/\cos\theta_c - 1)^{1/2}$. Subsequent works revealed various other features of hemiwicking like how morphology of texture can influence the diffusivity or lead to polygonal spreading [25–29].

Now that we have discussed hemiwicking, we come to liquid-infused solids: how to construct them, manipulate them and what is special about them. In the subsequent sections, we also give a brief synopsis of what has been done and *what is to be done*.

2.3 THE LIQUID-INFUSED SOLID

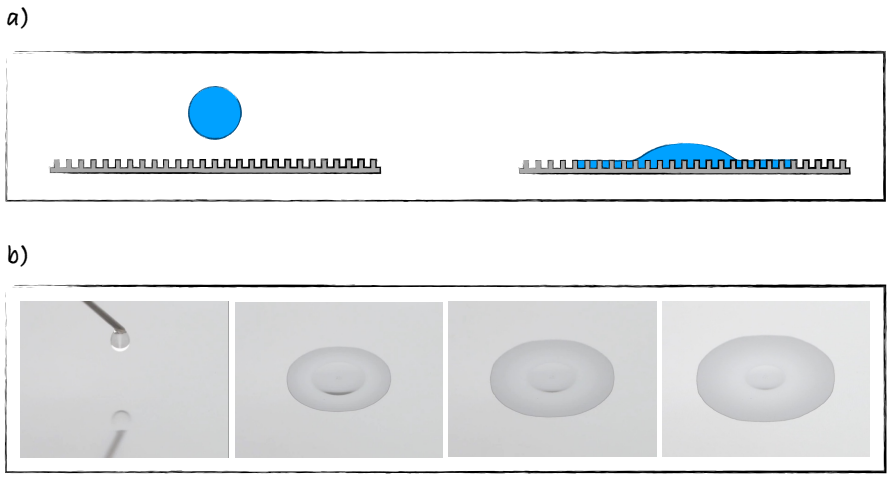

Figure 14: **Remus and Romulus.** a) Schematic of a wetting drop being deposited on a textured solid, which leads to a simultaneous wicking and wetting with two distinct fronts. b) A milimetric drop of silicone oil of viscosity $\eta = 19$ mPa-s deposited on an oleophilic textured solid with $h_p = 36\mu$m, pitch $p = 15\mu$m and solid fraction $\phi = 23\%$. Snapshots taken at 4 second intervals. Images by Daniel Beilharz [30].

If wicking and wetting be the *Romulus* and *Remus* of capillarity, Figure 14 illustrates the building of *Rome* - the liquid-infused solid. When a drop of wetting liquid is deposited on a textured surface, (hemi)wicking and wetting can be seen simultaneously in action, as the liquid infuses and spreads across the solid. However, if the volume of the deposited liquid is more than the volume that can be contained within the texture, then the solid at the end of the process would be submerged in liquid. In this context, the death of *Remus*, that is the wetting front is important to ensure that the solid is perfectly infused and not overfilled.

Let us first look at Figure 14, where a millimetric drop of silicone oil is deposited on a textured surface with a solid fraction $\phi = 23\,\%$ and $h_p = 36\,\mu$m and pitch $p = 15\,\mu$m. We see that the drop takes a 'fried egg' like shape where there are two distinct fronts - a hemiwicking front within the texture which is faster and a wetting front of the drop spreading on top of the textured suffused with the liquid. The extent of the liquid at the top is also eventually being fed into the wicking inside the texture. This leads to the radius of the wetting front increases and then decreases until it vanishes at a certain point, where only the wicking front remains.

However there is no volume constraint on the drop in this experiment, implying that the texture at the end might be overfilled with the liquid, as shown in Figure 15. A simple solution to ensure that is

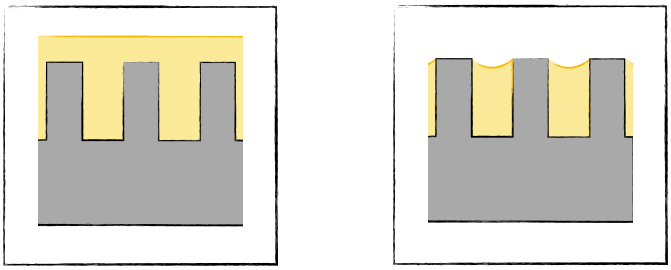

Figure 15: **Overfilled and Perfectly Infused Textured Solids** Left: Sketch of an overfilled textured solid, which is functionally not too different from a flat solid with a thin film on it. Right: Sketch of a perfectly infused textured solid, created by hemiwicking.

to bring the textured surface in contact with the reservoir vertically, in which case, only the hemiwicking front exists from the beginning to the end, as shown in Figure 12. The solid we construct in this process is hemi-solid, hemi-liquid, an ambiguous material between a liquid and a solid.

The ambiguity of such a solid is best noted by just depositing a drop of immiscible liquid on it. We illustrate this is Figure 16, where a 4 µL drop of water is deposited on a textured surface, that has been *perfectly* infused with silicone oil. We see that the drop is hemispherical with a contact angle larger than 90°, as expected on a hydrophobic surface. But the drop has a tiny meniscus, that is typically not visible on macroscopic scale. As shown in the inset, confocal microscopy reveals that there exists a meniscus or *wetting ridge* of $\sim$ 30 µm surrounding the drop. for a drop sitting atop a solid with a thin film, or an overfilled liquid-infused solid, this meniscus is much larger, typically $\sim$ 100 µm [31]. A large meniscus is also a way of roughly estimating whether the texture is overfilled or not.

2.3.1 *Two methods of preparation.*

In this section, we mention two more ways in which a *perfectly infused* textured surface can be made, where hemiwicking is not directly used. The first method has been described by Seiwert et al. [32] and is used by some researchers. The second method is novel.

- **The Landau-Levich-Derjaguin (LLD) Method.**

  When a flat plate is immersed in a liquid bath and drawn out at a constant speed U, a thin film deposits on its surface. In 1942-43, Landau and Levich, and Derjaguin separately showed that when a solid is coated in this manner, the thickness h of the

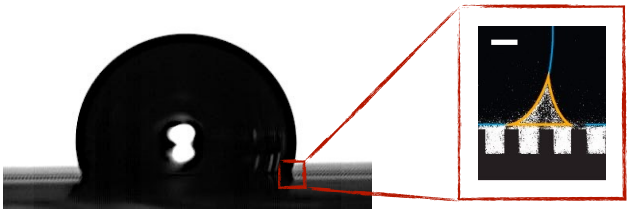

Figure 16: **A drop on an Infused Solid** A 4μL water drop on a perfectly infused solid. The meniscus is difficult to see on a macroscopic scale for perfectly infused solids. Inset shows a representative confocal microscopy image which reveals the meniscus in detail, outlined in yellow. Scale bar corresponds to 20 μm. Confocal microscopy image reproduced from the thesis of Armelle Keiser, taken by Philipp Baumli and Anke Kaltbeitzel at Max Planck Institute for Polymer Research at Mainz.

The LLD law can be derived by balancing of viscous dissipation in the dynamic meniscus with the capillary forces, in conjunction with a matching of the dynamic meniscus with the static meniscus

entrained thin film in such a process (also called dip-coating) is given by $h_{LLD} \approx 0.94\kappa^{-1}Ca^{2/3}$, where $Ca = \eta U/\gamma$ is the capillary number, that is less than 1 [33, 34].

Seiwert et al. in 2010 showed that when the same coating experiment is performed with a textured surface of pillar height h_p, the law is modified as [32]

$$\begin{aligned} h &\approx h_p & U &< U^* \\ h &\approx h_{LLD} & U &> U^* \end{aligned}$$

This critical velocity is given by $U^* \sim (\gamma/\eta)(h_p\kappa)^{3/2}$, below which the entrained film thickness is independent of the drawing speed and equal to the pillar size, h_p (see Figure 17). For typical values of $h_p \sim 10\,\mu m$, $\eta \approx 10$mPa-s, $\gamma \approx 20\,mN/m$ (silicone oil), we get $U^* \sim 1\,mm/s$. This is very helpful to design a workable range of drawing speeds at which we can make infused solids, more efficiently on an industrial scale.

- **Capillary Suction for Perfect Infusions**

  We propose here a novel way to get rid of the excess on an overfilled textured solid. This means the first step is to overfill, which can be by spincoating or just deposition. We demonstrate this in Figure 18, where we deliberately take a textured surface overfilled with 9 mPa-s silicone oil, unevenly distributed all over the surface. A thin capillary tube is now brought in contact with the over-infused solid from the top. Immediately, a capillary rise happens within the tube, creating an annular zone around the capillary tube (dotted red circle), which is perfectly infused, and

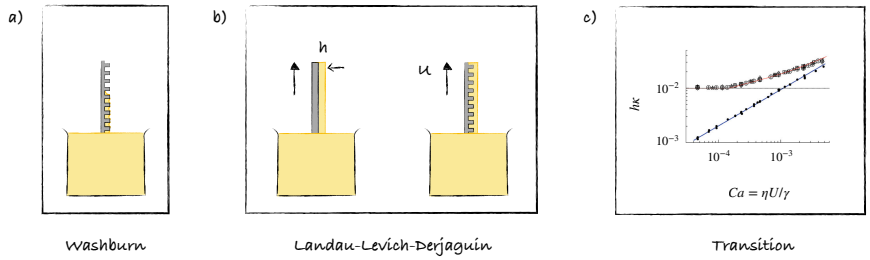

Figure 17: **Making of a Liquid-infused Solid.** Two approaches to make a liquid-infused solid: a) hemiwicking (Washburn), and b) dip-coating (Landau-Levich-Derjaguin). c). Coating thickness normalized by the capillary length plotted against the capillary number, $Ca = \eta U/\gamma$. Full symbols represent experiments on a flat plate, open symbols represent experiments on a textured solid. Straight line represents LLD law and the line through open symbols represents Seiwert's model. Reproduced from [32].

looks like a small 'hydraulic jump'. The rise can be predicted by Hawksbee's law of capillary rise, Eq. 2 and the maximal radius R_p of the zone of perfect infusion can be obtained by equating the volume of the capillary rise, $\kappa^{-2}R$, R being the radius of the capillary tube and the volume drained out, $(h_0 - h_p)R_p^2$, where h_0 is the initial thickness before the capillary tube is brought into contact. This gives R_p as

$$R_p \sim \kappa^{-1} \sqrt{R/(h_0 - h_p)} \tag{8}$$

Typical values of $R \sim 250\,\mu m$ and $h_0 - h_p \sim 10\,\mu m$ predict millimetric lengths of zone of perfect infusion, as can be seen in Figure 18. In order to scale up this process, we would need an array of periodically spaced capillary tubes that are brought into contact with the over-infused surface and removed after capillary suction is complete.

Note that this is just a variant of putting a piece of paper (porous medium) on the over-infused surface to imbibe out the excess. The critical difference being that papers and wipes when brought in contact with liquid-infused solids, almost always leave fibrous residues, which are extremely difficult to remove. These residues get stuck between the texture, sometimes partially sticking out, breaking the homogeneity of the surface and creating defects on the infused surface. A glass capillary tube, in this regard, is clean and has no such concerns.

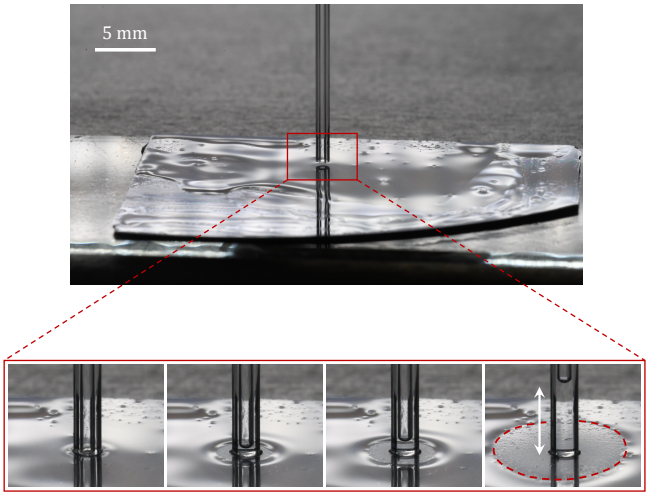

Figure 18: **Capillary Suction for Perfect Infusions.** A capillary tube of 250μm radius is brought in contact with a textured solid (with $h = 20 \pm 5\mu m$, diameter $d = 18\,\mu m$, spacing $p = 15\,\mu m$ and fraction $\phi = 23 - 25\,\%$ that is overfilled and unevenly coated with excess oil. This leads to a capillary rise of the excess liquid front into the capillary, creating an annular region of perfectly infused hemi-solid. Inset shows successive snapshots of the process. The first frame corresponds to the capillary tube coming into contact with the over-filled texture. Subsequent snapshots show how the capillary rise within the tube (white arrow) leads to the growth of an annular region of perfectly infused solid (marked in dotted red circle).

2.3.2 *Historical Development*

The first mention of a class of materials with properties in between solid and liquid, that can be prepared by hemiwicking can be found in the article *Non-sticking Drops* by David Quéré in 2005, where such hemi-wicked solids are referred to as *slippery composite surfaces*, with a short note on their slipperiness and marginal pinning properties. However, it was finally in 2011, when two articles published back to back by the Aizenberg group and the Quéré group elaborated on the potential applications in anti-icing and resistance to damage and the physics of creating such surfaces [37, 38]. The Aizenberg group also highlighted a naturally occurring liquid-infused surface - the pitcher plant of genus *Nepenthes* that has a curiously designed peristome (the rim at the top of the pitcher), functionalized with grooves, infused with a mixture of water and nectar, and the ants *'that step on it to slide from the rim into the digestive juices at the bottom'* (see Figure 19) [37]. This was followed by the Varanasi group identifying twelve different thermodynamic states of water drops on liquid-infused solids for stability of films on infused solids and the combinations of solid and liquid that lead to stable films for robust liquid infused solids [39].

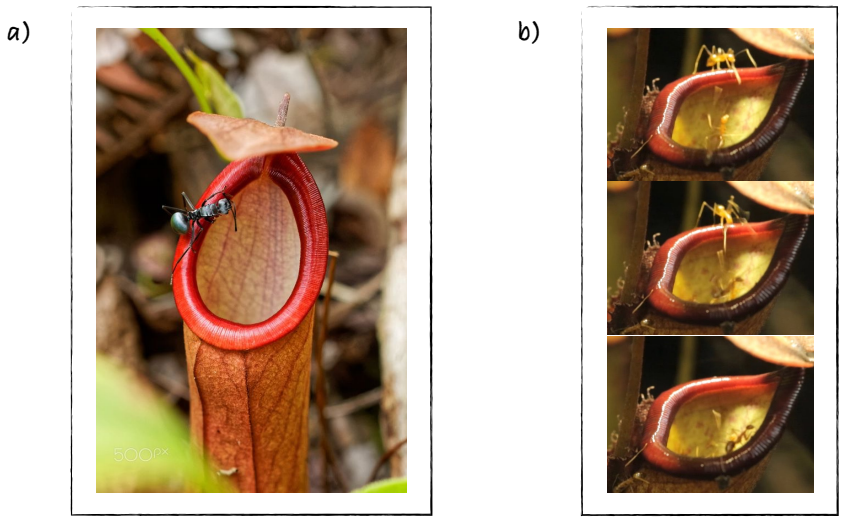

Figure 19: **Curiosity killed the ant.** a) A curious black ant at the rim of a pitcher plant (Picture by Ray Reinhard) [35] b) A yellow ant *Anoplolepis gracillipes* climbs up the infused rim of *Nepethes* sensing some sugar at the bottom of the pitcher. Curious, he 'looks down' and plop he falls! (Images by AntsCanada). [36]

All of these works highlighted the slippery nature of infused solids, where lateral adhesion, that is the force required to move a drop of water on top it was negligible. This adhesion can be measured by performing a classical roll-off angle experiment, where a millimetric drop of water (typically 20 µL) is placed on a solid surface, the inclination of which is increased until the drop rolls off. The adhesion of two surfaces can be compared by comparing the roll-off angles of the two surfaces for a fixed volume of the drop.

For Glaco treatment, dip-coat your textured surface with the Glaco solution, dry the surface and then heat at 150° *for half an hour. Repeat the process three times to get fresh hot nanorough microtextured superhydrophobic surfaces, right off the oven.*

Our common observations of raindrops stuck on windowpanes tells us even a vertical wall sometimes is not enough to detach the drops off the surface. For liquid-infused solids, the roll-off angle α is lower than regular surfaces, close to 10°, which shows that pinning defects are lower than on classical solids. However, the finite value of α is indicative of solid-liquid contact with pining at the pillar tops. This too may be minimized with a hierarchical roughness on the texture, which can be achieved by dip-coating the textured surface with *Glaco* solution (Glaco Mirror Coat Zero fournie par Soft99 Co), that leaves a coating of hydrophobic nanoparticles - *Glaco* beads of a few tens of nanometers on the surface [41]. When the textured surface is now brought in contact with an oil reservoir, oil wicks through the nanoroughness at the top as well, and this nanometrically thin film on top the pillars is stabilized by a positive disjoining pressure [42]. A direct consequence of this can be seen in the roll-off angle which becomes immeasurable, indicating a vanishing lateral adhesion.

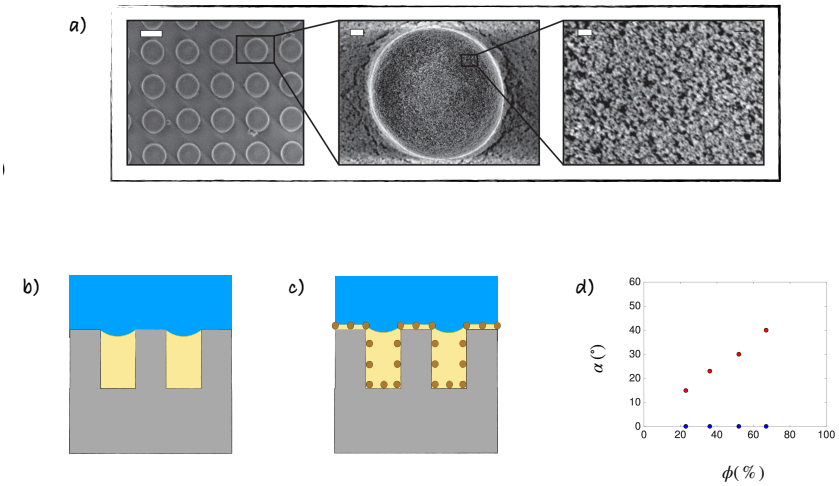

Figure 20: **Hierarchical Liquid-Infused Solid.** a) SEM images of a glaco-treated textured solid reveals evidence of nanoscale roughness on microtexture. Successive zoom-ins have scale bars corresponding to to 20 µm, 2 µm and 20 nm. Images taken by Florian Geyer. Schematic of liquid-infused solid with bare pillar tops (b) and with glaco particles (c), which allows a nanometrically thin oil to be stable on the pillar tops. d) Roll-off angle of a 20 µL water drop plotted against solid fraction of the infused solid. Blue and red data points correspond to with and without glaco-treatement. The existence of the nanometric oil film is evidenced in the $\alpha \approx 0°$ roll-off angle for blue data points. Reproduced from the thesis of Armelle Keiser [40].

The spectacular effect of hierarchy, texture and hemiwicking on adhesion is shown in Figure 4, where we plot the roll-off angle of a 20 µL water drop against the solid fraction of the infused textured solids on which the drop is placed. We see that the roll-off angle for a liquid-infused solid without Glaco treatment (red circles), while low (~ 10°), it increases as we increase the solid fraction. This means the depinning force originates from the solid-liquid contact itself, the more the contact the larger the adhesion. Conversely, on a Glaco-treated liquid infused surface, the roll-off angle is zero (blue circles), deviations being immeasurable with our present experimental set-up. This reveals that the hierarchical roughness has stabilized a ~ 10 nm oil film on top, minimizing solid-liquid contact so much so that pinning defects have been suppressed.

Philippe Bourrianne and Timothée Mouterde experimentally visualized this with a fluorescent protein: BSA (Bovine Serum Albumin) that adheres to a solid surface upon direct contact. Further details in the thesis of Philippe Bourrianne [43].

The lack of pinning can be further illustrated by the disappearance of the *coffee stain effect*: when a millimetric water drop with colloidal suspensions, like a coffee drop placed on a solid evaporates, it leaves behind an annular residue like a coffee stain. This happens for two reasons - the contact line is pinned and evaporation is maximal at the contact line inducing a flow that brings the solute towards the pinned

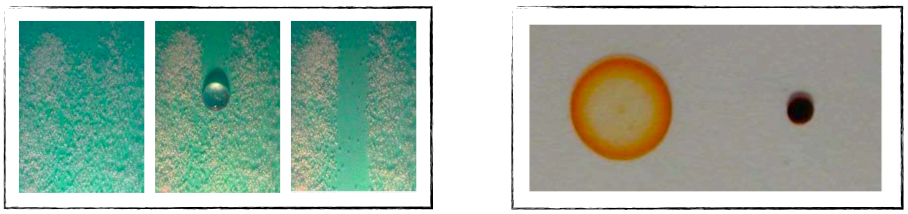

Figure 21: **Cleaning dusts and coffee stains.** Left: A 20 μL drop of deposited on a liquid-infused solid, coated by silica particles of 200 − 500 μm radii, kept at an angle $\alpha = 20°$, cleans the surface taking the particles away. Right: A 5 mm coffee drop evaporates off to leave a coffee stain (left), a consequence of the pinning of contact line, whereas on the liquid-infused solid, the coffee drop evaporates to a much smaller cluster of particles, because the contact line can move and shrink (right). Reproduced from [38].

contact line, that is left behind as a residue at the end. Lafuma et al. showed that a coffee drop evaporating on an infused surface does not show a coffee stain, precisely because the contact line is de-pinned (see Figure 21) [38].

2.3.3 *Highlights of the last decade*

A plethora of applications of the slipperiness and minimal adhesion of liquid-infused solids were identified in the last decade, alongside characterizations of these composite solids and their behavior in different limits. A non-exhaustive list is summarized below:

- **Applications**
  - In the context of applications, the Aizenberg group described anti-icing and biofouling properties of liquid-infused surfaces [44–47]. They have also subsequently reported infused solids that have tunable transparency and wettability properties and functionalizations that lead to self-regulated secretions to keep the infusion intact.[48–54].
  - The Varanasi group has made a company based on liquid-infused solids called *LiquiGlide* that helps in increasing efficiency and decreasing waste in packaging industries. For instance, ketchup bottles typically have ketchup adhering to the inside walls of the bottle, but an infused surface enable the removal of even tiny quantities of extremely viscous non-Newtonian liquids as ketchup. The Varanasi group and subsequently others showed that droplet condensation can be enhanced by liquid-infused surfaces, because these surfaces can shed off the condensate, thus al-

lowing for more condensation to happen on the surface itself. The condensate distribution and menisci-driven drop propulsion have also been investigated. [55–58].

- Anti-frosting properties of infused solids were also discussed [59]. Rykaczewski et al. performed direct observations of oil cloaking the frost via Cryo-FIB/SEM images [60]. Irajizad et al. in this context also developed a ferrofluid-infused magnetic slippery surfaces for icephobicity [61].

- **The *Wetting Ridge***
  - Butt, Vollmer and co-workers performed direct experimental visualization of the shape of the wetting ridge at the advancing end and receding of the contact line of a drop moving on a liquid-infused surface. They further showed that the size of the wetting ridge strongly depends on the thickness of the lubricating film, when the film is thin and for excess lubrication (overfilled textures), the wetting ridge is macroscopically thick and insensitive to film thickness [31, 62].
  - An apparent contact angle is difficult to define for drops on infused solids, because the three phase contact line (height of the wetting ridge) is strongly dependent on the thickness of infusion (or overinfusion), as well as the cloaking possibilities of the oil. This was discussed by Sempreborn et al. [63]. Sadullah et al. has performed numerical simulations on the wetting ridge and showed its contribution in the dissipation mechanisms of the moving drop [64].

- **Drop Impact**
  - Weber number is defined as $We = \rho V^2 R/\gamma$, where ρ is the density, V the impact velocity R the characteristic length and γ the surface tension. Drop impact studies have revealed broadly two regimes: at low Weber number We, air-film bouncing is observed, but at high We, the air film ruptures and the drop contacts the infused solid, spreading on it. This high impact spreading is typically independent of the oil viscosity. However, the retraction dynamics has been found to be strongly influenced by the viscosity of the infusion, the higher the viscosity, the slower the receding. [65–67]

- **Depletion dynamics and Replenishment**
  - Dynamic destabilization and shearing off of the infusion and tricks to effectively preserve the film using patterned wettability have been studied by the Howard Stone group [68–71].

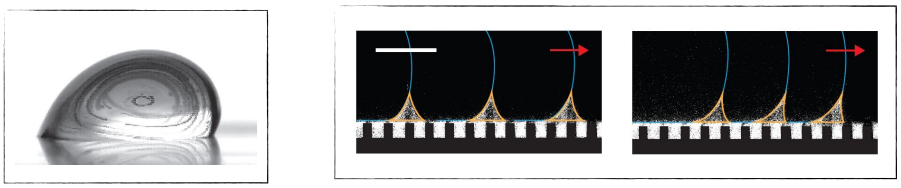

Figure 22: **Friction of Rolling Drops**Left: Tracer particles in a drop travelling down an inclined plane reveal rolling motion. Experiments by Armelle Keiser. Right: Confocal microscopy reveals the meniscus deforms at higher velocities.[40, 73].

  - Addition of small amounts of charged surfactant and oil drops in flow cells have also been proposed to replenish textured surfaces with depleted infusions.[72]

- **Friction**

  - In 2017, both Dan Daniel et al. and Keiser et al. independently performed experimental investigations on water drops moving on infused solids, and showed infused surfaces not only affects lateral adhesion but also significantly impacts the friction forces. [74, 75]

    They further observed that drops on infused solids do not slide, but roll. For drops which are less viscous than the infused liquid, the dissipation is dominated in the meniscus surrounding the drop. The meniscus is dynamically deformed during the motion, the extent of deformation depending on the speed of the drop (see Figure 22). Finally, at sufficiently high speeds, the rolling motion of the drops draws in a thin film of oil between the drop and the texture, on which the drops slip (or *oleoplane*). This shows that even when dissipation in the drop is marginal, there are multiple sources of dissipation: the lubricating film, the front and the back end of the menisci which have different geometries for the oil-water-solid and oil-air-solid contact. Despite multiple sources of dissipation, Keiser et al.in 2020 showed , the friction force has a universal scaling form, where it as $V^{2/3}$, where V is the terminal velocity. [76]

The two experimental setups were different, the former comprising a drop on an infused solid placed on a moving stage, with the drop in contact with a cantilever whose deflection gave the force. The latter set-up was an inclined plane, on which a water drop would be deposited, the drop would run for a millimeter before reaching a terminal velocity.

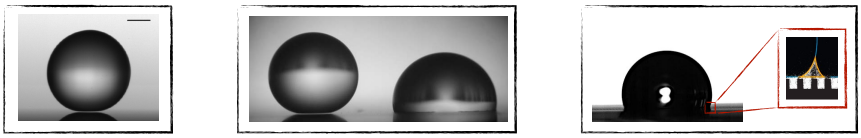

Figure 23: **Three attempts at the grail.** Left: A millimetric Leidenfrost droplet (from the thesis of Dan Soto), middle: from left to right -a drop gently deposited on to a superhydrophobic surface exhibiting a Cassie state and a drop impacted on the surface impales into the texture to a Wenzel state with a smaller contact angle. Right: A drop on a liquid-infused solid. Inset shows a meniscus, as seen in a confocal microscope. Experiments done by Armelle Keiser and Florian Geyer [40].

2.4 THREE ATTEMPTS AT THE 'GRAIL'.

This brings us to *now*, to the moment when the work done in this thesis began in October 2017. By then, the three attempts at the *grail of no pinning* had been made - a Leidenfrost solid, a superhydrophobic solid, and a liquid-infused solid.

The first - a Leidenfrost solid - only works at very high temperatures $> 160°C$, where a deposited water drop sits on a cushion of its own vapor, preventing contact. While the non-contact of Leidenfrost is the most true of all three, and in this sense, depinning forces are really zero, but the Leidenfrost state is a transient one and it ends with the death of the drop. Furthermore, the Leidenfrost state does not occur at normal temperatures, making it exotic and observable only if the plate is far beyond the boiling point and the liquid volatile.

The second - a superhydrophobic solid - works at all temperatures. The *Cassie* state where the drop sits atop pillar tops is known to be metastable with little but finite adhesion. However, recently discovered nanocone surfaces have exhibited adhesion forces that are vanishingly small [77]. In this sense, a nanocone superhydrophobic solid is a true challenger of a liquid-infused solid, and constitutes a benchmark for comparison.

The third - the liquid-infused solid - shows real promises. The adhesion forces for glaco-treated infused surfaces, are immeasurably small. They do not require a special temperature to function. Their other original features need to now be found out and compared against the superhydrophobic surfaces to get a measure of how they fare.

It is important (and interesting) to contextualize what my predecessors in this lab have done on this topic so that I have an understanding of where I am and how I have contributed. José Bico, a doctoral student in this lab, two decades ago, discovered *hemiwicking*. Aurélie Lafuma, a postdoc soon after studied the first liquid-infused solid and the conditions for making it. Jacopo Seiwert, thereafter showed

how to dipcoat a textured solid such that it is perfectly infused without hemiwicking. And finally my direct predecessor Armelle Keiser found out the laws of friction on infused solids.

I present to you the laws of spreading on infused solids.
And some other things.

2.5 AIMS OF THIS THESIS

This thesis has three parts and aims to ask three original questions, hitherto unaddressed regarding liquid-infused solids.

1. The first is a simple and fundamental one - what happens at short times when a drop first touches an infused solid. We study the question of spreading on infused solid in two limits: one where the viscosity of the spreading drop is always lower than that of the infusion (water spreading), and second, where the viscosity of the spreading drop is always higher (glycerol spreading). Both of these questions have been experimentally investigated and models have been made that capture the observed behavior.

   In the course of investigating this problem, we also go through the spreading laws on 'bare' solids, for which we develop scaling arguments to recover laws that have been derived more rigorously in previous works. Furthermore, as an auxiliary experiment, necessary to delve into for physical insight, we experimented with large puddles of water spreading on 'bare' solids. This too has become a problem in its own right, with novel observations.

2. In the second part, we delve in the vertical adhesion of infused surfaces. While the lateral adhesion of infused surfaces have been exhaustively shown to be of a negligible magnitude, no question has been asked in the context of the vertical adhesion of infused solids. We make adhesion force measurements on these solids and build a model to capture the adhesion forces as well as the behavior of capillary springs on infused solids.

   Subsequently, we report experiments with a 'viscous tweezer', where a drop is placed between two liquid-infused solids (the top one being more viscous than the bottom), separated at a constant speed. We show that depending on the speed, the drop ends up at the top or the bottom. This section is primarily experimental, that elaborates on the difficulties of the experiment and the nuances of the phenomenon.

3. In the third part, we probe solid friction on liquid-infused solids - we show experimental results of a sphere rolling down an infused textured solid. We discuss different regimes we observe -

rolling, walking, bouncing, and the tale of a curious 'tail' that the sphere drags along. This part too is primarily experimental, with an attempt to understand the walking of ants on *Nepenthes* with our experimental observations. Our experimental observations tell us that contrary to the general belief that ants walking on the nectar-infused rim of the *Nepenthes* 'slip and fall', the ants are stuck on the rim due to the viscous infusion, and in an attempt to un-stick themselves from the rim, they fall. In other words, the pitcher plant is not slippery but sticky to the ants.

Part II

SPREADING

3

DROPS SPREADING ON INFUSED SOLIDS

In this chapter, we wish to ask a simple fundamental question: what happens when a drop of water first contacts an infused solid? As discussed in the previous chapter, liquid-infused soilds are ambiguous materials which are hemi-solid, hemi-liquid. A drop of water placed on a silicone oil-infused surface is thus 'confused' - on one hand the drop 'feels' the solid because it cannot penetrate it, on the other hand it also 'feels' the infused liquid on which it can slip. To answer what happens when a drop touches such a special material, we first discuss the case of a droplet contacting a 'bare' solid and then come to our case of interest. In the process, we would also go through the historical arc of works relevant to both and how they converge to the particular question we wish to answer.

3.1 DROPS ON 'BARE' SOLIDS

3.1.1 *History of Spreading and Coalescence*

What happens when a drop contacts a solid has been the subject of many investigations, ranging from static considerations (what is the final state of the liquid?) to dynamic questions (how does the liquid reach equilibrium?) [78–80]. For the common case of water droplets with millimetric size R placed on solids they partially wet, the combination of limited spreading and low liquid viscosity η makes the dynamical resistance dominated by inertia [81–84], a regime followed by a relaxation toward equilibrium where both pinning and viscous forces can play a role — a short process on the whole, typically at the scale of a few milliseconds: seen with our naked eye, water drops deposited on plastic quasi-instantaneously form spherical caps. However when a drop contacts a philic surface, it spreads out thin and keeps spreading 'indefinitely' until it becomes molecularly thin (see Fig.24).

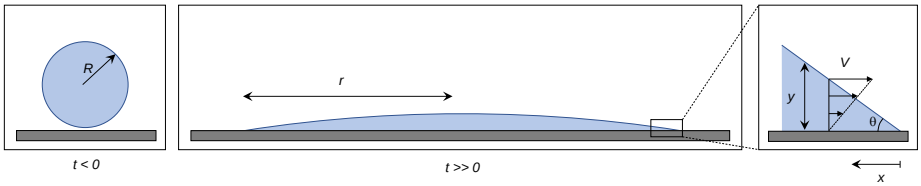

Figure 24: **Tanner Sketch.** Sketch of a droplet contacting a flat philic solid and spreading thin.

3.1.1.1 *Tanner*

Historically, the late stage of spreading of a droplet on a solid is the regime that was investigated first - in 1979, L. H. Tanner showed that in the late time regime, the (apparent) contact line radius r of the drop grows as $t^{1/10}$ [85]. The dynamics of such late stage spreading is slow and dominated by viscous dissipation close to the moving contact line, as shown in the zoom-in of the contact line in the sketch of Figure 24. The viscous stress can be expressed as $\eta V/y$ where V is the velocity of the growing contact and y is the height of free interface from the solid at a distance x from the contact line. The form of the viscous stress itself reveals that it diverges as we approach the contact line, $x \to 0$. This singularity can be regularized by introducing a molecular cut-off length when integrating the dissipation force per unit length which yields $F_\eta \sim \int (\eta V/y)\,dx \sim (\eta V/\theta) \int dx/x$, where θ is the dynamic contact angle which is a function of V. With the introduction of a molecular cut-off length a of the order of 1 nm, the integral $\int dx/x$ when $\beta = \ln(R/a)$ of the order 10 (the upper limit of x is the

size of the drop R, typically 1 mm). This viscous force is balanced with the uncompensated Young force per unit length $\gamma(1-\cos\theta)\sim\gamma\theta^2$ for small angles, where γ is the surface tension of the liquid with respect to air. Such a balance yields the Cox-Voinov law $\theta^3\sim Ca$, where $Ca=\eta V/\gamma$, also called the capillary number [86, 87]. For the case of a droplet of volume Ω that has spread out thin to size r, we may write $\Omega\sim r^3\theta$. Plugging this in $\theta^3\sim\eta V/\gamma$, and integrating over time we get

$$r\sim\left(\frac{\gamma\Omega^3 t}{\eta}\right)^{1/10} \tag{9}$$

This is the famous Tanner's Law [85]. The Cox-Voinov law, more strictly, reads as law $\theta^3-\theta_0^3\sim Ca$, where θ_0 is the equilibrium contact angle. This description of evaluating the dissipation near the contact line also known as the wedge dissipation or line dissipation, surprisingly has been found to hold true for θ as large as 120°.

Although Tanner's Law concerns the later stages of spreading (minutes or longer for millimetric droplets), it fails to capture the dynamics in the very early stages, owing to the very different geometry that the contact has and the flow it consequently creates. These early dynamics are typically in the order of a millisecond or less for a millimetric water droplet. Naturally, experimental investigations on the first steps of spreading of a drop on a solid had to wait until the advent of the high speed camera. It was not until 2004 when Anne-Laure Biance with a camera of 9000 frames per second conducting experiments with a water droplet being brought to contact with a hydrophilic surface showed that the size of the contact grew as $t^{1/2}$ in the very early time regime [81]. Curiously, the growth law that the authors derived in this case was the same as observed in case of coalescence of two drops. It is as though a mirror-plane symmetry of the substrate had been invoked for the flow. To understand why such an analogy should at all be valid, despite the fact that the substrate changes the boundary condition from a continuity of shear stress (for coalescence) to a no-slip boundary condition at the solid-liquid interface, it would help to go through the history of the development of coalescence models, before we re-build the model of spreading on a 'bare' solid.

3.1.1.2 *Coalescence: From Frenkel to Eggers-Lister-Stone*

The first work on coalescence of two (viscous) drops is by Yakov II'ich Frenkel in 1945 in the article *'Viscous Flow of Crystalline Bodies under the Action of Surface Tension'*, which is now considered as the starting point of the physical theory of sintering[88, 89]. Sintering is the phenomenon of fusing loose powdered solid particles into a solid mass by heat or applied pressure - something which apparently has noth-

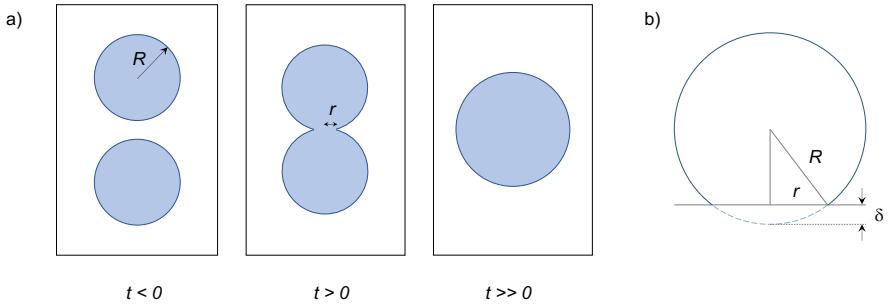

Figure 25: **Frenkel Sketch.** a) Sketch of two identical drops of radius R approaching each other, coalescing and merging into one larger drop, as imagined by Frenkel in the context of viscous sintering. b) Schematic of a Hertz contact of a sphere and a plane. The deformation region shown in blue dotted line has a height δ and a lateral extent r.

ing to do with liquids or coalescence. However, it is Frenkel's conjecture that 'Surface stress can cause viscous flow in crystal materials; and sintering of crystal materials can be explained by that phenomena' and the model he proposed thereafer in his article that makes it relevant to coalescence studies.

Fig.25 shows a sketch of the steps involved in the process of viscous sintering as imagined by Frenkel - two identical spherical droplets of radius R approach each other, form a zone of contact of size r and then finally merge into a larger single drop. Frenkel assumed that the spheres touch in a Hertzian contact (drawn in Fig.25b) which corresponds to a slightly deformed sphere, that is $r \ll R$, when intersecting with a plane, the deformation being of a size $\delta \ll r$. The size of δ can be evaluated by writing down the Pythagorian relation for the triangle shown in Fig.25b: $(R-\delta)^2 + r^2 = R^2$, which gives the Hertz Law of contact:

$$\delta \sim r^2/R \tag{10}$$

Frenkel's argument for the rate of viscous energy dissipated during coalescence can be written in a scaling fashion as $\eta(\dot{\delta}/R)^2R^3$, where $\dot{\delta}$ is the flow rate along the axis joining the two spheres. The surface energy per unit time that compensates for this dissipation is given by $\gamma R\dot{\delta}$. A balance between the two gives $\dot{\delta} \sim \gamma/\eta$, which when combined with the Hertz Law gives the growth law of the contact as

$$r \sim \sqrt{\frac{\gamma R}{\eta}}\, t^{1/2} \tag{11}$$

However, while Frenkel's work is of unquestionable significance, his arguments regarding the flow and consequently his law are not

true. Mired in controversies from the beginning, the incorrect description of Frenkel lies in his assumption that two spheres are in a state of uniform deformation when he integrates over the entire volume of the spheres to obtain the dissipation function. This was corrected by Hopper who gave a solution for inviscid coalescence of two viscous cylinders [90–93].

Finally, in 1999, building up on Hopper's solution to two-dimensional coalescence, Eggers, Lister, and Stone developed a theoretical solution to the problem of two spherical drops coalescing, where the external fluid also has a finite viscosity [94]. They predicted that there were two early time regimes: a viscosity-dominated one where the 'neck' of contact grows as $r \sim (\gamma/\eta)\, t \ln(\gamma t/\eta R)$ and an inertia-dominated one where the growth law follows $r \sim (\gamma R/\rho)^{1/4} t^{1/2}$.

This began what may be called a 'hunt' to observe the two laws in coalescence experiments. The early 2000-s also saw the dawn of high speed cameras which for the first time allowed sub-milisecond resolution in experiments, making them ideal for studying the early time dynamics hitherto impossible in coalescence experiments. First, the inertial law was verified in experiments where even the prefactor matched from potential flow calculations, but then for the viscous regime the $r \sim t \ln t$ law was never found — experimentally it was observed to be one of constant velocity [95–101]. Logarithmic corrections in time are arguably quite weak, and understandably so have never been experimentally verified in coalescence experiments.

3.1.1.3 *Spreading: From Biance to Eddi-Snoeijer*

As mentioned before, the story of early time spreading begins in 2004, when Anne-Laure Biance and co-workers did the first experiment of early stages of spreading by contacting a water drop with a solid (hydrophilic in her case), and discovered the same inertial law as seen in coalescence: $r \sim (\gamma R/\rho)^{1/4}\, t^{1/2}$ [81].

A direct observation that follows from this law is the lack of θ in the growth law - the wettability of the substrate seems to have no contribution in the initial steps of spreading. However, in 2008, Bird, Mandre and Stone proposed that for a partially wetting substrate, when a droplet first comes into contact with the solid the contact grows as $r \sim t^{\alpha}$ where $\alpha = f(\theta_0)$, θ_0 being the equilibrium contact angle, and $\alpha \to 1/2$, when $\theta_0 \to 0$ [82]. It must be mentioned here that the temporal resolution in all of these studies was limited: the 1/2-law in time was observed on only one decade which is from 0.1-1 ms.

Eventually, in 2012, Antonin Eddi, Jacco Snoeijer and co-workers with a camera of 600,000 frames per second, showed that when a droplet contacts a solid, in the early time regime, the contact grows as $t^{1/2}$, irrespective of the material properties of the substrate — whether the surface be perfectly wetting, partially wetting, chemically pat-

terned with anisotropic wetting properties or even soft, the contact always grows as $t^{1/2}$ [83, 84]. In this regard, the law is universal, and the reason for its universality is that its origin is geometric and not material - it is a consequence of only the sphere-plane geometry of the contact. Fig.26 shows a representative illustration of a classical spreading experiment and the temporal evolution of the contact line of the spreading that shows different regimes as observed in time and as discovered historically.

The reason for the apparent $r \sim t^{\alpha}$ behavior observed in [82] could now be understood as a regime where the radius was transitioning from a $t^{1/2}$ law to equilibrium: a crossover regime, where scaling laws do not hold.

Eddi, Snoeijer and co-workers subsequently also showed that the spreading-coalescence analogy can be extended further even for viscous drops, where spreading follows the same law as for viscous coalescence - $r \sim (\gamma/\eta)\, t \ln(\gamma\, t/\eta R)$, for $\eta > 10$ mPa-s [102].

The discovery of these two laws in the context of spreading shows that the spreading-coalescence analogy is indeed very strong and for some reason does not care about the change in the boundary condition. In the next subsection, we we will derive these laws based on physical arguments and try to understand why the analogy holds.

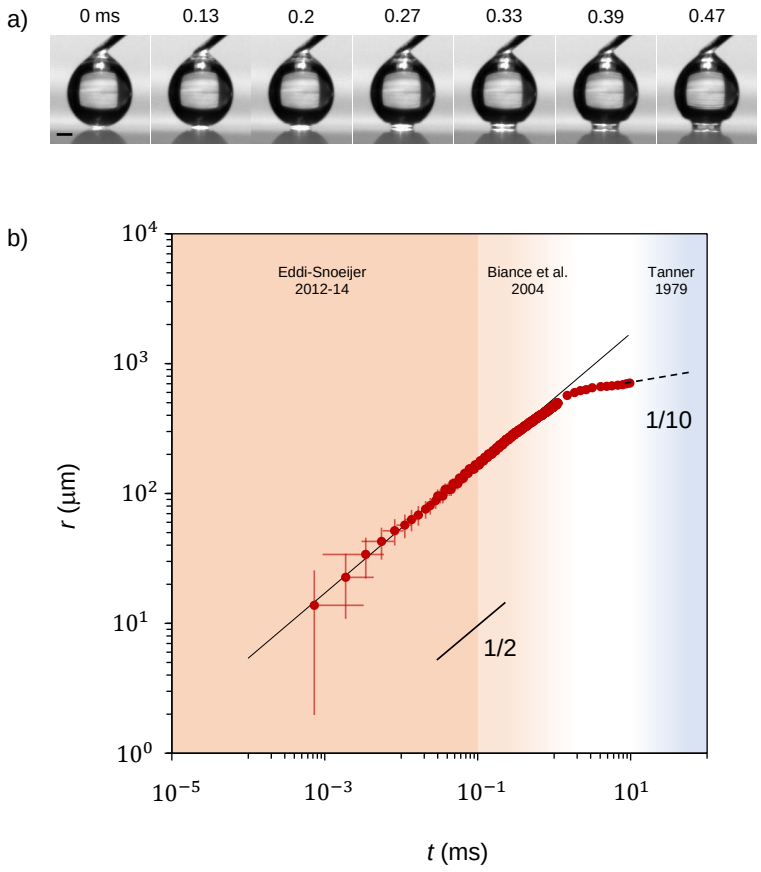

Figure 26: **Early Time Spreading.** a) Timelapse of a water droplet of 1 mm radius being gently deposited on a hydrophilic surface and spreading subsequently. Scale bar represents 500 μm. b) Temporal evolution of the growing contact line, solid line follows $t^{1/2}$ and dotted line follows $t^{1/10}$.

3.1.2 *The Model for Spreading on a 'Bare' Solid*

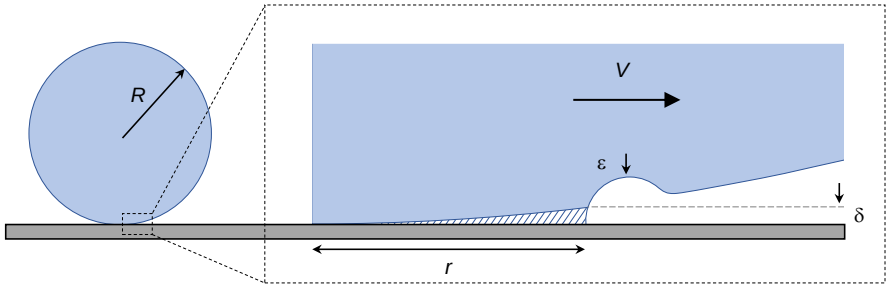

Figure 27: **First Contact.** Schematic of a spherical viscous drop (in blue) touching a flat solid. Close-up of the cuspoidal region reveals that the tip of the physical cusp is not a region of infinite curvature, rather is a hemi-toroidal region surrounding the contact line of size ϵ. The tip contains air that has been evacuated out from in between the water and the solid as a consequence of contact (striped region). This hemi-toroidal cusp moves at a speed V, as the droplet spreads progressively. The blue dashed line is the outline of the drop before contact.

The heart of the problem lies in the realization that the initial contact of a spherical viscous drop and a flat solid establishes a singularity. As sketched in Fig.27, a cuspoidal region forms upon contact where the solid/liquid contact propagates, as it does in the proximal situation of two coalescing viscous drops [94]).The cusp is regularized by surface tension, so that it ends with a tip of finite radius (as seen in Fig.27).

This tip contains the air displaced by water due to contact with the solid (drawn in orange in the Fig.27), which provides an estimate for its characteristic size ϵ. The height δ of the air gap right before contact is given the geometric Hertz law, r^2/R, so that the corresponding volume of air $\Omega \sim r^2\delta$ scales as r^4/R. We can equate this volume with the amount of air in the hemi-toroidal region of the cusp, $\epsilon^2 r$, which yields an estimate of the size of the cusp as

$$\epsilon \sim r^{3/2}/R^{1/2} \tag{12}$$

Also, if we look at the four length scales at play here: ϵ, δ, r, and R, we note their hierarchy at all times $\delta < \epsilon < r < R$. The singularity we alluded to before can now be mathematically stated: when $t \to 0$, that is, $r \to 0$, the Laplace pressure in the cusp $\gamma R^{1/2}/r^{3/2}$ diverges.

The inertial term for this propagating cuspoidal region, at any point of time t would be $\rho\Omega V/t$, as Ω is the volume of liquid being reorganized. Writing $V \sim r/t$, we get

$$F_i \sim \rho(r^2\delta)(V^2/r) \sim \rho r^3 V^2/R \tag{13}$$

In order to write the dissipation term for the flow near the contact region, we first note that the cusp that forms here is reminiscent of the cusp that develops between two counter-rotating cylinders partially immersed in a bath, also known as the Joseph-Nelson-Renardy-Renardy cusp, named after the people who took the first experimental picture of such a cusp in 1990 in a four-roll mill apparatus (see Fig.28). However, a four-roll mill is not necessary to see the cusp, even a single rotating cylinder that is partially immersed in a liquid that is sufficiently viscous can show a cusp-formation, as shown in the beautiful images of the cusp taken by Elise Lorenceau in Fig.28c. In fact, a careful observer can find free-surface cusps in everyday flows as a jet impinging on a bath - while for water, slight perturbations can lead to air entrainment, but for liquids 100 more viscous than water or more, the point where the jet meets the bath, a cusp develops. If the velocity of the jet is increased beyond a threshold value then it entrains a thin film of air, as shown first by Lin and Donnelly in 1966[106].

What we wish to remark here is that all these cusps (the Lin-Donnelly cusp, the Joseph-Nelson-Renardy-Renardy cusp and the cusp that forms at the initial contact between a drop and a solid or between two drops) are the same, in the sense that the forces and the flows around the cusp that sustain and regularize it with a tip are the same. However, while the Lin-Donnelly and the Joseph-Nelson-Renardy-Renardy cusp are static in shape for a fixed speed of impingement of jet or rotation of the cylinder, the Cusp in Spreading/Coalescence is not: as the contact region grows, the speed of the growth keeps decreasing, and when the velocity decreases sufficiently, the contact does not remain cuspoidal anymore. Nevertheless, the physical arguments for flow around a cusp should hold for all of these problems.

The tip of these cusps can be looked upon as a thin hemi-cylinder, which in the case of spreading is rather a hemi-toroid. In this sense, we can now imagine the problem has now been reduced to the classical problem of a cylinder falling in a viscous medium. Said differently, two dimensional cusps are but Stokesian cylinders, in the context of the flows they give rise to and the viscous drag they 'feel' (Fig.29). The viscous drag per unit length on such an expanding 'hemi-toroid' of length $2\pi r$, which is of the order of r and radius ϵ is given by Stokes' law,

$$F_\eta \sim \eta V r/\ln(r/\epsilon) \sim \eta V r/\ln(R/r), \tag{14}$$

where the last part follows from Equation 3.6.

The contact region is driven by Laplace pressure which scales as $\Delta p \sim \gamma(1/\epsilon + r) \sim \gamma/\epsilon$, because $\epsilon < r$. Integrating over the area ϵr, we

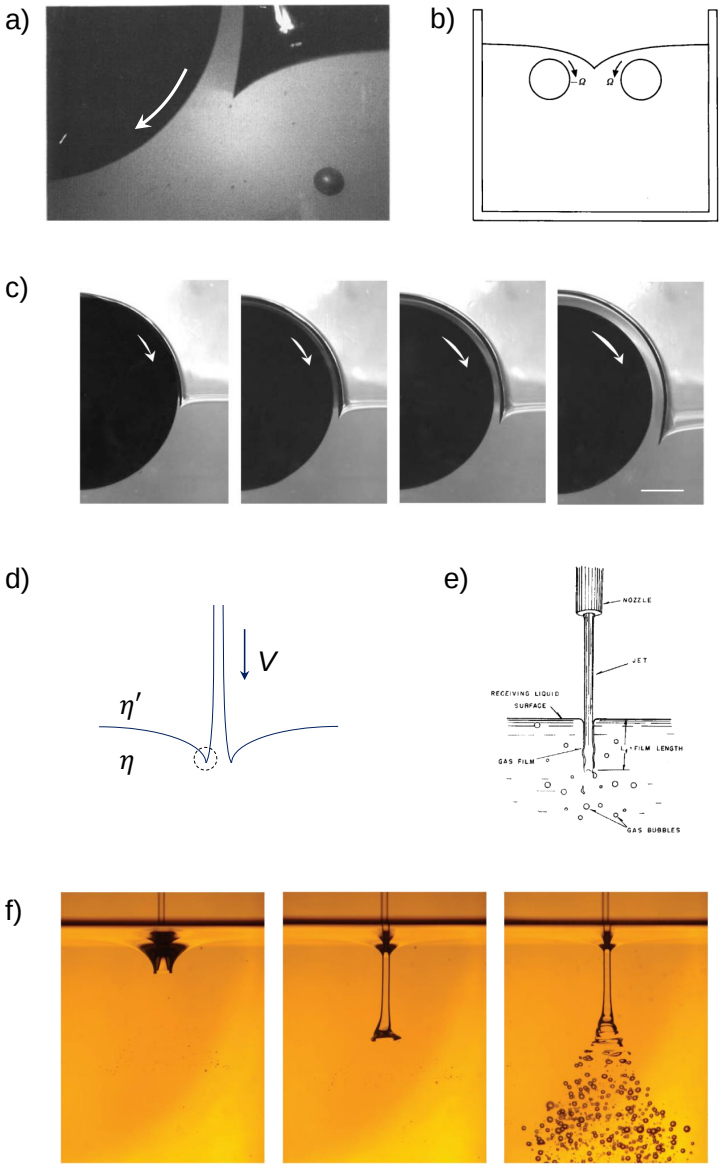

Figure 28: a-c) **The Joseph-Nelson-Renardy-Renardy Cusp:** One of the first experimental images of a cusp on the free surface of a liquid, as reported by Joseph, Nelson, Renardy and Renardy in 1991. Reproduced here from [103], in a) shows, we see a cylinder of radius 1.25 cm, rotating at 27 rpm in a bath of polyox $\eta \approx 6$ Pa-s. b) Moffat's schematic of the development of a cusp because of two counter-rotating cylinders below the free interface of a liquid [104]. c) Experiments of Lorenceau et al.: Development of growth of a cusp with increasing speed of rotation of the cylinder: 6, 10, 17, and 30 cm/s (left to right). The lower liquid is a silicon oil of viscosity $\eta \approx 1$ Pa-s and the upper fluid is air. Scale bar represents 1 cm. Reproduced here from [105]. d-f) **The Lin-Donnelly Cusp:** d) Schematic of the cusp - a liquid jet of viscosity η surrounded by a fluid of viscosity η' impinges on a bath of the same liquid. When $V < V_c$, a cusp forms. When $V > V_c$, a thin film of air is entrained, as shown by the original schematic of Lin and Donnelly from 1966 [106], reproduced in e). Experimental images of the air entrainment as obtained by Reyssat and Quéré. [107].

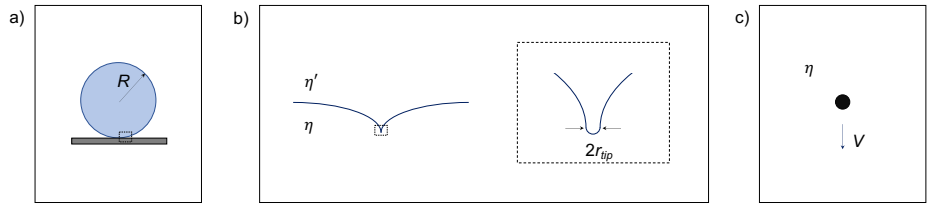

Figure 29: **Two dimensional cusps as Stokesian cylinders.** a) The Cusp of Spreading (or Coalescence) b) The Joseph-Nelson-Renardy-Renardy Cusp c) The Stokesian Cylinder: A cylinder falling in a viscous medium, perpendicular to its axis of symmetry.

can write the driving force $F_\gamma \sim \Delta p\, \epsilon r \sim \gamma\, r$. Thus, we can write the balance of forces as $F_i + F_\eta \sim F_\gamma$, that is

$$\rho r^3 V^2/R + \eta V r/\ln(R/r) \sim \gamma r. \tag{15}$$

This is the growth equation of the contact zone, with all its terms, in the limit where $t < (\rho R^3/\gamma)^{1/2}$, $\eta R/\gamma$, the capillary-inertial and visco-capillary time scale respectively.

We can now identify, within the sphere-plane geometry of the problem, two distinct regimes: a) a viscous regime where $F_\eta > F_i$ and b) an inertial regime where $F_i > F_\eta$. A balance of inertia and capillarity yields a diffusion-like law

$$r \sim \left(\frac{\gamma R}{\rho}\right)^{1/4} t^{1/2}, \tag{16}$$

where we can call $(\gamma R/\rho)^{1/2}$ the effective diffusivity.

On the other hand, a balance of friction with the driving surface tension provides a relationship between the contact velocity and size, $V \sim (\gamma/\eta)\ln(r/\epsilon) \sim (\gamma/\eta)\ln(R/r)$. Writing $r/R = r^*$, this leads to the integration $\int_0^{r^*} dr^*/\ln r^* \sim -\gamma t/\eta R$. The left hand side of this equation is a special function called the logarithmic integral function $\mathrm{Li}(x)$, and it can be shown that $\mathrm{Li}(x)$ can be approximated as $x/\ln x$ at small x. It follows that

A proof of $\lim_{x\to 0} \mathrm{Li}(x) \sim x/\ln x$ is given in the Appendix.

$$r \sim \left(\frac{\gamma t}{\eta}\right) \ln\frac{R}{r} \tag{17}$$

which allows us to substitute the r in the logarithm and to deduce Eggers' Law of viscous coalescence: $r \sim (\gamma/\eta)\, t \ln(t/\tau)$, plus logarithmic corrections, where $\tau = \eta R/\gamma$.

But which regime comes first? Experimentally, we see that for any drop (water or more viscous) spreading on a surface, the velocity

is the maximum at the smallest times, where we are only limited by the temporal resolution in our experiments, and the velocity decreases as the contact grows. It is natural to infer from this that inertia dominates in the earliest time scales which is then subsequently slowed down by viscosity until equilibrium, for partially wetting substrates, or in the case of a perfectly wetting surface the drop transitions to a thin radially spreading geometry where it follows Tanner's Law. However, the viscous dissipation which slows down the inertial regime is not the same as the viscous regime we have identified here, one which specifically relates to the cuspoidal geometry that exists at early times.

In order to determine the order of the regimes, we compare the viscous force with the inertial term to find out when the former dominates over the latter, that is when $\eta V r/\ln(R/r) > \rho r^2 \delta V^2/r$, which can be re-written as $\delta < \eta/\rho V \ln(R/r)$. From Eggers' Law, we know that in the viscous regime $V \sim (\gamma/\eta)\ln(R/r)$ which when plugged in to the previous relation, we get $\delta < \eta^2/\rho\gamma \ln^2(R/r)$. Substituting δ with the Hertz relation $\delta \sim r^2/R$, we obtain

$$r < \frac{\eta}{\sqrt{\rho\gamma}} R^{1/2} \ln\frac{R}{r}. \tag{18}$$

The above inequality showing the existence of maximal radial length for the viscous regime implies the viscous regime exists at the smallest length scales, followed by the inertial regime. For a millimetric drop of water with $\eta \sim 10^{-3}$ mPa-s, $\rho \sim 10^3$ kg/m^3 and $\gamma \sim 72$ mN/m, we get $r < 1\mu m$. Optical resolutions in experiments are limited to micron length. This is precisely why the viscous regime in water has never been seen optically. With submicrometric resolution by conductivity measurements, a constant velocity regime has been reported but the resolution has not been enough for experimental observations of logarithmic corrections [97]. The lowest value of viscosity where the viscous regime persists for $r > 1\,\mu m$ is $\eta > 10$mPa-s (for $R \approx 500\,\mu m$), and indeed the viscous regime was experimentally observed for all water-glycerol mixtures with η greater than 10mPa-s [102].

It is necessary to underline here how special this is that a viscous regime precedes an inertial one. Typically, in fluid flows, inertia goes as $1/t^2$ and thus naturally precedes viscous friction that has a scaling $1/t$ in time. However, implicit in this statement is the assumption of a similar length scale at play in different directions. This is precisely where geometry becomes very important, as we see in the case of our cuspoidal geometry, where inertia follows a viscous regime.

Equation 18 may also be re-written in a non-dimensional form $r/R \sim Oh$, where we neglect the logarithmic term that scales as 1 and $Oh = \eta/(\rho\gamma R)^{1/2}$ represents the Ohnesorge number that compares viscous forces with inertia in a capillarity-dominated flow. We now

take a step back and re-write Equation 18 in δ as it helps in making some important revelations, specially in the context of the boundary condition. Such a formulation reads as

$$\delta < \eta^2/\rho\gamma. \tag{19}$$

We note that the term on the right hand side of the equation represents a viscous length scale ζ that naturally emerges from this problem. As previously noted, the hierarchy of length scales in the problem is $\delta < \epsilon < r < R$, where r is the length scale in the direction of the flow (horizontal) and in the direction normal to the flow (vertical), ϵ represents the size of the cusp and δ the scale in which mass is re-organized as the cuspoidal contact moves, and it is this δ that appears on the length on the left hand side of the equation. Equation 19 thus reveals that when δ is smaller than the boundary layer thickness $\zeta \sim \eta^2/\rho\gamma$, we are in the viscous regime. For glycerol, with a viscosity of $\eta \sim 1.4$ Pa-s, $\zeta \approx 2.5$cm, that is larger than the capillary length! This means that for a millimetric glycerol drop, the entirety of early time spreading is viscous and follows Egger's Law. However, for water $\zeta \sim 14$ nm, which is why the flow within the region of δ beyond ζ turns inviscid and can be solved in the framework of Euler equations.

It is not that the no-slip boundary condition is violated, rather that there exists a thin boundary layer of the order of tens of nanometers beyond which the flow is inertial. This is precisely why the spreading-coalescence analogy holds, despite the difference in boundary conditions.

3.2 WATER DROPS ON INFUSED SOLIDS

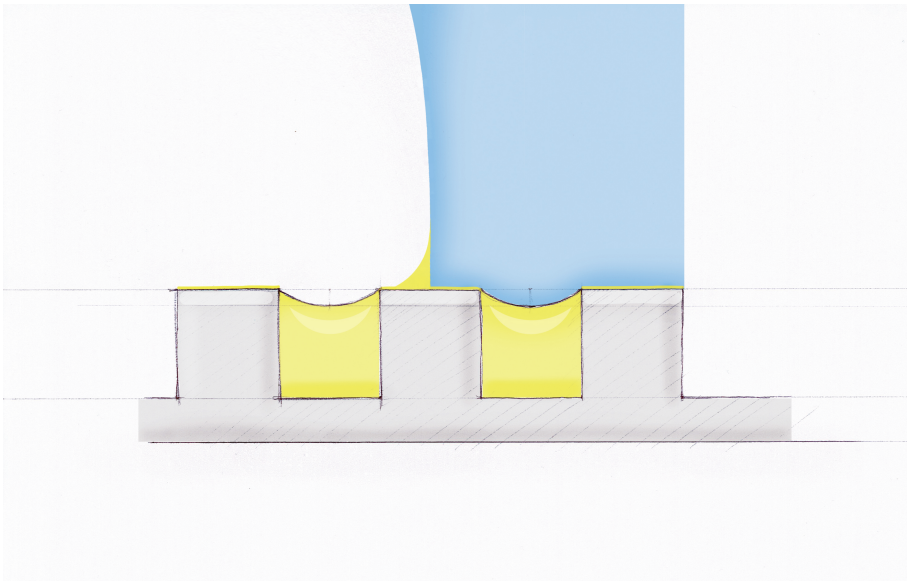

'The Foot of Water on Rome' by Benoît Pype

In this section, we revisit this classical problem of drop spreading by considering the case of water on textured solids infused by oil. We know that these so-called LIS have special dynamical properties, in particular because the liquid trapped in the texture lends them liquid-like properties, with little adhesion towards water and the possibility to promote slip [31, 37–39]. Conversely, LIS are known to generate a non-negligible friction when drops move on them (under the action of gravity, for instance), owing to the existence of a stationary meniscus of lubricant around the moving drop [11-12]. We wonder here whether liquid spreading on such surfaces obeys the universal contact law expressed by Eq. (3.1) or if it is affected by the special properties of these materials.

3.2.1 *Fabrication*

Capturing the early dynamics of a solid/liquid contact requires simultaneous side and top (or bottom) views, which necessitates the use of transparent LIS [108]. Such materials are made in a few steps. We first start by spin-coating a layer of SU-8 resin on a clean, dehydrated silicon wafer; the resin thickness is controlled by the speed of rotation. We then shine UV-light through a mask comprising square arrays of circular pillars. Thereafter a PDMS counter-mold of the SU-8 texture is made and we achieve a mold of this counter-mold with a transparent optical adhesive (NOA, Norland Optical Adhesive) on a glass slide, which results in a transparent microtextured surface [50, 108].. We finally infuse it with silicone oil, whose optical index is comparable to that of the resin, leading to a better transparency.

Just infusing oil inside the texture does not provide slippery surfaces, due to the presence of edges at the pillar tops [41]. This can be fixed by adding a second scale of roughness, that is, by drawing the textured substrate from a solution of hydrophobic nanobeads (Glaco Mirror Coat, Soft 99) [73]. The solvent is subsequently evaporated by drying at 70°C for 30 min and the beads ($\sim$30 nm) then coat both the substrate and the pillars without altering transparency. The process is repeated three times to ensure uniformity of the nanobeads coating. After contacting oil, the doubly-textured surfaces are impregnated both between the pillars and within the nanobead cavities, which ensures that we do not over-infuse the material, yet make it highly slippery for water (roll-off angle of $\sim 1°$ for 20µL drops). Infusion itself is performed by keeping the substrate vertical and bringing it in contact with the reservoir of silicone oil, so that the oil wicks in only within the texture.

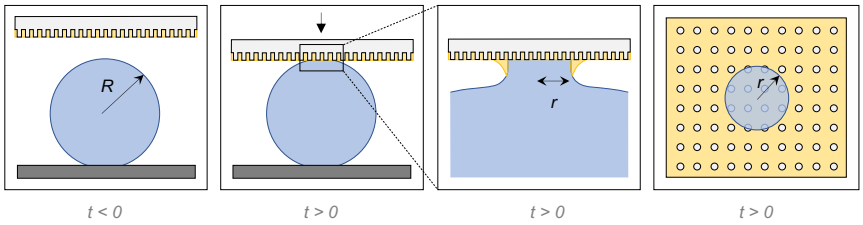

Figure 30: **Schematic of Experiment.** Left to right: Sideview sketch of our experimental setup - a water droplet sitting on a superhydrophobic solid; the drop is brought in contact (at t = 0) with the infused surface on the top; zoom-in on the liquid bridge with radius r that develops upon contact; top view sketch of the liquid bridge seen through the transparent infused material.

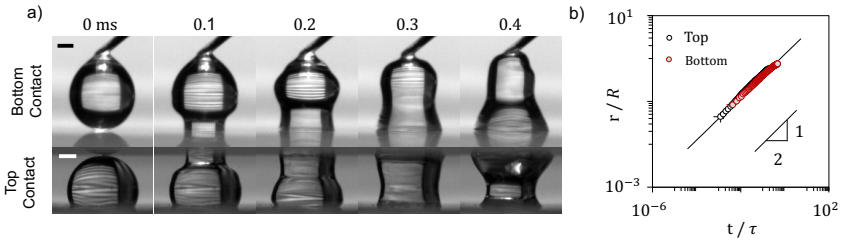

Figure 31: **Orientation Test.** a) Comparison between a classical spreading experiment done by depositing a droplet of $R = 1$ mm from a needle onto a hydrophilic surface at the bottom and a droplet sitting on a hydrophobic surface contacting a hydrophilic surface at the top. Successive snapshots are at 0.1 ms intervals. Scale bar represents 500μm. b) Nondimensionalized radius r/R of the two experiments plotted against nondimensionalized time t/τ, where $\tau = (\rho R^3/\gamma)^{1/2}$. Circles with black borders represent top contact and circles with red border represent bottom contact. The two data sets collapse on each other, which reveals that there is no orientational dependence on the way the experiment is performed.

3.2.2 *The Experiment*

The principle of the spreading experiment is schematized in Fig.30. Our substrates (top of the figure) are decorated with micro-pillars with density $\phi = 23 - 25\%$, height $h = 20 \pm 3\,\mu m$, lateral size $d = 18\mu m$ and spacing $p = 15\,\mu m$. The lubricant is a silicone oil with surface tension $\gamma_o = 20\,mN/m$ and viscosity η_o ranging from 5 mPa-s to 100 mPa-s. Millimeter-sized drops (in blue in the figure) are made of water, with surface tension $\gamma = 72\,mN/m$ and viscosity $\eta = 1\,mPa\text{-}s << \eta_o$. We start by placing a drop on a Glaco-treated superhydrophobic glass slide (dark grey in the figure), which preserves its sphericity and allows us to study spreading without impact, as it would necessarily happen if the drop were directly released on the infused material. Instead, we approach at a very small speed (about 50 $\mu m/s$) the transparent infused material from the top, with its infused side facing downward. Two high-speed cameras placed above and below image the contact with simultaneous top-down (with 400,000 fps) and side-views (with 5000 fps), using respective backlighting at the bottom and on the side. For the purposes of analyzing the early time evolution of the solid/liquid radius, we exclusively use the topdown data which is less prone to error than sideview, as has been shown in previous works.

Classically, all droplet spreading experiments have been done by depositing the droplet gently onto a surface from a needle. We wanted to be sure that the spreading behavior has no orientational effects. So, we performed the droplet spreading experiment by the classical deposition method, then repeated it in the way it is schematized in Fig.30. Fig.31 shows the snapshots of spreading in the two methods for a 1 mm droplet on a hydrophilic surface. Fig. 31 shows that both the data collapse with no discernible difference.

Back to the case on infused surfaces, each experiment is repeated multiple times for droplet volumes ranging from 1 μL to 40 μL and for seven oil viscosities, namely 5, 9, 19, 48, 96, 485 and 970 mPa-s. A separate set of experiments is also performed with the same set-up, yet replacing the infused surface by silanized hydrophobic glass of similar wetting properties, so as to extract the original contribution of infusion in the contact dynamics. We provide in the figure three top-views of the growing contact at early times and graphs of the evolution of the water contact radius with $R = 0.65 \pm 0.05$ mm.

Top view images reveal unusual features, in the context of spreading drops. Our main observation is the loss of universality: even at very short time, where inertia is expected to dominate viscous effects, the dynamics depends on the viscosity of the oil infusing the texture: the more viscous the oil, the slower the spreading. Other original behaviors are evidenced by the plot of the contact radius r as a function of time shown in Fig.32. The data at low oil viscosity are close to

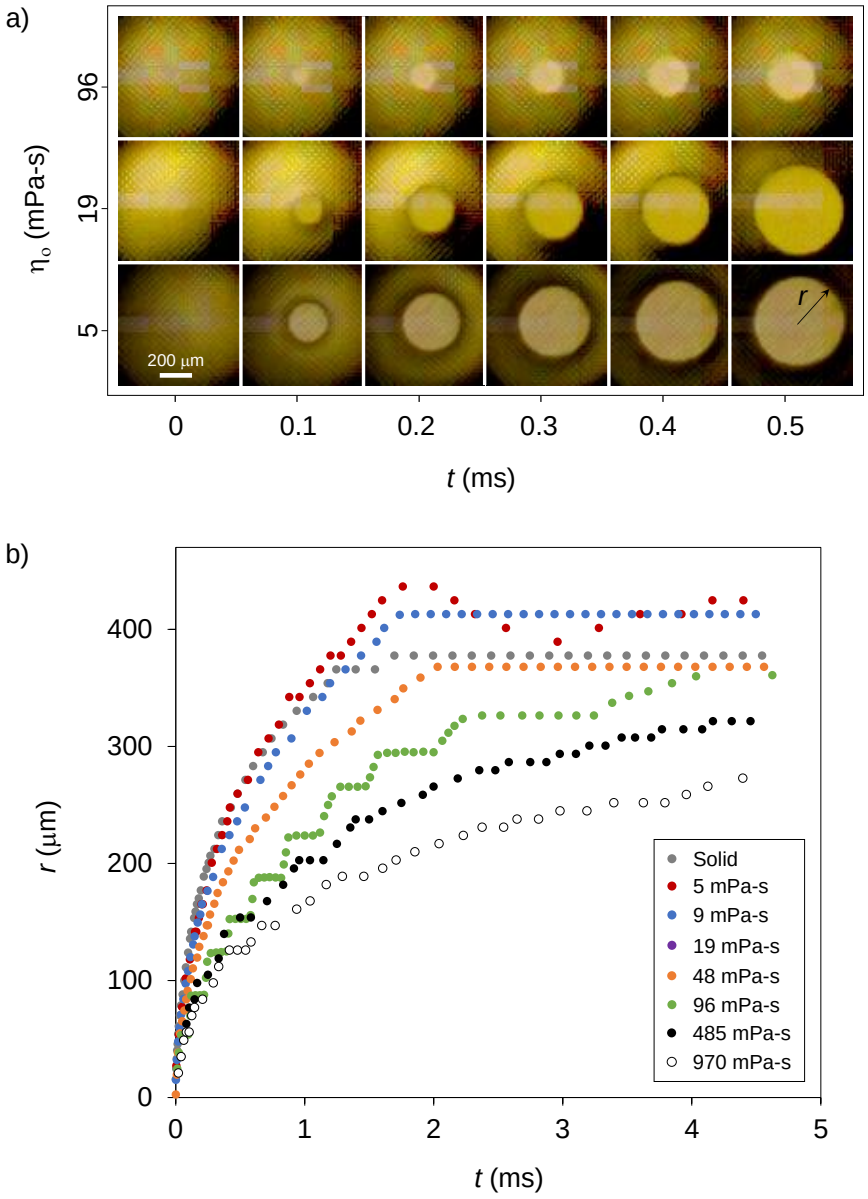

Figure 32: **Experimental Results.** a) Time-lapse topdown images of the growing water bridge on the surface of a LIS, right after the contact of a water drop (radius $R = 0.65$ mm) with a LIS, for four different oil viscosities: $\eta_o = 5, 19$ and 96 mPa-s, from top to down. b) Evolution of the radius r of the liquid bridge forming between water and its substrate, as a function of time t, either on a hydrophobic solid (grey data) or on a LIS with $\eta_o = 5, 9, 19, 48, 96, 485$, and 970 mPa-s.

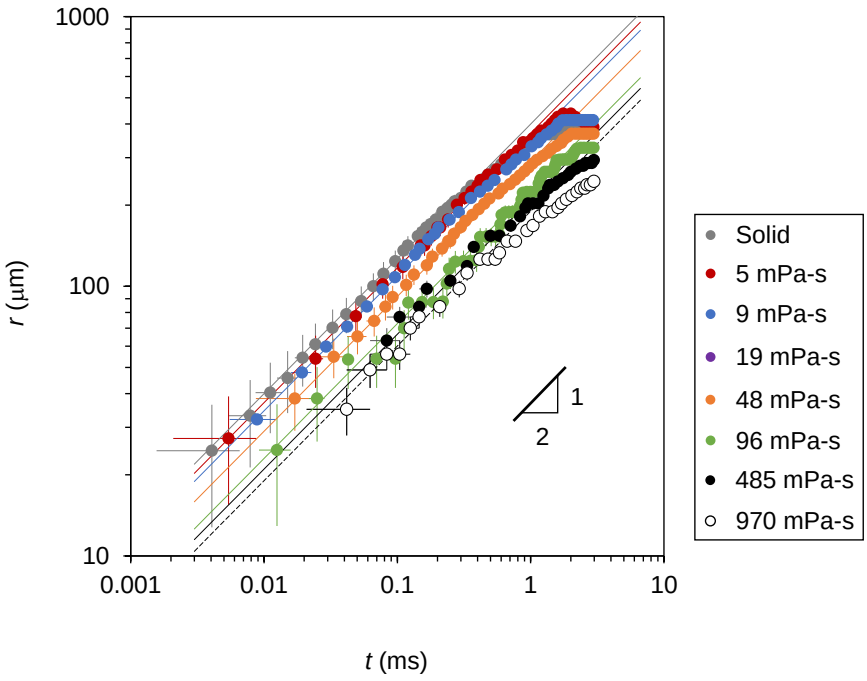

Figure 33: **Log-Log r − t plot** Temporal evolution of the radius r of the liquid bridge forming between water and its substrate in logarithmic scales, which reveals a diffusive-type behaviour for all the LIS. Error bars in time correspond to one standard deviation equal to the inverse of the frames per second and error bars in length correspond to one standard deviation equal to one-pixel size.

that on a solid, while water spreads slower on the more viscous oil, a case we could have thought solid-like. The influence of the viscosity is also noticeable in some details of the spreading: on the less viscous oil, equilibrium is approached with oscillations of the contact radius, a consequence of the high degree of slip on such a surface; this effect is suppressed at larger oil viscosity, but spreading with the more viscous oils takes place in a visibly step-like fashion, each step being fixed by the characteristic spacing $p + d = 33\,\mu m$ of the subjacent network. Finally, all data become similar at 'long' times, the wetting properties of silicone oil being nearly independent of the oil viscosity, and comparable to that of silanized solid surfaces.

Despite differences between the dynamics, a common scaling emerges when plotting the LIS-data in a logarithmic graph (inset in Fig.32). In a range larger than two decades in time, all data follow a diffusive-type dynamics (solid lines in Fig. 33), an observation that concerns most of the spreading, apart from the crossover toward equilibrium at large time. Such dynamics was established for the spreading of non-viscous liquids on regular solids (Equation 16) and found to be universal — which it is here from the exponent point of view, but not

for the 'Diffusivity' D. This raises a stimulating question: how can the oil viscosity modify the dynamics without affecting its scaling?

3.2.3 *The Model*

The Driving Force. We first discuss the force driving the spreading. As water advances on the LIS, the nature and areas of the interfaces change, and multiple cases are possible, depending for instance on the possibility that oils cloaks the water drop, or not — but none of them affect the scaling form of the interfacial driving force, F_d. For the sake of simplicity, we consider here that water mainly moves on oil, a reasonable statement in the presence of an infused subtexture: the top surface of a highly slippery solid is essentially oily. In the first steps of the spreading and as sketched in Fig.30, the spherical drop of water (radius R) develops a 'foot' of radius r that propagates radially. Laplace pressure is unbalanced in the bridge whose edges suck the drop with a pressure scaling as $\gamma R/r^2$, denoting γ as the surface tension of water, or as the sum of water/oil and oil tensions (of magnitude comparable to γ_w) if the bridge is covered by oil, as assumed in Fig.30. Once integrated over the bridge edge area $r\delta \sim r^3/R$, this pressure yields a spreading force,

$$F_d \sim \gamma r, \tag{20}$$

a usual fact in wetting.

Meniscus Dissipation. The force(s) resisting spreading are less obvious to establish. We already mentioned the role of inertia, most often dominant at short time, and leading to a diffusive-type dynamics for the bridge expansion (Eq. (3.2)). However, such dynamics is independent of the oil viscosity. For drops moving on infused surfaces, it is generally assumed that the dominant viscous dissipation occurs in the oil meniscus drawn by the water contact line. The corresponding 'line friction' per unit length scales as $\beta(\eta_o V/\theta)$, where β is a numerical factor accounting for the singular dissipation in the liquid wedge, close to the line [73]. The dynamic contact angle θ is given by the Cox-Voinov Law $\theta^3 \sim \eta V/\gamma$. When plugged in the previous formula, and after integrating the force over the contact line, we get a friction scaling as $\gamma_o r\, \beta(\eta_o V/\gamma_o)^{2/3}$. Its balance with the spreading force γr yields a constant speed of spreading inversely proportional to the oil viscosity — two facts inconsistent with the observations, where we report neither a linear relation between the bridge size and time nor the strong dependency on the oil viscosity expected from the latter argument.

Film Dissipation. A second source of dissipation arises from the slip of water bridge on the subjacent oil. The presence of this oil may indeed induce the slip of water, (instead of the usual no-slip bound-

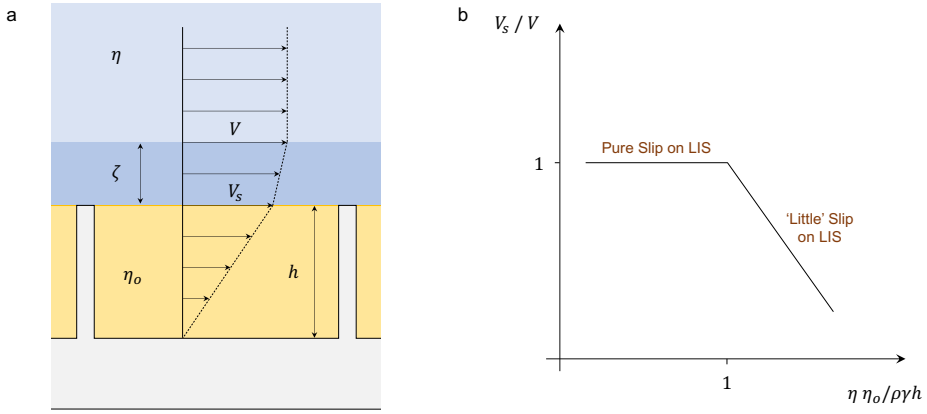

Figure 34: **Slip.** a) Schematic of velocity profile on a liquid-infused surface, where V_s denoted the slip velocity at the water-oil interface and V the velocity beyond the boundary layer. b) V_S/V is plotted against $\eta\eta_o/\rho\gamma h$ reveals two different regimes of slip velocity. The abscissa can also be expressed as $Oh_D Oh_o(R/h)$, which when less than 1, we are in a pure slip regime on LIS, and when greater than 1, the slip velocity decreases as $(1 + Oh_D Oh_o(R/h))^{-1}$.

ary condition used if the substrate were solid), as schematized in Fig. 34. Denoting that the slip velocity at the oil/water interface as V_s, we may now write the continuity of the shear stress condition at the water-oil interface as $\eta(V - V_s)/\zeta \sim \eta V_s/h$, where ζ is the boundary layer within the drop. We have previously discussed the characteristics of this thin viscous layer in the Section 3.1.2, in particular that ζ is typically of the order of $\eta^2/\rho\gamma$, which is $\sim$ 14 nm for water. Substituting for ζ in the continuity equation, we can now write the slip velocity as

$$V_s \sim V/(1 + \eta\eta_o/\rho\gamma h). \tag{21}$$

The above equation reveals that there exists a critical oil viscosity, η_o^* which transitions the slip velocity from a pure slip to vanishing slip regime. This value can be stated as:

$$\eta_o^* = \rho\gamma h/\eta. \tag{22}$$

When the viscosity of our infusion $\eta_o < \eta_o^*$, we have pure slip, that is $V_s \sim V$ and when $\eta_o > \eta_o^*$, the slip velocity scales as $V_s \sim \eta_o^* V/\eta_o$, that is inversely proportional to the oil viscosity. In other words, V_s quickly vanishes in comparison to V at sufficiently large oil viscosities. For our problem of spreading of water, $\eta \sim 1$ mPa-s, $\rho \sim 10^3$ kg/m^3, $\gamma \sim 70$ mN/m and height of texture as $h = 20 \pm 3\mu$m, we find this critical oil viscosity to be $\eta_o^* \sim 100$ mPa-s.

The corresponding viscous force is $F_f \sim (\eta_o V_s/h)r^2$. Substituting for V_s, we get

$$F_f \sim \eta_o V r^2/(1+\eta\eta_o/\rho\gamma h)h \tag{23}$$

The viscous force too would have two regimes dictated by the value of oil viscosity. If the oil is less viscous, $\eta_o < \eta_o^*$, we find a dissipation force proportional to η_o, that is, $F_f \sim (\eta_o V/h)r^2$ and for large oil viscosities, $\eta_o < \eta_o^*$, we find that the dissipation becomes independent of the oil viscosity itself: $F_f \sim (\rho\gamma h V/\eta)r^2$, which is indicative of the fact that the slip velocity vanishes on sufficiently viscous oils, as noted before.

Nevertheless, in both the regimes of dissipation, the force scales as r^2. Thus a balance with the driving force γr yields a diffusive-type law $r^2 \sim Dt$, where for low viscosities, $\eta_o < \eta_o^*$, we expect the diffusivity to be $D_1 = \gamma h/\eta_o$, logically a kind of a Washburnian Law of a liquid with viscosity η_o impregnating a material with a roughness with height h [16]; for high oil viscosities, $\eta_o > \eta_o^*$, the diffusivity would be $D_2 = \eta/\rho$, which is in fact the momentum diffusivity of water that represents the diffusion of a boundary layer. If we plot the 'diffusivity' D of the spreading as a function of the oil viscosity (Fig.35a), we observe that D decreases with η_o for all tested volumes. The function $D(\eta_o)$ seems to follow not two, but three successive regimes: while it tends to plateau at large η_o beyond $\eta_o^* = 100$ mPa-s, for $\eta_o < \eta_o^*$ we see $D(\eta_o)$ approach another plateau at the smallest oil viscosities, and it is between $10 < \eta_o < 100$ mPa-s, that we see D decreases with η_o, even though the variation remains weaker than predicted by the scaling $D_1 \sim 1/\eta_o$.

We can also plot, at fixed viscosity, how D varies with the drop volume Ω (Fig.35b). Again, we note a clear separation of regimes based on the magnitude of the oil viscosity: for viscosities less than 100 mPa-s, large drops spread slightly quicker than small ones, D roughly tripling when the volume is multiplied by a factor 40, whereas for $\eta > 100$ mPa-s, D becomes independent of the volume Ω. This corroborates our expectation from the form of $D_2 = \eta/\rho$ which predicts the diffusivity to be independent of volume and oil viscosity, although the average of the experimentally measured $D(\Omega)$ for $\eta > 100$ mPa-s that comes out to be 28.2 ± 6.8 mm^2/s, one order of magnitude higher than η/ρ. On the other hand, $D_1 = \gamma h/\eta_o$ does not capture the size dependence and predicts a stronger variation in η_o than observed. We discuss further these different behaviors.

Meniscus or Film? We described two sources of viscous dissipation in the oil, occurring respectively in the meniscus and in the film. For a water drop moving on a LIS (owing to gravity, for instance), the friction in the meniscus generally exceeds that in the film, for two reasons. On the one hand, the stationary oil meniscus joins the

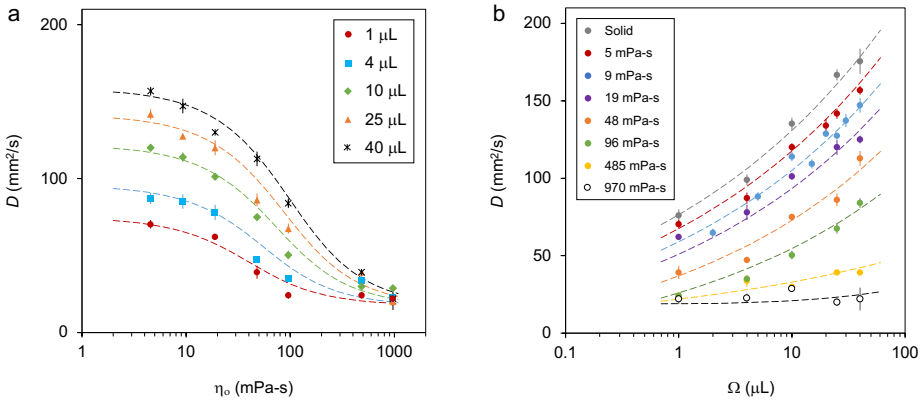

Figure 35: **Diffusivities.** a) Effective diffusivity for water drops as a function of the viscosity η_o of the infusing oil, at a fixed drop volume ($\Omega = 1\mu L$, circles; $\Omega = 4\mu L$, squares; $\Omega = 10\mu L$, diamonds; $\Omega = 25\mu L$, triangles; $\Omega = 40\mu L$, asterisks). The diffusivities were extracted from a fit of $r^2 = 2Dt$ in the respective $r - t$ plots. b) Effective diffusivity for water drops as a function of the drop volume Ω at a fixed η_o, viscosities varying from $\eta_o = 5$mPa-s to $\eta_o = 970$ mPa-s. Gray data points correspond to the case of 'bare' hydrophobic solid. The dotted lines in both a) and b) serve as a guide for the eye.

substrate with an acute angle, which accentuates the dissipation; on the other hand, the speed (typically 0.1 to 10 mm/s) is much smaller than in our experiments of spreading, and the slip is then negligible at the water/oil interface, thus minimizing the film friction [73, 75, 76]. In the case of spreading, we note that the oil meniscus is not stationary (it gradually builds when the bridge propagates), and it does not meet the substrate with an acute angle (beginning of the contact). Moreover, the liquid bridge grows at a large speed, typically 1 to 10 cm/s, compared to that of gravity-driven drops. It is known that at speeds greater than 1 cm/s, even gravity-driven drops exhibit a dynamically deformed meniscus and a completely different friction scaling, the physics of which has not yet been appropriately captured [73]. Thus, for the case of spreading, there is no reason to believe a priori that the meniscus force would exceed the film friction. We can go further by comparing their amplitude.

Because the classical scaling of meniscus friction corresponds to acute angles, it overestimates (by far) the dissipation in an obtuse wedge. However, even if we consider this scaling and compare it to the expression in the film, we find that the film friction dominates only when the contact line radius r is larger than a distance scaling as $\beta h^{3/2}\gamma^{1/2}/(\eta_o D)^{1/2}$. For making the latter expression more explicit, we take the inertial diffusivity $(\gamma R/\rho)^{1/2}$ as a scale for D, so that the previous relation can be re-written as $r^2 > \beta^2 h^2(\gamma_o/\gamma)^{1/2}/\psi$ where we introduce $\psi = Oh_o(R/h)$, denoting $Oh_o \sim \eta_o/(\rho\gamma R)^{1/2}$ as the Ohnesorge number of the oil. For our range of oil viscosities and

droplet sizes, ψ is of order unity, so that the film friction should dominate the meniscus friction for a contact size r larger than a few times h, the typical distance where we start our measurements.

Alternative Argument. An alternative way to approach the comparison between meniscus and film dissipation is to ask whether the meniscus have enough time to form. The water 'foot' or bridge of the drop grows to a length r in time $t \sim r/V$. The time to form a meniscus around this circular foot of size r is given by $t_m \sim r/(\gamma_{ow}/\eta_o)$, where γ_{ow} is the surface tension of oil with respect to oil and $\gamma_o w/\eta_o$ is the typical speed V_m at which the meniscus builds [109]. A meniscus can successfully form around the foot if the time t_m to form the meniscus, is smaller than the time t to grow the foot. In other words, the criterion for a meniscus can be written as

$$V < V_m \sim \gamma_{ow}/\eta_o \tag{24}$$

Experimentally, the maximum velocity we see is close to 1 m/s (at the earliest times). For $\gamma_{ow} \approx 50$ mN/s, $V_m > 1$m/s as long as $\eta_o \leqslant 50$ mPa-s. This means upto viscosities of 50 mPa-s, the meniscus does not form and hence the question of meniscus dissipation does not arise. However, for higher viscosities this is not as trivial as V_m is less than 1 m/s: this means as the contact grows with decreasing velocity, it reaches a critical contact size when the condition $V < V_m$ is satisfied, only beyond this length would we see a $t^{1/2}$ behavior. Indeed, in experiments with $\eta_o > 100$ mPa-s, we see this length to be 30-50µm, beyond which a $t^{1/2}$ behavior prevails, an exponent that the meniscus force would not have allowed for.

Inertia. Another source of resistance being inertia, we can finally compare the film friction to the inertial force. The volume of the mass re-organized being $r^2\delta$, the inertial resistance scales as

$$F_i \sim \rho r^3 V^2/R. \tag{25}$$

In order to see how F_i compares with F_f, we look at Figure 36, where we see a schematic of the variation of the two forces with respect to the oil-viscosity. The inertial force is constant in η_o, but F_f increases with η_o initially and then becomes constant. The inertial force dominates over film dissipation when $\rho r^3 V^2/R > (\eta_o V/h)r^2$, a condition that can be re-written as $rV > \eta_o R/\rho h$. We further this by noting that the diffusivity rV is necessarily less than that on a solid, $D_o \sim (\gamma R/\rho)^{1/2}$. This in conjunction with the previous inequality gives us $(\gamma R/\rho)^{1/2} > \eta_o R/\rho h$. From this we observe that there exists a critical oil viscosity, η_o^{**} below which the infused surface behaves as a 'bare' solid, which is given by

$$\eta_o^{**} = (\rho\gamma h^2/R)^{1/2} \tag{26}$$

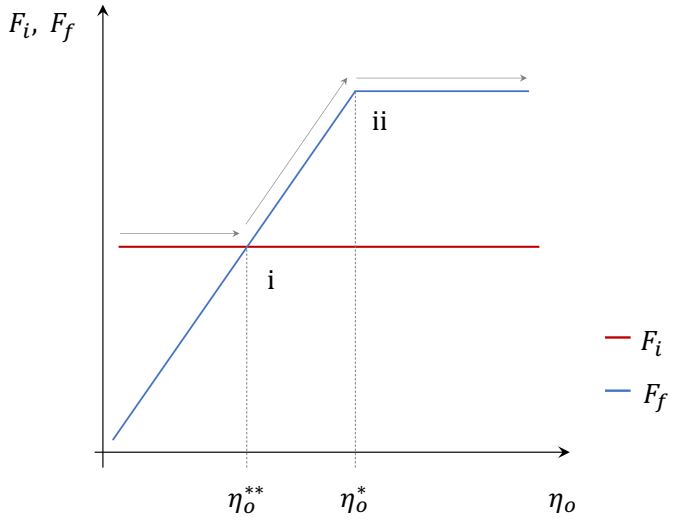

Figure 36: **Transition Points.** Schematic of the variation of inertial force F_i (red line) and dissipation force in the film F_f (blue line) with oil viscosity η_o. The grey arrows show the evolution of the total force $F_i + F_f$, which essentially follows the larger of the two forces. The intersection of the blue and the red line mark the first transition called i and the turning of F_f from increasing to a constant marks the next transition, called ii.

This criterion is shown in Figure 36 as the intersection of the red (F_i) and blue (F_f) curves, marked as transition i. For a millimetric water drop of water on our pillars of height $h = 20\,\mu m$, we get $\eta_o^{**} = 1$ mPa-s. Silicone oils of 1 mPa-s are extremely volatile and not conducive for experimentation as they create underfilled patches in the infused solid. So, we did the next best thing - experiments with $\eta_o = 5$ mPa-s and compared it with that of a 'bare' hydrophobic surface for a droplet of $R = 687 \pm 27\mu m$. The diffusivity for the infused surface came out to be $D = 70 \pm 3$ mm^2/s which is within 10% of the diffusivity of the 'bare' solid $D_o = 76 \pm 8$ mm^2/s. Thus in our experimental regime, we approach η_o^{**}, but never go below it.

Alternatively, higher pillars of the order of 100μm may be used which can push η_o^{**} to 10 mPa-s.

As marked in Figure 36, the second point of transition ii corresponds to $\eta_o^{*} = \rho\gamma h/\eta$, as we obtained from Equation 22. This transition be directly observed in our experiments. In this regard, in Figure 36, we can mark our experimental parameter space as the entire region beyond i, for the region below i, we have one data point corresponding to a 'bare' solid, where F_f is naturally zero.

It is also interesting to point out here that dividing F_i by the viscous force, F_f in the film, for the region below ii, generates a kind of Reynolds number, $Re = \rho r V h/\eta_o R$, which also shows that inertia can dominate viscosity ($Re \gg 1$) at low η_o, a limit in which rV would approach D_o and viscous effects just become a perturbation of the inertial regime, as suggested by Figure 32. Then, the number Re sim-

ply reduces to $1/\psi$, where $\psi = Oh(R/h)$, a quantity of order unity (as mentioned earlier): even at early times, viscous effects can perturb the inertial spreading and reveal an influence of the subjacent layer of oil.

Equation of Motion. We may now construct our equation of motion of the contact line with all the dominant forces at play which reads as $F_i + F_f \sim F_d$. Substituting for each force from Equations 20, 23 and 25 and dividing by $F_d \sim \gamma r$, we get:

$$\frac{\rho}{\gamma R} V^2 r^2 + \frac{\eta_o}{\gamma h\left(1+\frac{\eta_o \eta}{\rho \gamma h}\right)} Vr - 1 \sim 0 \tag{27}$$

The first thing we note in the above equation is that the entire equation, as a quadratic in Vr, preserves $t^{1/2}$ kinetics in all its branches of solutions. We substitute Vr as D and re-write equation 27 succinctly in terms of $\psi = Oh_o(R/h)$ and $Oh_D = \eta/(\rho\gamma R)^{1/2}$, as

$$D^2 + \frac{\psi}{1+\psi Oh_D} DD_0 - D_o^2 \sim 0 \tag{28}$$

We identify two limits of the above equation: one, when when $\psi Oh_D \gg 1$. In this case a comparison of the inertial and the viscous term shows that the inertial term can dominate over the viscous term only if $D/D_o > 1/Oh_D$, which is equivalent to $\eta > \rho\gamma R$, a condition always satisfied for millimetric water drops. This gives a solution $D \sim Oh_D D_o \sim \eta/\rho$.

In the opposite case of $\psi Oh_D \ll 1$, we can write a general solution to Equation 28 as

$$D \sim D_o((4+\psi^2)^{1/2} - \psi)/2, \tag{29}$$

which itself has two asymptotic limits: at small ψ, Equation 29 reduces to $D \sim D_o$, that is, the behavior expected when inertia is dominant — a logical result since ψ was found to correspond to the inverse of the Reynolds number of this problem; at large ψ, the solution tends towards $D \sim D_o/\psi \sim D^*$, the case where the effect of viscosity becomes dominant. These asymptotic laws are drawn with dotted lines in Fig.37, where we add both the solution of Equation 29 (solid line) and our data for $\Omega = 1\mu L$ and $\Omega = 4\mu L$.

In Fig.37, the measured diffusivity is normalized by the inertial diffusivity D_o and plotted as a function of ψ. We restrict the comparison between experiments and model for microlitric drops: a drop with a volume larger than $10\mu L$ has a size comparable or larger than the capillary length, so that gravity effects also matter: the force driving the motion becomes a combination of surface and gravitational effects,

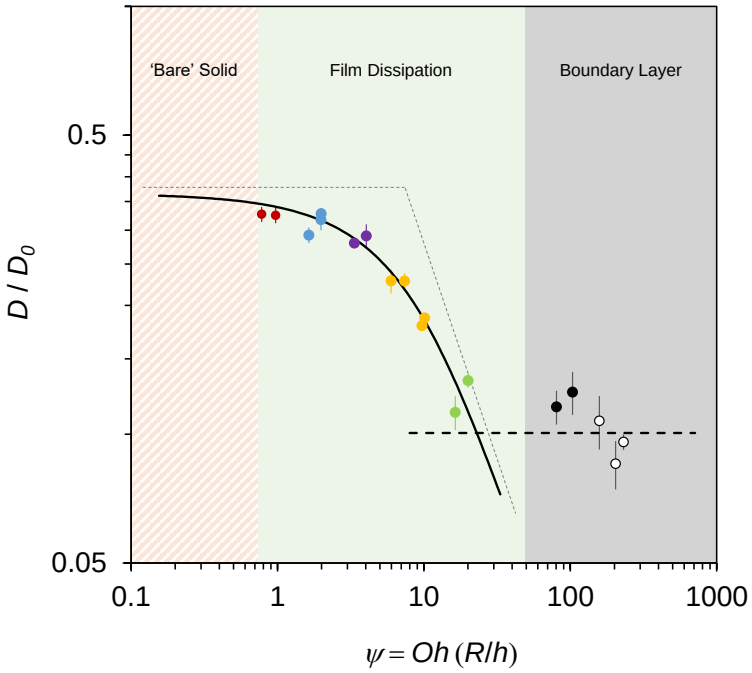

Figure 37: **Theory and Results.** Non-dimensionalized effective diffusivity plotted against ψ. The solid line is a fit to Eq. 29. The dashed line corresponds to $D/D_0 = 0.1$.

and the liquid shape deviates from a sphere, so that our geometric arguments (for deriving D_o) become questionable. As predicted by the model, we obtain in Fig.37 a collapse of all data upto $\eta_o = 100$ mPa-s on the same curve when plotted as a function of ψ, this curve itself being well fitted by the solution of Equation 29. The oil viscosity is present in the Ohnesorge number Oh_o (to which it is proportional), while the effect of the drop volume is included both in D_o and in ψ. The latter parameter being of order unity in our experiments, most data lie in the cross-over regime between the inertial and viscous ones ($\psi \ll 1$ and $\psi \gg 1$, respectively). The fit provides the numerical coefficients ignored in our scaling arguments: as seen from the asymptotic behaviors, D/D_o tends towards 0.36 at small ψ, in close agreement with the value found on a solid (Fig.35); at large ψ, the fit is $D/D_o = 2.5/\psi$, where the numerical factor remains to be understood from a complete calculation of the dissipation in the oil film. Beyond $\eta_o = 100$ mPa-s, which here corresponds to $\psi > 10$, we see all of the data collapse on a fixed value of $D/D_o = 0.1$, which also reveals that the pre-factor in front of ψOh_D in Equation 28 is 9.5.

Thus, in Fig.37, we see a revelation of three regimes: one approaching the 'bare' solid as $\psi << 1$, the second is a regime of pure slip, where we see a mixture of inertia and viscous dissipation in the infused film within the textures – this regime begins at $\psi > 1$ and with

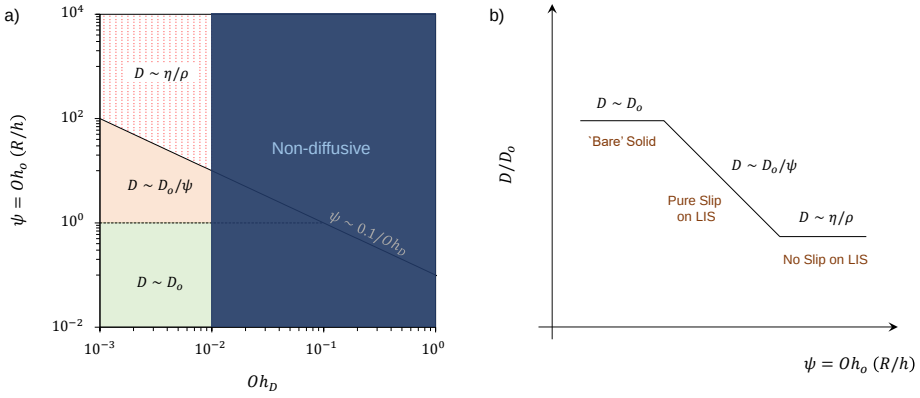

Figure 38: **Phase Map.** Phase Map of different regimes of spreading on a liquid-infused surface: $\psi = Oh_o(R/h)$ plotted against Oh_D, where $Oh_o = \eta_o/(\rho\gamma R)^{1/2}$ and $Oh_D = \eta/(\rho\gamma R)^{1/2}$. The dark blue shaded region corresponds to $Oh_D > 10^{-2}$, that is $\eta_D > 10$ mPa-s, where drops do not spread diffusively. The solid line corresponds to the criterion $\psi \sim 0.1 Oh_D$, below which spreading is a pure slip phenomenon on LIS, and above which there is no slip. For the former, we approach $D \sim D_o/\psi$; for the latter, the diffusivity is that of momentum diffusivity for the drop, η/ρ. The dashed line corresponds to $\psi = 1$, below which spreading on an infused surface is equivalent to spreading on a 'bare' solid, where $D \sim D_o$. These give us three distinct diffusive regimes within the diffusive regime itself. In our experiments, we take a water drop of fixed radius, which fixes the abscissa value; by changing the viscosity of the infusion, we move along the ordinate and transition from one phase to another. b) Sketch of a plot of nondimensionalized diffusivity versus $\psi = Oh_o(R/h)$, as seen in Fig.37, showing the three distinct regimes of diffusivity as we increase ψ. At the lowest values, we approach the case of spreading on 'bare' solid, then with increasing ψ we sharply decrease to approach D_o/ψ, until we reach a critical ψ, for sufficiently viscous liquids where the slip velocity essentially goes to zero, and we get a diffusive regime, only a function of the drop characteristics.

increasing ψ, the diffusivity was approaching a Washburnian hemicking regime, but was cut short by the limiting criterion of $\psi = 0.1/Oh_D$, beyond which the infused surface is so viscous that the slip velocity vanishes, and we see the contact grow in the same way boundary layer does. We use these three criteria for transition to construct the phase space in ψ and Oh_D in Fig. 38a. The dark blue shaded region where $Oh_D > 10^{-2}$ corresponds to the condition of $\eta > 10$mPa-s where spreading is non-diffusive in nature and follows Egger's Law (Equation 17). Our experimental phase space is limited to $10^{-3} < Oh_D < 10^{-2}$, where for a fixed abscissa Oh_D, that is a water drop of a fixed size, we travel along the ordinate ψ by changing the viscosity of the infused liquid, thus successively passing through three regimes. Fig.37b shows the same in $D/D_o - \psi$ phase space.

3.2.4 *Conclusion*

A water drop spreading on a LIS reaches its equilibrium very quickly, a consequence of the combination of partial wetting and low water viscosity. Inertia is thus *a priori* expected to be the dominant resistance to spreading, as observed for water contacting a hydrophobic solid. However, the oil contained in the LIS is found to affect significantly the spreading dynamics: the contact between water and its substrate develops slower than that on a solid, the slowing down being an increasing function of the oil viscosity η_o – which we show to be due to an additional friction at the water/oil interface.

LIS are often viewed as slippery surfaces, which they are from the adhesion point of view, but not necessarily from the friction point of view. Three regimes of spreading were identified as a function of the viscosity of the infusion, which remarkably preserve the scaling of the contact with time, despite their different physics - at low viscosities the spreading behavior asymptotically approaches that of a 'bare solid'; at intermediate viscosities, $(\rho\gamma h^2/R)^{1/2} < \eta < \rho\gamma h/\eta$ the drop spreads with pure slip on the infused surface; for very high viscosities, $\eta > \rho\gamma h/\eta$, drops spread on the infused liquid with a vanishing slip velocity, which we could model. We could deduce from the calculation simple scaling laws for the spreading time in the three limits of oil viscosity. In the first case, the spreading time τ scales as R^2/D_o, that is, as $(\rho R^3/\gamma)^{1/2}$, the usual inertio-capillary time of a drop. In the second limit, τ scales as R^2/D^*, that is, as $\eta_o R^2/\gamma h$. This time scale, now a function of η_o, is not the trivial viscous time $\eta_o R/\gamma$ of relaxation of a drop driven by surface tension; rather, it includes the texture thickness, showing that the spreading of water on a viscous LIS results from an interplay between the drop relaxation and the film response. In the third limit, τ scales as $\rho R^2/\eta$, where the LIS is so viscous the drop does not 'feel' it - its spreading time has not signature of the oil viscosity; it is the same as time to form a viscous boundary layer within the drop.

We end by highlighting that typical phenomena in fluid flows have inertia and friction exhibit different scalings in time, which help differentiate the regimes in which they dominate and crossover to the other. What we saw here was a unique example of a fluid dynamical problem where inertial and viscous frictional forces (of two different kinds) betrayed the same scaling in time (when balanced with capillarity), in not one but three successive regimes which one can transition through by changing a single non-dimensional parameter: $\eta_o/(\rho\gamma R)^{1/2} \times R/h$.

3.3 VISCOUS DROPS ON INFUSED SOLIDS

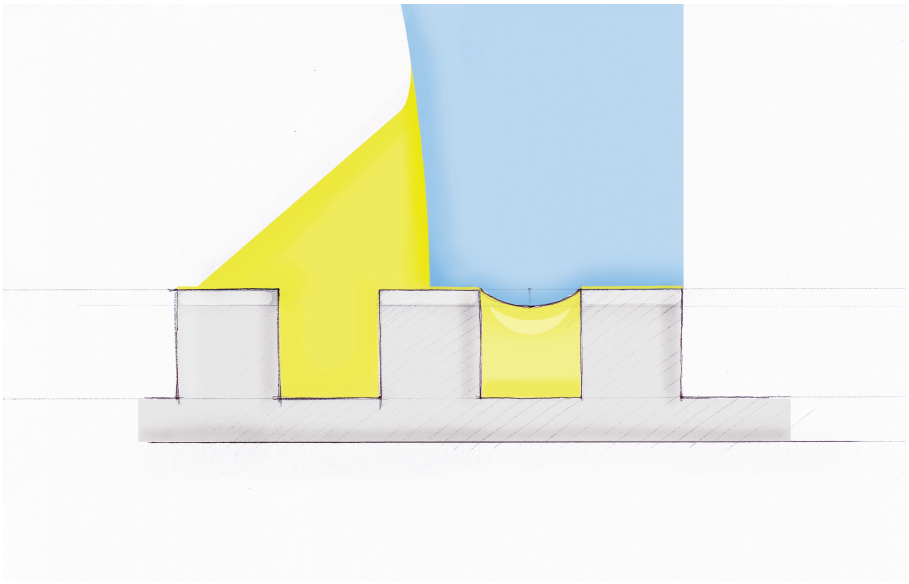

'The Foot of Glycerol on Rome' by Benoît Pype

A natural question that follows from the previous section is what happens in the opposite limit of a viscous liquid (such as glycerol) spreading on a non-viscous LIS, a case where the kinetics could benefit from the lubricating effect of the subjacent layer. As discussed in the Section 3.1.2, the growth of the contact of a viscous drop on a 'bare' solid substrate is governed by a balance between the friction force on the expanding 'hemi-toroid' of air $F_\eta \sim \eta V r / \ln(R/r)$ and the driving force $F_\gamma \sim \gamma r$, which results in the Eggers' Law -

$$r = A_o(\gamma/\eta)t \ln(R/r) \tag{30}$$

where A_o is a prefactor which has no dimensions. Although the theoretical prediction of A_o for coalescence of two identical drops in a medium of non-zero viscosity is $1/4\pi$ [94], the experimentally determined value of A_o previously has been close to 1 [102].

Our objective here is to test the validity of this law, and to understand how it is modified by the presence of lubricating layer: if our arguments are correct, Eggers' law should be universal (since it is mostly dictated by the geometry, and its consequences on hydrodynamics), but the coefficient A be impacted by the change of boundary condition – at least if the lubricating layer is chosen with a viscosity smaller than that of glycerol.

3.3.1 *Experiments*

To do so, we design an experiment where we bring a 1 µL-drop of glycerol in contact with either a solid or with a so-called LIS, namely a textured solid infused with a silicone oil, the same way as we did in the experiments with water in the previous Section 3.2. As a benchmark for comparison, we use a hydrophobic solid. Figure 39 shows top-down images of how the contact line of a glycerol drop grows when brought in contact with a hydrophobic solid and for infused surfaces with oil viscosities of $\eta_o = 9$, 96 and 970 mPa-s. We observe from the images that for the case of $\eta_o = 9$ mPa-s, the glycerol drop spreads much faster than that on a solid. With increasing viscosity, the rate of growth becomes slower and slower, and for $\eta_o = 970$ mPa-s, the contact spreads almost the same way as it does on a solid.

In order to make our understanding more quantitative, we know plot the temporal evolution of the radius of contact in Fig. 40. The first observation we make is that all the glycerol drop spreading on hemi-solid or solid surfaces follow Eggers' law (Equation 30), but on hemi-solids, the drop spreads faster, the fastest being on the LIS with the lowest viscosity of infusion, which in our experiments is $\eta_0 = 4.6$ mPa-s (Fig. 40). For this viscosity, we see that the contact grows to a radius 100µm in 0.3 ms which is nearly six times less than the time it takes to spread the same extent on a hydrophobic solid,

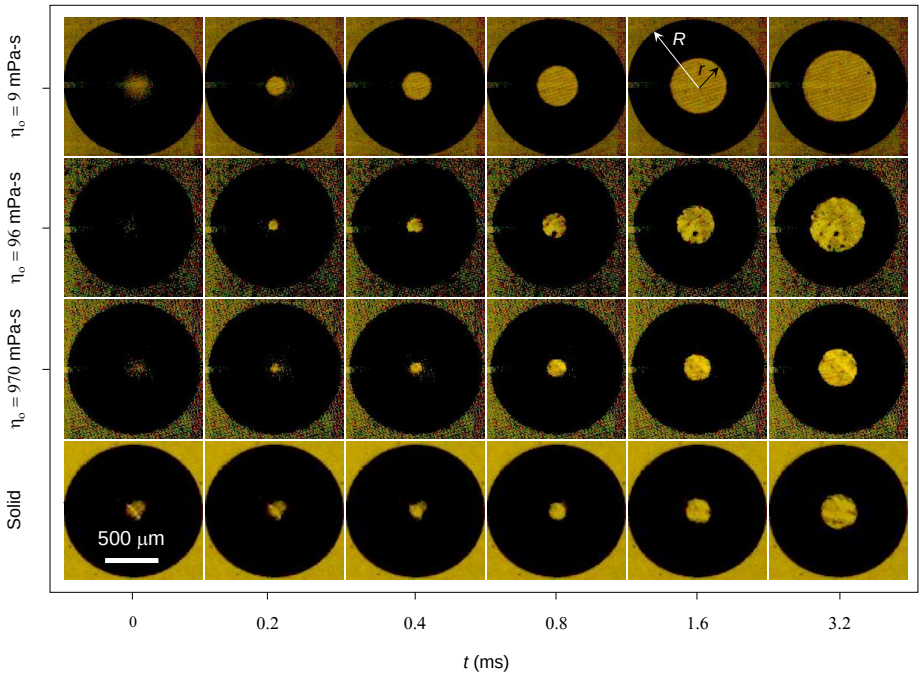

Figure 39: **Timelapse.** Time-lapse top-down images of the growing contact of a 1μL glycerol drop on the surface of a LIS for three different oil viscosities: η_o =9, 96 and 970 mPa-s, and also on a 'bare' hydropobic solid. We see that in comparison to the spreading on a solid, spreading on LIS is faster - the fastes being on the lowest viscosity

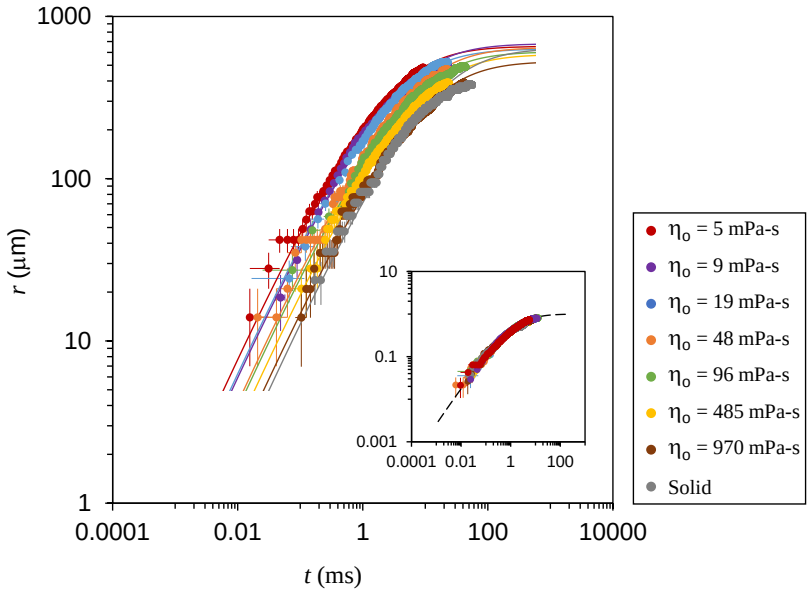

Figure 40: **r-t plots.** Temporal evolution of the contact line radius when a 1μL glycerol drop touches a LIS infused with different oil viscosities: η_o =5, 9, 19, 48, 96, 485 and 970 mPa-s, and for the case of a 'bare' hydrophobic solid. Error bars in time correspond to one standard deviation equal to the inverse of the frames per second and error bars in length correspond to one standard deviation equal to one-pixel size. Solid lines are fits to the Equation 30. b) Non-dimensionalized radius r/R plotted against At/τ, for different values of η_o.

thus demonstrating the spectacular effect of lubrication engendered by the infused surface. Furthermore, the lubricating nature of the infusion decreases with increasing viscosity and for $\eta_0 = 970$ mPa-s we see that the r—t plot is very close to the case of glycerol spreading on a hydrophobic surface itself. The solid lines in Fig. 40 are fits to (Equation 30), where a different A is chosen for a different η_o. The inset of Fig. 40 shows that the $r - t$ curves can be collapsed when the nondimensionalized radius r/R is plotted against At/τ, the value of A being only a function of η_o. This shows that indeed all the curves follow and preserve the same law Equation 30 and are thus governed by the same physical mechanisms at play. Moreover, there exists a unique A for every η_o, that can collapse all the curves.

3.3.2 *The Model*

The natural question that follows from this is how does the lubricating effect of the infused oil modify the dissipation and generate a slip that preserves the nature of the law of spreading on a solid. Said differently, how does the dissipation of the infused oil get absorbed within the prefactor A itself.

Herein, we note as the contact grows, there would be an oil meniscus that would form around the 'foot' or the 'cusp' of the contact, as shown in Fig. 41, which would grow at a typical speed of γ_{og}/η_o for $\eta_o > 10$mPa-s where $\gamma_{og} = \gamma_g - \gamma_o$, which is the surface tension of silicone oil with respect to glycerol [109]. This speed is faster than the typical spreading velocity of the foot in the initial stages γ/η, as $\eta > \eta_o$. Note that this is precisely what was not happening for the case of a water drop spreading on the infused surface, as η of water was strictly less than η_o always. The existence of a meniscus immediately tempts us to consider the dissipation in the corner of oil, which would scale as $F_o \sim \gamma_o r\phi\beta(\eta_o V/\gamma_o)^{2/3}$, as we know from Tanner's Law and as discussed in the previous Section 3.2. Balancing the Stokesian dissipation and the line friction with the driving force we get -

$$\eta V r/\ln(R/r) + \beta(\eta_o V/\gamma_o)^{2/3}\gamma_o r\phi \sim \gamma r \tag{31}$$

The above equation can be re-written as

$$V\left(1 + \frac{\eta_o^{2/3}\gamma^{1/3}}{\eta V^{1/3}}\beta\phi \ln(R/r)\right) \sim \frac{\gamma}{\eta}\ln(R/r) \tag{32}$$

Since the experimental curves all preserve the logarithmic law, it implies that F_η and F_γ give us the dominant scale of the velocity and that F_o is, in fact, a perturbation to that solution. In other words, the

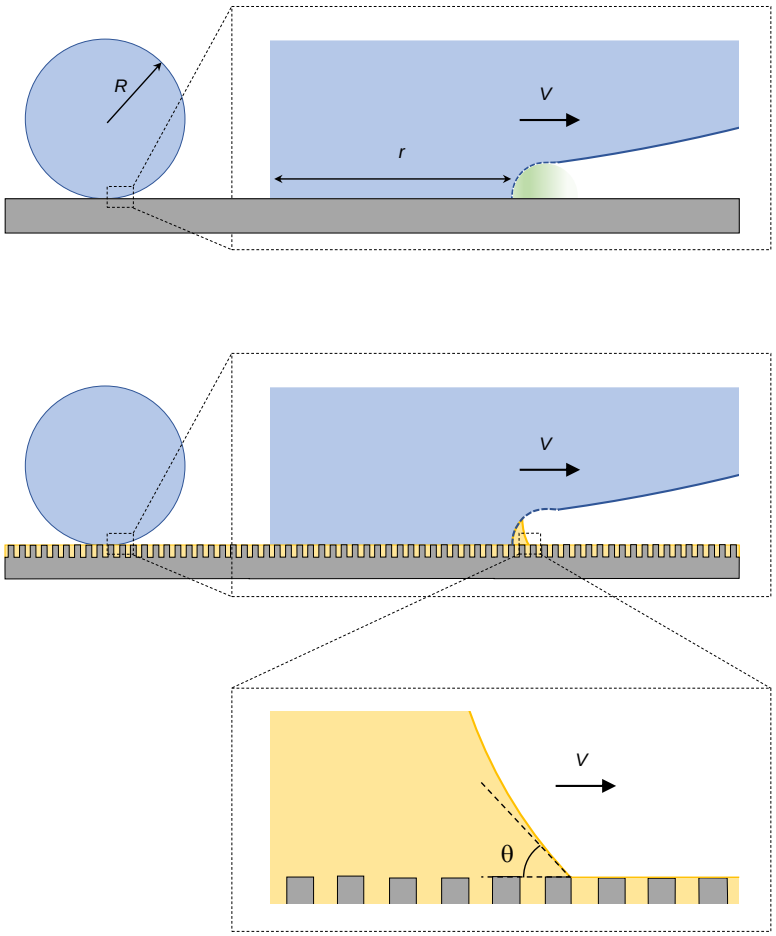

Figure 41: **Sketch of Contact Zone.** Top: A viscous drop touches a 'bare solid' to forms a cuspoidal contact where a 'hemi-toroid' of air is pushed out. Below: A viscous drop touching an infused surface forms a cuspoidal contact which has a meniscus formed within. A further zoom shows the meniscus has a dynamic contact angle θ where wedge friction dominates.

pre-factor multiplied to V on the left hand side of the Equation 32 is predominantly 1 − a rough estimate of its deviation from 1 can be obtained by plugging in γ/η for V. This would give us a solution of the form $r = A\gamma/\eta \ln(R/r)$, where

$$A = \frac{a}{1 + b(\eta_o/\eta)^{2/3}}, \tag{33}$$

where a and b are pre-factors that should be independent of η_o and R. However, this argument has its weaknesses - for example, we take b to be a constant where it has the term $\ln^{2/3}(R/r)$ which we take to be a constant. This can only be defended by saying that $\ln(R/r)$ is of the order of 1 with its largest value being 3 corresponding to $r \sim 1\mu m$ which is the optical resolution of our experiments and the fact that it is raised to the power 2/3 decreases its value further in comparison to the driving force term where it is raised to the power of 1. Nevertheless, whether such a crude approximation can capture the primary features of our observation would illuminate us regarding the limitations of our approximations.

In Fig. 42 we plot that A values against η_o/η for two different volumes of drops 1μL and 4μL. The data points reveal that there is no effect of R on A, in this limit where we are below the capillary length. Next, we see that the A values decrease from $A = 7.3 \pm 0.3$ for $\eta_o = 4.5$ mPa-s to $A = 1.9 \pm 0.3$ for $\eta_o = 970$ mPa-s, the latter value being very close to what we see on a 'bare' hydrophobic solid where $A_o = 1.4 \pm 0.2$. The solid line corresponds to a fit to Equation 61 with $a = 7.5$ and $b = 3.6$. We also note that as η_o/η approaches 1, $A \sim (\eta_o/\eta)^{-2/3}$. However, it must be kept in mind that our approximation of plugging in γ/η to obtain $A = f(\eta_o/\eta)$ holds only in the limit $\eta_o > \eta$.

We must now rationalize the values of a and b to see if our model is is consistent. The theoretical value of $b \sim \beta\phi(\gamma_o/\gamma)^{1/3} \ln^{2/3} R/r$, where $\beta \sim 10$ and $\phi = 23 - 25\%$. This yields a prefactor of 1.2 between the experimental and theoretical values of b. The value of $a = 7.5$ might appear to be inconsistent with the idea

Regarding the value of $a = 7.5$, we note that it is far from is far from A_o, but there is no inconsistency here. It must be emphasized that although it might appear that setting $b = 0$ does not help us recover the case of spreading on a 'bare' solid, because that requires an added condition $\phi = 1$. The absence of the latter condition in conjuntion with $b = 0$ essentially takes us to a the case of a textured solid. However a glycerol drop when brought in contact with a textured solid would also impregnate and wick inside the textures, along side spreading, which is not accounted for in our model because on a hemisolid, the drop cannot penetrate within. Hence, $b = 0$ and $\phi \neq 0$ is corresponds to the hypothetical case of a textured solid, on which a drop can spread but not penetrate, say a textured solid infused with

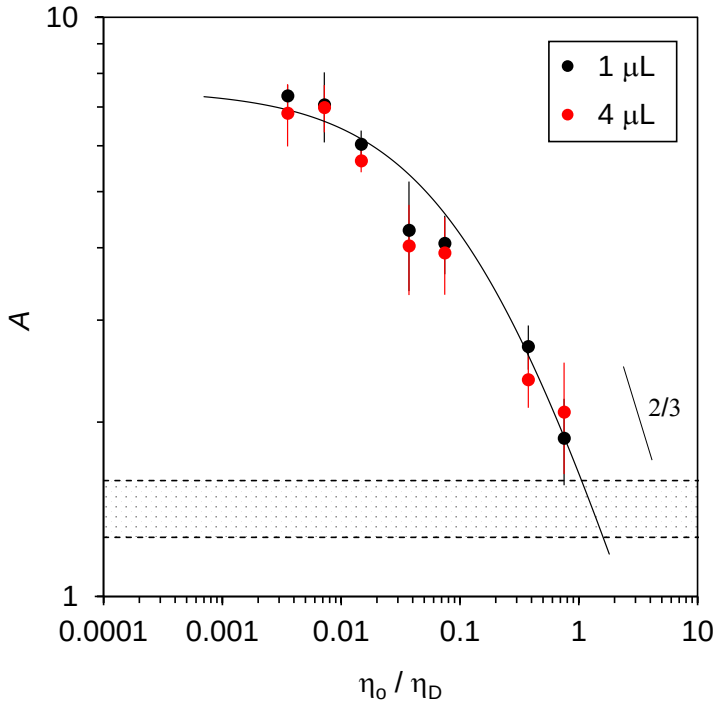

Figure 42: **Model and Results.** A values plotted against nondimensionalized oil viscosities η_o/η_D, for two different volumes of drops - 1μL and 4μL. Note that A is independent of droplet volume and only a function of η_o/η_D. The shaded region corresponds to the values of A corresponding to experiments on a 'bare' hydrophobic solid with error, which is 1.4 ± 0.2. Error bars are obtained from multiple trials of each experiment. The solid line is a fit to Equation 61 with $a = 7.5$ and $b = 3.6$.

an oil of zero viscosity — a limit we approach as we decrease η_o/η, which is fundamentally different from a flat 'bare' solid. Hence, the value of $a = 7.5$ being different from $A_o = 1.4 \pm 0.2$ is not inconsistent. Said differently, as we decrease η_o/η, and in the process decrease the contribution of dissipation from the liquid-liquid contact increases in the contact area, and all that remains is the contribution of dissipation from the solid-liquid contact, but the solid liquid contact is lesser than that on a flat 'bare' solid, which is why the friction is lesser than what would be on a bare solid. This is precisely why a is expected to be larger than A_o, because A is representative in a sense of how fast the drop spreads on the surface. Therefore, the value of a too should vary with ϕ, however that is beyond the scope of the present study.

A glycerol drop spreading on a solid is slow — viscosity dominates, capillarity drives and inertia is dead. However, when placed on an infused surface, glycerol drops are accelerated in comparison — the infused oil of lower viscosity forms a meniscus around the drop decreasing its friction, the texture too contributes by decreasing the glyceol-solid contact, minimizing the friction further. Typically a micro-liter glycerol drop spreads on a solid in about a second, but on an infused surface with $\eta_o = 5$ mPa-s, the glycerol drop spreads in a few milliseconds. In the opposite limit, where $\eta_o = \eta$, the spreading time is the same as that on a solid. We could describe the entire picture of this unique spreading behavior with simple scaling laws.

3.4 CONCLUSION

Thus, we see liquid infused surfaces have a unique unifying trait in the context of spreading of drops - these hemisolids preserve the nature of the law of spreading as observed on solids, but dramatically change the amplitude of it. If a low-viscosity drop as water spreads on a LIS infused with an oil of higher viscosity, then spreading is slowed down - the more viscous the oil, the slower the spreading, the fastest being that on a 'bare solid'. But, if a drop of high-viscosity as glycerol spreads on low viscosity LIS, the drop is accelerated in comparison to how it spreads on 'bare solid'. It would however be interesting to see what happens when a viscous drop as glycerol spreads on a hemisolid which is infused with an even higher viscosities — a regime not investigated here.

4

LARGE DROPS SPREADING ON INFUSED SOLIDS

In this chapter, we ask what happens when a large drop or a puddle of water touches an infused surface. We proceed by first asking this question for a 'bare' solid. In the process, we find some original features of puddles touching a 'bare' solid surface. We contrast this with the character of spreading, as we find on infused solids.

4.1 LARGE DROPS AND PUDDLES ON 'BARE' SOLIDS

In the last chapter, we saw that when a droplet of a low viscosity liquid ($\eta < 10$ mPa-s) as water touches a 'bare' solid, its contact first grows as $r^2 \sim Dt$, where $D \sim \sqrt{\gamma R/\rho}$. However the two necessary conditions that must be fulfilled for this law to be valid are:

i) Geometry: the drop must be spherical, in other words, its radius $R \sim \Omega^{1/3}$ must be less than κ^{-1}, where $\kappa^{-1} = \sqrt{\gamma/\rho g} \sim 3$ mm for water, and

ii) Time: the time t elapsed from the point of first contact must be less than the capillary inertial time scale $\tau = \sqrt{\rho R^3/\gamma} \sim 1$ ms for water.

The first condition is necessary because the very origin of the diffusive nature of inertial spreading - the 'Hertz Contact' - is true only for a sphere-plane geometry. The second condition ensures that capillarity and inertia will be the only dominant antagonistic forces dictating the dynamics of the contact.

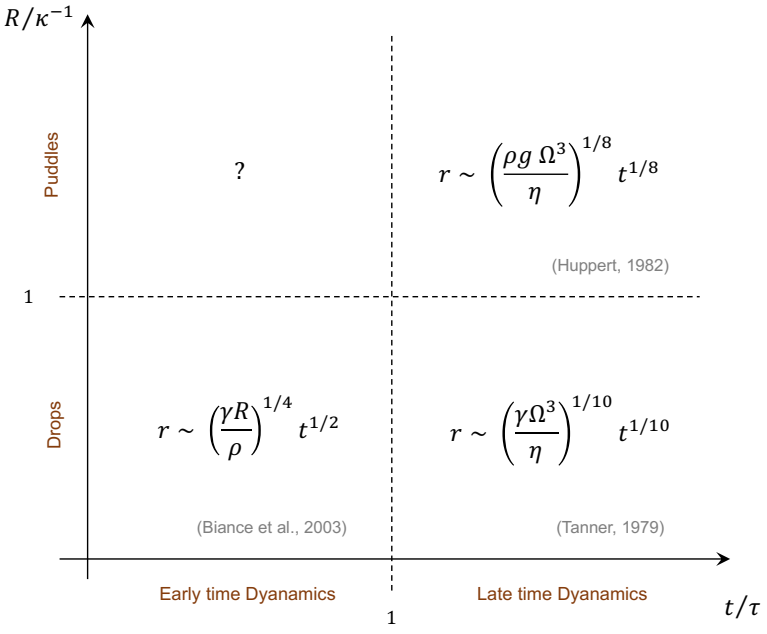

Figure 43: **All the Laws.** Phase Map of a drop spreading on a flat solid: nondimensionalized radius of the drop R/κ^{-1} plotted against nondimensionalized time t/τ, where τ is the capillary inertial time scale and κ^{-1} is the capillary length.

Tanner's original experiment was with Silicone oil, not water.

In light of this, we can now ask what happens when we violate these conditions. Fig. 43 shows a phase map where the dimensionless radii R/κ^{-1} is plotted against t/τ which reveals that different regimes that emerge based on the constraints of geometry and time. Historically, the first of these four regimes, in the chronology of discoveries was by L. H. Tanner in 1979 and it corresponds to the case

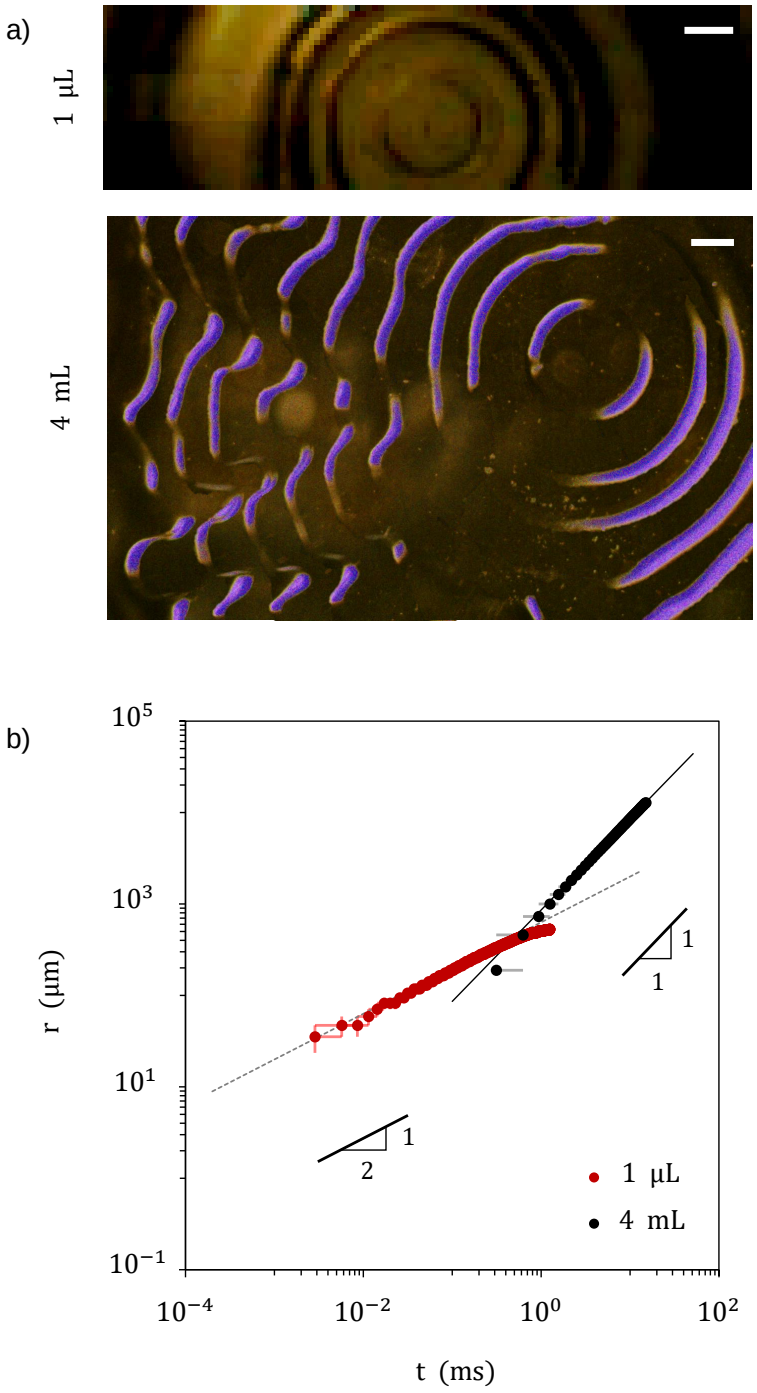

Figure 44: **The Puddle and the Drop.** a) Topdown timelapse of the growing contact line when a 1 μL and a 4 mL drop first touches a hydrophilic glass slide/plate from the top. For the 1 μL drop, we see the first position at 28 μs, and successive positions are at 86 μs intervals, and for the 4 mL, successive positions are tracked at an interval of 1.56 ms from time $t = 0$. Scale bars for 1μL and 4 mL drop represent 100μm and 1 mm respectively. b) When the radial positions from the experimental micrographs of a) are plotted against time, we see the contact of 1μL drop grows as $t^{1/2}$ (dotted line), while the contact for the 4 mL drop grows as t^1 (solid line).

of $R/\kappa^{-1} \ll 1$ and $t/\tau \gg 1$, that is when a small drop of a few microliters of water is deposited on a perfectly wetting surface and we measure the radial extent of its spread in the order of minutes or more [85]. In this regime, surface tension is balanced by the 'line friction', and the contact line grows as $r \sim (\gamma\Omega^3 t/\eta)^{1/10}$. The regime that was discovered after Tanner's was by Huppert in 1982: this corresponds to case of $R/\kappa^{-1} \gg 1$ and $t/\tau \gg 1$ - something we will see if we pour a large puddle of water of hundreds of mililiters and see how it spreads in a duration of minutes or more [110, 111] This regime also known as the regime of gravity currents is where gravity dominates over capillarity and is balanced by the bulk dissipation which dominates over line friction to yield the law $r \sim (\rho g\Omega^3 t/\eta)^{1/8}$. The third regime that was found by Biance et al. corresponds to the case of a drop of a few microliters of water spreading in a duration of less than a milisecond: $R/\kappa^{-1} \ll 1$ and $t/\tau \ll 1$ [81]. We have extensively discussed this regime in the previous chapter.

Seminal contributions in gravity currents were also made by von Kármán and Brooke Benjamin before.

The only regime that remains to be looked into thus is the fourth one: $R/\kappa^{-1} \gg 1$ and $t/\tau \ll 1$, that is what happens in the very first moments of a puddle touching a solid. Naturally, a puddle cannot be deposited on a solid surface without impact, owing to its weight. So we place a puddle on a superhydrophobic surface and bring a flat hydrophilic glass plate in contact with it from the top 'gently', akin to the setup we had in our previous experiments on spreading on infused surfaces. We do simultaneous topdown and sideview imaging with a high speed camera of 4000 frames per second for the puddle experiments and 400,000 frames per second for the droplet experiment.

Fig. 44a shows a timelapse of the topdown view of a 1 μL droplet and a 4 mL puddle immediately after contact is established, and Fig. 44a shows the temporal evolution of the contact line radius on a log-log plot. We immediately note a striking difference between the two cases: while for the droplet, the 'foot' of contact grows diffusively, as $t^{1/2}$, for the puddle we report a constant velocity of 0.9 m/s. Furthermore, unlike the case of the droplet, the contact line for the puddle starts to destabilize with a wavelength of roughly $2-3$ mm.

More features of the nature of the contact for the puddle can be seen in Fig. 45 where a 6 μL puddle looks from the side and the top and how the contact grows after contact is established. The topdown images reveals that that the contact is not at the center, rather near the periphery of the puddle — a generic feature of the puddle-plane contact. This is a signature of the existence of a 'dimple' of air: as the air film gets squeezed between the top of the puddle and the flat solid, a dimple forms — the thickness of such dimples are known to be the maximum at the center and the minimum at the periphery, where the film is the most prone to rupture [112].

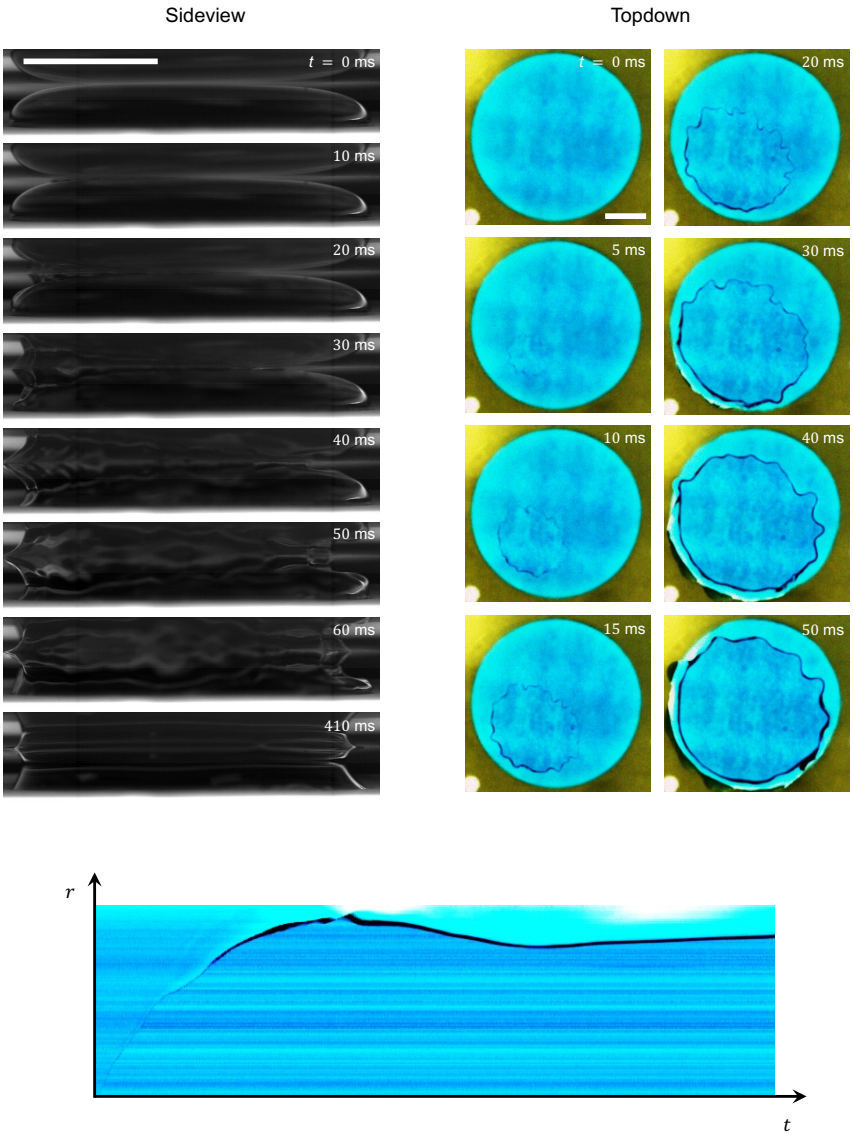

Figure 45: **The Puddle.** Top: Sideview and topdown images of a 6 mL puddle on a superhydrophobic surface brought in contact with a hydrophilic glass plate from the top. Bottom: a rotated reslice of the spread from the point of contact, which essentially is radius plotted against time, but in pixels. Scale bars represent 1 cm.

Following the rupture, the air film 'dewets' to a millimetric size in miliseconds at a constant speed. While a 1 μL droplet too reaches a millimetric size in miliseconds but not at a constant speed: in fact, by the time the 1 μL droplet reaches millimetric dimensions, its velocity is near zero. Conversely, for a puddle, the speed is 1 m/s when the contact line has grown to a milimeter in size — such fast motion of the contact line at millimetric scales can destabilize the contact line and occasionally air bubbles are captured as seen in Fig. 46.

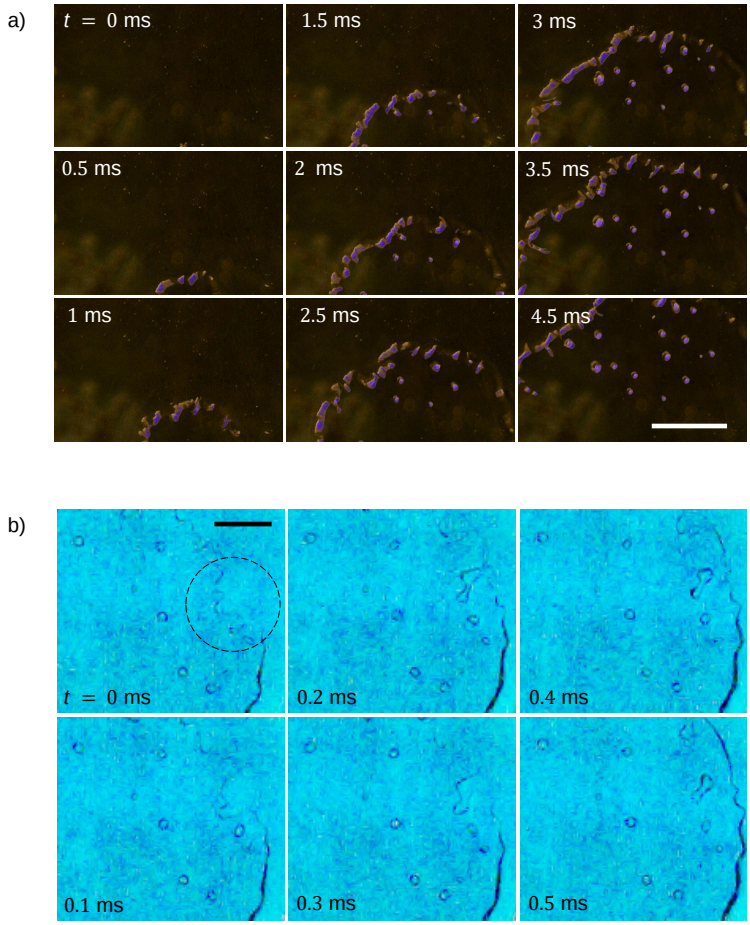

Figure 46: **Bubbles.** Topdown view of a puddle contacting a hydrophilic glass plate reveals that contact line can destabilize (dotted circle) to capture multiple bubbles, as observed in two different trials. Scale bars represent 5 mm.

However in the present study we would not concentrate on the capturing of the bubble, rather the transtion to a t^1 law for puddles from a $t^{1/2}$ law as observed for droplets. The inertial law as given by Equation 16 can be written in a nondimensionalized form as

$$r/R_c \sim (t/\tau)^{1/2} \tag{34}$$

where τ is the capillary inertial time scale. In Fig.47 a, we plot the radius of the contact line r nondimensionalized by the local radius of curvature R_c at the point of first contact (obtained from sideview images) against time t, normalized by the capillary inertial time scale τ, for different drop volumes ranging from 1 µL to 4 mL, which in terms of the radius of curvature varies from 600 µm to 17.2 cm.

The first thing we note from the figure is that apart from the case of $R_c = 17.2$ cm, the nondimensionalized contact size of all the other drops collapses on the same line at long times. This line drawn in dotted grey corresponds to Equation 34 with a prefactor of 1.3, which is the same as obtained in previous spreading experiments [84]. Next we see that while for small droplets, the data follows Equation 34 from the earliest times, for R_c greater than 2 mm, there is a consistent deviation from the 1/2 - law at the early times, and finally for 4 mL, the exponent is 1. In Fig.47b, we remove the 4 mL data and the error bars and zoom in to show the consistent deviation from the 1/2 - law as observed with increasing volumes. We do so because while for the 4 mL puddle we see a clear t^1 behavior, all the drops smaller than this volume showed an early deviation from the 1/2 - law, but not a t^1 law, and it is possible that the reason for the deviation is not the same as that of constancy of speed for the 4 mL case.

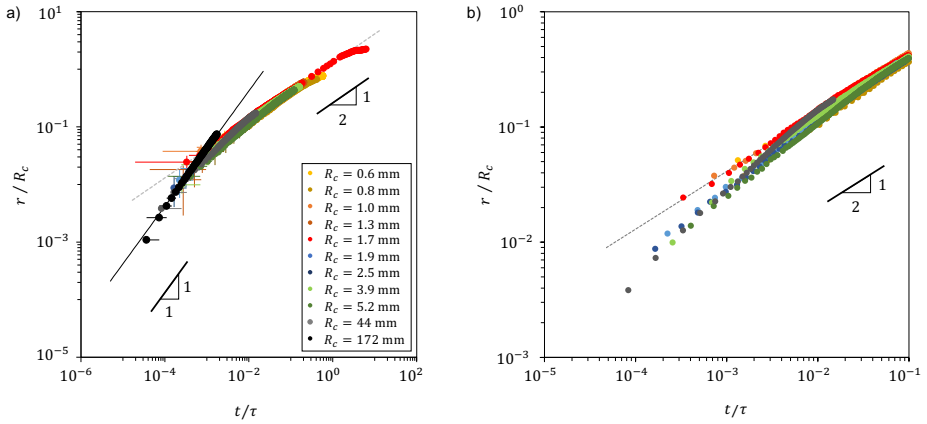

Figure 47: **Deviation from the 1/2 Law.** a) Nondimensionalized radius of the contact line r/R_c where R_c is the local radius of curvature R_c at the point of contact plotted against non dimensionalized time t/τ, where $\tau = \sqrt{\rho R_c^3/\gamma}$ is the capillary inertial time scale for different drop volumes ranging from 1 µL to 4 mL. Error bars correspond to the pixel size and frames per second of experimental video. b) The same plot zoomed in without the 4 mL and error bars to show the deviation from the $t^{1/2}$ law at early times.

This brings us to the real question - why does the $r - t$ plot for larger droplets deviate from the 1/2- law at early times? One could

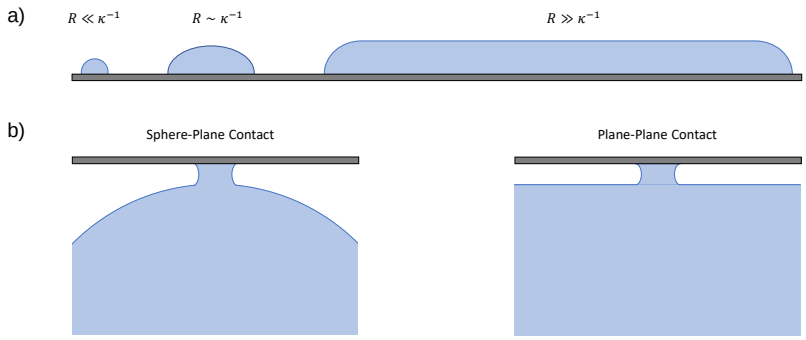

Figure 48: **Drop to Puddle.** a) Schematic showing how the geometry of the drop changes from a spherical cap to a puddle with flat top, as we increase the volume. b) Two different types of contact between the drop and the flat solid.

imagine the loss of sphericity of a large drop to be a reason for this. To elaborate, as the droplet volume increases, the drop flattens and transitions from a sphere to a puddle, which means the radius of curvature is larger at the top and smaller near the periphery (as sketched in Fig. 48). Such a flattening of the drop at the top could possibly weaken the Hertz Law, and consequently the 1/2 - law. It is also tempting to argue along this line because consistent deviations are observed for R_c equal to 2 mm or greater, which is not too far from the capillary length.

We can test the sphericity argument with a simple experiment. We take two droplets of different volumes but the same radius of curvature: a 4 µL droplet on a hydrophilic surface and a 100 µL drop on a hydrophobic surface, both of whom have a radius of curvature larger the capillary length. As seen in Fig. 49a, the 4 µL drop on the hydrophilic surface spreads out thin to become a perfect spherical cap (dotted red line) with a radius of curvature $R_c = 3.9$ mm everywhere, whereas the 100 µL drop on the hydrophobic surface is flattened with a radius of curvature $R_c = 3.9$ mm at the top. A hydrophilic glass slide is brought in contact with both of them from the top and the growth of the 'foot' of liquid contact that forms is tracked. If loss of sphericity is the reason for the deviation at early times, then the 4 µL droplet should not deviate from the 1/2 - law at early times, but the 100 µL should. However, in Fig. 49b where we plot r/R_c against t/τ, we see that both deviate and deviate identically. This means that not only is gravitational flattening not the reason for the deviation, the extent of deviation from the 1/2 - law depends on the very value of the local radius of curvature at the point of contact, and not whether its magnitude is relatively greater or smaller than the capillary length.

This tempts us to wonder if the deviations are a signature of an even earlier viscous regime. As discussed in the previous chapter, the point of first contact of a droplet and a flat substrate represents a sin-

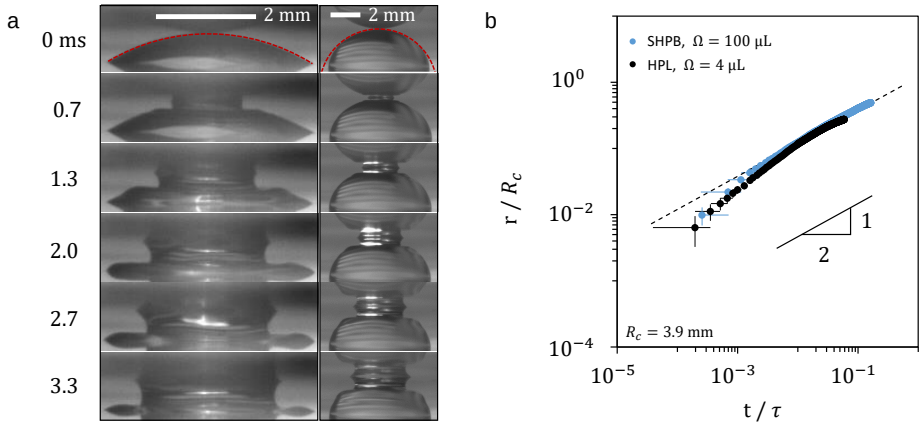

Figure 49: **Influence of Sphericity.** a) Two drops with the same local radius of curvature at the top $R_c = 3.9$ mm contact a flat hydrophilic plate from above. Left: 4 μL droplet on a hydrophilic plate. Right: 100 μL drop on a hydrophobic plate. Dotted lines show a circle with $R_c = 3.9$ mm which perfectly fits the 4μL drop everywhere, but does so only locally for the 100μL drop.

gularity: a cusp where the capillary stresses diverge and the dynamical law of spreading becomes $r \sim \gamma/\eta t \ln(R/r)$[94, 102]. This viscous regime supposedly gives way to the inertial one where the radius grows diffusively. However, for the case of water no experiment to date has been able to find the existence of a viscous regime preceding the inertial one, because its viscosity is $\eta = 1$ mPa-s is too low for any experimentally detectable viscous regime, if one existed. The viscous regime has been experimentally observed, but only for $\eta > 10$ mPa-s where the 1/2 - law has been swallowed up by entirely the viscous regime [102]. Perhaps what we see here is the remnant of a viscous regime crossing over to an inertial one, which is why the data points in the early times fit neither $t \ln t$ nor $t^{1/2}$, rather somewhere in the transition, where no scaling law holds.

This can be tested: the crossover from the $r \sim \gamma/\eta t \ln(R_c/r)$ to $r \sim (\gamma R_c/\rho)^{1/4} t^{1/2}$ would happen at a crossover length r^* and time t^* which satisfies both the equations. Eliminating t^* from the two equations and solving for r^*, we get the crossover length as

$$-(r^*/R_c)\ln(r^*/R_c) \sim Oh \tag{35}$$

where $Oh = \eta/\sqrt{\rho\gamma R_c}$, and is also known as the Ohnesorge Number. Now, for the function $f(x) = -x \ln x$, where $10^{-3} < x < 0.1$, $f(x)$ is of the order of x as $\ln x$ is a much weaker function in x. Dropping $\ln(R_c/r^*)$ and rearranging the terms we get

$$r^* \sim (\eta/\sqrt{\rho\gamma}) R_c^{1/2} \tag{36}$$

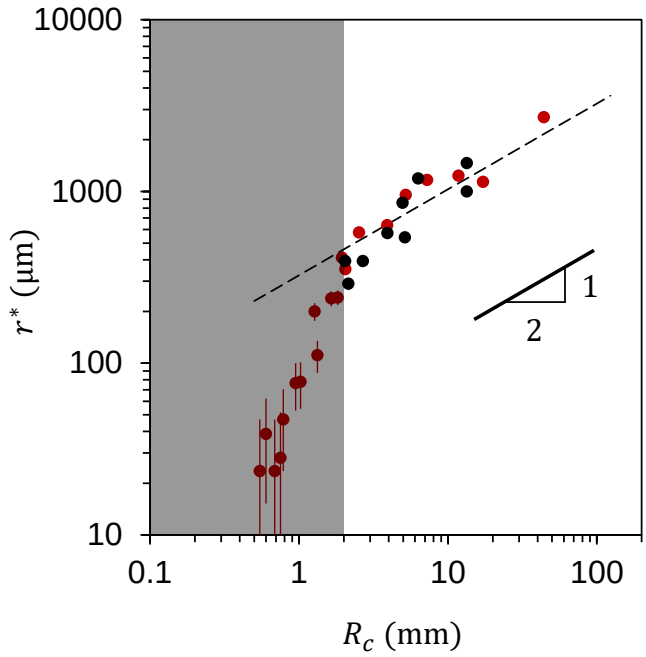

Figure 50: **Crossover.** Experimentally obtained crossover lengths of the contact plotted against the local radius of curvature at the top of the drop. Dotted line is a fit to Equation 36 with a prefactor of 87. Black and red circles correspond to experiments where the bottom substrate is hydrophilic and superhydrophobic respectively. The gray shaded region does not follow the Equation 36.

The pre-factor for the above equation is expected to be $1.3^2/A_o\beta$, where 1.3 is the prefactor of the diffusive law (Equation 34), A_o is the prefactor of the viscous law given by Equation 30 and $\beta = \ln(R/r)$ is of the order 1 (a value close to 3). In Fig. 50, we plot crossover lengths obtained from spreading experiments against the local radius of curvature at the point of contact. In these experiments, the top surface was hydrophilic but the bottom substrate was either superhydrophobic or hydrophilic, the drops being more flattened for the former case for the same volume. We observe that beyond 2 mm, the data can indeed be fairly captured by Equation 36 with a prefactor of 87. However, below $R_c = 2$ mm, shaded in grey, we see that the data quickly falls below the theoretical prediction of r^*. Both of these observations need to be commented on. We first address our experimentally obtained pre-factor. The viscous law in Equation 30:

$$r = A_o(\gamma/\eta)t\ \ln(R/r) \tag{37}$$

has a prefactor A_o theoretically predicted to be $1/4\pi$ by Eggers, Lister and Stone for the case of coalescence in a medium of non-zero viscosity [94]. However, for the case of spreading of a droplet, Eddi, Winkels and Snoeijer showed that the value of A_o curiously was not a constant, rather varied as $\sqrt{\eta}$ [102]. They showed that the value of A_o changes from $13/4\pi$ to $1/4\pi$ for η varying from 1120 mPa-s to 11.5 mPa-s. While it still remains a mystery why A_o is at all a function of η, but what we can say more boldly is that for a given viscosity, A_o is constant and Eggers' Law is valid. Now, there exists no experimentally reported value of A_o for water, because for water no viscous regime has yet been observed. However, if we were to extrapolate from the A_o values for different η as obtained by Eddi and coworkers, we obtain $A_o = 0.3/4\pi$, which should give us a prefactor of the order of 10 for the crossover equation, consistent with what we see.

The second observation we make is that below $R_c = 2$ mm, shaded in gray, the data quickly fall below the theoretical prediction of r^*. It is not entirely clear why this is so. Presumably for smaller droplets there is not experimental resolution to get a large enough deviation from which a crossover length can be extrapolated. This is also not incongruous with the fact that previous studies experimenting with 1 mm droplets have never observed any signature of the viscous regime for water. In this regard, the 2 mm cut-off appears to stem from an experimental limitation rather than a deviation owing to a different physics, although this needs to be further investigated.

Nevertheless, the most important conclusion we can draw from Fig. 50 is that just by increasing the size of the drop of water, one can make an otherwise 'invisible' early viscous regime 'visible', not entirely but just enough to see the transition to the inertial regime that starts to occur at millimetric length scales. Hidden within the crossover relation,

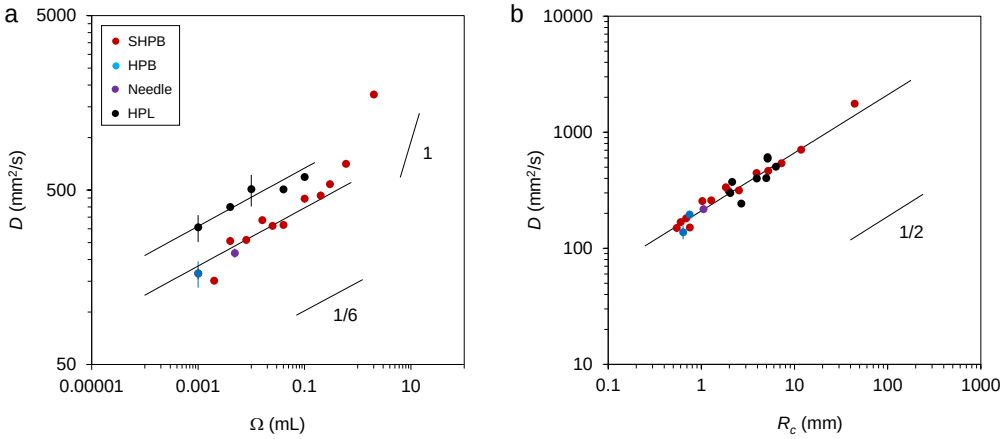

Figure 51: **Diffusivity.** a) Diffusivity values plotted against the volume of the drop spreading. Red data points coresond to a superhydrophobic bottom surface (SHPB), blue correspond to hydrophobic (HPB), purple corresponds to a drop deposited from a needle and black corresponds to a hydrophilic bottom surface (HPL). Solid lines are fits to $\Omega^{1/6}$. b) Diffusivity plotted against the radius of curvature at the point of contact collapses all the data on the same curve. Solid line follows the equation $D = 0.8(\gamma R_c/\rho)^{1/2}$.

as described by Equation 36, also is the resolution to an older question regarding the no-slip boundary condition in the inertial law. We had pointed out that the no-slip boundary condition is not violated in the inertial regime because there exists a boundary layer of size $\eta^2/\rho\gamma$ which must be less than the extent of the Hertz contact δ. This viscous length $\eta^2/\rho\gamma$ is tens of nanometers for water, which remains the same even for drops as large as hundreds of microliters. What changes is that, thanks to the Hertz Law, $\delta \sim r^2/R_c$, by increasing R_c to milimeters, we can push the crossover length scale to hundreds of microns, where it can be easily detected.

This reveals that the inertial law, originally derived for a spherical drop, is amazingly resilient to changes in volume. In Fig. 51a, we plot the experimentally obtained values of diffusivity for volumes varying from 1 µL to 1 mL, where the red, blue and black data points correspond to the bottom surface being superhydrophobic, hydrophobic and hydrophilic respectively, and contact is established from the top with a hydrophilic surface; the purple data correspond to the classical case where a drop is deposited from a needle onto a hydrophilic surface. We see that the black data points and the rest form two separate data sets, which is expected because drops sitting on the hydrophilic surface are substantially thinner in comparison to the non-wetting substrates, thus while in both cases the volume would scale as $\Omega \sim R_c^3$, the prefactor would be smaller for the thinner droplet. Consequently, the diffusivity values are expected to scale as $R_c^{1/2}$, that is $\Omega^{1/6}$ with a

larger prefactor for the thinner drops, which is indeed what we see in Fig. 51a. Such a scaling should hold upto a volume $\Omega^* \sim \kappa^{-3} \sim 10\,\mu L$. We see that for the case of drops on superhydrophobic surfaces this relationship holds upto 300μL, beyond which while diffusivity values can be obtained even for larger volumes - even for the case of a 1 mL puddle, these diffusivity values strongly deviate from a 1/6 - slope, increasing sharply with Ω, almost with an exponent 1. However, when plotted with respect to the local radius of curvature, all the data points collapse on a single curve that follows $D = 0.8(\gamma R_c/\rho)^{1/2}$, as seen in Fig. 51b. This plot shows concretely that even when the drop is far from a spherical cap, as long as the drop has a uniform curvature locally at the point of contact, the Hertz Law is valid and so is the inertial law.

Yet, this remarkable resilience of the regime of 'diffusive' inertia, too must end. When gigantic puddles of 1 mL to 0.1 L are brought in contact with a hydrophilic surface from the top, the 'foot' of contact grows, not as $t^{1/2}$, rather at a constant speed of 0.9 ± 0.1 m/s. These are puddles where the radius of curvature at the point of contact is 10 centimeters or larger - which is so flat it is experimentally extremely difficult to measure R_c, also because the first point of contact is unknown - typically at the edge, because of the dimple formation in the air film. Nevertheless the constancy of speed at very early times is observed repeatably. This constant speed regime typically exists for a few miliseconds after contact during which the contact line grows to the size of a few milimeters - beyond which the contact line starts destabilizing (not necessarily capturing bubbles) and eventually slowing down. Beyond 10 ms usually multiple surface waves start ineracting creating a complicated dynamic. We therefore limit ourselves only to the initial regime, where the speed is constant.

The constancy of speed suggests that the Hertz criterion has finally been broken, in other words, the contact has transitioned from a sphere-plane to a plane-plane. Fig. 52a shows a schematic of a constant air film of thickness e, dewetting at a speed V, as a liquid 'foot' of the same volume replaces it. The inertia of the liquid 'foot' is given by $\rho r^2 e(V^2/r)$. The driving force is the uncompensated Young force given by $\gamma r(\cos\theta_A - \cos\theta)$, where θ_A is the advancing contact angle and θ is the dynamic contact angle with which the bridge grows. This gives us a constant velocity that can be written as

$$V \sim \left(\frac{\gamma(\cos\theta_A - \cos\theta)}{\rho e}\right)^{1/2} \tag{38}$$

The above equation is remarkably similar to the law of inertial dewetting where we have the converse case - a thin metastable film of water with air on one side and a (preferably non-wetting) solid on the other, in which case dewetting speed is given by

$$V_{DW} = \left(\frac{\gamma(\cos\theta - \cos\theta_R)}{\rho e} \right)^{1/2} \tag{39}$$

This law of inertial dewetting is a variant of the Culick Law derived by F. E. C. Culick in 1960 [115] in the context of bursting soap films where he showed that the velocity of rupture is a constant and equal to $(2\gamma/\rho e)^{1/2}$; this is in fact a limiting case of Equation 39 with $\theta = 0$ and $\theta_R = \pi$.

where θ_R is the receding angle on the surface [113, 114]. It is necessary that we rationalize why the dewetting of an air film in water and dewetting of a water film in air have almost identical speeds. The answer to this can realized by looking at the two sketches in Fig. 52a and b which show the two cases of dewetting of water and air respectively. First, in the case of dewetting of an air film, a bridge of water forms with the volume $r^2 e$ and an equivalent volume of displaced air collects in a rim at the periphery of moving contact line. However the density of air ρ_a being far less than that of water, the inertial contribution of the rim $\rho_a r^2 e V^2/r$ is negligible relative to that of the bridge. Conversely, in the case of dewetting of a water film, the bridge has negligible inertia as it is made of air, but the rim where an equivalent volume of water collects has the dominant contribution in inertia. Thus despite the fact the film and the medium are the exact opposite, in both the cases, the inertial term $\rho r^2 e V^2/r$ contains the density of water ρ and the volume of the bridge $r^2 e$. For the case of dewetting of water, naturally the receding angle θ_R appears in the uncompensated Young force, and in the case of dewetting of air, water is advancing, and hence we see the advancing angle θ_A. Thus, quite surprisingly, the dewetting of an air film and a water film of a given thickness have the same characteristic velocity.

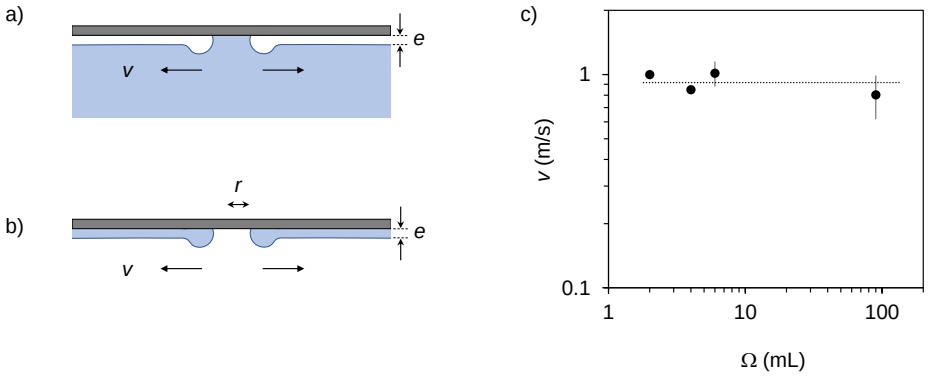

Figure 52: **The Fourth Regime.** a) Schematic of an air film of constant film thickness e dewetting at a speed V and being replaced by a liquid bridge of water of the same size. b) Schematic of the opposite phenomenon: a film of water of constant thickness e dewetting at a speed V. c) Experimentally obtained velocities for spreading of puddle volumes ranging from 1 mL to 0.1 L plotted against their respective volumes. Dotted line represents 0.9 m/s. Error bars correspond to one standard deviation obtained from at least three trials.

For the case of a hydrophilic plate, $\theta_A \to 0$, and while the dynamic contact angle cannot be visualized from the sideview of the puddle experiments because of the uncertainty of where the contact happens, it can be for a droplet as can be seen in Fig. 26. Dynamic angles in the inertial regime are close to $\pi/2$ for water. This makes $(\cos\theta_A - \cos\theta)$ close to 1, further simplifying Equation 38. Previous works impacting drops have reported that the air cushion ruptures when it thins to a critical thickness at the edge of the dimple [112]. Although we do not control the air film thickness but we see a constant speed in different experiments which seem to imply the same - the existence of a critical thickness. For our experimentally measured speed of 0.9 ± 0.1 m/s as seen in Fig. 52c for droplet volumes ranging from 1 mL to 100 mL on hydrophilic plates, we obtain a thickness e of the order of tens of microns. However, further work needs to be done to obtain direct evidence of this.

Equation 38 can now be integrated in time to obtain the dynamical law of growth in the fourth regime of the phase space Fig. 43:

$$r \sim \left(\frac{\gamma}{\rho e}\right)^{1/2} t^1 \tag{40}$$

There is another interesting observation regarding the transition from the $t^{1/2}$ to a t^1 law which we can trigger by increasing drop size. The Reynolds Number in the diffusive inertial regime is $Re = \rho V r/\eta$, where $Vr = D = (\gamma R_c/\rho)^{1/2}$, which gives us $Re = (\rho\gamma R_c)^{1/2}/\eta = 1/Oh$. The maximum size of the radius of curvature for which we could observe the diffusive regime was $R_c \sim 1$ cm, and for R_c of the order of 10 cm or larger we saw the constant velocity regime. Plugging in $R_c \sim 1$ cm, we get $Re \sim 100$. Had the diffusive inertial regime persisted up until $R_c \sim 10$ cm, we would have obtained a Re of the order of 1000, which does not happen and it is precisely at this critical Reynolds Number, we switch to a constant velocity regime $v \sim (\gamma/\rho e)^{1/2}$ which is 1 m/s. Now, in the constant velocity regime, the Reynolds number $Re = \rho V r/\eta$ is not a constant, rather increases as the contact size r grows up until millimetric lengths beyond which it slows down. Therefore the maximum Re in the dewetting air regime corresponds to $r \sim 1$ mm and $V \sim 1$ m/s, which again gives us $Re \sim 100$. This means that the moving contact line for the case of spreading of water resists going to $Re \sim 1000$, and switches regimes to stay below this threshold.

As a final illustration of this transition $t^{1/2}$ to a t^1 Law we briefly summarize a separate experiment where this can be seen in the same drop itself, unlike the previous experiments. We take a generic Petri dish made of plastic (hence, hydrophobic) of radius 6.8 cm, and deposit inside a puddle of 17 mL exhibiting an equatorial radius R_c of 5.4 cm. We now gently bring it in contact with the sidewall of the

This little experiment was done together with Bachar Obeid and Aditya Jha.

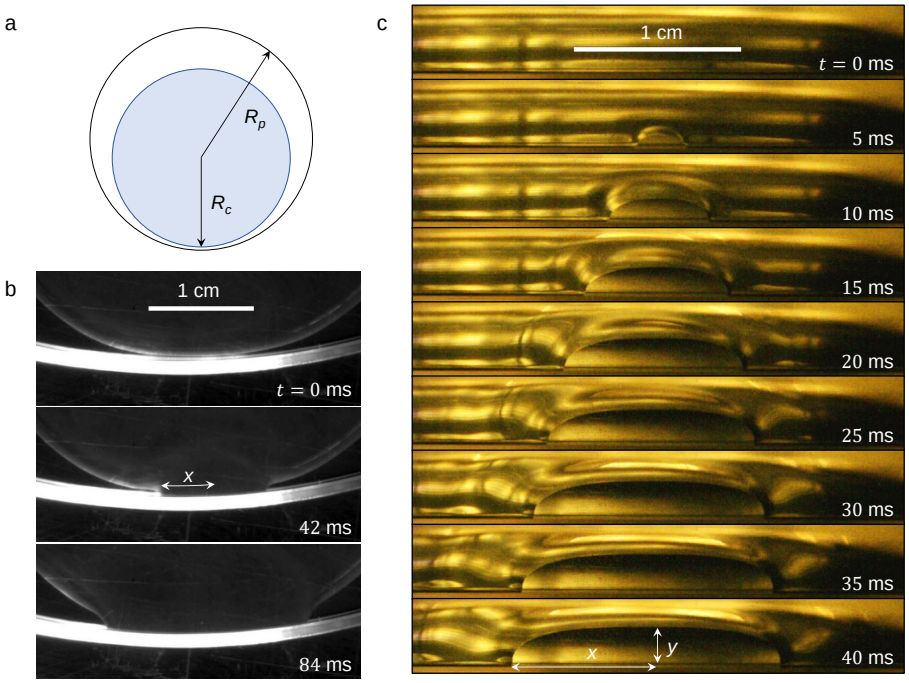

Figure 53: **Puddle Touching a Sidewall.** a) Schematic of a topdown view of a puddle of equatorial radius R_c placed in a petri dish of radius R_p, gently touching the sidewall. b) Topdown experimental images of a puddle of $R_c = 5.4$ cm touching the side-wall, forming a liquid 'foot' and spreading. c) Looking into the puddle through the transparent wall of the petri dish, where contact is established. High speed images of this sideview show the contact grows in a family of puddle-shapes.)

petri dish - Fig. 54a shows a definition sketch of the geometry and b shows a topdown view of the contact. In Fig. 54c we see a timelapse of the successive growth of the contact over 40 miliseconds, which reveals that the contact grows in a family of puddle-like shapes.

In our previous experiments of touching a puddle from the top was a means to transition from a sphere-plane to a plane-plane contact. Touching a puddle from the side is a toroid-plane contact if $R_e \ll R_p$, where there are two radii of curvature at the point of contact - the equatorial radius R_e and the vertical radius of curvature which scales as κ^{-1}; also $R_e > \kappa^{-1}$ because it is a puddle. Our illustration, however, corresponds to the case where $R_e \sim R_p$ which makes the contact a plane-plane one in the horizontal direction, with a constant air film thickness, while the contact in the vertical direction remains the same. Said differently, we expect the vertical growth to be diffusive $y^2 \sim D_y t$, where D_y should scale as $\sqrt{\gamma\kappa^{-1}/\rho}$ and the horizontal growth to be constant in velocity. This is indeed what we see in Fig. 54b where the vertical growth of the contact follows $t^{1/2}$, while the lateral growth has a constant speed. The empty black circles track the position of the vertical growth from the bottom of the meniscus

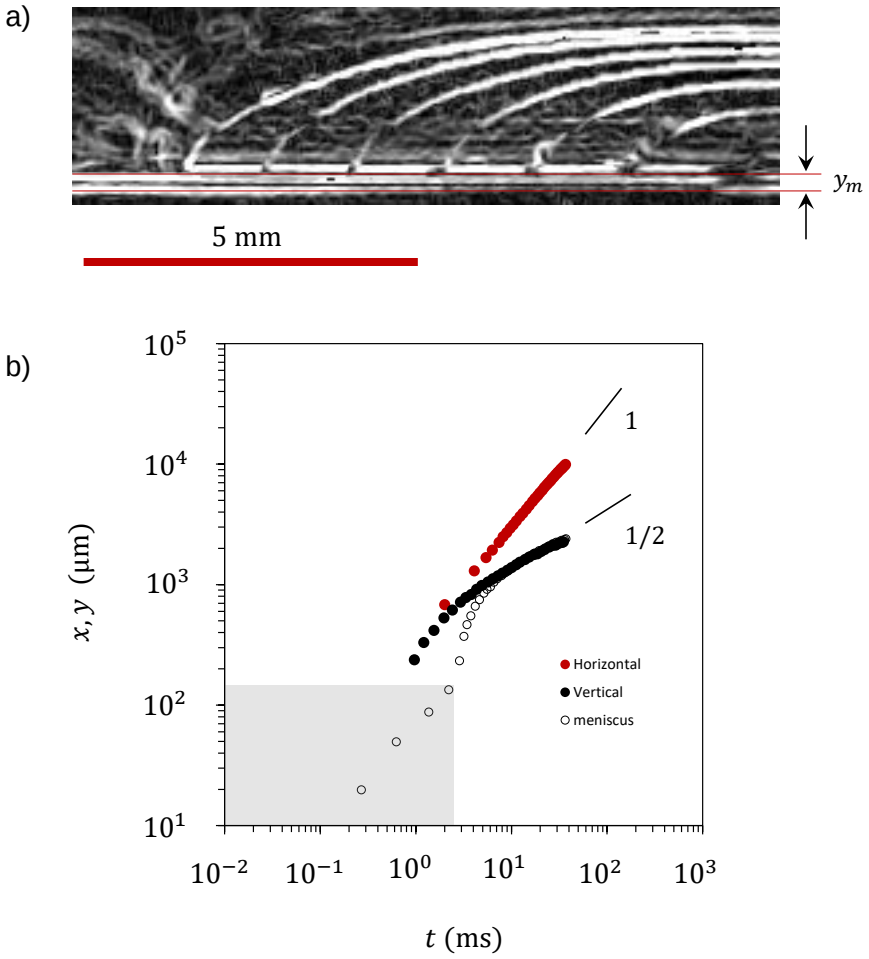

Figure 54: **Transition in the same drop.** a) Timelapse of successive sideview contours of the contact line after a puddle touches a side-wall. y_m represents the size of the radius of curvature of the corner of the petri dish, in this case 150μm. When the puddle approaches the side-wall, it first forms a tiny meniscus climbing this corner, and then progresses to spread more 'globally' in the lateral and vertical direction. b) Temporal evolution of the lateral and vertical spreads show two different regimes existing in the same drop: the vertical growth grows diffusively, while the horizontal growth is a constant.

(the very base of the drop). The black data points take the top of the meniscus as the starting point. The gray shaded region has a different dynamics owing to the climbing of the meniscus at the corner, however this does not affect the approach to the 1/2 law at later times. The red data points track the horizontal extent of the contact from the first point of contact, starting at the top of the meniscus. Both the vertical and horizontal spread eventually deviate from their respective $t^{1/2}$ and t^{1} behavior at later times to equilibriate (not captured in the plot).

While both the regimes are observed in the same drop here, the speed horizontally $V \approx 0.4$ m/s and the diffusivity $D \approx 135$ mm^2/s are both lower than their expected values, something that needs to be developed further. This work is still ongoing, hence a detailed analysis is beyond the scope of the present writing.

4.2 LARGE DROPS ON INFUSED SOLIDS

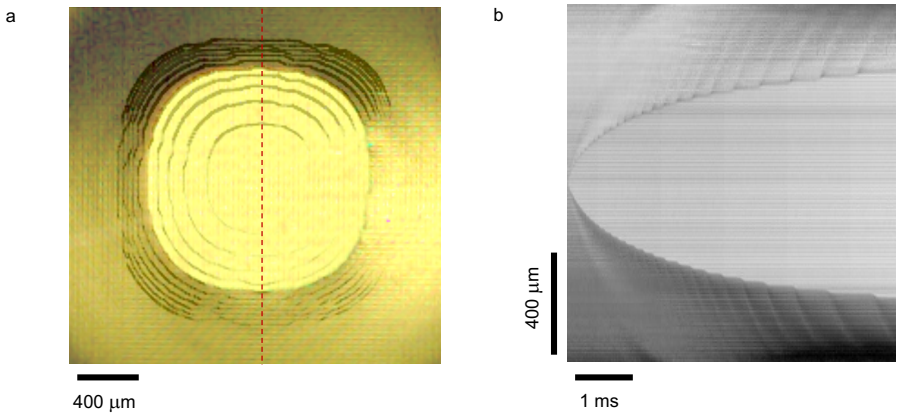

Figure 55: **Generation of Waves.** a) Timelapse of a topdown images of a 25 µL drop contacting a hemisolid infused with silicone oil $\eta_o = 10$ mPa-s. Black lines correspond to successive contours of the spreading drop at every 0.5 ms which have been overlayed on a snapshot of spreading at 2 ms from start. b) A spatio-temporal diagram of the spread obtained by taking a reslice along the red dotted line as show in a. The streaks in the diagram are a signature of waves emitted continuously by the spreading contact line.

Large drops spread on infused surfaces with some striking dissimilarities with the case of spreading on 'bare' hydrophobic surfaces. We begin by illustrating the differences with the case of a 25 µL drop (radius of curvature 2 mm) spreading on a liquid infused surface which is infused with silicone oil $\eta_o = 10$ mPa-s.

Fig. 55a shows a timelapse of the spreading contact line of such a drop with the successive topdown contours at 0.5 ms intervals overlayed on top of a snapshot of spreading at 2 ms from start. What we immediately note is that the contact line is not circular as in the case of a 'bare' solid, rather square-ish. In fact, the growing contact line actually transitions from a circle to a square around $r = 100\mu m$ and back to a circle when it comes to an equilibrium, at its equilibrium radius, in this case 2 mm, at late times. The transition from a circle to a square tempts us to think that the drop can 'feel' the textures underneath, and what we see in the square-ish is a footprint of the lattice of the texture underneath.

To test this hypothesis, we look at the spatio-temporal diagram ($r - t$ plot) in Fig. 55b, which corresponds to a reslice taken along the dotted red line in Fig. 55a. The spatio-tempral diagram reveals that the entire growth happens in a step like fashion, where at constant spatial intervals or steps, it has a 'jump' or a quick motion in r. When we measure the lengths of this constant spatial interval or step size, we find it to be equal to the sum of the inter-pillar distance and the

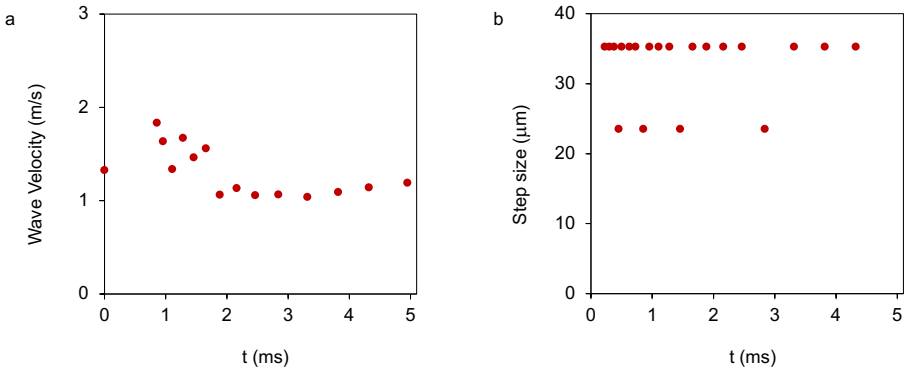

Figure 56: **Wave Characteristics.** a) Experimentally obtained wave velocities from the spreading a 25 μL drop contacting a hemisolid infused with silicone oil $\eta_o = 10$ mPA-s plotted against time. b) Step size of emmission of waves plotted against time to determine the interval at which the waves are emitted.

diameter of each pillar, that is $p + d = 35\mu m$, thus proving the drop can indeed sense the texture underneath, which makes the contact line create a footprint of the lattice. We discuss the mechanism for this soon after, but before that we address another crucial feature of the spatio-temporal diagram we see in Fig. 55b — the streaks that emanate at every step.

What are these streaks? These streaks are waves generated at every 'step' which corresponds to the contact line touching the texture. These waves are not on the infused surface, which is textured, rather these are capillary waves generated on the surface of the drop. The first capillary wave that emanates at $t = 0$, upon first contact, is observed even in the case of a drop touching a 'bare' solid surface. The subsequent capillary waves are a signature of spreading on a perfectly infused solid. In Fig. 56, we plot the velocity of these waves, obtained from the slope of the streaks in the spatiotemporal diagram against time, which reveals that the magnitude of the wave velocity beyond 2 ms is a constant and equal to 1 m/s. Between 1 ms and 2 ms it decreases from 1.8 m/s to 1 m/s and before 1 ms there is not enough experimental resolution to say convincingly whether the magnitude of the velocity is any higher.

The magnitude of the wave velocities remain the same even when the viscosity of the infusion is five times more, that is $\eta_o = 50$ mPa-s.

What we can say more boldly is that the waves generated on the surface of the drop are also reflected in the $r - t$ plot of the growing contact line as quick 'jumps' occurring at distinct intervals, in between the intervals the contact line moving at a much slower velocity. The magnitude of time intervals between successive 'jumps', which are also the points of emission of the waves, keeps increasing in time, although the interval in length (step size) remains constant (Figure 56b). The mechanism of generation of waves essentially bleeds into our previous discussion on why a timelapse of the growing contact revealed a footprint of the lattice underneath.

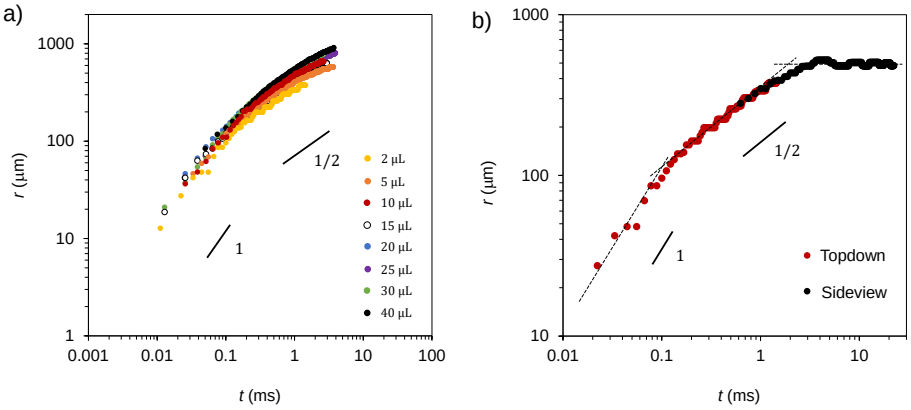

Figure 57: **Classical r-t plots.** a) Temporal evolution of the size of the contact for drops of increasing volumes contacting a liquid infused surface, infused with with silicone oil $\eta_o = 10$ mPa-s. b) The same plot for only 2μL. Dotted lines represent three different regimes: constant speed: $r \sim t$, diffusive inertial: $r \sim t^{1/2}$ and equilibrium: $r \sim R$.

Before we proceed to understand the mechanism of these 'jumps', we note in Fig. 57 that these 'jumps' and step-like progression is a generic feature that can be seen in the $r - t$ plots of a growing contact line, when a drop touches an infused surface. The steps are particularly distinct for larger drops as for 25μL, however even for a drop as small as 2μL, a careful look reveals the step like features within it, which all correspond to a size of $p + d = 35\mu m$. So, it becomes natural to ask what is the mechanism that governs this 'jumps'.

In order to understand the mechanism, we take a closer look of the contact line when it undergoes one such 'jump'. Fig. 58 shows such a representative case for a 25 μL drop spreading on a 10 mPa-s LIS. We look at the contact line, which is distinctively square-ish, at 3.4 ms after contact, when it is at a distance of 790 μm from the centre and about to perform the 'jump'. The inset shows how in the subsequent 0.5 ms, the front first progresses a length $p + d = 35\mu m$ and then subsequently zips perpendicular to the progression.

Fig. 58 b shows a schematic of this zipping process, which can be summarized as follows:

i) The contact line is initially at the end of an array of pillars.

ii) A bridge grows across the oil channel. This happens typically at the mid-point on the contact line, that is the point on the contact line which is at the least distance from the first point of contact of the drop with the surface. The formation of this bridge is accompanied with invading into the adjacent cell in the next array of pillars.

iii) Once one unit cell across the channel has been filled (of length p), the liquid starts zipping along multiple unit cells along the channel, coming to a 'momentary rest' at the end of an array of pillars.

iv) Another bridge grows across the next oil channel, and the process continues.

The extent to which the front zips along the channel before the next bridge grows depends on the distance of channel from the centre of the contact — the larger the distance, the longer the zip or the longer time taken for the next bridge to form.

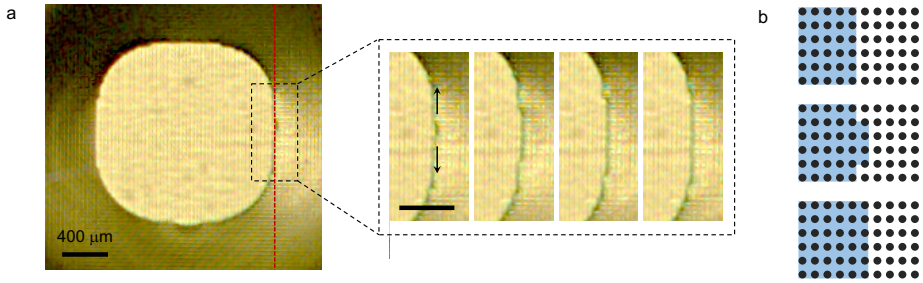

Figure 58: **Zipping.** a) A topdown snapshot, 3.4 ms after a 25 μL drop has contacted a LIS with $\eta_o = 10$ mPa-s: inset zoomed in shows how in the subsequent four frames, 0.125 ms each, where we see the contact zips through in the direction shown by the black arrows in inset. The red dotted line represents the line along which one needs to take a reslice to obtain a spatio-temporal diagram of zipping, along a specific channel. b) Schematic of the zipping process.

This phenomenon is called 'zipping' and has been observed before, not in the context of spreading on liquid infused surfaces but Cassie to Wenzel transitions liquid invades into the texture, replacing air and does so array by array [116, 117]. It has also been observed in hemiwicking processes where liquid invades a forest of micropillars. A key difference in the zipping that we observe in our case is that the water front that is zipping is not replacing the oil underneath, rather zipping above the oil as hemiwicking through a forest of circular pillar tops. We know that no oil was replaced, because that would create a significant adhesion of the drop to the surface, but we measured a near-zero roll off angle after the spreading process was complete.

We now look at the zipping characteristics for three different channels at a distance of $x = 0\mu m$, $212\mu m$ and $671\mu m$ from the centre. All of them correspond to a 25 μL drop spreading on a 10 mPa-s LIS. In Fig. 59 we their respective spatio-temporal diagrams and $r - t$ plots on a log-log scale. In all three plots, we see an initial regime tentatively appears to be of constant velocity $r = V_z t$ where V_z is the initial zipping velocity, followed by a diffusive regime $r^2 = 2Dt$, followed by a final third regime of equilibrium. A fit through the initial regime reveals an initial velocity of $V_z = 1.5$ m/s, although for $x = 0$ channel, it looks more of a deviation from a subsequent diffusive regime than a constant velocity regime. However, for zipping in the other channels, the velocity seems to be indeed constant in the

early times, particularly for the channel that is farthest from the centre. Conversely, the diffusive regime for zipping in the central channel exists for more than a decade before transitioning to equilibrium, and is less and less clear and convincing for zipping in the other channels, the most deviant being again the one which is farthest from the centre.

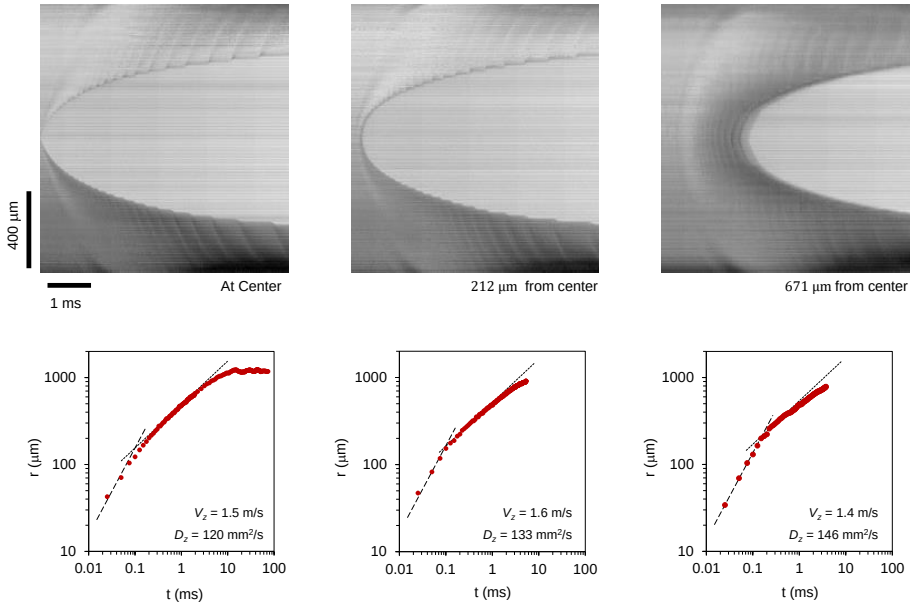

Figure 59: **Zipping Reslices.** Top: Zipping reslices taken along different inter-pillar channels (dotted red-line in Fig. 58) at distance $x = 0\mu m$, $212\mu m$ and $671\mu m$ from the center. Below: Corresponding $r - t$ plots where dashed line is an initial linear fit representing a possible constant velocity regime and dotted line is a subsequent fit to $r^2 = 2Dt$, representing a possible diffusive regime.

We first note that the case of zipping through the channel at the centre is a special one as it is also the case of spreading of the the drop after contacting the infused surface. In this regard, the channels farthest from the centre (the channel $x = 671\mu m$ in Fig. 59) are the more ideal for studying the process as it does not have any contributions from the out of equilibrium contact of the drop, as it would have for the channels closer to the centre. From the $r - t$ plot of zipping in the $x = 671\mu m$ channel, we see that we do not have sufficient evidence to claim that there exists a diffusive regime. However, the evidence of a constant velocity regime is far more convincing, that is, the existence of a constant initial zipping speed V_z. The zipping velocity V_z also manifests itself in the $r - t$ plot of the contact line of the drop spreading on the infused surface as the 'jumps' that appear at different steps, and V_z remains a constant and equal to 1.5 m/s even when the global speed V has almost come to zero, which would correspond to the last channel the liquid zips through before the entire drop equilibriates.

This helps build a simple criterion for the circle to square transition of the contact line when a drop spreads on an infused surface — when the global speed is less than the zipping speed, the contact line is no longer circular. It is tempting to postulate the zipping speed as a balance of inertia ρV_z^2 and the Laplace pressure that builds between two pillars γ/p, which gives us $V_z \sim (\gamma/\rho p)^{1/2} \sim 1$ m/s for our pitch $p = 15\mu m$. The global dynamics follows the law $Vr \sim D$, which can be used to find the radial length at which the circle to square transition sets in at the length r_{sq} which follows the condition

$$r_{sq} > D(\rho p/\gamma)^{1/2} \tag{41}$$

We know that D itself is a function of the drop size, oil viscosity, pillar height, surface tension of the oil, surface tension and density of the drop, and if the infusion is too viscous, D is a function of the viscosity of the drop. But for the limiting case of low η_o, D approaches the diffusivity of spreading on a solid, that is $(\gamma R/\rho)^{1/2}$, which gives us a much simpler limiting condition of

$$r_{sq} > (Rp)^{1/2} \tag{42}$$

For $R \sim 1mm$, this gives us a $r_{sq} \sim 100\mu m$. Indeed we see typical circle to square transitions for $\eta_o = 5$mPa-s and $\eta_o = 10$mPa-s happen when the contact has grown to $100\mu m$ size. However, both the Equations 41 and 42 remain to be systematically tested.

We end this section by giving an example of when even an infused surface does not show these 'steps'. Fig. 60a and b show a comparison between two timelapse images of a 25 μL drop contacting a $\eta_o = 10$ mPa-s LIS one which is perfectly infused (Fig. 60a) and one which is *overfilled* with an excess of $\sim 5\mu m$ (Fig. 60b). We see that all the steps and all the jumps have disappeared — the contours are perfect circles. A mere $5\mu m$ overfilling on a LIS with $20\mu m$ high pillars is enough to make the textures invisible to the drop. This means that the step-like characteristic of the spatio-temporal diagram or the emission of waves is a signature of a perfectly infused surface and not an overfilled one.

Fig. 60c compares the temporal evolution of the growing contact a 25 μL touching a 'bare' hydrophobic surface, a perfectly infused surface with $\eta_o = 10$ mPa-s and an overfilled LIS with $\eta_o = 10$ mPa-s. We see that overfilled textures can engender such a high degree of slip that the drop spreads on it faster than it can on a 'bare' hydrophobic surface! The perfectly infused surface in this regard is the slowest and also has all the step-like features previously discussed. Finally, on a log-log plot, we see that the $r - t$ plot of spreading on a hydrophobic surface has an early deviation from the $t^{1/2}$, which not linear rather a signature of an earlier viscous regime, we discussed. For the cases of

overfilled and perfectly infused textures deviations are stronger and closer to a constant velocity, implying a more complex mechanism, not necessarily a zipping speed.

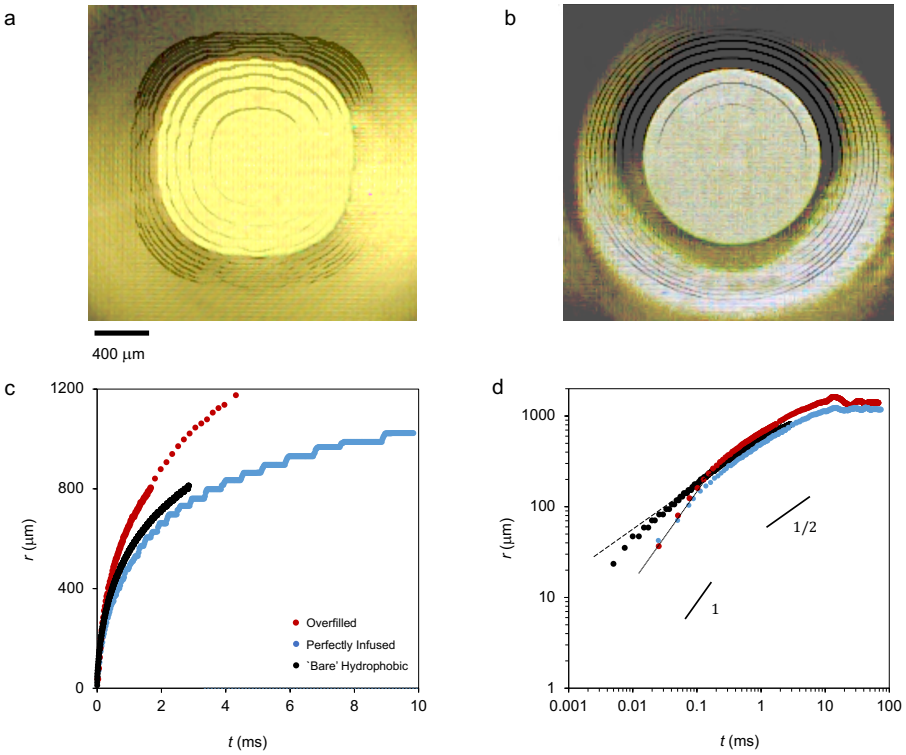

Figure 60: **The Overfilled and The Perfectly Infused.** a) Timelapse of a top-down images of a 25 μL drop contacting a $\eta_o = 10$ mPa-s LIS which is perfectly infused b) The same for textures overfilled with an excess of $\sim 5\mu m$. Note the contours in b) are perfectly circular, denoting the drop does not feel the textures underneath at all. b) $r - t$ plot of a 25 μL contacting a 'bare' hydrophobic surface (black circles), a perfectly infused surface with $\eta_o = 10$ mPa-s (blue circles) and an overfilled LIS with $\eta_o = 10$ mPa-s (red circles). c) The same plot in a log-log plot. Dashed line represents a fit to $t^{1/2}$ and solid line is a fit to t^1.

Part III

ADHESION

5

CAPILLARY SPRINGS

A drop of water between two fingers - an apparently simple little system, rich in its many implications - forms a 'capillary spring', which attracts the two fingers with a typical force equivalent to its own weight. However, when squeezed to the order of microns, this force can be almost 100 times its own weight! Such is the exemplary effect of the force of adhesion generated by capillary springs that transforms flour to dough to make the very baguette we eat, that functionalizes the insect's feet and makes it climb up the wall - a microcosm of all of which is this drop of water between two fingers. In this chapter, we study the characteristics of such a spring - not between two fingers, rather between a liquid-infused surface and a 'bare' hydrophobic surface. Thereafter, we measure the vertical adhesion of infused solids and see that unlike its lateral adhesion, the vertical adhesion is far from negligible.
[1].

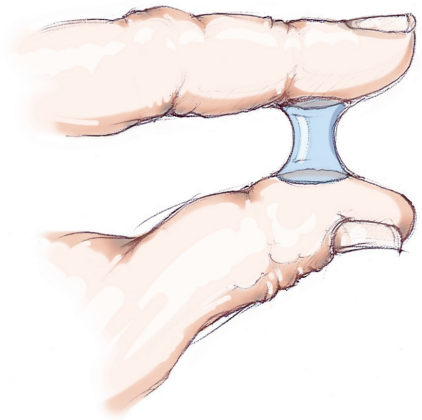

'Capillary Springs' by Benoît Pype

1 The experiments of this chapter were performed at Max-Planck-Institut for Polymer research Mainz, in collaboration with Doris Vollmer and Abhinav Naga, and initial discussions with Armelle Keiser.

5.1 FORCE MEASUREMENTS

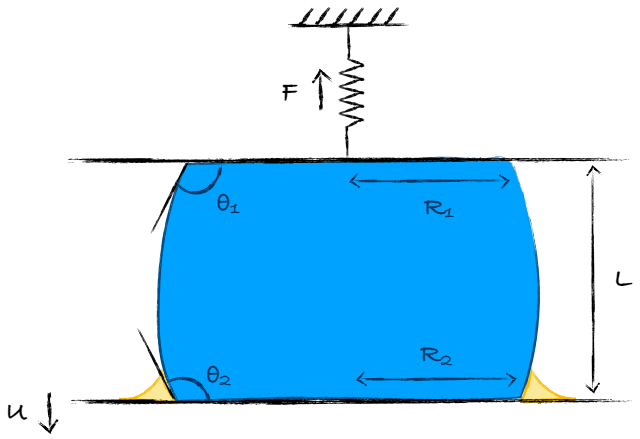

Figure 61: **Schematic of Set-up.** A sketch of our experimental set-up. The top surface is a silanized hydrophobic plate, whereas the bottom plate is a liquid-infused surface. The drop in blue is water and the meniscus in yellow is oil. The spring pulls the plate with a reaction force F, which is seen in the tensiometer.

Liquid-infused surfaces are celebrated for their slipperiness and extremely low adhesion. Such low adhesion is in the context of lateral motion, rather onset of motion - a hallmark of minimal pinning defects. While the lateral adhesion is near-zero, the vertical adhesion of these special surfaces is far from zero, in fact quite high - almost ten times its own weight, for a 1µL drop - as we will see in this chapter. We are interested here in characterizing this adhesion force - finding out its maximum value and dependence on viscosity, if any.

In order to measure the adhesion we build the experimental set-up as shown in Figure 61 where a droplet of volume ranging from 0.2µL to 16µL is first placed on a liquid-infused surface, and then brought into contact with a hydrophobic surface (silanized silicon wafer) at the top, to form of capillary bridge. The top surface is attached to a force tensiometer which gives us a measurement of the force with which the plate is pulled by the drop, as we bring the bottom surface down at a constant velocity U. Owing to the hydrophobic nature of both the top and bottom plates, the drop always adopts a convex shape. In the notation followed in this thesis, *convex* means the drop curves outward (that is has a bulge), and *convex* means the drop curves or caves inward.

We performed three different kinds of adhesion experiments we perform, which we discuss now. The first experiment is with constant pulling speed $U = 10\mu m/s$, but different droplet volumes $\Omega = 0.2\,\mu L$, $0.4\,\mu L$, $1\,\mu L$, $2\,\mu L$, $6\,\mu L$, $10\,\mu L$ and $16\,\mu L$. The top surface is hydropho-

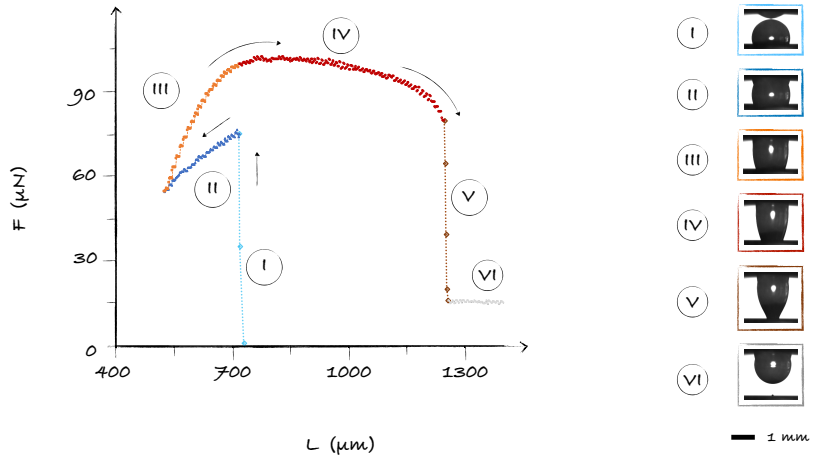

Figure 62: **A Typical Force Measurement.** A force versus inter-plate distance curve for a droplet of volume $\Omega = 2\mu L$ and pulling speed $U = 10\mu m/s$. The top surface is hydrophobic and the bottom surface is a LIS with $\eta_o = 9$ mPa-s. The force curve shows five distinct stages before 'capture' - where the drop detaches completely from the bottom surface and adheres to the top. Snapshots of the different stages are shown on the side as inset.

bic and the bottom surface is an infused surface with $\eta_o = 9$mPa-s. The experiment begins when the drop is just below the top surface and has not yet contacted the top surface, where-after the bottom plate would be moved up to bring the drop in contact and then pulled down until the point of detachment. Meanwhile, we make force measurements at an interval of 0.2 s for the entire duration until droplet has detached from either of the two surfaces, which gives us a typical force versus time curve. Such a plot can be converted subsequently into a F versus L plot, where L is the inter-plate distance.

In Figure 62, we see a typical force curve, corresponding to an experiment with a droplet of volume $\Omega = 2\,\mu L$ and pulling speed $U = 100\,\mu m/s$ where the viscosity of infusion of the bottom infused surface is $\eta_o = 9\,$mPa-s. The force curve shows 6 different regimes, the corresponding droplet shapes for which are shown in the inset.

1. **First Contact:** The droplet first contact the top plate, and transforms from a hemisphere to a quasi-cylindrical capillary bridge of height $L_0 = 717\,\mu m$. We see a sudden rise in the attractive force with which the drop pulls the top plate, and the adhesion force reaches a value of $F_0 = 74\,\mu N$, in a span of 0.4 s. Why the force would be attractive is not immediately obvious, because the drop clearly exhibits a convex shape. We discuss this soon after. The force F_0 is also called the snap-in force in the literature.

2. **Compression beyond L_0:** The drop is now compressed by 80 μm in a span of 20 ms, which in the force curve registers as a linear decrease in the adhesion force, reaching a minimum of $F = 55\mu N$.

3. **Elongation to L_0:** The drop is now elongated back to its initial value of separation, $L_0 = 717\,\mu m$, corresponding to which we see an increase in the adhesion force, revealing the spring-like nature of the capillary bridge. Curiously the forces registered during elongation are higher than their corresponding values during compression, eventually manifesting a value of $100\,\mu N$ at $L_0 = 700\,\mu m$, which is $26\,\mu N$ higher than F_0. This shows that this 'liquid spring' is not a reversible one.

4. **Saturation:** We now further elongate the bridge to 1246 μm, that is close to double that of its initial length at a constant speed of $U = 100\,\mu m/s$. Here we note that during the entire process of elongation beyond L_0, the adhesion force remained nearly constant, decreasing only marginally (less than one-fifth of its peak value) at a meagre rate of $0.03\,\mu N/\mu m$. We call this saturation zone - the shape of the drop in this regime changes from a quasi-cylinder to a quasi-'bottom-up truncated cone' where $R_2 < R_1$.

5. **Pinch-off:** The drop when further elongated pinches off at the bottom surface within a span of milliseconds, in other words at the same spring length. The adhesion force plummets down rapidly.

6. **Capture:** The drop now sticking to the top surface, we register the dead weight of the drop.

Regimes II and III help in characterizing the capillary spring we form bounded by an infused surface on one end with the possibility of slip, and a regular hydrophobic surface on the other. Regime IV is the 'true' adhesion test, where we find the maximum adhesion force.

When we look at the force versus time curves for different volumes plotted together, as in Fig. 63a, we see that all the curves are similar only increasing in amplitude, with the increase in volume, which we also observe when we plot the maximum adhesion force against the volume in Fig. 63b. Except for $\Omega = 16\,\mu L$ for all the other volumes, the drop completely detaches off the infused surface and is stuck to the top, which registers as a dead weight, seen in the horizontal line at the end of each curve at late times. For $\Omega = 16\,\mu L$, the drop when sufficiently elongated breaks close to the top due to its weight, thus resulting in a final force which is near zero.

A second experiment is now performed by fixing the drop volume at $\Omega = 2\,\mu L$, and changing the pulling speed - for five different speeds $U = 10\,\mu m/s$, $50\,\mu m/s$, $100\,\mu m/s$, $500\,\mu m/s$, $1000\,\mu m/s$.

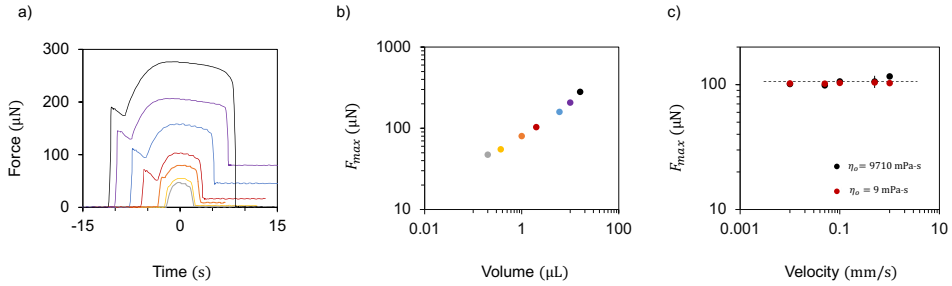

Figure 63: **Force Characteristics.** a) Adhesion force measurements a LIS infused with silicone oil of viscosity $\eta_o = 9$ mPa-s plotted against time, for volumes $\Omega = 0.2\,\mu$L (green circles), $\Omega = 0.4\,\mu$L (yellow circles), $\Omega = 1\,\mu$L (orange circles), $\Omega = 2\,\mu$L (red circles), $\Omega = 6\,\mu$L (blue circles), $\Omega = 10\,\mu$L (purple circles), and $\Omega = 16\,\mu$L (black circles). b) The maximum adhesion force obtained from the previous curves plotted against their respective volumes. c) Maximum adhesion force measured with a $\Omega = 0.2\,\mu$L plotted against different pulling velocities. Black circles correspond to $\eta_o = 9710$ mPa-s and red circles correspond to $\eta_o = 9$ mPa-s. For $\eta_o = 9$ mPa-s, at all velocities we observe depositions. However, for $\eta_o = 9710$ mPa-s , for $U = 50\,\mu$m/s and $U = 100\,\mu$m/s, both capture and deposition are observed; for larger values, only depositions are observed.

Such a force curve looks similar to the typical one shown in Fig. 61. The maximum adhesion forces, when plotted against pulling speeds were also were found to be independent of velocity, and equal to $F_{max} = 102\mu$N, thus revealing that LIS with $\eta_o = 9$ mPa-s have no viscous effects on their vertical adhesion forces, even when drops on such surfaces are detached at speeds as high as 1 mm/s. So, we tried the same experiment (at different speeds) with an surface infused with a viscosity 1000 times higher - $\eta_o = 9,710$ mPa-s, to look for viscous effects. In this series of experiments, with $U = 10\,\mu$m/s and $U = 50\,\mu$m/s, the drop always detached off the infused surface at the bottom, registering similar maximum forces as before ($F_{max} = 101\,\mu$N and $F_{max} = 99\,\mu$N respectively). However, in the case of $U = 100\,\mu$m/s and $U = 500\,\mu$m/s, in some trials, drops detach from the bottom and in some cases they detached off the top regular hydrophobic surface. The measured adhesion forces are only marginally higher ($F_{max} = 106\,\mu$N, but more importantly not changing with whether drop detaches of the bottom or the top. Finally, for $U = 1000\,\mu$m/s, drops always detached from the bottom surface, registering an adhesion force of $F_{max} = 116\,\mu$N. So, while we can say that viscous effects do start manifesting themselves at pulling speeds of 1 mm/s for $\eta_o = 9,710$ mPa-s, these effects are marginal and the increase in the force is by less than 2%. Hence, vertical adhesion forces can be said to be independent of the viscosity of infusion and pulling speeds. We demonstrate this in Fig. 63c, where we plot the maximum

adhesion forces for the two different viscosities against the pulling speeds and show that the forces are constant

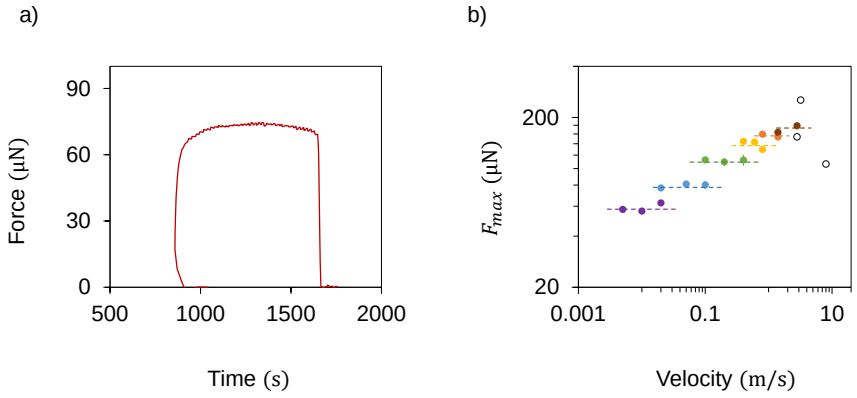

Figure 64: **Adhesion with Both Plates Infused.** a) A typical force versus inter-plate distance curve for a droplet of volume $\Omega = 2\,\mu L$ sandwiched between two infused surfaces with viscosity of the infusion of the bottom surface $\eta_o = 9$ mPa-s and the viscosity of the infusion of the top surface $\eta_o = 9710$mPa-s. b) The maximum adhesion force plotted against pulling speed for eight different volumes $\Omega = 1\,\mu L$, $4\,\mu L$, $6\,\mu L$, $8\mu L$, $10\,\mu L$, $12\,\mu L$, $14\,\mu L$ and $16\,\mu L$. For every volume except $\Omega = 16\,\mu L$, the maximum adhesion force is independent of velocity. Furthermore, some of these velocities lead to complete detachment from the bottom surface or detachment from the top surface, without significant manifestation in the adhesion force.

A final third experiment is performed by replacing the top regular hydrophobic surface with an infused surface with viscosity $\eta_1 = 9710$ mPa-s, the bottom surface being a LIS infused with $\eta_2 = 9710$mPa-s, to see if the maximum adhesion force has much more of a 'viscous effect' if both surfaces are viscous. We skip the 'spring test' (Regime II and III), concentrating just on the maximum adhesion force. Figure 64 show that a typical force curve in this case too exhibits a saturation zone (which is more constant than with a hydrophobic top), which is saturated at F_{max}. These adhesion forces for a given volume were found to be independent of velocity, but an increasing function of the volume, as shown in Fig. 64b. Typically, for a given volume, the experiments at lower pulling speeds led to detachment from the bottom and higher pulling speeds led to detachment from the bottom, but no general co-relation was found between a distinctive change in the adhesion force triggered by which surface the drop detached from. Although viscosity does not manifest itself in the magnitude of the vertical adhesion force, it does appear to decide which surface the drop detaches from, thus recasting this set-up as a viscous tweezer, actuated by velocity. The subsequent chapter is dedicated entirely to our observations on this tweezer.

5.2 THE MODEL FOR CAPILLARY BRIDGES.

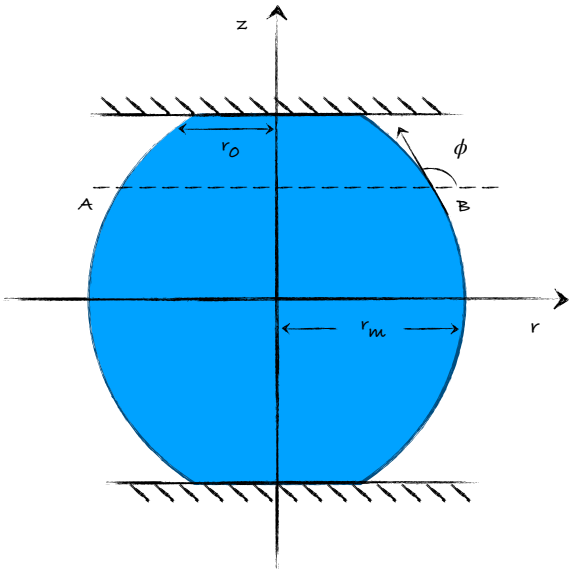

Figure 65: **Definition Sketch of a Capillary Bridge.** An axisymmetric capillary bridge between two parallel plates, where ϕ denotes the running slope at an arbitrary section AB, denoted by the dotted line. Along the line AB, the radial distance from the $z-$axis is r. For the convex-most section, $r = r_m$ and $\phi = \pi/2$. For the top plate, $r = r_0$ and $\phi = \phi_0$. Note that $\phi_0 = \pi - \theta_0$.

What is the adhesion force exerted by a capillary bridge on the top plate?

To answer this, let us consider a generic axisymmetric capillary bridge of height L, made of a liquid with surface tension γ. As shown in the definition sketch in Figure 65, we take the origin of our axis at the center of the bridge. Any point on the interface is at a distance r from the $z-$axis of symmetry, and has a running slope ϕ. For the top-plate, $z = L/2$, $r = r_0$ and $\phi = \phi_0$, and for the convex-most section, $r = r_m$ and $\psi = \pi/2$.

The convex-most section of the bridge, where $\psi = \pi/2$ is called the 'haunch' in the literature sometimes. When the bridges are concave, it is called a 'neck'.

We follow here the arguments of Kralchevsky and Nagayama and build upon them [118].

First, we look at the force at the convex-most section of the drop, that is we cut the drop by an imaginary plane $z = 0$ and ask what would be the force exerted by the bottom half on the top half. Axial symmetry implies that the net adhesion force is along the $z-$axis, be it attractive or repulsive. It is important to realize that there are two forces here. First, there is a force with which the contact line pulls the the top part, which is $F_c = \gamma\, 2\pi r_m$. This is separate from a second force which comes from the Laplace pressure ΔP within the drop with which the drop pushes the top plate upwards with a force

$F_L = \Delta P \pi r_m^2$. A summation of these two forces gives us the force exerted by the bottom half of the drop on the top half as

$$F_m = \gamma 2\pi r_m - \Delta P \pi r_m^2 \tag{43}$$

The above equation reveals that the contact line *pulls* the drop (first term on the left hand side), the Laplace pressure *pushes* the plate (the second term). Hence, one cannot a priori say whether force is attractive or repulsive.

Despite that, we claim that the force we have obtained in Equation 43 is also the force on the top plate, in fact it is the same as the force we would have obtained by cutting the drop along any arbitrary cross-section AB. In order to prove this, we first write down the force at any any arbitrary cross-section as

$$F(\psi) = \gamma 2\pi r \sin\psi - \Delta P \pi r^2, \tag{44}$$

which can be obtained by performing a force balance across AB similar to what we did for $z = 0$.

Next, we write the Laplace pressure as

$$\Delta P = \gamma \frac{d(r \sin\phi)}{r dr}, \tag{45}$$

where $\tan\phi = dz/dr$. The integration of Equation 45 from r_m to any arbitrary position r gives us

$$\gamma(r \sin\phi - r_m) = \frac{1}{2}\Delta P(r^2 - r_m^2), \tag{46}$$

The above equation when compared to Equation 44 and Equation 43 reveals a unique property of the capillary bridge: $F(\psi) - F_m = 0$, where $F(\psi)$ is the force across any arbitrary cross-section of the drop.

In other words, while forces at any cross-section of the drop can be obtained by a force balance, the integration of the Laplace Equation promises that these forces will all be the same. Furthermore, the Laplace pressure can be different from one point to the other on the bridge because the radii of curvature can be, and in general are, different at different points on the bridge, but the integration of the Laplace Equation guarantees that the force will be the same at all of these points.

This beautiful property of a capillary bridge suddenly allows us to write the equation of the force in a form where we can interpret it physically in its different limits. This form can be obtained when we substitute the Laplace pressure in Equation 43 as $\gamma(1/r_m + 1/R_m)$, where r_m and R_m are the two principal radii of curvature at $z = 0$,

and utilize the relation $F(\psi) - F_m = 0$ to write the adhesion force on the top plate as

$$F = \pi\gamma\, r_m(1 - r_m/R_m). \tag{47}$$

We can also nondimensionalize Equation 47 by dividing both sides by $\pi\gamma|R_m|$, which gives us

$$\frac{F}{\pi\gamma|R_m|} = \frac{r_m}{|R_m|}\left(1 - \frac{r_m}{R_m}\right). \tag{48}$$

The above equation to construct a phase map in Fig. 66 where the ordinate represents the force exerted by capillary bridge and the abscissa represents the morphology of the different bridges. There exist interesting limits to Eq. 47 (interchangeable with Equation 48) which we discuss now in conjunction with the phase map.

- **Onset of a repulsive force:** The onset is marked in Figure 66 as 'sphere'; it is the point where the solid black curve intersects the $x-$axis and plunges down.

  We note that the force predicted by Equation 47 has two antagonistic terms - the first term is necessarily attractive, which comes from the contact line and the second, a contribution of the Laplace pressure which may or may not be attractive depending on the shape, and ratio of its two principal radii of curvature. We note that although concavity, that is $R_m < 0$, implies that the force is necessarily attractive, convexity is not enough for the net adhesion force to be repulsive. The critical condition for the net force to be repulsive, $F < 0$ is when $R_M < r_m$.

  Hence, for a family of convex shapes between a cylinder and a sphere, the adhesion force exerted by the capillary bridge is attractive. Mathematically, this can be written as $+\infty > R_m > r_m$, where the two limits on the left and the right are a cylinder and a sphere respectively. These two points are represented in Figure 66 and the intermediary region is shaded in blue. This phase space corresponds to ridges that are convex but exhibit a positive force.

- **Sphere and Cylinder:** The limit of a sphere ($R_M = r_m$), rather truncated sphere, is where the Laplace pressure force is equal in magnitude to the contact line force $2\pi\gamma r_m$, thus balancing each other to give a zero force. On the other hand, the limit of a cylinder $R_m \to \infty$ is where the Laplace pressure force $\Delta P\pi r_m^2$ is half the magnitude of the contact line force but repulsive in nature. As a consequence, we get an adhesion force which is of the same magnitude as the Laplace pressure force but attractive in nature.

- **Zero Laplace Pressure:** We may also consider a case where $R_m = -r_m$, which corresponds to zero Laplace pressure. This is the case where one can happily integrate Equation 45 a second time, to obtain an analytical solution to the shape of the capillary bridge - which in this case is a catenoid. For this special shape, the force we find from Equation 47 is $2\pi\gamma r_m$, just that of the contact line. The point of catenoid is represented in Figure 66 as a black circle on the red solid curve marked 'catenoid'.

- **Negative Laplace Pressure:** This brings us to the final regime of negative Laplace pressure which corresponds to the most common case of a drop squeezed between two fingers. We see this regime when R_m is negative with a magnitude larger than r_m. This regime in the phase space corresponds to the region to the left of the point marked 'catenoid'.

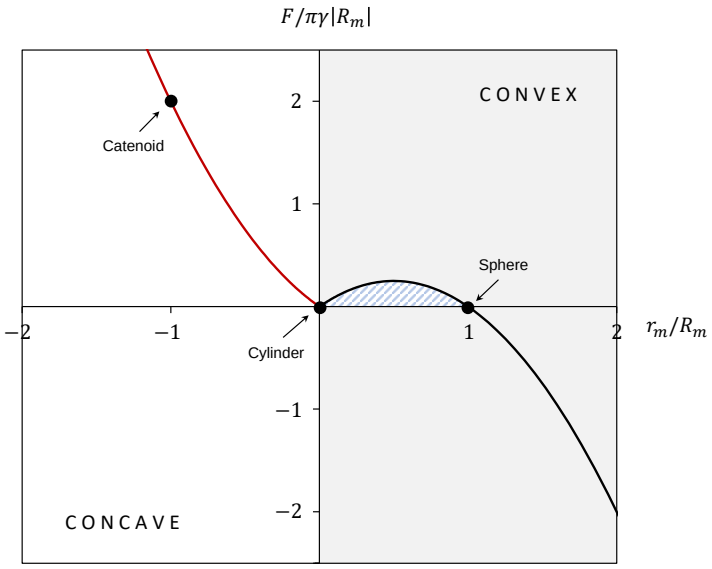

Figure 66: **Phase Diagram of Capillary Bridges.** $F/\pi\gamma|R_m|$ plotted against r_m/R_m creates a phase map of all capillary bridges where the y-axis represents the force exerted by the capillary bridge - its magnitude and sign, whereas the abcissa represents the shape morphologies of the bridges. Solid lines follow Equation 48. The gray shaded region corresponds to convex bridges, and the white region corresponds to concave bridges. The blue-striped region corresponds to convex bridges that exhibit a positive force.

It is necessary that we answer where exactly does the material or the substrate contribute to the adhesion, if it is all dictated by shapes and surface tension. The answer to this is hidden in the question itself - the shape of the capillary bridge. The substrate fixes the boundary condition which allows only a certain range of morphologies; and

while the volume of the capillary bridge does change the adhesion force, for a fixed volume the shape, hence the force, is fixed by the surface. For example, a hydrophilic surface will only allow concave bridges, its contact angle fixing the maximum force that the liquid bridge can exert for a fixed volume. Conversely, a superhydrophobic surface, in a Cassie state typically exhibits repulsive forces, that is in the phase map of Fig. 66 lies to the right of the black circle marked sphere, where $F < 0$. However, even superhydrophobic surfaces may also exhibit attractive forces where they are within the blue-striped region in the vicinity of $r_m/R_M = 1$. Such values are typically of the order of $1\mu N$ as shown by Ras and coworkers on butterfly wings [119]. On liquid-infused solids, we see that this force is 100 times more, showing LIS have very high vertical adhesion, in comparison to classical non-wetting solids.

Our experimental results lie in the blue-striped region in the phase map that represent bridges that are convex but exhibit a positive force - in fact we right after contact the value of r_m/R_m in our experiments is close to 0.5, where the adhesion force for convex drops is maximal. We now discuss and model our different regimes.

5.3 BACK TO REGIMES

Now that we have established that convex bridges can exert attractive forces, the positive snap-in force we see upon contact is not a surprise. We can be more quantitative here and use equation Equation 47 to evaluate the snap-in force F_0. Every single term on the left hand side of the above equation can be evaluated by measuring the principal radii of curvature and contact angle from the experimental image and the corresponding adhesion force can be checked. We do so in Figure 67, where we plot direct measurements of the adhesion force against the values we obtain using Equation 47. The data points fall on the solid line following $x = y$, showing the predicted and measured values are in agreement. It must be mentioned here that there exists a cloaking layer of oil on the water drop. This necessitates that the surface tension value to be to be used here in Equation47 is $\gamma = \gamma_o + \gamma_{ow}$, where γ_o is the surface tension of oil with respect to air and γ_{ow} is the surface tension value of oil with respect to water.

In the plot shown in Figure 67, the first data point is the red closed circle which corresponds to the snap-in force $F_0 = 74\,\mu N$ right after contact at the equilibrium length of the bridge L_0. This is followed by a compression (Regime II) shown by a red arrow where the minimum force reached at the end of the compression regime is $F = 55\mu N$, denoted by a white circle with red border. The bridge is subsequently extended to L_0 (Regime III) which gives a higher force than before $F = 100\mu N$, denoted by a white circle with black border. Further elon-

gation leads to an increase and subsequent decrease in the force until detachment (Regimes IV-VI).

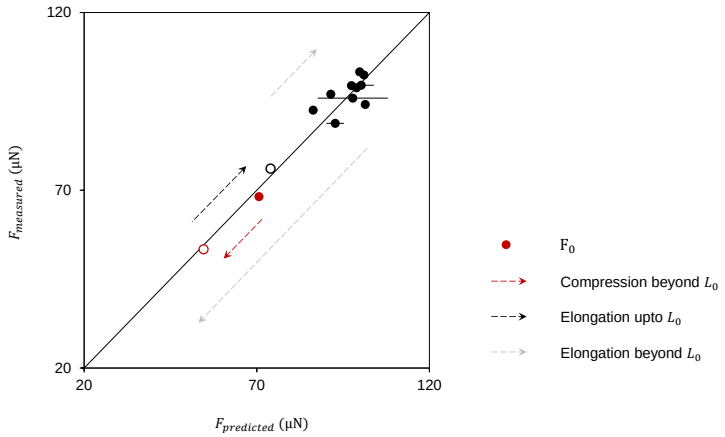

Figure 67: **Forces Predicted and Measured** Experimentally measured adhesion force plotted against predicted values of the force from Equation 47, when the corresponding r_m and R_m as obtained from experimental images are plugged in. Solid line follows $x = y$. The first data point is the red closed circle corresponding to the snap-in force $F_0 = 74\,\mu N$ at equilibrium length L_0. Red arrow indicates subsequent compression which leads to the minimum force $F = 55\,\mu N$ (white circle, red border) at the end of the compression regime. Black arrow indicates elongation back to L_0, and dashed gray arrow arrow denotes elongation beyond L_0 until detachment. White circle, black border shows that the force is higher when the bridge is extended back to L_0. Error bar corresponds to measurement error in obtaining the radii of curvature from experiments.

The most important inference we can draw from this plot is that Equation 47 can capture the forces in the capillary bridge, irrespective of the nature or magnitude of its extension or compression. We will now move onto specific regimes where we will make a model for the spring constant in Regime II and the maximum adhesion force, as seen in Regime IV.

5.3.1 *Regime II and III - Spring Constants*

We begin by reminding the reader that Regimes II and III correspond to compression beyond the equilibrium length of the bridge L_0, and elongation back to L_0. In this sense, these two regimes are more a test of the 'spring'-like nature of the capillary bridge rather than its adhesion, which would be Regime IV, discussed subsequently. The behavior of the spring would, however, depend on the boundary conditions of the capillary bridge, in this case fixed on one side by an infused surface (hydrophobic) with minimal pinning and a hydrophobic surface with the possibility of pinning. Indeed our experimental observations

show that the the differences in the possibilities of pinning become absolutely key in explaining and understanding our results.

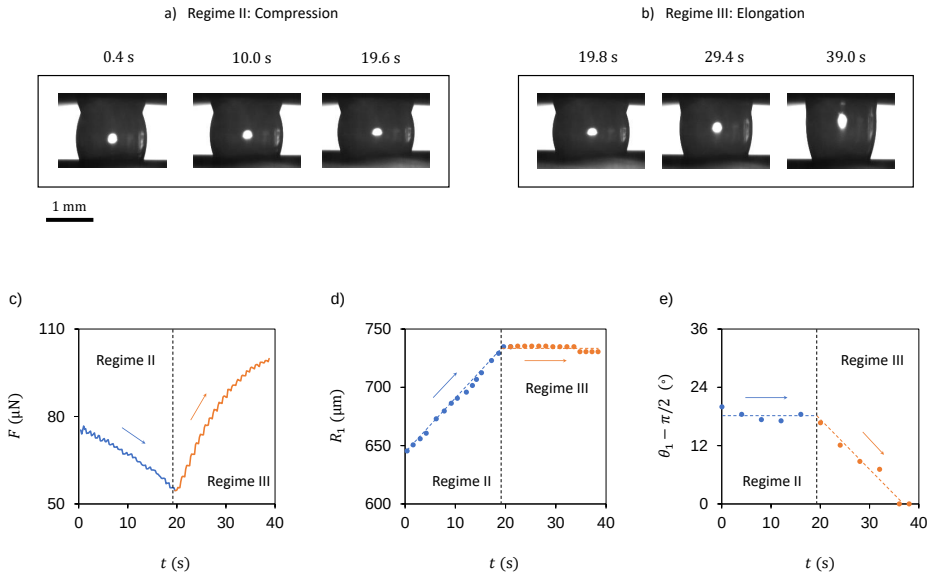

Figure 68: **Compression and Elongation.** a) and b) Snapshots corresponding to the experiment corresponding to force curve in Figure 62, where a capillary bridge of volume $\Omega = 2\,\mu L$ between a hydrophobic top plate and a bottom infused surface with viscosity $\eta_o = 9\,mPa\text{-}s$, is separated at a constant pulling speed $U = 10\,\mu m/s$, by bringing down the bottom surface. a) and b) correspond to Compression (Regime II) and Elongation (Regime III) regimes. The length of the liquid bridge at the start and end are the same and equal to $L_0 = 717\,\mu m$, as formed when the drop is first brought into contact with the top to form the bridge. c) The corresponding force diagram reveals that during the compression regime the force decreases from $F_0 = 74\mu N$ to $F = 53\,\mu N$ almost linearly, but during elongation the force increases to $F = 103\,\mu N$, showing the spring is not reversible. d) The temporal evolution of the top contact line during the two regimes. e) The temporal evolution of the contact angle at the top plate during the two regimes. d) and e) reveal that compression is a constant contact angle regime, whereas elongation is a pinned contact line regime in the context of the top plate.

We begin our experiment with a capillary bridge of volume $\Omega = 2\,\mu L$ placed on a liquid-infused surface with $\eta_o = 9\,mPa\text{-}s$ in contact with a silanized hydrophobic surface from he top, which transformed the hemispherical drop into a quasi-cylindrical bridge of length $L_0 = 717\,\mu m$. Our region of interest is when the capillary bridge was first compressed beyond L_0 at a constant rate of $10\mu/s$ for 20 s. We observed that first, the force of the capillary spring, *decreased* due to compression, and secondly this decrease was linear. When the drop was now elongated at the same speed for the same duration, the forces registered were higher than what they were during the compression

stage for every length of the bridge, reaching a value of $F = 100\mu N$ at $L_0 = 700\mu m$, which was $26\,\mu N$ higher than F_0.

Strictly speaking, it does not preserve top-down symmetry because the contact angle at the top is $\theta_1 \approx 108°$, whereas θ_2 is closer to $102°$.

The reasons for the differences in the capillary spring-force become clearer when we look at the experimental images corresponding to the compression and elongation regimes, as shown in Figure 71. Although the length of the bridge, the compression/elongation speed and duration of compression/elongation are the same, its effect on the morphology of the drop is not. As the drop gets compressed, we see in Figure 71 it not only preserves its radial symmetry but also a top-down symmetry. In other words, the contact angle at the top remains the same as the drop gets squished and so does it at the bottom.

However, when the drop is elongated, the drop breaks this 'top-down symmetry'. This is because the while the contact line at the bottom recedes owing to infused nature of the bottom surface, the contact line at the top is pinned, as shown in Figure 71d, where we plot the radius of the top contact line R_1 with respect to time. When we plot the contact angle at the top θ_1 with respect to time, we note that it is constant during the compression stage (Regime II), which is in accordance with a linear increase in R_1 as seen in Figure 71d, but θ_1 decreases linearly in the elongation phase in accordance with our observation of a constant R_1.

This shows us that the break in top-down symmetry is introduced precisely by the regular silanized hydrophobic surface which has pinning defects. On the bottom surface, the contact line can advance and recede at the same angle because of its negligible hysteresis. However, it cannot do so on the top plate - during the compression stage, the top contact line advances with an advancing contact angle of $\approx 108°$, but when it has to recede the angle must first come down and reach its receding value for this surface, which in this case is $\approx 89°$ for our surface. In the process, the entire elongation phase becomes a pinned contact line regime, whereas the compression phase is a constant contact angle regime, with regards to the top surface.

But how do we explain the decrease in the spring-force with the length of the spring? Let us look at the Equation 47 again:

$$F = \pi\gamma\, r_m(1 - r_m/R_m).$$

It is true that r_m increases, when L decreases. However, that is not enough to comment on why dF/dL should be positive, because it would also depend on how R_m changes with L. This is where we see that while Equation 47 by itself is sufficient to comment on the positive and repulsive nature of the force based on the shape, to know how the force changes with length, we need to know the constraints. As already noted, the droplet in the compression regime preserves its radial as well top-down symmetry. We can be more specific here.

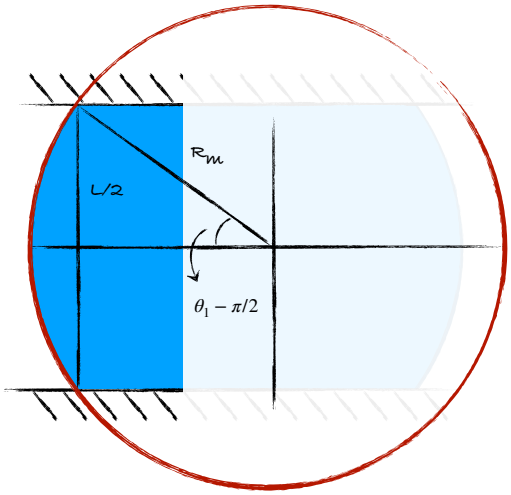

Figure 69: **The Liquid Spring.** Definition sketch of a liquid bridge during compression. The red circle has a radius of curvature R_m. We note that a right-angled triangle forms at the center of the red circle with the $L/2$ and R_m as two of its sides, and an angle $\theta_1 - \pi/2$ between the horizontal and the R_m.

We can use this top-down symmetry to realize that a right-angled triangle can be constructed with the center of the circle with radius of curvature R_m where $L/2$ and R_m are two of its sides, as shown in Figure 69. The angle at the center is $\theta_1 - \pi/2$ which we have seen experimentally to be a constant and a necessity for the preservation of top-down symmetry. We may now relate R_m, L and θ_1 as

$$L/2 \sim R_m(\theta_1 - \pi/2) \tag{49}$$

Next, we can use volume conservation to write

$$\pi r_m^2 L \sim \Omega, \tag{50}$$

to the first order. Using Eq. 50 and Eq. 49, we can now substitute for r_m and R_m in Equation 47, to write an equation of F in terms of L as

$$F \sim \pi\gamma\sqrt{\frac{\Omega}{\pi L}}\left(1 - 2(\theta_1 - \pi/2)\frac{\sqrt{\Omega}}{L^{3/2}}\right) \tag{51}$$

The first thing we note about the above equation is that it is highly nonlinear, with the possibility of the force being negative or repulsive

if $L < 2^{2/3}(\theta_1 - \pi/2)^{2/3}\Omega^{1/3}$, which is identical to the criterion $r_m < R_m$, as follows from Equation 47, and a condition we satisfy in our experiment where $r_m/R_m = 0.52$ in the beginning of compression. However this form of the criterion highlights more the contribution of wettability. In other words, $\theta_1 \approx \theta_2$ from top-down symmetry, so we can write this criterion as

$$L < 2^{2/3}(\theta_2 - \pi/2)^{2/3}\Omega^{1/3} \tag{52}$$

The above form of the criterion for the onset of a repulsive force reveals that the larger the contact angle θ_1, the larger the maximum length of the spring corresponding to a repulsive force. Said differently, for large θ_1 as in the case of superhydrophobic surfaces, the length of the bridge would have to be increased to get an attractive force, if one can be achieved at all. Conversely, for hydrophobic surfaces where θ_2 is close to $\pi/2$, the drop would have to be squeezed substantially to reach a regime where the force can be attractive. We can now differentiate F with respect to L, which gives us

$$\frac{dF}{dL} \sim -\pi\gamma\frac{\sqrt{\Omega}}{2\sqrt{\pi}L^{3/2}}\left(1 - 8(\theta_1 - \pi/2)\frac{\sqrt{\Omega}}{L^{3/2}}\right) \tag{53}$$

It follows from the above equation that $dF/dL > 0$ when $L < 2^{4/3}(\theta_1 - \pi/2)^{2/3}\Omega^{1/3}$. This means our drop of $\Omega = 2\mu L$ and $\delta = 74\mu m$, we would need to squeeze the drop $L < 1mm$ to be in a regime where the adhesion force is an increasing function of its length. Using Equation 49 and Equation 50 we can rewrite this criterion as $r_m/R_m > 1/4$. This condition in conjunction with Equation47 gives the criterion for convex capillary springs to exhibit a positive force,that is also an increasing function of the length of the spring.

$$1 > r_m/R_m > 1/4, \tag{54}$$

Note that the right hand side condition of the equation only holds if the elongation or compression of a spring preserves top-down symmetry along with radial. We would also like to comment here on the numerical value 1/4, which is not an empirical finding. It is a consequence of the specific scaling of the force $F \sim 1/\sqrt{L} - 1/L^2$, where we can understand the $1/\sqrt{L}$ term physically as a consequence of the volume constraint and the $1/L^2$ term as a consequence of no pinning when the contact lines at the top and bottom are moving at the same angle. It follows that $dF/dL \sim 1/2L^{3/2}(1 - 4/L^{3/2})$, which gives us $L^* \sim (1/4)^{2/5}$ as the critical L^* where it turns negative. Dividing Equation 49 by Equation 50 for this critical length already gives us the relation $r_m^*/R_m^* \sim (L^*)^{2/5} = 1/4$.

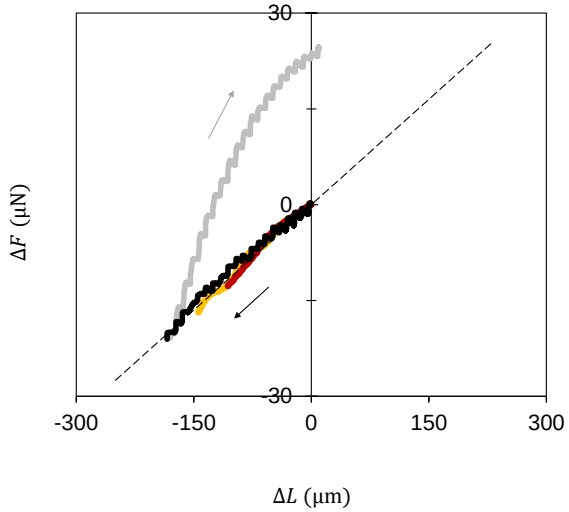

Figure 70: **Spring constant and Hysteresis.** $\Delta F = F - F_0$ plotted against $\Delta L = L - L_0$ for three different experiments with $\Omega = 2\,\mu L$ at different pulling speeds $U = 10\,\mu m/s$ (black curve), and $U = 50\,\mu m/s$ (yellow curve) $U = 100\,\mu m/s$ (red curve). The linearity of the spring corresponds to a spring constant of 0.11 $\mu N/\mu m$. The grey data points correspond to an elongation curve for $U = 10\,\mu m/s$. The curves together provide a measure of spring hysteresis.

Our experiments clearly lie within the $1 > r_m/R_m > 1/4$, which is why we see a decrease in the force as the length of the bridge decreases. Furthermore, given that our textures are of the order of $20\,\mu m$, our infused surface would not even be geometrically flat at that scale, so other effects would possibly take over. Nevertheless, the limit is not an unfeasible one - it is possible to imagine surfaces with sub-micron textures and slightly larger volumes of drops $\sim 10\,\mu L$ which would allow for a convex capillary spring where the force would be a decreasing function of its length.

We now finally move our attention to the fact that the spring constant, k, which is $\frac{dF}{dL}$ in the vicinity of L_0. This is given as

$$k(L_0) \sim -\pi\gamma \frac{\sqrt{\Omega}}{2\pi L_0^{3/2}} \left(1 - 2(\theta_1 - \pi/2)\frac{4\sqrt{\Omega}}{L_0^{3/2}}\right) \tag{55}$$

Note that our spring is only compressed to about 0.2 of its size and despite its nonlinear nature, the deformation and spring-force is well captured by Equation 55 in Figure 70 where we plot $\Delta F = F - F_0$ against $\Delta L = L - L_0$ for three different experiments that have the same droplet volume of $\Omega = 2\,\mu L$ but different pulling speeds $U = 10\mu m/s$ (black curve), and $U = 50\mu m/s$ (yellow curve) $U = 100\,\mu m/s$ (red curve). Our experimentally obtained spring constant is $k = 0.11\,\mu N/\mu m$

and the prediction by Equation 55 is $k = 0.23\,\mu N/\mu m$. This means Equation 55 has a pre-factor of 0.5 in front of it. Equation 55 not only captured the physics of the problem and correct scaling, could also predict the functional relationship between F and L. Finally, the gray data points in Figure 70 correspond to the elongation regime where the forces are always higher than their corresponding compression values, thus giving us a hysteresis curve.

5.3.2 *Regime IV - Maximum Adhesion Force*

Classical Adhesion tests are done with a more or less pinned contact line at the top and the test surface at the bottom. In this regard, Regime IV is the true Adhesion test, whereas Regime II and III were more of a measure of the capillary spring one may form with infused solid on one side.

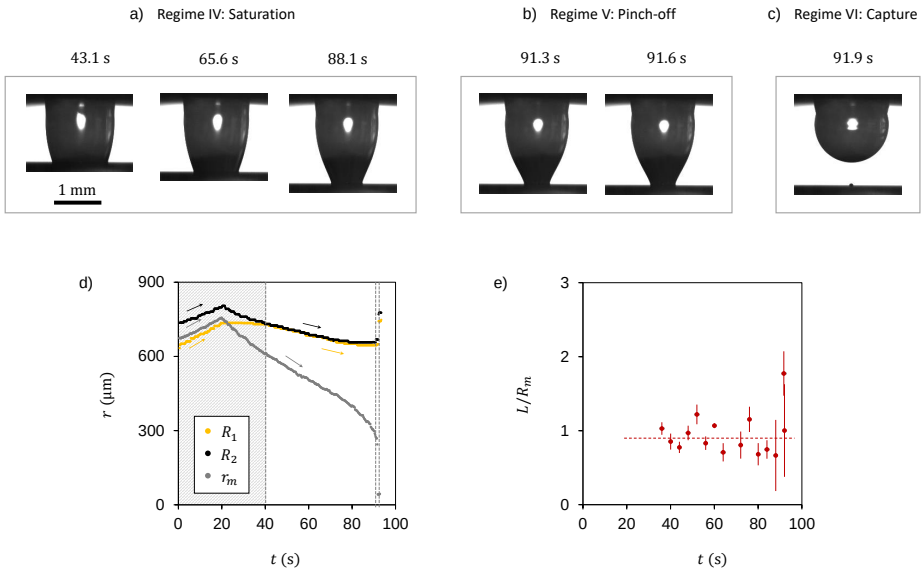

Figure 71: **Regimes IV, V and VI.** Snapshots corresponding to Regimes IV, V and VI of the experiment where the drop is extended beyond its equilibrium length $L0 = 717\,\mu m$. The droplet volume is $\Omega = 2\,\mu L$ and pulling speed $U = 10\,\mu m/s$. The top surface is hydrophobic and the bottom surface is a LIS with $\eta_o = 9\,mPa\text{-}s$. Regime VI is the saturation zone where the force does not substantially change upon elongation. Regime VII is where the force quickly falls off as the bottom contact line quickly recedes to pinch-off. Regime VI corresponds to complete detachment where the drop is sitting at the top. d) Temporal evolution of the top contact line R_1 (yellow), bottom contact line R_2 (black) and the azimuthal radius of curvature at the point where $\psi = \pi/2$, r_m (gray data points). e) L/R_c plotted against time shows that we have $L/R_c \sim 1$ in Regimes IV and V.

In this regime, we elongate the capillary bridge beyond L_0 upto a length $L = 1246\,\mu m$ at the same constant speed of $U = 10\mu m/s$. The force remains constant at $F_{max} = 116\,\mu N$, decreasing only marginally at a small rate of $0.03\mu N/\mu m$, which separates it from the previous regime where the force was increasing with length. However, there are two more crucial differences from the previous regime of elongation. First, as seen in the experimental images of Fig. 71a, the convex-most part of the drop is at the very top. In other words, $r_m = R_1$, which we see quantitatively in 71d. Second, R_m in this regime scales as the length of the bridge, as revealed by 71d where we plot L/R_m against time. This enables us to substitute r_m and R_m in Equation 47 and rewrite it as

$$F \sim \pi\gamma R_1(1 - R_1/L) \tag{56}$$

This is where we recall Plateau's criterion for droplet break up. For a cylindrical liquid bridge with contact lines of radii R_1 and R_2, we can define an aspect ratio $\lambda = L/2R$, where $R = (R_1 + R_2)/2$ is the mean radius. Plateau's criterion states that a liquid cylinder becomes unstable when $\lambda_c = \pi$, when $R_1 = R_2$. Subsequently, Meseguer showed that for bridges with unequal R_1 and R_2, λ_c lies between π and $\pi/2$, the latter criterion being for the limiting case of a cone. We discuss this criterion in greater detail in the subsequent chapter, but can already use it to say that the capillary bridge in our experiment becomes unstable at the end of the Regime IV, where it is still within the saturation zone. We can use this to argue that F_{max} is reached in the limit where

$$R_1/L \sim 1/\lambda_c. \tag{57}$$

Furthermore, we can write in this limit the volume of the bridge as $\Omega \sim \pi L R_1^2$ which in conjunction with the previous argument, gives us an equation of R_1 in terms of λ_c as

$$r_m \sim (\Omega/\pi\lambda_c^2)^{1/3} \tag{58}$$

Equation 57, Equation 58 and Equation 56 can be combined to write the equation for the maximum adhesion force as

$$F_{max} \sim \pi\gamma(\Omega/\pi\lambda_c^2)^{1/3}(1 - 1/\lambda_c) \tag{59}$$

Dividing the above equation by the weight of the drop gives us $F_w \sim \rho g\Omega$ gives us

$$F^*_{max} = A\,(\Omega^*)^{-2/3}\,, \tag{60}$$

where $F^*_{max} = F_{max}/F_w$ and $\Omega^* = \Omega/\kappa^{-3}$ and A is given by

$$A \sim (\pi^2/\lambda_c^2)^{1/3}(1 - 1/\lambda_c), \tag{61}$$

and λ_c has a value close to $\pi/2$.

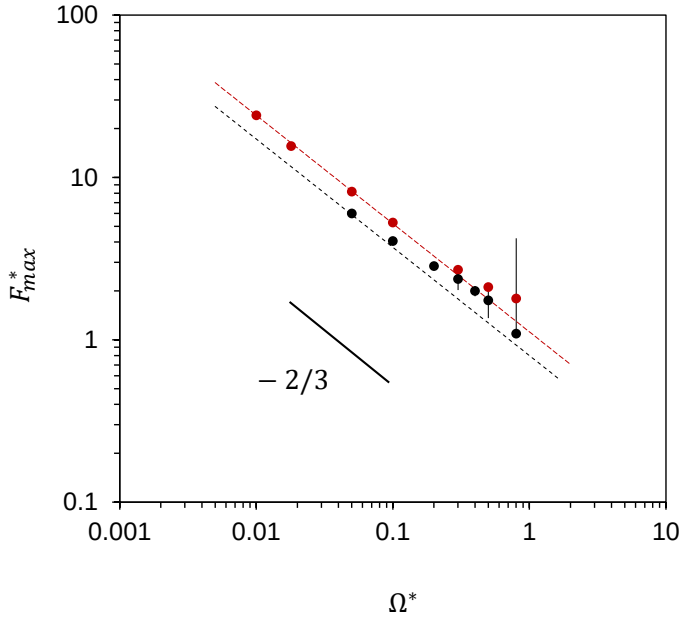

Figure 72: **Maximum Adhesion Force.** Maximum adhesion force normalized by the weight of the drop F_{max}/F_w plotted against the volume of the drop, red data points indicate experiments with a hydrophobic surface on the top and LIS with $\eta_o = 9$ mPa-s, whereas black data points correspond to experiments with LIS on both sides with top viscosity being $\eta_1 = 9710$ mPa-s, while the bottom is $\eta_2 = 9$ mPa-s. The red data points collapse on the red dotted line which follows the Equation 60, corresponding to $A = 1.9$. The black data points are bounded by the red dotted line and the black dotted line which follows Equation 60, corresponding to $A = 0.82$. Note that the for drops of volumes 1µL or less, the maximum adhesion force is more than 10 times its weight.

We test equation 60 in Figure 72 where we plot our experimentally measured F^* values against Ω^* for experiments with drop volumes varying from 0.2 µL to 16 µL, all pulled at the same speed $U = 10\,\mu m/s$ and the bottom surface infused with $\eta_o = 9$ mPa-s. We find that indeed that the maximum adhesion force varies as Ω^* raised to the power $-2/3$, as captured by the red dotted line which follows Equation 60 with a value of $A = 1.9$. which corresponds to a prefactor of 1.6 in Equation 61.

Fig. 72 also shows that the maximum adhesion force is not only always greater than the weight of the drop for drops upto 16 µL, it

can be the order of ten times or higher for drops when the volume is less than or equal to 1 μL. Such high increase in adhesion force with volume is courtesy the $-2/3$ dependence with volume, which owes its origin to the contact line at the top being pinned and at the bottom being free - a consequence of the infused nature of the surface.

We also show here that if the 'pinned' nature of the contact line at the top is removed, by replacing the hydrophobic surface with an infused surface with $\eta_1 = 9710$mPa-s, the maximum adhesion forces are lower than that measured with hydrophobic surfaces by about 25% for small volumes in the vicinity of $\Omega = 1\mu$L, and approach the ones obtained with 'pinned' contact lines at the top at larger volumes. The exception again is at 16μL where gravitational effects might induce large variations in the drop shape and adhesion measurements.

5.4 CONCLUSION

Unlike other non-wetting materials as superhydrophobic surfaces that typically exhibit a repulsive force in Cassie state, liquid-infused solids are materials with high vertical adhesion - the adhesion force is attractive and its magnitude is eight times the weight of the drop, for a 1 μL drop. Textured materials infused with silicone oil, courtesy their hydrophobic nature with a contact angle in the vicinity of $\pi/2$, enable the construction a convex bridge that is more cylindrical than spherical, thus generating an attractive adhesion force. This makes liquid infused solids a truly unique class of solids, which have negligible lateral adhesion, tunable dynamical friction and high vertical adhesion. Thus, liquid infused solids contrast spectacularly with their non-wetting cousin - a superhydrophobic surface, which has comparatively higher lateral adhesion, negligible vertical adhesion in Cassie state and a very low friction which cannot be tuned as much.

6

VISCOUS TWEEZER

In this chapter, we discuss the physics of a curious little viscous tweezer[1]: an elementary system consisting of a millimetric water droplet placed between two surfaces, infused with oils of different viscosities. We find that if the upper plate viscosity is greater, then by pulling the upper plate at sufficiently high velocities it is possible to detach the droplet completely off the bottom plate; the captured droplet can be subsequently deposited on the lower plate by bringing it in contact and pulling the plates apart slowly. This chapter is primarily experimental, where we elaborate on the complexities of the problem with experimental evidence and lay out a pathway for possible solutions in future work.

1 This phenomenon was first observed by Armelle Keiser, who did the initial experiments. The project was done in collaboration with her.

6.1 PLATEAU CYLINDERS

A drop of water held between two fingers, when pulled slowly apart, breaks. But, exactly at what length does it break?

In 1845, Belgian physicist Joseph Plateau asked this question. More precisely, he asked why is a cylindrical liquid interface unstable. He realized that it is necessary to remove gravity from the problem, to probe the question experimentally and he devised an absolutely ingenious method to do so. In a tank of water-alcohol mixture where the alcohol creates a density stratification, he deposited an oil droplet, which came to an equilibrium at a position where the density was matched. As a consequence, the drop was now effectively in a zero-gravity condition, or in other words, having an infinite capillary length. He now held the drop at its two side by hoops of the same diameter to form a liquid cylinder and slowly pulled them apart until the cylinder broke into two. Plateau discovered a curious result: *the ratio of the length of the liquid cylinder to its diameter, at the point of break-up was always* π.

The cylinder actually breaks into at least three parts, where the third part is a tiny satellite droplet in the middle.

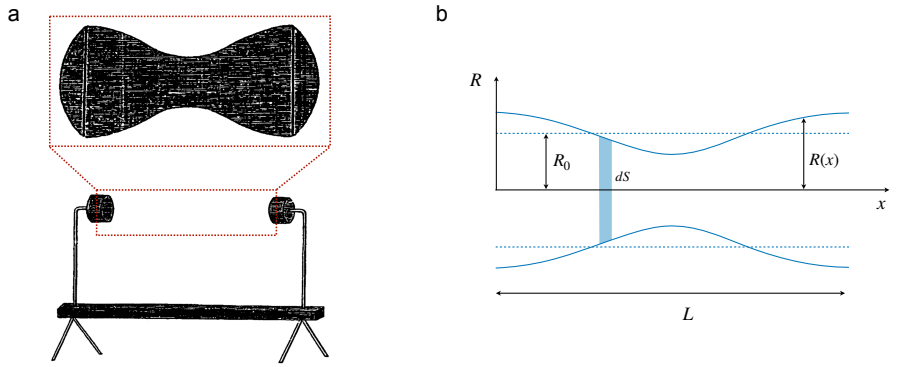

Figure 73: **Plateau Cylinder.** a) Plateau's original drawings of his set-up with two hoops. Inset shows his sketch of a deformed liquid cylinder, before break-up. b) Definition sketch of a generic deformed liquid cylinder of length L, mean radius R_0.

We can understand the Plateau criterion by considering a generic liquid cylinder of length L and initial radius R_0, whose deformed interface may be written to the first order in the perturbation ϵ as $R(x) = R^* + \epsilon \cos qx$, where R^* is the mean radius and $q = 2\pi/L$ is the wave number, and the deformation is maximum at the beginning and the end. The relationship between the mean radius and the initial radius can be established by equating the volume of the perturbed cylinder with that of the unperturbed state: $\Omega = \pi R_0^2 L = \int \pi R^2(x) ds$,

where $ds = dx(1 + 1/2(dR/dx)^2)$ is a differential length along the interface. This gives the mean radius as

$$R^* = R_0 - \epsilon^2/4R_0 \tag{62}$$

The initial surface energy of the cylinder is given by $E_0 = \gamma 2\pi R_0 L$, whereas the surface energy of the perturbed cylinder can be written as $E = \int \gamma 2\pi R(x) ds$, which upon integration across one wavelength gives us $\gamma 2\pi R^* L(1 + \epsilon^2 q^2/4)$. Substituting for the mean radius using Equation 62, we can now write the difference in surface energy between the perturbed and unperturbed state, to the first order as

$$\Delta E = E_0 \frac{\epsilon^2 q^2}{4}\left(1 - \frac{1}{q^2 R_0^2}\right) \tag{63}$$

The liquid cylinder would become unstable and break up when the deformed state is energetically more favorable than the initial, that is when $\Delta E < 0$, which from Equation 63 we see, is satisfied when $q = 2\pi/L < 1/R_0$. If we now define the ratio of the length of the liquid cylinder to its diameter as $\lambda = L/2R_0$, the critical value of this ratio λ_c where the instability sets in can be written as

$$\lambda_c = \pi, \tag{64}$$

which was the original observation of Joseph Plateau.

We now revisit the original problem of Plateau by removing its classical constraint: the pinned contact line. We replace the two boundaries of the liquid cylinder by two liquid-infused surfaces which makes the contact lines free to move.

6.2 THE EXPERIMENT

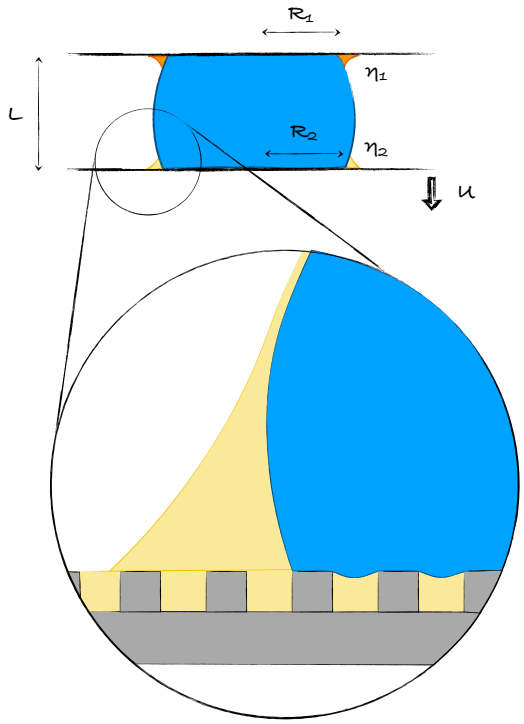

Figure 74: **Schematic of Tweezer.** A sketch of our experimental set-up, where a drop of water (in blue) is placed between two liquid-infused surfaces, the viscosity of the infused oil at the top η_1 being greater than that infused at the bottom. The plates are separated typically by moving the bottom plate at a constant speed U until the drop detaches from the bottom or the top. Inset shows that the existence of an oil meniscus and texture in which the oil is infused..

The aim of the experiment is to capture a water drop by utilizing the viscosity of an infused solid. Thus, for a water drop sandwiched between two liquid infused solids, the upper viscosity η_2 should be much greater than that at the bottom η_1. The bottom plate is then moved down at a constant speed U until the drop detaches from the top or the bottom. If the drop detaches from the bottom - it is a 'capture', and if it detaches from the top, it is a 'deposition'.

Fig. 74 shows a definition sketch of our experimental set-up. For a typical experiment, we start at a shape where the two contact line radii R_1 and R_2 are close in magnitude (R_1 is typically slightly smaller than R_2) and L is typically 1.5 times the size of the drop. As we increase the separation length L, we observe that both the contact lines at the top and the bottom recede, owing to the slippery nature of the two surfaces. If the pulling speed is sufficiently high $U > U_{cr}$, then

the drop completely detaches off from the bottom and is captured at the top surface. However, for the case of $U < U_{cr}$, we see that the drop pinches off close to the top surface and deposits at the bottom, leaving a tiny satellite drop at the top. In Fig. 75, we see a representative case of a 4μL drop between two infused surfaces of $\eta_1 = 9,710$ mPa-s and $\eta_2 = 9$ mPa-s and initial radii $R_1 = 850\mu m$ and $R_2 = 693\mu m$ and initial distance of separation $L = 1.2mm$. A timelapse is shown for the cases of two different pulling speeds of $U = 200\mu m/s$ and $U = 400\mu m/s$, where the former velocity corresponds to deposition on the bottom plate and latter corresponds to a capture of the drop on the top plate. This highlights the very unique property of this system that it can be actuated by velocity to switch between capturing and depositing drops, thus behaving as a 'viscous tweezer'.

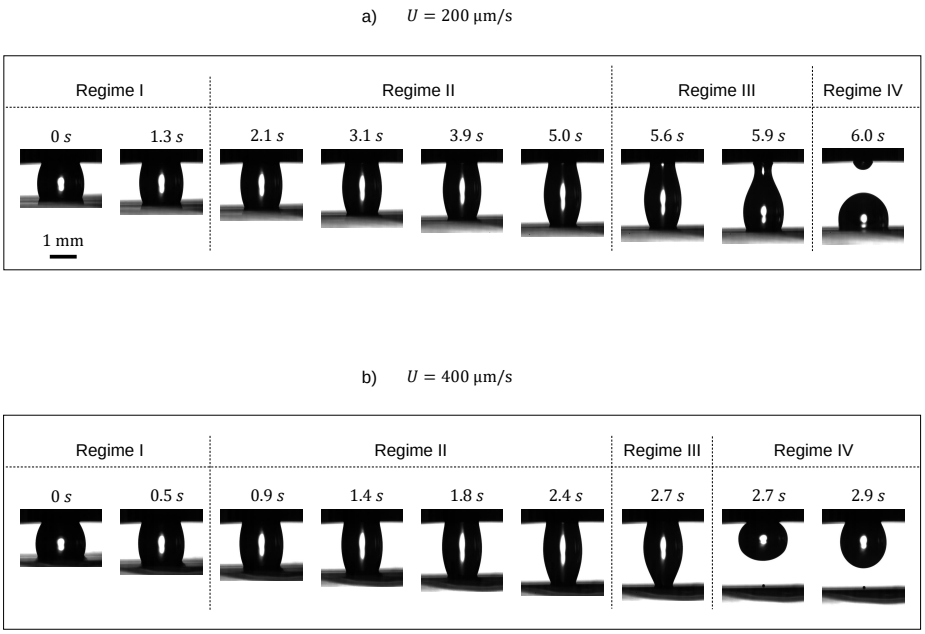

Figure 75: **Capture and Deposition** Snapshots of a 4μL drop sandwiched between two infused surfaces of $\eta_1 = 9710$ mPa-s and $\eta_2 = 9$mPa-s, one pulled at a speed of $U = 200\mu m/s$ which leads to a deposition and the other corresponding to $U = 400\mu m/s$ which leads to a capture.

The evolution of the contact line radii R_1 and R_2 with time reveal four regimes for $U < U_{cr}$, as seen in in Fig. 76 :

i) **Initial 're-organization':** where the asymmetry in R1 and R2 is removed and they become of a similar magnitude.

ii) **Constant Velocity Regime:** where the two contact lines move at the same speed which in this case is $V_1 = V_2 = 52\mu/s$, shown in gray shaded region in Fig. 76. This constant velocity regime persists for a few seconds up until the cylinder reaches a length of 2.2 mm.

iii) **Pinch-off:** in this regime, the velocities quickly become different from each other, V_1 increasing sharply being in the vicinity of the formation of a neck that decreases the value of R_1, whereas V_2 transiently going to zero, as it is far from the neck.

iv) **Deposition:** Following the pinch-off, V_2 increases quickly and R_2 goes to a value close to its initial. The drop has now been deposited at the bottom and a small satellite drop of 300µm radius hangs from the top.

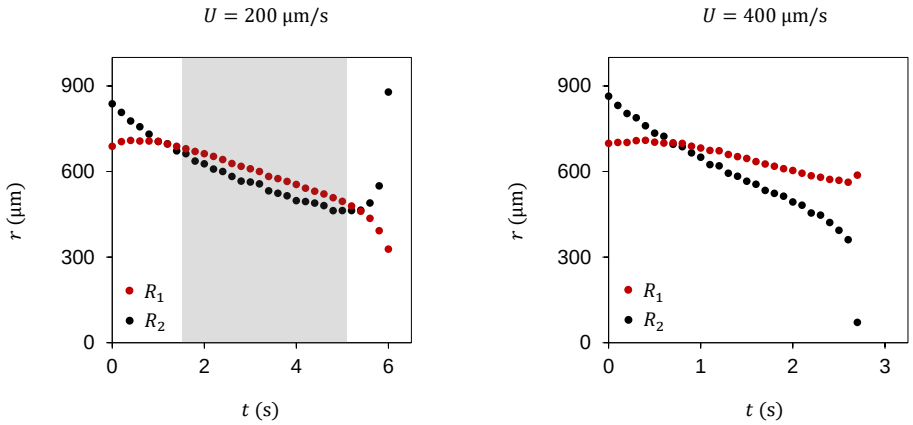

Figure 76: **Capture and Deposition** Temporal evolution of the contact line radii R_1 (red circles) and R_2 (black circles) corresponding to experimental images of Fig. 75: a 4µL drop between two liquid infused surfaces of $\eta_1 = 9710$ mPa-s and $\eta_2 = 9$mPa-s, one pulled at a speed of $U = 200\mu m/s$ (deposition) and the other at $U = 400\mu m/s$ (capture). The shaded region represents a constant velocity regime - a hallmark of deposition cases.

For the case of $U > U_{cr}$, we again see the four regimes, with one critical distinction: the missing constant velocity regime. The four regimes are:

i) **Initial 're-organization':** where the asymmetry in R_1 and R_2 is removed and they become of a similar magnitude.

ii) $V_1 < V_2$ **Regime:** where the top contact line moves substantially slower in comparison to the bottom one, we see $V_1 = 79\mu m/s$ is almost half the receding velocity of the bottom contact line, $V_2 = 162\mu m$. Unlike the previous case, we see that R_1 and R_2 become increasing dissimilar until the length of the drop reaches 2.2mm.

iii) **Pinch-off:** The bottom contact line quickly speeds up, whereas the top contact line halts transiently. This regime is faster than the pinch-off regime in the previous case, of the order of 10 ms in comparison to the 100ms for $U < U_{cr}$. This is because pinch-off position is practically at the bottom surface which directly affects R_2, whereas the neck, in the previous case, formed at a distance of 300µm from the top surface, thus R_1 was less affected by the necking process comparatively.

iv) **Capture:** Following the pinch-off there remains, at times, a tiny satellite drop of the order of 10μm at the bottom too. But, 'practically' the drop has been detached completely off the surface. In this regard, captures are clean, but depositions are not.

However, the important distinction between the two cases is the **Regime ii**: the middle regime, before pinch-off, which ends at the same length of the drop, whether the drop is symmetrical with $R_1 \approx R_2$ (for $U < U_{cr}$), or asymmetric with $R_1 > R_2$ (for $U < U_{cr}$) but decides that at the point the drop becomes unstable.

6.3 REPRODUCIBLILITY AND THE CRITICAL VELOCITY.

The previous discussion was indicative of the existence of a critical pulling speed U_{cr}, separating captures from deposition. In this discussion, we elaborate further on the nature and existence of such a speed.

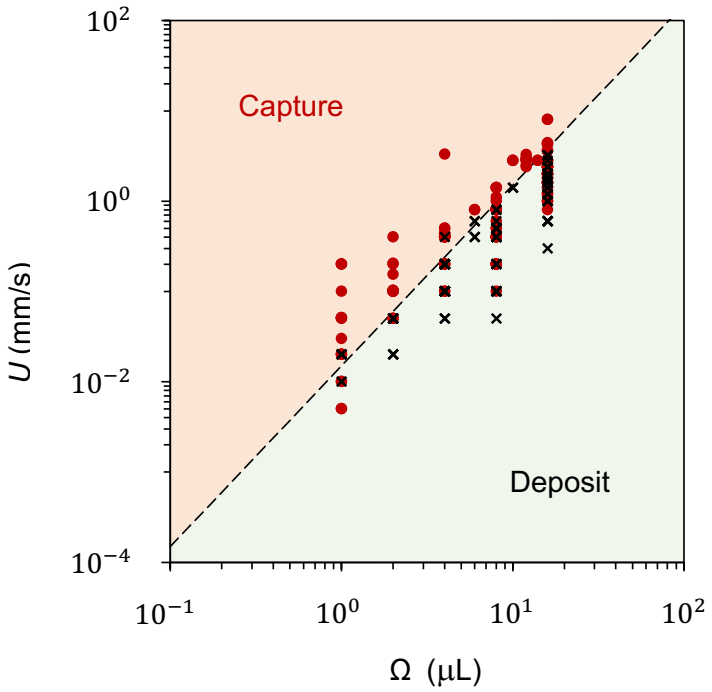

Figure 77: **Phase Map.** A phase map of capture and deposition where pulling speeds U are plotted against the volume of the drop Ω for $\eta_1 = 9710$ mPa-s and $\eta_2 = 9$mPa-s. Red circles represent captured drops, while black crosses represent depositions. The dotted line is a guide for the eye, showing the transition.

We first perform the experiments by fixing the volume Ω, and the two viscosities of infusion η_1 and η_2 and pull the lower plate at different speeds U. We repeat the experiments for a given volume multiple times, on some occasions about a hundred times for the determina-

tion of this threshold speed. Then we change the volume and do the same. In Figure 77, we create a phase map where the pulling speed U is plotted against Ω for experiments performed with $\eta_1 = 9,710$ mPa-s and $\eta_2 = 9$ mPa-s; red circles denote capture, while black crosses represent deposition. The dotted line is a guide for the eye for broadly separating the 'capture' and 'deposition' regimes.

While the plot clearly reveals that the capturing speed increases with increasing volumes, we note that there exists a big region of overlap: speeds spanning across a decade, for instance for $\Omega = 16\mu L$, where the drop is sometimes captured and sometimes deposited, making the definition of U_{cr} ambiguous We demonstrate this further in Figure 78 where we show reproducibility maps for three representative volumes of $\Omega = 2\mu L$, $\Omega = 4\mu L$ and $\Omega = 16\mu L$, where we plot the pulling speed against the trial number, with red circles representing capture and black crosses representing deposition. Each single trial represents a new drop, data points connected by dotted line represent experiments performed on the same set of surfaces. Experiments were performed for different surfaces of the same infusion (to check for possible defects), and with a new drop every time. Experiments with the same drop show much more deviation and hence were removed from the figure.

Figure 78 reveals the extent of the overlap, shown in the shaded region, and how it persisted despite changes in volume and surfaces. The red dotted line indicates U_C, the minimum pulling speed corresponding to which captures are observed but *no depositions in any trial*. The dotted black line represents U_D which is the maximum pulling speed corresponding to which depositions are observed but *no captures in any trial*. If the transition were clean, then there would have been no overlap and we could have written $U_{cr} = U_C = U_D$, where U_{cr} is the critical speed for transitions. However, we see from Fig. 78 that transitions are far from clean. For $\Omega = 2\mu L$, $U_D = 20\mu/s$ and $U_C = 100\mu/s$, which is five times mores. These speeds increases to $U_D = 80\mu/s$ and $U_C = 400\mu/s$ for $\Omega = 4\mu L$ and to $U_D = 300\mu/s$ and $U_C = 3600\mu/s$ for $\Omega = 16\mu L$.

It is not entirely clear why this variation is so pronounced. However, what we can say is that the overlap has a volumetric effect, as is indicative from the increase in the ratio of U_C/U_D from 5 to 12 when the volume is increased from $\Omega = 2\mu L$ to $\Omega = 16\mu L$. One possible mechanism in which volumetric effects might pronounce the overlap is small degrees of over or under-infusion, which could strongly affect the dissipation mechanisms in the two menisci. Larger drops have a larger menisci compounding this effect and creating reproducibility issues. urthermore, gravitational effects also become non-negligible for drops larger than $\Omega > 6\mu L$, corresponding to which the Bond number $Bo = \rho g R^2/\gamma$ becomes greater than 1. Further still, the initial aspect ratio when pulling begins might have some effect. Although

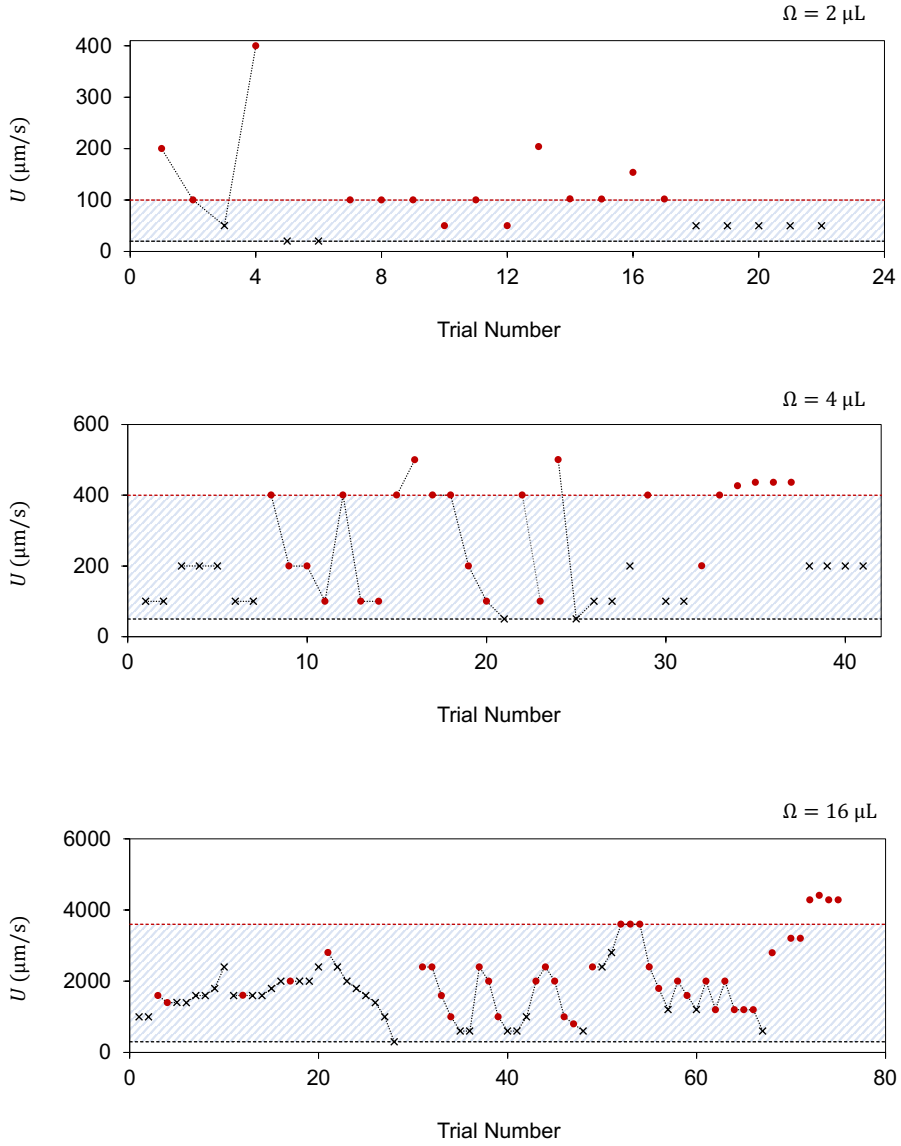

Figure 78: **Reproducibility Map.** Pulling speeds plotted against trial number for experiments done with three different volumes $\Omega = 2\mu L$, $\Omega = 4\mu L$ and $\Omega = 16\mu L$. Red circles denote a capture and black crosses denote failures. Shaded region shows the range of velocities where both captures and deposits were observed.

this value $\lambda_0 = L_0/(R_1 + R_2)$ was typically between 0.5 to 0.8, its effect on U_{cr} and the transition have not been looked into. We remark on them in the subsequent section.

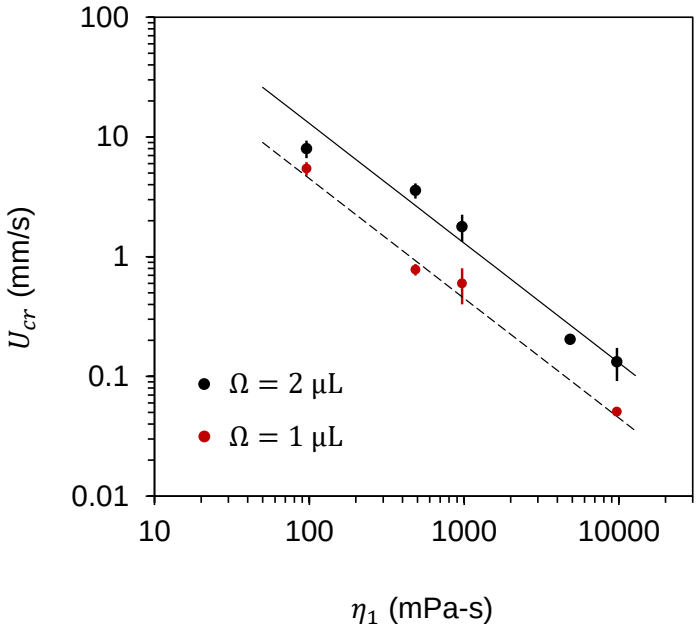

Figure 79: **Viscous Origin.** The minimum pulling velocity where captures are observed without depositions in any trial, plotted against the viscosity of infusion of the top plate, η_1. The viscosity of infusion of the bottom plate is fixed at $\eta_2 = 9$mPa-s. Red circles represent 1μL and black represent 2μL.

Nevertheless, with such large fluctuations over hundreds of experiments, it becomes natural to ask how does one define a critical speed. We note that despite the zone of overlap, where both captures and depositions are observed, there appears to exist, for all the cases, an upper bound of the pulling speed for depositions (red dotted line). If we were to define the threshold speed for capture U_{cr} as this speed which we have previously called U_C (the minimum value of the pulling speed at which captures are observed but no depositions for at least 20 trials), then we can plot this speed against η_1, for a fixed volume and fixed $\eta_2 = 9$mP-s, and test its dependence on viscosity. In Fig. 79, we do so for volumes of 1 and 2μL, and we see that U_{cr} increases with decreasing viscosities. More specifically, there is an inverse proportionality represented by the black lines which are fits with a -1 slope, revealing that $\eta_1 U_{Cr}$ is a constant. This confirms that the captures indeed have a viscous origin. The viscosities of the drop $\eta = 1$mPa-s and the infusion of the bottom surface $\eta_2 = 9$mPa-s, being significantly lower than that at the top, at least by factor of 10,

the viscous dissipation in the infused oil of the top surface is what dominates.

Nevertheless, we must be careful here as such an inference would not hold for U_D (black dotted line in Fig. 78 or in the entire zone of overlap where we see both captures and depositions happening for different trials. This seems to be strongly indicative of the fact that the pulling speed is perhaps is not the correct variable here to understand the transition from deposition to capture, as the dependence of the transition with the pulling speed seems to be quite fragile.

Perhaps, a better variable to understand the transition is the aspect ratio λ_c of the drop where the transition happens, as originally observed by Plateau. This would be more true for cases where gravity is not important, that is for $\Omega < 6\mu L$, and in a regime where inertia is also removed, which would be satisfied as long as our pulling speeds as less than $\sqrt{gR}$, which is of the order of 10cm/s - a condition naturally satisfied in our experiments. Thus the question becomes rather of the stability of the drop, dictated directly by its geometry - which also reminds us of a point we made at the end of the Section 6.1: the viscous tweezer is essentially a Plateau cylinder with its classical constraint of pinned contact line removed. Indeed, despite the ambiguity in the critical velocity of capture, what we have observed to be true through the hundreds of experiments performed is that the contact lines at the top and the bottom both were always free to move.

6.4 TWEEZERS AS PLATEAU CYLINDERS

We now shift our gaze to the stability of a drop placed between two infused surfaces, as its length is increased.

Plateau's original problem constituted a cylinder of equal radii. In our case, however the radii R_1 and R_2 are different and free to move, two steps away from Plateau. So, we look for a problem that is between Plateau and our problem - the stability of truncated cone - in other words, a capillary bridge of unequal radii but pinned contact lines, which was analyzed by Jose Meseguer theoretically in 1983.

We first define a mean radius is defined as $R = (R_1 + R_2)/2$ which would be used for the determination of λ as $L/2R$, at the point of break-up. Note that λ captures the extension of the drop. Next, we define a variable that captures the asymmetry of the drop as $H = (1 - w^2)/(1 + w^2)$, where $w = R_1/R_2$. The elegance of this variable is that it is an even function of R_1/R_2 and always lies within -1 and 1, where $H = 0$ corresponds to a liquid cylinder, $H = 1$ and $H = -1$ correspond to an upright and upside down cone. Performing a stability analysis on a capillary bridge with unequal radii, Meseguer showed that the drop becomes unstable when

$$\lambda_c = \pi\left(1 - (3/2)^{4/3}(H/2\pi)^{2/3}\right). \tag{65}$$

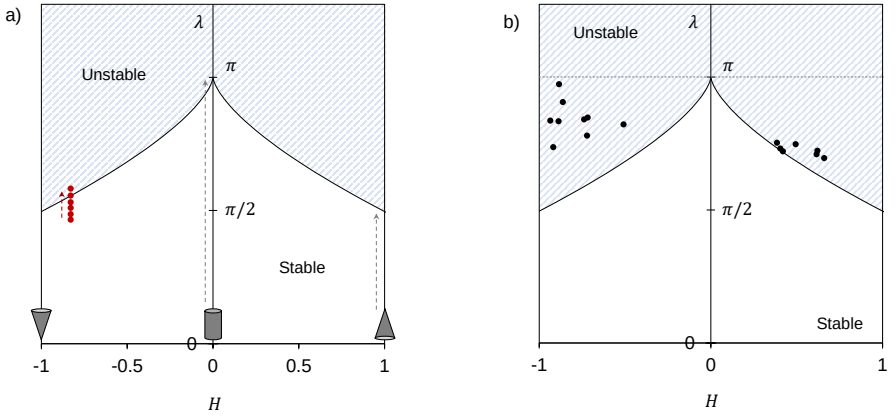

Figure 80: **Plateau Instability.** a) A Plateau-Meseguer phase space where λ is plotted against H. Any capillary bridge with fixed contact lines when extended starts from a fixed value of H and moves vertically as shown by dotted lines until they cross the solid black line and become unstable. Black lines are a solution to Equation 65. $H = 0$ is the classical solution for a liquid cylinder as given by Plateau which shows $\lambda_c = \pi$. The two other limits correspond to $H = 1$ and $H = -1$ which denote a cone and an inverted cone respectively. Red dotted line corresponds to an experiment performed with a 2µL capillary bridge with pinned contact lines and $H = -0.83$. When extended, it started with its initial value of $\lambda_0 = 1.4$ and moved along fixed the fixed value of $H = -0.83$, denoted by the red dotted line and because unstable and broke right after crossing the black line. The blue striped region is unstable, where bridge breaks into two drops, whereas the white region below is where the bridges are stable. b) λ_c plotted against H for experiments done with volumes $\Omega = 1\mu L$, $2\mu L$, $4\mu L$ and $6\mu L$ with the two infused surfaces at the top and bottom having viscosities with $\eta_1 = 9710$mPa-s and $\eta_2 = 9$mPa-s. The velocities are different for each volume to see the switch between capture and deposit. For instance, the data points corresponding to $\Omega = 2\mu L$ are for speeds $U = 20\mu m/s$ (deposition), $U = 50\mu m/s$ (capture) and $U = 100\mu m/s$ (capture).

There are quite a few remarks to be made about this variable. First, Equation 65 shows that λ_c is an even function of H, as seen in Figure 80. We note that when $H = 0$, we recover from Meseguer's criterion the classical solution for a liquid cylinder as given by Plateau, that is $\lambda_c = \pi$. Equation 65 also shows that in the limiting case of a cone, where one of the radii tends to zero, λ_c approaches $\pi/2$, thus revealing that $\pi/2 < \lambda_c < \pi$. These two bounds may be physically understood in the following way - while for a cylinder or equal radii, the two ends can hold one wavelength, leading to the aspect ratio of π at the point of instability, for the case of unequal radii, only a smaller proportion of the wavelength can be contained, which is fixed by the magnitude of the two radii. Also, the pinch-off point in the case of equal radii happens at the mid-point of the length of the liquid column, whereas for unequal radii, the pinch-off point is pushed further and further towards the smaller radius. In the limiting case of a cone, the pinch-off point goes to the end which has the tip of the cone, that intuitively means it can contain only one half of the wavelength, making the aspect ratio $\pi/2$.

In Figure 80a, we plot λ versus H to create a phase map of stable and unstable capillary bridges. We first show that in a $\lambda - H$ phase space, any capillary bridge with fixed contact lines when extended starts moves vertically at a constant H as shown by dotted lines until they cross the solid black line which is a solution to Equation 65, which also divides the phase space into stable and unstable bridges (blue stripes). The red dotted line corresponds to an experiment performed with a 2µL capillary bridge with pinned contact lines $R_1 = 633\mu m$ and $R_2 = 193\mu m$, which gives $H = -0.83$. When extended, it started with its initial value of $\lambda_0 = 1.4$ and moved along fixed the fixed value of $H = -0.83$, denoted by the red dotted line and because unstable and broke right after crossing the black line.

Our experiments in this section deal with drops of volumes volumes $\Omega = 1\mu L$, $2\mu L$, $4\mu L$ and $6\mu L$ (such that $Bo < 1$), bounded by surfaces infused with $\eta_1 = 9710$mPa-s and $\eta_2 = 9$mPa-s, and pulled at different speeds until detachment. We can now extract the L, R_1 and R_2 from the last frame before pinch-off and determine the corresponding λ_c and H and plot them against each other for experiments with different volumes (less than $6\mu L$) and at different speeds. Fig. 80b) shows the plot of λ_c vs H with the black solid line corresponding to Equation 65. The shaded region shows the unstable region which is above the theoretical prediction of stability.

We immediately observe all our data points, irrespective of the nature of the break-up: capture or deposition, are in the unstable regime as predicted by the Plateau-Meseguer line: they are below the value of π, which is for a perfect Plateau cylinder and above the stability line for a liquid cylinder with unequal but pinned contact line radii. This is not trivial because morphologically we are far from a cylin-

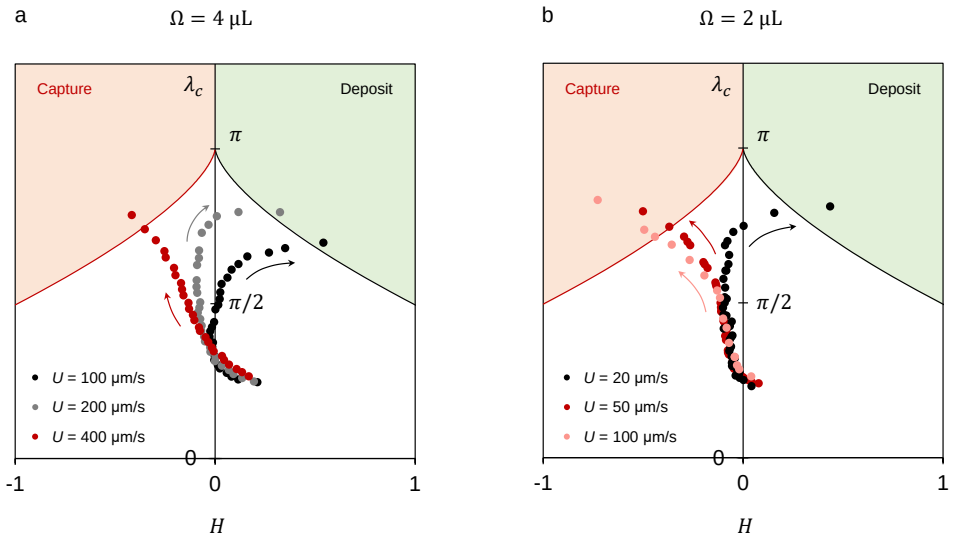

Figure 81: **Plateau-Meseguer Maps.** $\lambda - H$ evolution for experiments done with two drop volumes: $\Omega = 4\mu L$ (a) and $\Omega = 4\mu L$. In both cases, the drops are bounded by surfaces infused with $\eta_1 = 9710$mPa-s and $\eta_2 = 9$mPa-s, and pulled at different velocities. Black and grey circles denote trajectories that lead to a capture, while red and pink circles represent trajectories leading to a capture. Orange and green shaded regions correspond to capture and deposition, bounded by the black and red solid lines which are a solution to Equation 65.

der and far from a cone, yet the stability can be captured by Equation 65. The data points corresponding to deposition (H¿0) are closer to the Plateau-Meseguer line, which means that the critical length at which the drop becomes unstable is indeed close to the length at which pinch-off happens, where we did our measurements. Conversely, for the capture cases the data points are further from the Plateau-Meseguer line, denoting the drop became unstable at a length before the pinch-off occurred.

This can be further investigated as the phase space of $\lambda - H$ can be used to see the entire evolution of the drop shape, where both λ and H are free to evolve, unlike the case of a liquid cylinder with pinned contact lines, where the value of H is fixed. We can analyze such Plateau-Meseguer Maps for different velocities to see precisely where the instability sets in.

In Figure 81a, we plot show the entire evolution of $\lambda - H$ during the course of a pulling experiment, where the volume is fixed at $\Omega = 4\mu L$, the viscosities of infusion are $\eta_1 = 9710$mPa-s and $\eta_2 = 9$mPa-s. We plot the trajectories corresponding to three different speeds of $U = 100\mu m/s$ (black circles), $U = 200\mu m/s$ (gray circles) and $U = 400\mu m/s$ (red circles), where the first two lead to eventual depositions, whereas the last one is a capture.

All the trajectories begin with a positive value of H, indicating R_1 is slightly smaller than R_2 and a typical starting value of $\lambda_0 = 0.7 - 0.8$ - close to the aspect ratio one obtains when a hemisphere transforms to a cylinder preserving the volume and height: $(3/8)^{1/2}$. As the pulling begins, we see all the trajectories falling on the same curve initially where λ increases due to elongation and H decreases and becomes slightly negative - this is the initial re-organization regime, we had previously noted. Following this, we see that for the two trajectories corresponding to deposition λ increases with a fixed H, whose absolute value is less than 0.1, implying R_2 is smaller than R_1, but the difference is less than 10%. In this regard the trajectory corresponding to the maximum velocity, $U = 200\mu m/s$ is more spectacular - the climb at constant H continues for $\lambda_c \approx 2.4$, when it sharply turns to the right into the deposition regime. For a lower speed $U = 100\mu m/s$, the climb is of a smaller height, but the general nature of the trajectory is the same. However, for a higher speed $U = 400\mu/s$ (red circles), we see a marked difference - the 'climb' never happens: following the initial re-organization, the trajectory monotonously moves towards a lower and lower value of H and finally into the 'capture' zone. Said differently, $d\lambda/dH$ is never greater than zero. Furthermore, the trajectory corresponding to $U = 400\mu m/s$ leaves the others at a value of $lambda$ less than $\pi/2$.

For $\Omega = 2\mu L$, as in Figure 81b, we plot trajectories for $U = 20\mu/s$ (black circles, deposition), $U = 50\mu m/s$ (red circles, capture) and $U = 100\mu m/s$ (pink circles, capture). Here, too observe the same features manifest again: a) corresponding to the maximum velocity for deposition, there is a 'climb' with constant H, which turns at a λ close to 2.4, as seen in experiments with the previous volume and b) for the trajectories corresponding to capture, general deviations from the deposition curves start happening before $\lambda = \pi/2$, and $d\lambda/dH < 0$.

To summarize, the most important conclusion we draw from this section is that

a) When a liquid cylinder is pulled in such a way that its contact lines are free to move, the drop self-selects two contact line radii at the point of instability which follows the same solution as a drop with unequal but pinned contact lines - in this regard, the drops are still Plateau cylinders.

b) There exists a $\lambda_{turning}$ for all the deposition cases, which corresponds to the value of λ at which the $\lambda - H$ curve first starts moving away from the from the vertical 'climb' into the first quadrant (said differently, where $d\lambda/dH \geqslant 0$), and $\lambda_{turning}$ peaks for the maximum velocity of pulling corresponding to deposition.

What we must ask now is if this $\lambda_{turning}$ depends on what the initial value of the aspect ratio, λ_0 was when the experiment was started. In other words, we wish to know if the initial values of L, R_1

and R_2 influence the transition, not in terms of the velocity of capture, but in terms of the $\lambda_{turning}$.

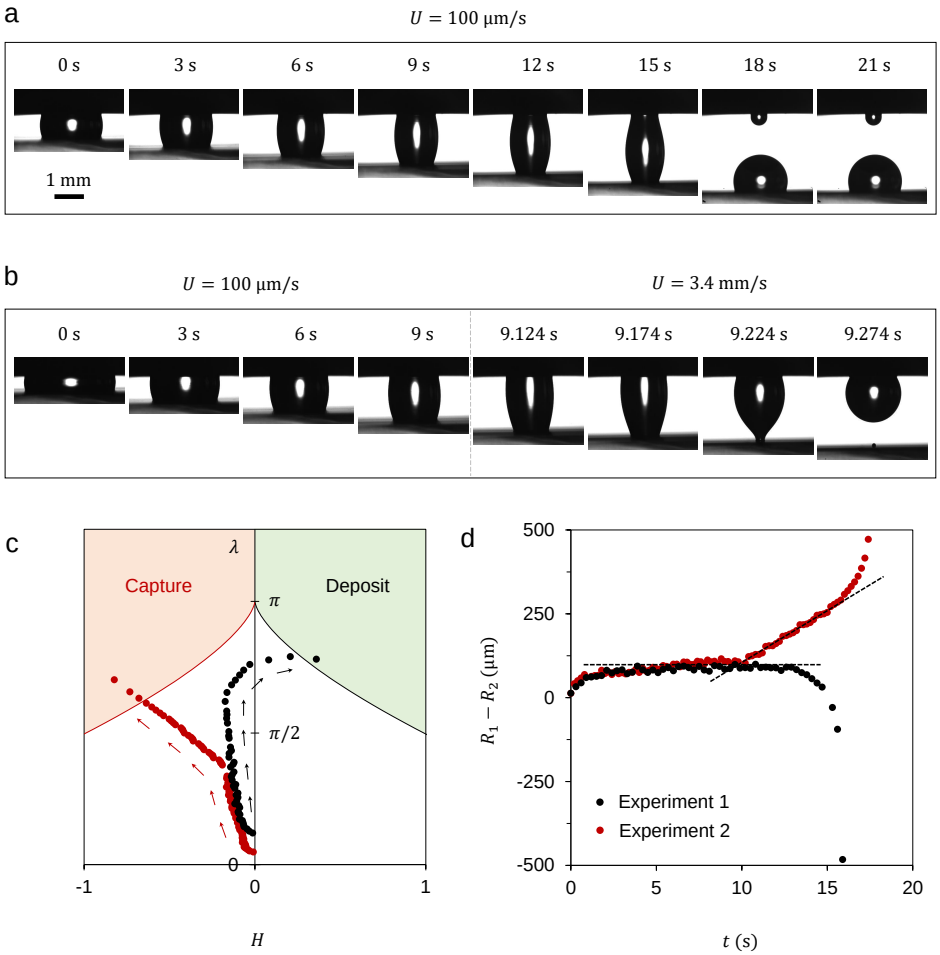

Figure 82: **Compression Test.** a) Snapshots of a drop of $\Omega = 4\mu L$ between two infused surfaces, with $\eta_1 = 9710$mPa-s and $\eta_2 = 9$mPa-s, when pulled at $U = 100\mu m/s$. b) The snapshots of another experiment with same drop and surfaces, initially pulled at $U = 100\mu m/s$ and suddenly changed to $U = 3.3$mm/s. c) $\lambda - H$ plot of the two experiments. d) $R_1 - R_2$ plotted against time for the two experiments. The flat dotted line represents constancy in time and the other dotted line represents a linearity in time: a constant $V2 - V_1$ regime.

Fig. 82 shows such an experiment where a $\Omega = 4\mu L$ drop is compressed initially to $\lambda_0 = 0.35$, half the value at which previous experiments were done, and then the bottom plate was pulled at $U = 100\mu m/s$ - a speed at which we have seen deposition previously. When we look at the $\lambda - H$ plot of this experiment (black circles in Fig 82d), we see that the curve has a 'climb' identical to the previous experiments that started at a higher value of λ_0 and led to deposition. When we repeat the experiment with an even lower starting value, $\lambda_0 = 0.15$, we see the trajectory again following the 'climb'

in a manner that is indistinguishable from the former curve When we suddenly change the velocity at $\lambda = 1.2$ from $U = 100\mu m/s$ to $U = 3.3m/s$, we see that the $\lambda - H$ curve immediately leaves the vertical 'climb' and starts becoming increasingly asymmetric with the magnitude of H increasing and eventually goes into the 'capture' regime.

The difference between the capture and deposition cases becomes particularly distinct when we plot $R_1 - R_2$ against t for the two experiments, black circles representing a deposition and red circles a capture. The first experiment which led to the deposition has an entire middle regime where $R_1 - R_2$ is constant in time, shown by the dotted black line, implying $V_1 = V_2$ and this is the 'climb'. For the second experiment, we see that as long as the velocity is $U = 100\mu m/s$, $R_1 - R_2$ is not only constant in time, its value is the same as that of the previous experiment, where the starting values of R_1 and R_2 were smaller. However, when the pulling speed is suddenly increased to $U = 3.3mm/s$, a new regime kicks in where $R_1 - R_2$ evolves linearly in time. In fact, a close attention to Fig. 82b reveals that the top contact line on the more viscous surface has stopped moving in this regime, that is $V_1 \approx 0$; only R_2 decreases in time linearly until the pinch-off regime sets in.

This helps establish the important conclusion that there exists a peak value of $\lambda_{turning}$, which is $\lambda^* \approx 2.4$, where the transition happens, and this peak value is independent of λ_0. Furthermore, as seen in Figure 81a, for a fixed λ_0, $\lambda_{turning}$ increases with U, for deposition cases, but for fixed U, $\lambda_{turning}$ increases with decreasing λ_0, as seen in Figure 82.

This implies that a better method to study the transition would be at a value of λ_0 which is in the vicinity of λ^*, and then do experiments at different U to determine the critical velocity of the transition from deposition to capture, U_{cr} for a fixed η_1. This would remove any dependency of λ_0, which in experiments previously done were not accounted for, possibly creating the large dispersion in the critical velocity. However, that remains as the future scope of this work.

6.5 CONCLUSION

The most important conclusion of the viscous tweezer experiments is to demonstrate that liquid-infused surfaces which are celebrated for their slipperiness, can be 'sticky' as well. A water drop placed between two infused surfaces, the top one being more viscous, when separated can lead to a capture or deposition of the drop. Such a transition is not triggered by the contrasting wettabilities, which is the same for both the surfaces, rather the contrasting viscosities.

Defining a critical pulling speed corresponding to a capture proved to be difficult as there exists a large range of pulling speeds where

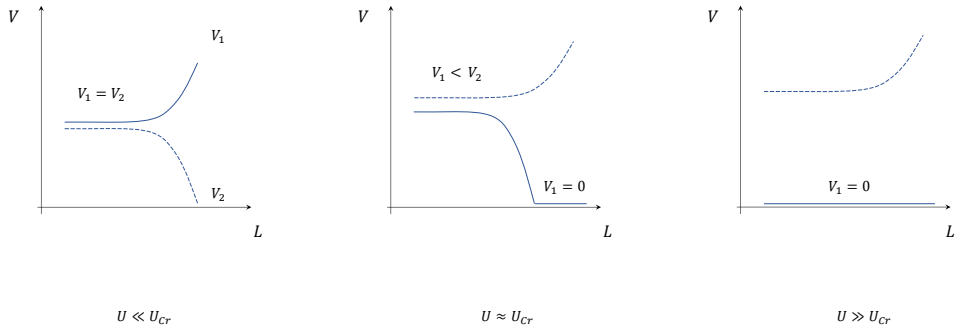

Figure 83: **Regimes.** Schematic sketches of V_1 and V_2 behave in the three regimes of the experiment: $U \ll U_{cr}$, $U \sim U_{cr}$ and $U \gg U_{cr}$

both captures and depositions were observed. Nevertheless, the characteristics of the drop dynamics corresponding to capture and deposition have been identified, as shown in Fig83, where for $U \ll U_{cr}$, there exists a regime where both the top and the bottom contact line recede at constant speeds. Conversely, when $U \gg U_{cr}$, the contact line does not move - exhibits a kind of 'viscous arrest'. The physics of this 'viscous arrest' have to be further investigated.

Although the relationship of 'capture' and 'deposition' has been difficult to establish with the pulling speeds, the stability of the drop - which includes both capture and deposition cases could be explained by the Plateau instability for drops with unequal radii. In this regard, necessary conditions for capture and depositions can be written in terms λ and H as:

- Capture corresponds to a case where there exists no λ corresponding to which $d\lambda/dH \geqslant 0$.

- Deposition corresponds to a case, where there exists some λ for which $d\lambda/dH \geqslant 0$.

For the case of deposition, the first value of λ where $dH/d\lambda \geqslant 0$, is called $\lambda_{turning}$, the maximum value of which corresponds to the maximum velocity where a deposition is observed, and comes out to be 2.4. This is where we believe the dynamics comes in. Previous criteria based on $d\lambda/dH$ do not have any dynamics in them, which sets in only at $\lambda_{turning}$. Experiments for velocity transitions need to be performed at $\lambda_0 = \lambda_{turning}$ to shed light to this hypothesis.

Finally, we conclude with a general guideline for viscous tweezers with water droplets from $2 - 6\mu L$: a deposition is always ensured for $U < 10\mu m/s$ and a capture is always ensured if $U \gtrsim 1000\mu m/s$. Further work remains to be done to make a model for the 'viscous arrest' - to predict the transition between the capture and deposition.

Part IV

FRICTION

7

SPHERICAL ANTS

As a first step towards understanding ants walking on the pitcher plant *Nepenthes*, we study in this descriptive chapter the friction on a sphere rolling down a liquid-infused solid. We identify three distinct regimes of motion - *sticking*, *rolling* and *bouncing* - determined by the existence of a symmetric meniscus, a *tail* or asymmetric meniscus and the breaking of the *tail*. Based on experimental observations, we propose that contrary to the general conception, ants on the pitcher plants do not appear to necessarily slip and fall; rather they struggle to un-stick themselves from the viscous nectar-infused peristome and fall in the process.[1].

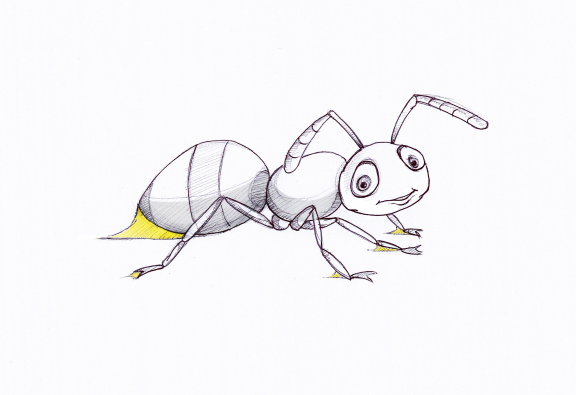

'I heard there was food, but they gave me a tail!' by Benoît Pype

1 The original conception of *rolling spherical beads* comes from Armelle Keiser.

7.1 NEPENTHES AND THE ANT

7.1.1 *The Rainmaker*

Figure 84: **The Nepenthes** Left: *L'histoire de la Grande Isle Madagascar* by Étienne de Flacourt, where we find the first record of the *Nepenthes* dating back to 1658. Right: Depictions o flora of Madagascar in the book which also describe report pitcher plants, which Étienne de Flacourt believed contained 'a good half-glass' of rain-water. [120, 121]

In 1658, French colonial governor Étienne de Flacourt published what would be the first record of a pitcher plant in his book *L'histoire de la Grande Isle Madagascar*, where he describes the flora and fauna of Madagascar in great detail [120].

In the section on the *Nepenthes*, he narrates that the people of the island of Madagascar believed that if one were to pick up the 'flower' of the pitcher plant, that is the pitcher itself, then rain was inevitable. He writes [120]

> *I and all the other Frenchmen*
> *did pick them, but it did not rain.*
> *After rain these flowers are full of water,*
> *each one containing a good half-glass.*

Nepenthes has also been called monkey-cups because of the belief that monkeys drink from the pitcher of pitcher plants. This, also, is not true.

We have come a long way since, not only in the context of *Nepenthes* not being rain-makers, but also in identifying the real specialty of *Nepenthes* - its carnivorous nature. Etienne Flacourt's argument that the pitcher contains rain water is only partially true. It is primarily digestive juices mixed with rain-water, where ants and other insects that fall into the pitcher are digested.

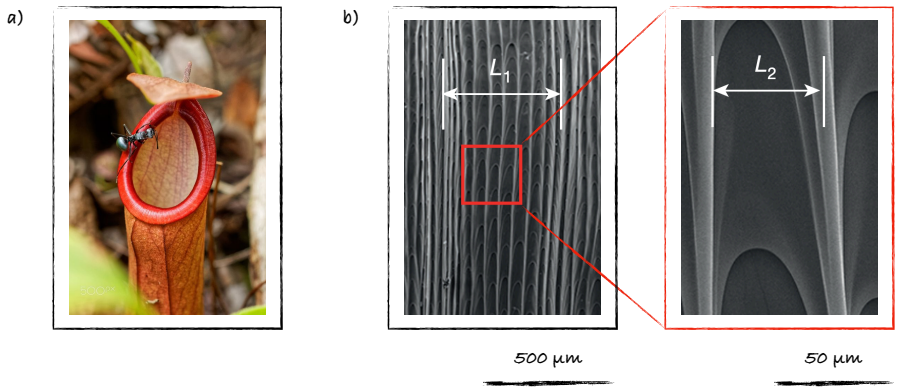

Figure 85: **Pitcher Plant.** a) A pitcher plant with a black ant on its peristome (Picture by Ray Reinhard) [35]. b) and c) Close-up reveals there are hierarchical grooves on the surface with the smaller scale grooves at a distance of 50 µm distance between each other. Reproduced from [122]

In the subsequent section, we describe how the *Nepenthes* captures ants using its specialized slippery peristome.

7.1.2 *The Ant-killer*

The peristome or rim of the pitcher plant is decorated with grooves, which are infused with a nectar-water mixture. Figure 85 shows a close-up of the grooves on the peristome, where we can see the two scales of grooves: the bigger scale is a set of grooves half a millimeter wide and high and the smaller hierarchical scale is a set of grooves that are 50 µm in height and spacing.

The generally perception or hypothesis regarding the ant-capturing mechanism is that the grooves are rendered slippery by the mixture of nectar and water, which fill the grooves. A typical ant senses the nectar and climbs up the peristome from outside, but as it tries to probe the inside of the pitcher, it falls off the precipice of the peristome into the digestive juices of the pitcher. The hypothesis here is that the peristome is slippery which makes *the ant slip and fall*.

In Figure 86, we provide two instances of ants being captured by the pitcher plant - one, where the ant tries to climb down the inside of the peristome into the pitcher, and the other where the ant has fallen off and is trying to climb up the inside of the peristome. In both cases, we see the ant's legs eventually lose contact with the nectar-infused peristome and falls.

However, we wish to point out here that there is no strong evidence from the images based on which we can say that ants on the *Nepenthes* necessarily 'slip and fall'. The ants typically fall off the rim where the slope is practically vertical, which reveals the significant

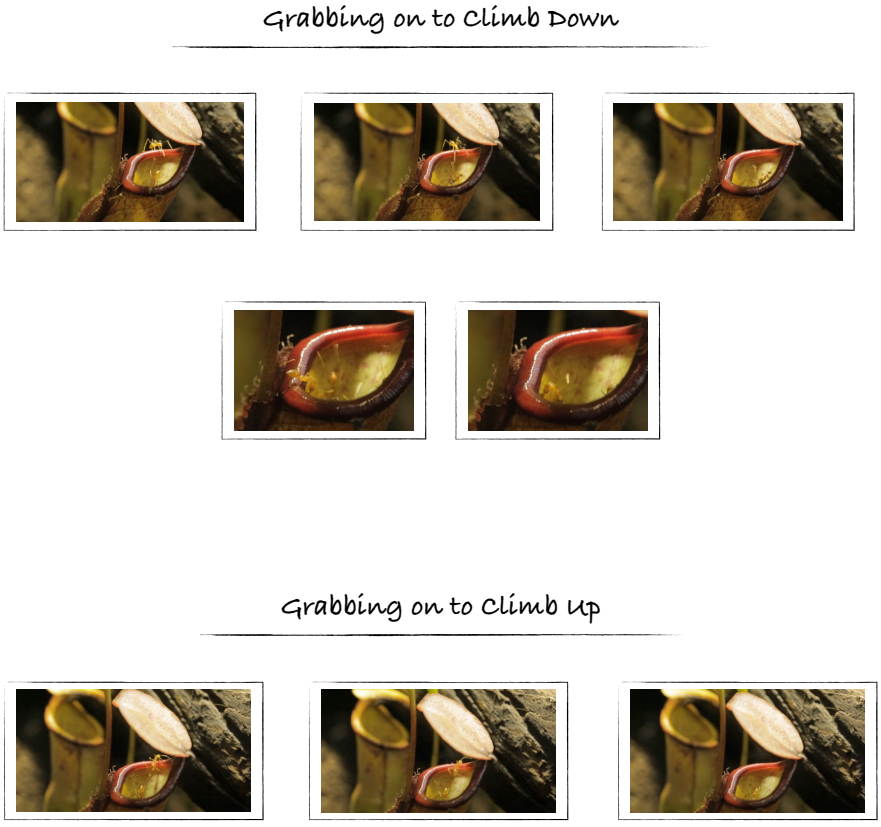

Figure 86: **Two kinds of fall.** Top: Two instances of a yellow ant *Anoplolepis gracillipes* standing on the peristome, trying to climb down to probe the inside of the pitcher, and falling down in the process. Down: A yellow ant *Anoplolepis gracillipes*, that previously fell off the precipice of the inside of the peristome, tries to climb up but eventually falls. [36]

adhesion that prevents ants from sliding off the rim at smaller slopes. This also might seem in apparent opposition to our previously emboldened statement of infused surfaces having negligible adhesion. All of this needs elucidation, or in other words, we must ask what is the mechanism of ants falling off the peristome of the *Nepenthes* into its pitcher.

The postulate of 'slipperiness' of the peristome of the *Nepenthes* as presented in [37] was utilized to essentially extend this argument to droplets sliding off infused surfaces. While the analogy serves to highlight the 'slipperiness' of infused surfaces, there is a critical difference between the two cases, the former being that of solid friction and adhesion on infused surfaces, whereas the latter corresponds to lateral adhesion and friction of liquid drops on infused solids. While an infused solid may have negligible lateral adhesion for water drops, its lateral adhesion for solids may be significantly high, to the point that it might not be 'slippery' at all.

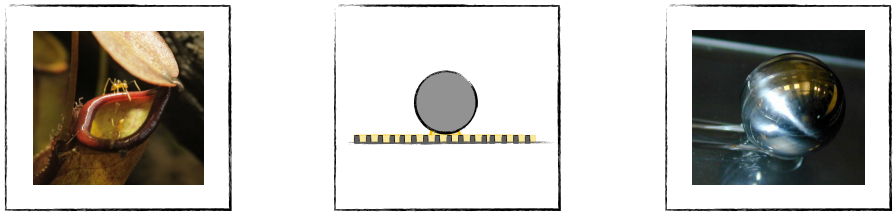

Figure 87: **Sperical Ants to Rolling Stones.** Left to right: An ant on the peristome of the *Nepenthes*, about to fall, a sketch of a sphere on an infused solid with a meniscus at the bottom and a sphere rolling down a flat solid with a thin film on it, also known as the *Rolling Stones* problem [123].

To this end, as a first approach to understand the mechanism of ants falling off the peristome of the *Nepenthes*, we study the friction of solid spheres on infused solids which mimick the peristome of the *Nepenthes*. In this sense, we may say that while ants are not water drops, they perhaps can be approximated as spheres, at least for the region of contact of the legs with the infused solids. This immediately becomes reminiscent of an older problem known as *Rolling Stones* by José Bico and others, where a solid sphere is rolled down a flat solid which has a thin film of oil on it [123]. A natural question might be that if we are willing to approximate ants as spheres, then why not approximate the nectar-infused peristome as solid with a thin film on it as in the *Rolling Stones* problem. In other words, is the half solid, half liquid nature of an infused solid necessary in making a first model of how ants walk on peristome. The answer is yes, and in fact that is what makes all the difference - in the subsequent section we elaborate on this.

The Rolling Stones problem has been notoriously difficult to model in the literature. Although experimental data gives empirical laws, but the complexity of the flow in the meniscus has eluded modelling by the most brilliant minds.

Figure 87 shows the three problems of ants walking on *Nepenthes*, spheres rolling on infused solids and spheres rolling down solids covered with a thin film, our claim being the first problem can be reduced to the second, but not the third.

7.2 THE PHYSICAL EXPERIMENTS

In accordance with the morphology of a typical peristome of a pitcher plant, we fabricate 50 μm high SU-8 pillars on a silicone wafer[2], where the grooves are also separated by a 50 μm distance. The textured surface is glaco-treated and infused with silicone oil. A polystyrene bead of diameter 3.2 mm and weight 23 mg is used for experiments.

Typical nectar-water mixtures are $\sim 10 - 100$ *mPa-s*

2 Courtesy: Armelle Keiser.

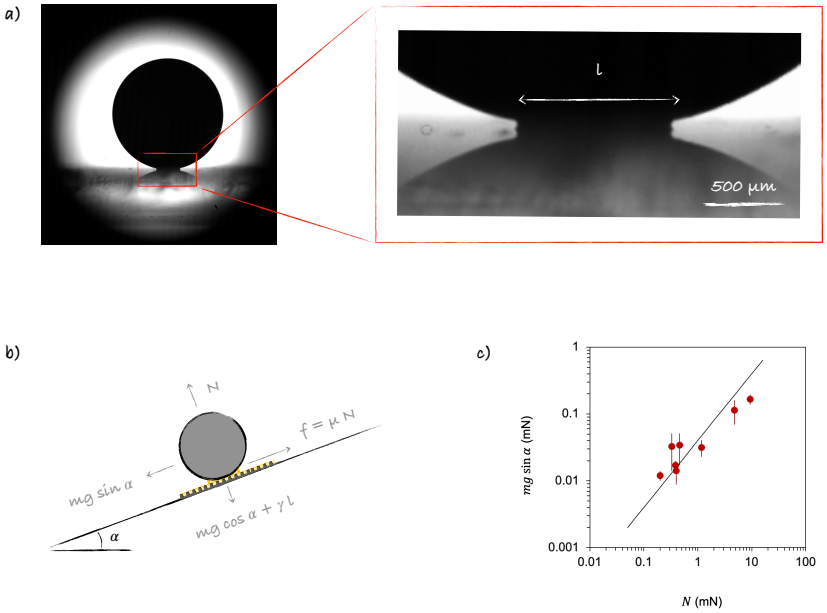

Figure 88: **The Foot of the Spherical Ant.** a) A polystyrene bead placed on an infused solid, develops a meniscus at the point of contact. Inset shows the meniscus in better detail. The diameter of this meniscus is l. b) Sketch of a sphere on an infused solid, inclined at an angle α, with all the forces acting upon the sphere shown in gray arrows. l is the diameter of the annular ring of a meniscus that the sphere develops. c) $mg \sin \alpha$ plotted against normal force N for spheres of different materials and sizes. The black solid line follows Equation 67 with $\mu = 0.04$.

7.2.1 *Lateral Adhesion*

We start with the solid infused with $\eta = 9$ mPa-s and place the polystyrene bead on it. The bead touches the infused solid and draws up a symmetrical meniscus around its region of contact at the bottom (see Figure 88). We now tilt the infused solid with the bead on top of it by an angle $\alpha = 5°$ with the horizontal. We observe that the bead remains stuck at the top of it just as before, without any change whatsoever. This already shows that the lateral adhesion of infused solids to other solids as polystyrene is non-negligible and higher than it is for water drops.

This experiment was performed with the wonderful prépa student Marc-Antoine Ourradour

We keep increasing the angle of inclination until the bead rolls off. For polystyrene bead, the roll-off angle was typically around 8°. There are two possibilities for generating adhesion in this system - one, the solid sphere itself has asperities and thus the silicone oil would have some hysteresis on it. Second, the infused solid itself being a half-solid, the contact between the sphere and the solid part of the infused solid may give rise to Coulombic friction between the

two. In order to simplify the problem as well as to remove hysteritic problems, we glaco-treat the sphere and also run it down the infused surface a few times so that it has a precursor layer of oil on it, and then perform the roll-off experiment.

Having minimized hysteresis of the sphere, the major contributor of the adhesion should be the Coulombic friction. If this be true, then a plot of the driving force $mg \sin \alpha$ against the normal force N should reveal a constant friction coefficient μ, typically less than 0.1. Indeed we obtain a friction co-efficient $\mu \approx 0.04$, when we make the said plot in Figure 88. The experiments correspond to spheres of different sizes (radius ranges between 0.7 mm and 3.5 mm) and different materials - aluminum, brass, copper, chrome steel and polystyrene. Although it is true that different materials have different μ, we see that the Coulombic friction approach captures all of the data fairly well, perhaps because Glaco on all surfaces makes them similar in nature.

We briefly discuss the model and the normal force here. The forces acting on the sphere are $mg \sin \alpha$ down the incline, a friction force f up the incline, $mg \cos \alpha$ perpendicular to the incline (downwards), a normal reaction force N perpendicular to the incline (upwards) and a force $F_c \sim \gamma l$ exerted by the capillary bridge or meniscus which is perpendicular to the incline (downwards). The equilibrium perpendicular to the incline gives us

$$N \sim mg \cos \alpha + \gamma l \tag{66}$$

If the coeffecient of friction be μ, then we can write $f = \mu N$ and substituting this for the equilibrium along to the incline, we get

$$mg \sin \alpha \sim \mu(mg \cos \alpha + \gamma l) \tag{67}$$

The above equation fits the data in Figure 88 for $\mu = 0.04$.

The simple adhesion test of the infused solid reveals important differences in the behavior of solids and liquids on infused solids. While water drops on infused solids roll off at angles that are immeasurable, even a 7° tilt may not be able to roll off a polysterene sphere on the same infused solid. In fact, the adhesion force exerted by infused solids on solid spheres is typically 1/10—th of the weight of the sphere, which is substantially higher than lateral adhesion for water (near-zero). Furthermore, the adhesion force of the solid sphere on an infused solid is also higher than what the sphere would experience on a 'bare' solid - a polystyrene bead on a silicone wafer starts to roll off before 3°, but on an infused solid can go up to 7°. This is because of the existence of the meniscus, which pulls the sphere with an extra force γl, than increases the normal reaction and consequently the friction force, or lateral adhesion force (as velocity is zero here).

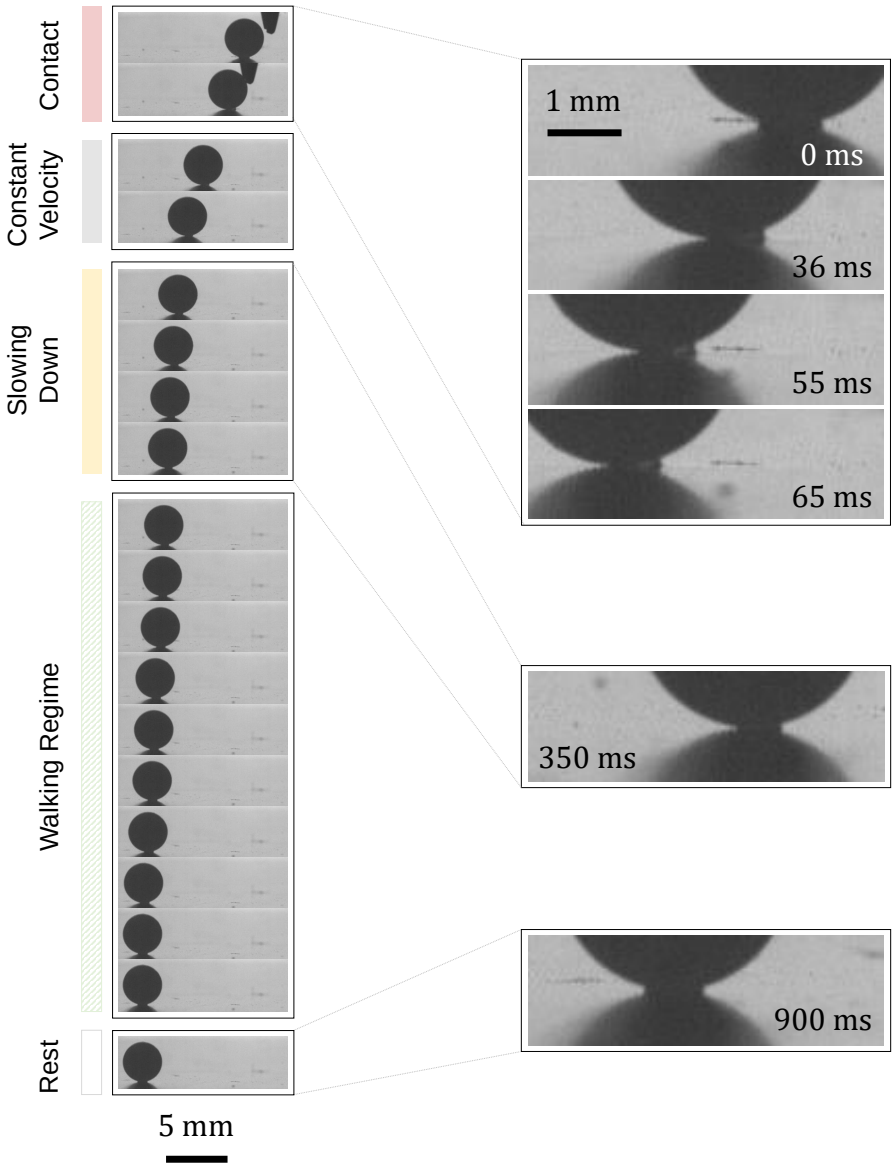

Figure 89: **Appearance and Disappearance of the Tail** A polystyrene bead of 3.2 mm diameter placed on a micro-grooved surface infused with silicone oil of $\eta = 9$ mPa-s. The bead is kicked with a stick and on the left we see a chronophotography of the sphere move and slow down and come to rest. Insets show the deformation of the meniscus as it transitions from symmetric to asymmetric to symmetric again.

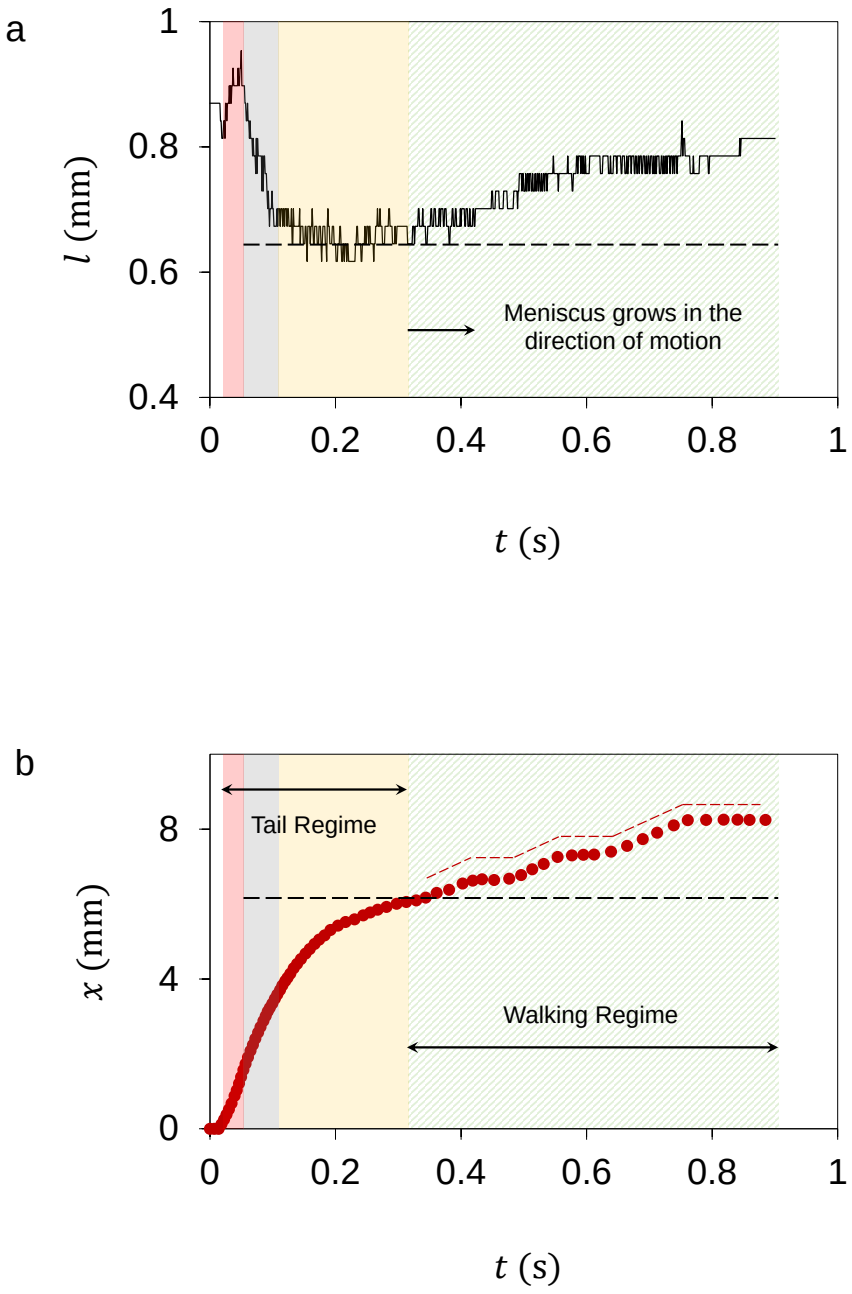

Figure 90: **Dynamical Regimes.** a) Size of the meniscus (end to end) as a function of time. The dashed black line corresponds to the minimum meniscus size. b) Distance traversed by the sphere, x with respect to time. The dashed black line in b) corresponds to the distance where the sphere would have come to stop, had the walking regime not initiated. The color codes red, gray, yellow and green denote the contact regime, constant velocity regime, the slowing down regime and the walking regime, respectively.

7.2.2 *The Kick*

From the last section, we see that the spherical ant, without even moving, has started to 'feel' that the infused solid is not slippery, rather sticky. To test how sticky it is in the 'stuck' phase, that is when the inclination is low enough, we perform another simple test. At an inclination angle where the bead is stuck ($\alpha = 5°$), we give the bead a 'kick' with a stick and see what happens. For instance, it is possible that the sphere has high lateral adhesion but low dynamical friction, in which case once it has been kicked to overcome the adhesion barrier, the sphere would just keep rolling.

However, we see that the sphere after the 'kick' has been imparted, starts to roll, then gradually slows down and eventually comes to rest. This is also accompanied with a deformation of the meniscus (symmetrical) into a 'tail' (asymmetric) which eventually transforms back into its original state of symmetric meniscus as it comes to rest.

In Figure 90 we provide a chronophotography of the rolling sphere, color-coded with the dynamical regimes that emerge, and in Figure 90 we see how the size l of the meniscus evolves with time in a) and the displacement versus time plot of the sphere in b). We now discuss these two figures together in tandem with the description of the five regimes. These are as follows:

- **Contact.** The stick contacts the sphere and remains in contact for 65 ms, during which the sphere moves forward at a speed of ≈ 1 mm/s and the meniscus shifts in the direction opposite to the direction of motion, forming a clear 'tail'. The end to end size of the meniscus is l, originally close to 0.8 mm, it increases by 0.1 mm during the duration of contact, which is the size of the 'tail'.

- **Constant Velocity.** Right after losing contact, the sphere starts rolling at a constant speed briefly for 0.4 ms. In this duration, the 'tail' size decreases from 0.9 mm to 0.7 mm, although dx/dt is constant. The tail has now become shorter.

- **Slowing Down.** The tail keeps a constant size for almost 0.3 s, during which the velocity of the sphere decreases to near-zero, as if the sphere is about to come to rest with the tail at one side.

- **Walking Regime.** The walking regime begins when the meniscus starts growing back in the direction of motion of the sphere, and the sphere rolls and moves with pauses and rotations in between. The growth the meniscus length is continuous whereas the translation of the sphere is step-like (Figure 90). This is because the silicone oil wicks through the bottom contact of the sphere and the top of the grooves to reach the next set of grooves to form a meniscus. In the process, the sphere translates slowly

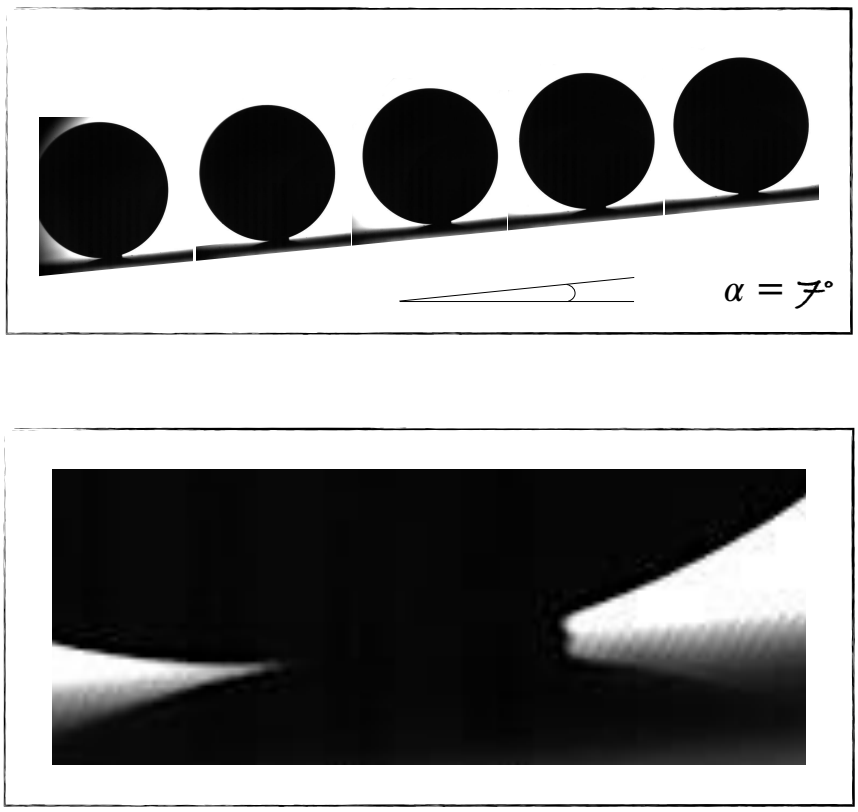

Figure 91: **Dragging the Tail.** A polystyrene bead of 4 mm radius on textured surface infused with silicone oil of viscosity $\eta = 9\,\text{mPa-s}$. The bead starts to roll when α is beyond the critical angle. Inset reveals that when the sphere rolls, there is a tiny tail, which it drags as it moves

groove by groove, until the meniscus has grown enough to be perfectly symmetric on both sides as it is in the very beginning of the experiment. It then comes to rest.

One inference we draw from the above results is that even if the ball is 'kicked' to overcome the the lateral adhesion, or de-pinned, the friction of the system is high enough to bring it back to rest. This further highlights the stickiness of the infused solid to the solid sphere.

7.3 ROLLING AND BOUNCING

We now go back to the roll-off experiments but for inclination angles larger than the roll-off angle, which for polystyrene beads corresponds to $\alpha_c = 7°$. For infused solids, with $\eta = 9\,\text{mPa-s}$, at $\alpha > \alpha_c$, the bead started rolling with a tail and did not reach terminal velocity within the dimension of the infused solid $\sim 10\text{cm}$, which also

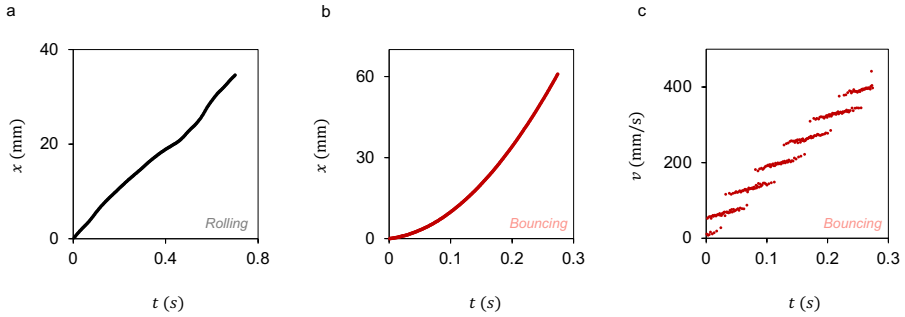

Figure 92: **Rolling and Bouncing.** A polystyrene bead of 23 mg and 3.2 mm radius is placed on micro-grooved solid, infused with silicone oil of viscosity $\eta = 96$ mPa-s. The infused solid is kept at an inclination $\alpha > \alpha_c$. $x - t$ plot of the sphere at $\alpha = 10°$ a) and at $\alpha = 25°$ b), which correspond to rolling and bouncing respectively. c) Velocity plotted against time, for the case of bouncing shows velocity increases linearly in time. The discontinuity in the velocity plot denotes jumps, where the sphere detaches from the infused solid.

implies that the terminal velocity U, if we had a large enough sample, is larger than 10 cm/s.

In order to obtain smaller terminal velocities, or terminal velocities that may be attained within the length of the sample, we need to increases the dissipation. So, we used a higher viscosity silicone oil $\eta = 96$ mPa-s to infuse the textured solid. In this case, as we increased α beyond α_c, we registered a constant velocity of ~ 10 mm/s. In this case the sphere rolled with a 'tail' being dragged behind it. However, when the slope was increased to 25° (occasionally also at angles as low as 15°), the ball started bouncing, with small jumps. This becomes particularly evident when we look at $x - t$ plot for the two cases, as shown in Figure 92. The $x - t$ plot corresponding to small α is linear, denoting a constant speed (Figure 92 a)), whereas the $x - t$ plot corresponding to large α rather increases quadratically in time. In Figure 92 c, we plot the velocity versus time and we note that it has a step-like shape and is linearly increasing in time, implying a constant acceleration. The velocity versus time curve has two parts: a slower step which is 'flatter' in time - this corresponds to the sphere in contact with the infused solid and rolling on it, and a faster step where the sphere is detached from the infused solid is travelling through air.

We plot the driving force $F = mg \sin \alpha$ against the terminal velocity U in Figure 93, for spheres rolled down parallel to the grooves (red) as well as perpendicular to the grooves (black). We note that there are three distinct regimes: stuck (gray), rolling (white) and bouncing (blue). When comparing the black data points with the red, we observe that to attain the same U, a larger driving force is required to move the sphere perpendicular to the grooves in comparison to

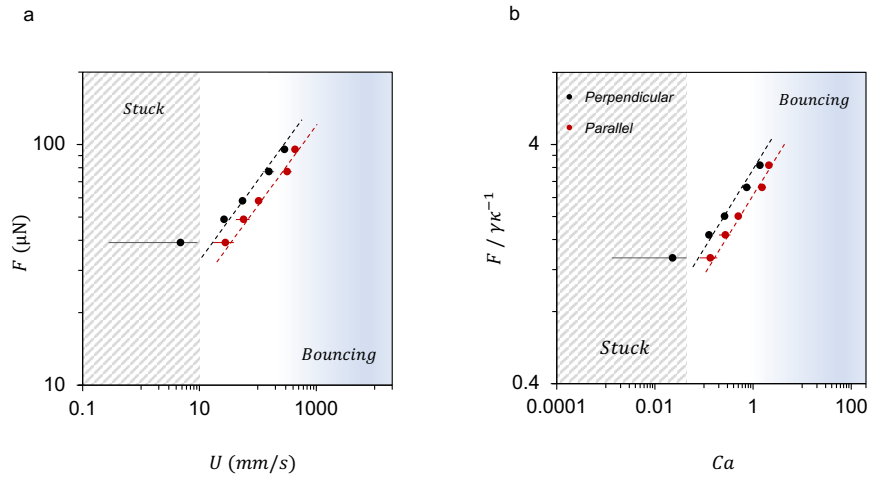

Figure 93: **Force vs velocity.** a) Driving force plotted against the terminal velocity for spheres moving on an infused solid with $\eta = 96\,\mathrm{mPa\text{-}s}$. b) Driving force nondimensionalized by $\gamma\kappa^{-1}$ plotted against Capillary number $Ca = \eta U/\gamma$, where η is the viscosity of the oil infused in the textured solid. Dotted lines are fits raised to an exponent 1/3. Gray, white and blue shaded regions denote stuck, rolling and bouncing.

moving it parallel to the grooves, which is expected. The dynamical friction force in this case is $\sim 10\,\mu N$ and in the limit U goes to zero, that is the stuck phase, F matches the lateral adhesion force measured from roll-off experiments, which is $\approx 40\,\mu N$ for polystyrene beads.

The dotted lines represent a fit with an exponent 1/3. It is very tempting to consider a Cox-Voinov framework here, where we say that the dissipation is given by the integration of the wedge dissipation over the perimeter of the tail, that is $F \sim \eta U l/\theta$. In the Cox-Voinov framework, $\theta \sim (\eta U/\gamma)^{1/3}$. This would give the force to scale as $F \sim (\eta U/\gamma)^{2/3}\gamma l$. Multiple problems arise now - firstly l is dynamical and we do not know the relationship between l and U. Furthermore, Landau-Levich-Derjaguin framework holds true only when $Ca < 1$. Figure 93b reveals that the data points are very close to $Ca = 1$, and all the forces in the rolling regime are larger than $\gamma\kappa^{-1}$, which means the usual formulations are not applicable here as is. In order to make a model for dynamical friction, we need more information about the nature of the flow in the 'tail'. This roadblock is similar to that in the *Rolling Stones* problem, where only empirical laws could be made.

Nevertheless, we can try to understand the rolling to bouncing transition, which is not observed in the *Rolling Stones* problem. The breaking of the the 'tail' owes its origin to the hemi-solid nature of the infused solid, and is thus observed only on infused solids but not on flat solids with thin films on them. The critical velocity at which the sphere must move to break the 'tail' is $\gamma/\eta \sim 0.2\,m/s$, which also cor-

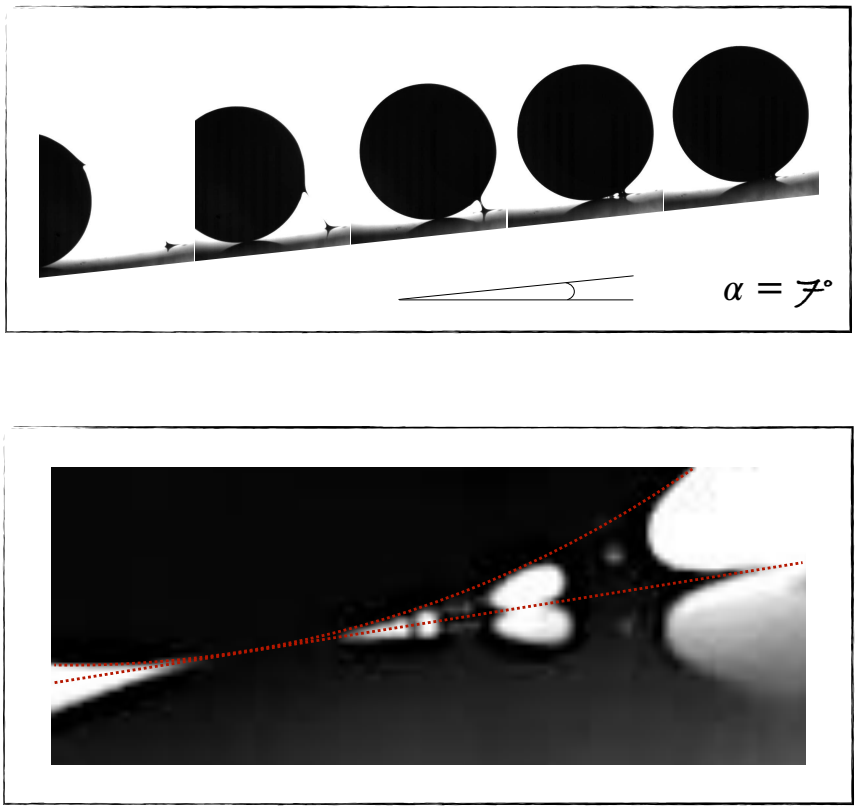

Figure 94: **Breaking the Tail** A polystyrene bead on a micro-grooved surface infused with silicone oil of viscosity $\eta = 4850\,\text{mPa-s}$. At the critical $\alpha_c = 7°$, the starts to roll, but it does so by breaking the tail. This happens by a process is akin to 'fibrillation' where the meniscus is divided into multiple capillary bridges which, as the sphere rolls, move further and further away from the point of contact of the sphere and the infused solid, until they all break and the sphere rolls away. This sudden detachment may lead to a loss of contact with the bottom surface. Note that now when the sphere rolls, it moves faster than the time it would take for the viscous infusion to form a tail. Dotted red lines represent the contour of the sphere and the infused solid.

responds to the Capillary number $Ca > 1$. We see this in Figure 93b, but the question is why is this the criterion?

This is because for the tail to break, the sphere must move faster than the tail can move or 'develop' from the reservoir in the grooves. For a viscous liquid, the rate at which a meniscus is formed is γ/η. It follows that the rolling regime is limited to speeds of the order of γ/η. If the sphere moves faster then the tail breaks starting from the point of contact of the sphere with the flat infused solid, where a 'bubble' develops, which is essentially a manifestation of the capillary bridge not being able to match up to the speed of the sphere. The effect is particularly spectacular for viscous infusions like $\eta = 4850\,\text{mPa-s}$ as we show in Figure 94.

The process of breaking looks reminiscent of 'fibrillation' which occurs when two plates attached with an adhesive are pulled apart. It begins with the formation of 'bubble' at the point of contact between the sphere and the infused solid, which leads to the formation of a capillary bridge travelling in a direction opposite to the direction of motion of the sphere. Often there are multiple 'bubbles', as we see in Figure 94. But, eventually all these capillary bridges break as the sphere rolls away.

The moment the 'tail' breaks the sphere does not 'feel' any adhesion, because it is moving faster than the rate at which the tail can form. This also means minimal dissipation, as the viscous tail is where all the dissipation was concentrated before. So, we see the sphere unboundedly accelerate. The breaking of the tail can cause detachment from the solid itself as the corner of the grooves or minor imperfections and impurities can lift off the sphere which keeps bouncing, and does not adhere to the surface anymore.

One last point that needs to be made is that the rolling regime is quite narrow and vanishes for for higher viscosities. For $\eta > 970\,\text{mPa-s}$, we see that the tail breaks immediately after $\alpha > \alpha_c$. For lower viscosities like $\eta = 9\,\text{mPa-s}$, the tail is intact but our experimental limitation of the size of the sample did not allow us to experimentally obtain the terminal velocities and get an force-velocity curve. Nevertheless, our observations are quite general which may now be extended to the walking of ants on the *Nepenthes*.

7.4 CONCLUSION: LIFE OF A SPHERICAL ANT

The life of a spherical ant on an artificial *Nepenthes* is quite sad and sticky. There is nothing remotely slippery about it. The spherical ant, firstly cannot even move, unless it exerts a force typically 1/10−th its body weight and a velocity typically 1cm/s. Even when the ant can move, it has a viscous 'tail' of meniscus of nectar adhering to its feet, making it sticky and difficult to move. The ant tries to detach its legs from the viscous liquid, but if the local slope is too high, that is

if the terminal velocity corresponding to the driving force is greater than γ/η, then the ant falls. For a sphere of polystyrene, this slope is $\alpha \approx 25^\circ$. For an ant on nectar-infused peristome, it may be different, but experimental images of ants falling show that they fall close to where the local slope of the rim is vertical, that is where the driving force is maximized.

To cut a long story short, contrary to the general perception, ants do not necessarily slip and fall on the nectar-infused peristome of the *Nepenthes*. The ants find it difficult to move on the sticky peristome, and in trying to un-stick themselves from the viscous menisci of nectar and water, they break the 'menisci' and lose adhesion and fall, only to be digested by the clever *Nepenthes*.

EPILOGUE

8

RADIO YEREVAN

We begin the end to this thesis with a classic old Soviet joke from the genre of *Radio Yerevan*.

A listener calls *Radio Yerevan* and asks "Is it true that Rabinovitch won a new car on lottery?". *Radio Yerevan* answers: "In principle yes, it's true, only it wasn't a new car but an old bicycle, and he didn't win it but it was stolen from him."[1]

In the context of liquid-infused surfaces (LIS), a listener may now call *Radio Yerevan* and ask "Is it not true that LIS is just some liquid put on a solid to make a slippery solid?"

And, *Radio Yerevan* would answer: "In principle yes, it's true, only the liquid is not *on* the solid, it is *in* the solid, and LIS is not usually slippery - it is sticky, and also LIS is not really a solid, it is a hemi-solid, hemi-liquid which may or may not be sticky or slippery or both or neither."

Indeed, while liquid-infused solids have been celebrated for their legendary slipperiness for a decade now, in this thesis we saw that these materials are far more ambiguous and being slippery is not necessarily a signature of these materials. They can be sticky (for solids, where lateral adhesion increases) or slippery (for liquid drops, where lateral adhesion is negligible) or both (water drops on infused solids with very high viscosity infusion: negligible adhesion, extremely high friction) or neither (spheres rolling down infused solids after breaking their 'tail').

We began this work by asking a simple question in the part called *Spreading*- what happens, at short times, when a water drop touches an infused solid. We found out that the spreading of a water drop on an infused solid is slower than it is on a 'bare' solid, although the law of spreading curiously preserves the same scaling in time as on a 'bare' solid. We further showed that there exist three different $t^{1/2}$ laws at low, intermediate and high viscosities, which emerge from different modes of dissipation dominating over each other, and thus each mode yielding a $t^{1/2}$ law is special indeed. For viscous liquids (as glycerol) spreading over infused solids (with lower viscosity), we see that the spreading is faster than it is on 'bare' solids. In this case, the possibility of slip on infused solids can be truly harnessed as the lower the viscosity of the infused liquid, the faster the spreading. Through these two contrasting cases, we can see that whether an in-

1 This version of the joke is taken in the exact form it is narrated by Slovenian philosopher Slavoj Žižek in many of his lectures.

fused solid will enable motion on its surface or decelerate it depends on the viscosity ratio of the drop spreading and infused liquid.

In the next part called *Adhesion*- we make direct measurements of adhesion on infused solids and show that they have high vertical adhesion. The adhesion force can be ten times the weight of the drop with which the adhesion test is performed, if the drop volume is 1 μL or smaller. We also show that the viscous adhesion of infused solids can be used to create a kind of 'viscous tweezer' - where a water drop is placed between two infused solids, the top being infused with a much higher viscosity than the bottom one. This device can be actuated with velocity to capture or deposit the water drop, sandwiched between the two surfaces. Said differently, if the two plates are pulled apart quickly, the drop is captured at the top plate, but if the plates are pulled apart slowly, then the drop breaks close to the top and deposits on the bottom plate. This section too demonstrates and elaborates on the 'sticky' nature of infused solids, as we have seen in the previous part.

Finally in the part called *Friction* - we take the famous example of an ant falling off a nectar-infused rim of a pitcher plant, which is celebrated as an illustration of a naturally occurring infused solid (the nectar-infused peristome) and their slipperiness. To test the general postulate that ants on the *Nepenthes* slip and fall on nectar-infused peristomes, we fabricated an artificial peristome, infused with silicone oil of different viscosities, and rolled down solid spheres on them at different angles to test their adhesion and friction. We found that the lateral adhesion of infused solid with respect to the sphere is significantly enhanced due to solid-solid contact and the existence of the meniscus. This is the very opposite of what we observe for water drops, where later adhesion vanishes for infused solids. Furthermore, at higher inclinations, when the sphere rolls, it drags a tail behind, at higher inclinations still, it breaks the tail and starts bouncing. Extending from our observations with the solid sphere, we posit that contrary to the general perception that ants on the *Nepenthes* slip and fall, ants are stuck in the viscous infused solid, and in trying to break the viscous meniscus around their foot, they fall.

There, of course, remain a lot of unanswered questions that need further investigation. For instance, the problem of 'viscous tweezer' needs further elucidation, especially the mechanism of 'viscous arrest' - when the two plates are separated very fast, the contact line of the drop at the top (which is much more viscous than the bottom plate) gets 'frozen'. Consequently, as the contact line at the bottom recedes to zero, the drop is captured at the top. A better understanding of the mechanism of 'viscous arrest' would perhaps shed more light on the problem. Another unfinished work is modelling the force versus velocity curve in the rolling regime as observed for spheres rolling down infused solids. The highly dynamical nature of the regime and

lack of information about the flow geometry in the tail pose difficulties that need be circumvented in clever ways.

Nevertheless, through the series of experimental works presented in this thesis, we saw what a unique ambiguous material a liquid-infused solid is! It is hemi-solid, hemi-liquid, sometimes slippery, sometimes sticky, sometimes both, sometimes neither. Such are its many original properties that the only true description of a liquid-infused solid can perhaps be given only in the words of *Radio Yerevan*:

"In principle, yes."

Part V

APPENDIX

A

A PROPERTY OF $\int x/\ln x$

We wish to prove here that $\int dx/\ln x \sim x/\ln x$ for small x, where the left hand side is also called the logarithmic integral function, $\mathrm{Li}(x)$.

$$\int \frac{dx}{\ln x} = \frac{x}{\ln x} + \int \frac{dx}{(\ln x)^2} \qquad \text{(Integration by parts)}$$

$$\int \frac{dx}{(\ln x)^2} = \frac{x}{(\ln x)^2} + \int \frac{2x}{(\ln x)^3}.\frac{1}{x}\,dx \qquad \text{(Integration by parts)}$$

Adding the equations, and cancelling $\int dx/(\ln x)^2$ from both sides, we get

$$\int \frac{dx}{\ln x} = \frac{x}{\ln x} + \frac{x}{(\ln x)^2} - \int \frac{dx}{(\ln x)^3}$$

$$\therefore \quad \int \frac{dx}{\ln x} = \frac{x}{\ln x}\left(1 + \frac{1}{\ln x} + \frac{1}{(\ln x)^2} + \ldots\right)$$

From the above expression it follows that for small x (as well as for large x),

$$\mathrm{Li}(x) = \int \frac{dx}{\ln x} \to \frac{x}{\ln x}$$

B

WHEN BUBBLES DON'T DIE

Acknowledgement:
This work was done in collaboration
with the intern Guillaume Ricard.[1]

A bubble of a pure liquid is ephemeral. If one blows air bubbles in pure water, the bubbles do not even last a second, but add a little bit of surfactant, the lifetime of the bubble can be dramatically increased, the extent of the increase depending on the quantity and nature of the surfactant. However, addition of surfactants inevitably make the system impure. Is it possible to have a way to not alter the 'purity' of the liquid, but increase the lifetime of the bubble?

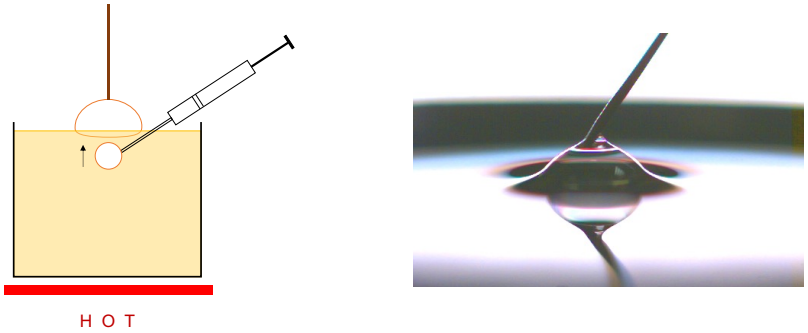

Figure 95: **The Experiment.** Left: Schematic of the experiment. A bath, roughly 5 cm deep, full of silicone oil, is kept on a hot plate. A syringe is used to blow a bubble within the oil. The buoyant bubble emerges out from the bath, and is held in place by a copper wire. c) Experimental image of a bubble on a silicone oil bath held in place by the copper wire.

In an attempt to answer this question, we came up with a simple idea - blowing bubbles into a hot bath. Perhaps a Marangoni flow would make the ephemeral bubbles live longer.

Our experimental set-up comprises a bath of silicone oil that has $\eta = 96\,\text{mPa-s}$ at room temperature placed on hot plate set a fixed temperature. The temperature at the interface of the bath is measured with a separate thermocouple. We blow a bubble into the silicone oil bath using a syringe. As the bubble detaches from the needle, buoyancy makes its move up to the interface where we hold it in

1 The germ of this problem came from the observation of chimneys in Leidenfrost drops in the experiments of Ambre Bouillant.

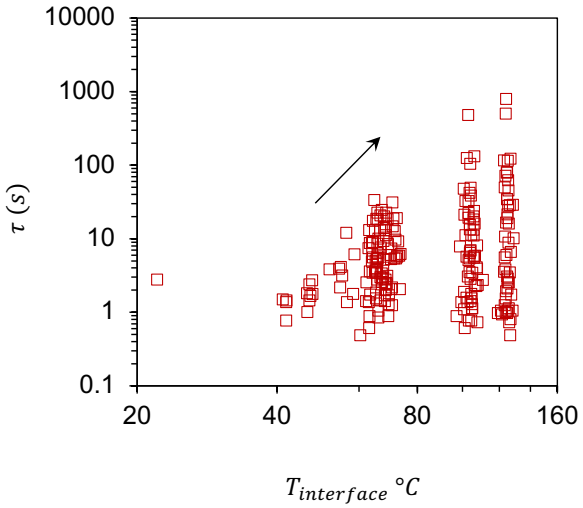

Figure 96: **Lifetime of a Bubble.** Lifetime of bubbles (whose radius of curvature is greater than 4 mm) plotted against the temperature at the interface reveals an increase by three orders of magnitude in lifetime, when the silicone oil is heated to 160°C. The experiments were done using silicone oil of viscosity $\eta = 96$mPa-s (at room temperature)

place with a copper wire, as shown in Figure 95. We now observe the bubble until it pops.

Bubbles which are the size of the capillary length or smaller tend to live indefinitely, irrespective of the temperature of the bath temperature. This is why we limit ourselves to bubbles whose radius of curvature are greater than 4 mm, to look at the effect of temperature on big bubbles (larger than the capillary length $\sim$ 2 mm). In Figure 96, we plot the lifetime of the bubbles versus the interface temperature. Despite the consistent scatter, a hallmark of the fragility of the bubbles, the lifetime of the bubbles increase by three orders of magnitude, when the temperature is increased from 40°C to 160°C. The lack of data points below 40°C is because it is extremely difficult to generate a large bubble near room temperature. Nevertheless, the dramatic increase in the lifetime shows that indeed bubbles live longer and longer on hotter and hotter baths.

In order to accurately measure the temperature differential ΔT between the top and the bottom of the bubble, we perform infra-red imaging of the bubble, which gives us the temperature profile of the bubble. We note that ΔT increases linearly with the interface temperature (Figure 97). This means that the lifetime is also an increasing function of ΔT, increasing by three orders of magnitude in lifetime when ΔT is increased by a factor of 6, from 10°C to 60°C. The scatter persists, nevertheless, as it does in Figure 96.

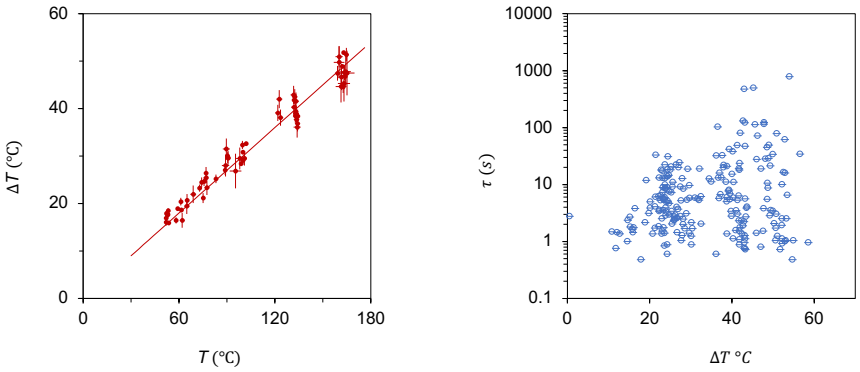

Figure 97: **Lifetime and Temperature gradient.** Left: Temperature differential between the top and bottom of the bubble plotted against the interface temperature reveals a linear relationship. Right: Lifetime of the bubble plotted against the temperature differential reveals a general increase by three orders of magnitude in lifetime, as ΔT is increase by a factor of 6.

The next observation we make about the temperature distribution in the bubble is that the temperature differential is independent of the size of the bubble. This can be seen in Figure 97 where the temperature gradient for bubbles with a fixed temperature differential when plotted against the radius, we find an inverse proportionality. We also note from Figure 97 that at higher temperature differentials, it is possible to make larger and larger bubbles. For instance, with a $\Delta T = 45°C$ to $55°C$, we see that it is possible to make centimetric bubbles, whereas for a $\Delta T < 15°C$, bubbles are typically 4 mm in size.

This brings us to the most curious part of the heated bubble - its cold 'cap', that keeps dripping. In Figure 99, we show successive top-down infra-red images of a heated bubble. The first frame shows that bubble has a colder blue region on the top, surrounded by a hotter yellow region. A temperature profile taken along the dotted line reveals the temperature is higher at the ends $\approx 95°$ and colder at the center $\approx 65°$. After 0.27 s, we see that a tongue of colder fluid drips down from the top into the bath in the next 0.1 s. Four successive snapshots are shown at 30 ms interval to show the successive steps in the dripping. The corresponding temperature profiles reveal a lowering of the temperature in the region where the tongue flows down, and back to the original thermal distribution, once dripping is complete.

The drip is not an isolated incident, it continues to happen periodically. In this particular example, at an interval of 0.27 s the drips would start to fall and falling time would be typically 0.1 s. The sum of the two may be called the total dripping time $\tau_D \approx 0.37$ s.

The formation of the cold 'cap' and the drip both are inextricably related to the long life of the bubble. The temperature differential between the top and the bottom of the bubble sets up a surface tension

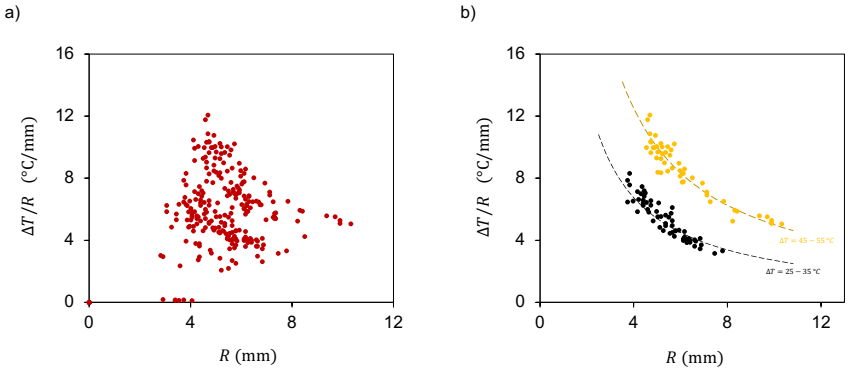

Figure 98: **Temperature gradient.**a) Temperature gradients plotted against the radius of the drop for experiments done at different temperatures from 40°C to 160°C. At first glance there appears to a lot of scatter, but when we plot the data corresponding to a fixed temperature differential 25°C to 35°C (black) and 45°C to 55°C (yellow), we see that the temperature gradient is inversely proportional to the radius (as shown by the dotted line fits which are inversely proportional). This reveals that ΔT is independent of R.

gradient $\Delta\gamma$, which generates a Marangoni flow across the bubble. This flow is precisely what counters the gravitational drainage of the bubble and increases its lifetime. However the flow also leads to an accumulation of liquid at the top, which is colder than the bath temperature. The copper wire also helps here is maintaining a colder temperature, but the cap is observed even without the copper wire. The accumulation happens around the copper wire thickening its menisci with the bubble (distinctly visible in Figure 95). Once the accumulated liquid is too heavy to remain adhered to the copper wire in an annular cap, it drips onto one side as a tongue of liquid. In the absence of the copper wire, there is a continuous flow from the top down, and the stream of cold liquid flowing down can be directly visualized in an IR video. In this sense, the dripping effect which happens with a very regular period is a direct consequence of the existence of the copper wire. However, this has a great advantage, that we discuss now.

A signature of the lifetime of a bubble is its fragility - its scatter. This makes lifetime not a good reproducible physical parameter to quantitatively demonstrate the effect of increase or decrease in the lifetime. This is precisely where the dripping time τ_D serves as a great substitute. The dripping time is the time in which the Marangoni flow has accumulated at the top. The longer the dripping time, the slower the Marangoni flow, the stronger the gravitational drainage, the smaller the lifetime of the bubble. In other words, long-lived bubbles should have small dripping times.

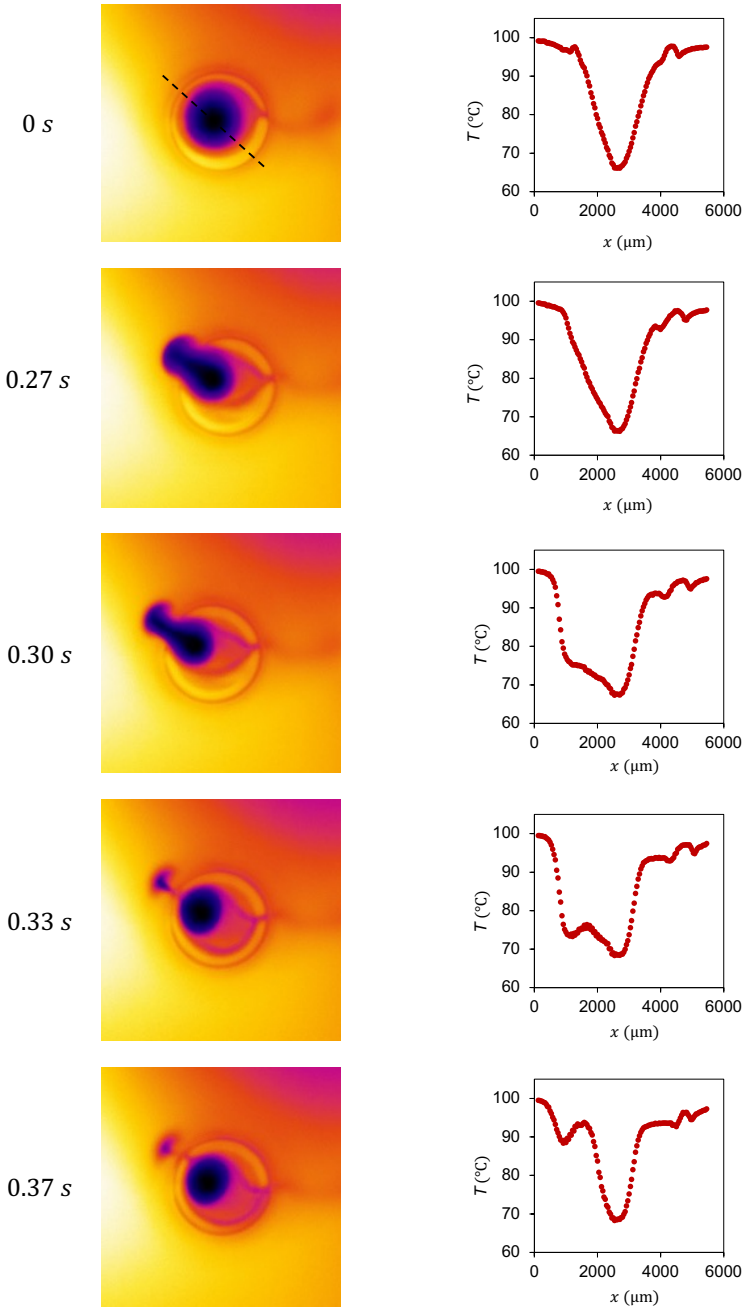

Figure 99: **Drips and Temperature profile.**IR imaging of a bubble on a silicone oil at an interface temperature of 100°C. Successive snapshots show the formation and drip of a colder 'cap' of fluid from the top. On the right, we have the corresponding temperature profiles as measured across the dotted line.

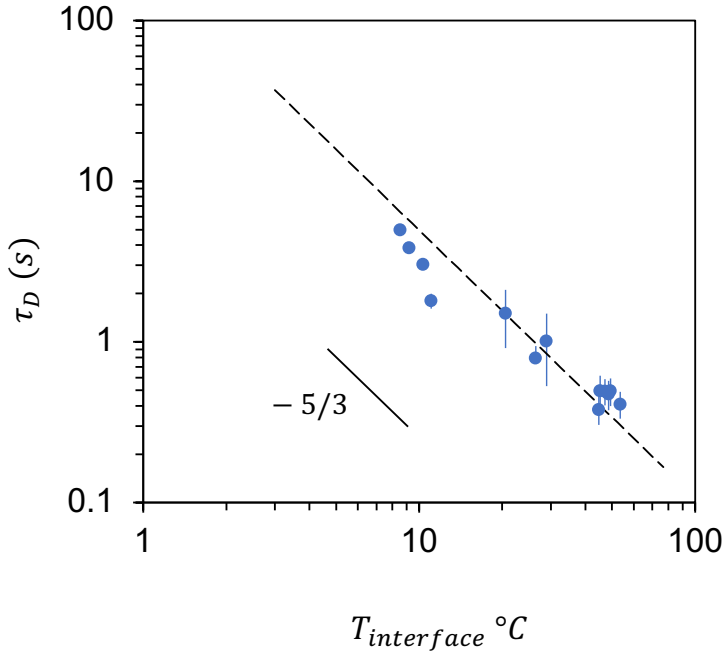

Figure 100: **Dripping Time.** Dripping time plotted against the interface temperature. The dashed line follows a slope −5/3.

Let us now see if we can build a small model to predict the dripping time. Given that there exists a thermally induced Marangoni flow in the bubble, we can now argue that the bubble thickness is bulit in a Landau-Levich-Derjaguin framework, which allows us to write the thickness e of the bubble as $e\kappa \sim (\Delta\gamma/\gamma)^{2/3}$, where we have replaced the velocity in the Capillary number by the Marangoni velocity $U \sim \Delta\gamma/\eta$. The mass flow rate is given by $\dot{m} \sim \rho(Re)V \sim \rho R\kappa^{-1}(\Delta\gamma/\gamma)^{2/3}(\Delta\gamma/\eta)$. The maximum amount of liquid that can accumulate at the top between the copper wire and the bubble is $M \sim \rho\kappa^{-3}$. Equating M/τ_D with $\dot{m}$, we get the dripping time as

$$\tau_D \sim (\kappa^{-2}/R)(\eta/\gamma)(\Delta\gamma/\gamma)^{-5/3} \tag{68}$$

As $\Delta\gamma \propto \Delta T$, and from Figure 97, we know that in our experiments $\Delta T \propto T$, we can write $\Delta\gamma \propto T$. Substituting this relation in Equation 68 gives us $\tau_D \propto T^{-5/3}$. Indeed, in Figure 100, we see that the lifetime follows a −5/3 law in temperature. This gives us more confidence in our original hypothesis - blowing bubbles into a hot bath may increase the lifetime of bubbles.

In other words, *Marangoni would not let a bubble die young!*

C

THE HYDROPHILIC MAP

Acknowledgement:
This work was done in collaboration
with the intern Cillian Jézéquel.[1]

A cold surface in contact with the atmospheric air forms dew drops, turning the surface opaque, if it is a transparent one. One of the quests in the field of anti-fogging has been to create a surface where dew drops are naturally removed or suppressed from coming into existence. In this context, a decade ago, it was shown that on superhydrophobic surfaces, dew drops may coalesce and eject spontaneously [124]. Unfortunately jumping rates on typical superhydrophobic surfaces are very modest $\sim$ 1% of the entire droplet population, thus making it not as ideal for anti-fogging characteristics.

However, more recently, Timothée Mouterde, in collaboration with Thales teams, showed that on surfaces nanotextured by cones, also called nanocone surfaces, the ejection rate typically reaches 90%, compared to less than 1% when the surfaces are nanotextured by cylinders of the same geometrical characteristics as the cones (identical height and spacing, of the order of 100 nm) [77]. Such remarkable ability to eject droplets in conjunction with really low nucleation rates indeed makes nanocone surfaces a potentially a 'truly' anti-fogging material.

In this short note, we look at the nucleation characteristics of such nanocone surfaces. In particular, we wish to ask two questions - first, does a nanocone surface has a intrinsic set of nucleation sites - a *hydrophilic map* of itself that it 'remembers'? If so, is it the memory of the intrinsic *hydrophilic map* or the memory of the drop that has taken off that stays with the nanocone surface?

We start the experiment by bringing the nanocone sample to a temperature of 4°C in 11 s, and the water nuclei formed are observed after 55 s as shown in Figure 102, where the square has a side length of 700 µm. The observation time is chosen just before the first coalescence occurs. In this particular case, 1066 nuclei are observed, very homogeneous in size (about 5 µm in radius) and separated from each other by an average distance of 22 µm . Two experiments are then conducted.

1 Other characters in the story are Timothée Mouterde, Pierre Lecointre, and Krishan Bumma.

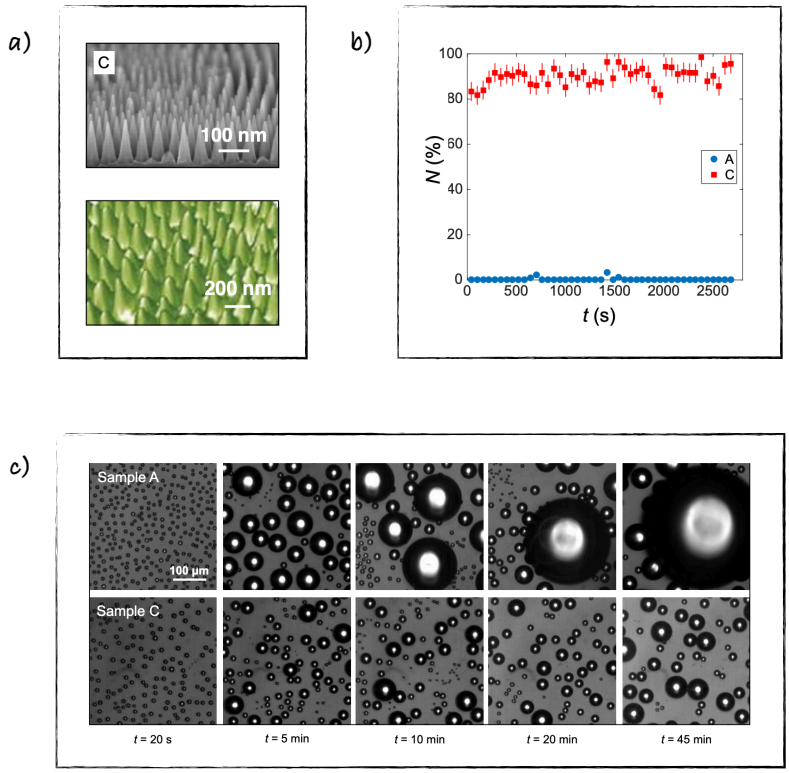

Figure 101: **Nanocone Solids.** a) Top: SEM image of a nanocone surface (sample C) where the cones are 115 nm high and spaced 52 nm apart. Below: AFM of nanotextures on cicada (Psaltoda claripennis) wings shown by atomic force microscopy, adapted from [125]. b) Perecntage of drops jumping off from the surface. b) Temporal evolution of the percentage N of coalescences that successfully result in droplet jumps for nanopillar surface (sample A) and nanocone surface (sample C) (red squares). c) Breath figures on nanpillar (sample A) and nanocone surface (sample C) under a microscope after 20 s, 5 min, 10 min, 20 min, and 45 min. While the nanopillar surface (sample A) is gradually invaded with dew drops that keep growing larger and larger due to the lack of droplet departure, for the nanocone surface (sample C,) a stationary state is reached after 10 minutes, because the droplet jumping is compensated by the nucleation and growth of new water nuclei. All figures are adapted from the work of Timothée Mouterde et al. [77]

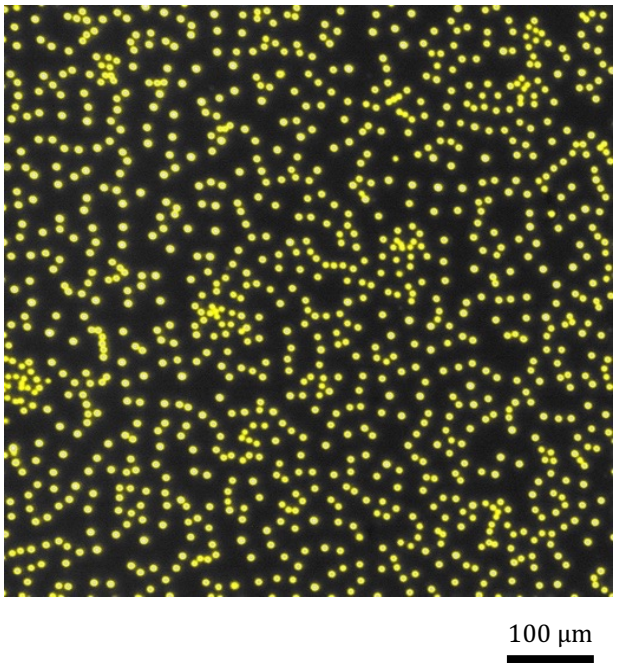

Figure 102: **Nucleation.** Experimental micrograph of a nanocone surface 55 s after nucleation at a temperature of 4°C.

1) First, we consider a subpopulation of 150 nuclei and we plot the number n of nuclei reappearing on these same sites throughout a condensation experiment lasting about 30 minutes. Figure 6 shows the recondensation histogram. We can see that the probability of having at least one re-nucleation ($n > 1$) on a given site is 96%, a very high percentage. These sites are often very active, since 35% of them will give more than 10 re-nucleations. Thus, the initial nucleation map or hydrophilic map (Figure 102) appears to be of primary importance for understanding what happens next, and it confirms the idea that observation over time is strongly correlated with the existence of such a hydrophilic map of the sample.

It is instructive to compare these numbers to those related to a site where a droplet appears "extrinsically": we have observed in our videos about a hundred drops appearing suddenly, at a "blank" location on the sample, the result of a coalescence that propelled a droplet parallel to the surface rather than perpendicularly. These droplets stop at a certain location in the sample not defined by the hydrophilic map, and they grow there before merging with their neighbor and taking off. However, the probability of re-nucleating at these locations is only 7% (instead of 96% in Figure 103), showing that the presence of "intrinsic" hydrophilic sites is more important than the "memory" of a drop that has taken off, and, one would assume, left behind a little water acting as a hydrophilic site.

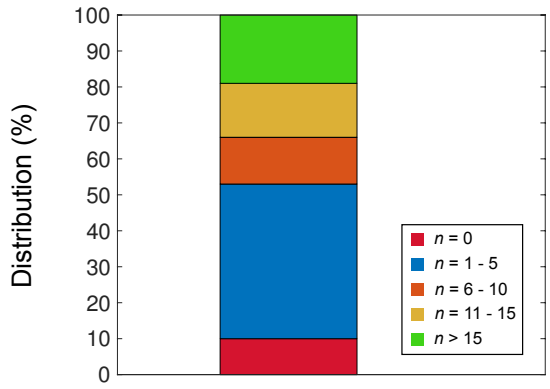

Figure 103: **Histogram of Re-nucleation.**

2) In a second step, we continue the experiment of Figure 102 by heating the sample at room temperature until the water nuclei disappear, then by cooling it again either at the same temperature (here 2.4°C), or lower, as in Figure 104 where we went down to 1.4°C, temperature at which the supercooling of water allows it to remain liquid. The correlation between the two successive hydrophilic maps is thus measured.

The representation convention is as follows: the black dots circled in yellow are those where nucleation had taken place in Figure 102 and where nucleation is taking place again: the approximately 1,000 sites revealed by Figure 102 are all, without exception, reactivated; 148 new sites also appear, a logical fact since the temperature was lowered in this second experiment - a temperature that "activated" new nucleation sites. But the initial map remains largely in the majority, the proportion of new sites being only 14%.

Doing the same experiment by going down to 5.1°C, instead of2.4°C in Figure 102, activates 986 sites, a slightly lower but comparable figure; and warming and then cooling to this same 5.1°C temperature shows an almost absolute correlation, the number of sites being then 989 (with a complete overlap). Reheating then cooling to 4.6°C (it is not easy to achieve perfect temperature cycles) leads to the activation of 1020 sites, a slightly higher number, with again an exact overlap of the sites already activated.

These experiments thus confirm the prevalence of the initial hydrophilic map and justify its existence (this distribution could have been random, and a new experiment would reveal a new distribution de-correlated from the first one). It suggests that this map could be used to drive the blast pattern, for example by encouraging nucleation on points or areas that are non-hazardous for the user (sacrificial sites), allowing to minimize nucleation on other windows of the sample.

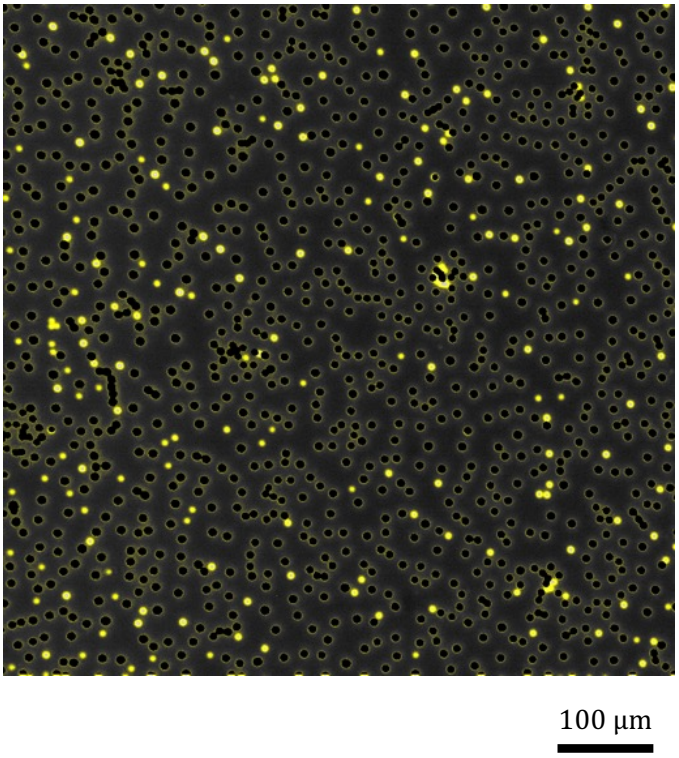

Figure 104: **Hydrophilic Map.** A nanoncone surface is cooled to 4°C and dew drops appear. The surface is then subsequently heated up to room temperature and cooled down to 1.4°C, when dew drops appear again. Black dots circled in yellow are those where nucleation had taken place at 4°C and where nucleation is taking place again at 1.4°C, whereas yellow circles are where dew drops nucleate at 1.4°C, but had not at 4°C.

Part VI

BIBLIOGRAPHY

BIBLIOGRAPHY

[1] S. Chatterjee. "Plague and Politics in Bengal 1896 to 1898." In: *Proceedings of the Indian History Congress*. Vol. 66. JSTOR. 2005, pp. 1194–1201.

[2] S. Basu. "Strikes and'communal'riots in Calcutta in the 1890s: industrial workers, bhadralok nationalist leadership and the colonial state." In: *Mod. Asian Stud.* 32.4 (1998), pp. 949–983.

[3] C. Hoene. "Jagadish Chandra Bose and the anticolonial politics of science fiction." In: *J. Commonw. Lit.* (2020), p. 0021989420966772.

[4] Robert C Hilborn. "Sea gulls, butterflies, and grasshoppers: A brief history of the butterfly effect in nonlinear dynamics." In: *Am. J. Phys.* 72.4 (2004), pp. 425–427.

[5] C. Tanford. *Ben Franklin stilled the waVes: an informal history of pouring oil on water with reflections on the ups and downs of scientific life in general*. OUP Oxford, 2004.

[6] F. Ostendorf, C. Schmitz, S. Hirth, A. Kuhnle, J. J. Kolodziej, and M. Reichling. "How flat is an air-cleaved mica surface?" In: *Nanotechnology* 19.30 (2008), p. 305705.

[7] J. C. Y. Watt. *China: dawn of a golden age, 200-750 AD*. Metropolitan Museum of Art, 2004.

[8] British museum (London). Department of British, Mediaeval Antiquities, Ethnography, and Charles H Read. *Handbook to the ethnographical collections: with 15 plates, 275 illustrations and 3 maps*. British Museum, 1910.

[9] R. Boyle. *New Experiments Physico-Mechanical, Touching the Spring of the Air, and Its Effects. Miles Flesher, London (1682)*.

[10] W. B. Hardy. *Historical notes upon surface energy and forces of short range*. 1922.

[11] A. Ponomarenko, D. Quéré, and C. Clanet. "A universal law for capillary rise in corners." In: *J. Fluid Mech.* 666 (2011), pp. 146–154.

[12] P. G. de Gennes. *Capillarity and wetting phenomena: drops, bubbles, pearls, waves*. Springer Science & Business Media, 2013.

[13] F. Hauksbee. *Physico-mechanical Experiments on Various Subjects: Containing an Account of Several Surprizing Phaenomena Touching Light and Electricity, Producible on the Attrition of Bodies. With Many Other Remarkable Appearances, Not Before Observ'd. Together with the Explanations of All the Machines,(the Figures of which are*

Curiously Engrav'd on Copper) and Other Apparatus Us'd in Making the Experiments. To which is Added, a Supplement, Containing Several New Experiments Not in the Former Editions. J. Senex, 1719.

[14] J. M. Bell and F. K. Cameron. "The flow of liquids through capillary spaces." In: *J. Phys. Chem.* 10.8 (1906), pp. 658–674.

[15] R. Lucas. "Rate of capillary ascension of liquids." In: *Kolloid Z* 23.15 (1918), pp. 15–22.

[16] E.W. Washburn. "The dynamics of capillary flow." In: *Phys. Rev.* 17 (1921), pp. 273–283.

[17] C. H. Bosanquet. "LV. On the flow of liquids into capillary tubes." In: *Philos. Mag.* 45.267 (1923), pp. 525–531.

[18] T. Young. "An essay on the cohesion of fluids." In: *Phil. Trans. R. Soc. Lond.* 95 (1805), pp. 65–87.

[19] R. N. Wenzel. "Resistance of solid surfaces to wetting by water." In: *Ind. Eng. Chem.* 28 (1936), pp. 988–994.

[20] R. N. Wenzel. "Surface roughness and contact angle." In: *J. Phys. Chem.* 53 (1949), pp. 1466–1467.

[21] A. B. D. Cassie and S. Baxter. "Wettability of porous surfaces." In: *T. Faraday Society* 40 (1944), pp. 546–551.

[22] A. B. D. Cassie. "Contact angles." In: *Discuss. Faraday Soc.* 3 (1948), pp. 11–16.

[23] Aniket Mitra. *Bheeshma*. 2015. URL: https://www.behance.net/gallery/28411785/Mahabharata-Saga-of-Deprivation.

[24] J. Bico, C. Tordeux, and D. Quéré. "Rough wetting." In: *Europhys. Lett.* 55 (2001), pp. 214–220.

[25] G. McHale, N. J. Shirtcliffe, S. Aqil, C. C. Perry, and M. I. Newton. "Topography driven spreading." In: *Phys. Rev. Lett.* 93.3 (2004), p. 036102.

[26] L. Courbin, E. Denieul, M. Roper E. Dressair and, A. Ajdari, and H.A. Stone. "Imbibition by polygonal spreading on microdecorated surfaces." In: *Nat. Mater.* 6.9 (2007), pp. 661–664.

[27] R. Xiao, R. Enright, and E.N. Wang. "Prediction and optimization of liquid propagation in micropillar arrays." In: *Langmuir* 26.19 (2010), pp. 15070–15075.

[28] S.J. Kim, M.-W. Moon, K.-R. Lee, D.-Y. Lee, Y.-S. Chang, and H.-Y. Kim. "Liquid spreading on superhydrophilic micropillar arrays." In: *J. Fluid Mech* 680 (2011), p. 477.

[29] E. Spruijt, E. Le Guludec, C. Lix, M. Wagner, and D. Quéré. "Liquid filmification from menisci." In: *EPL* 112.1 (2015), p. 16002.

[30] D. Beilharz. "Liquids guided by texture." PhD thesis. Université Paris-Saclay (ComUE), 2018.

[31] F. Schellenberger, J. Xi Jing, N. N. Encinas, Alexandre A Hardy, Markus Klapper, Periklis P. Papadopoulos, Hans-Jürgen H.-J. Butt, and D. Vollmer. "Direct observation of drops on slippery lubricant-infused surfaces." In: *Soft Matter* 11.38 (2015), pp. 7617–7626.

[32] J. Seiwert, C. Clanet, and D. Quéré. "Coating of a textured solid." In: *J. Fluid Mech* 669.february (2011), pp. 55–63.

[33] B. Levich and L. Landau. "Dragging of a liquid by a moving plate." In: *Acta Physicochim. URSS* 17 (1942), p. 42.

[34] B.V. Derjaguin. "Thickness of liquid layer adhering to walls of vessels on their emptying and the theory of photo-and motion-picture film coating." In: *CR (Dokl.) Acad. Sci. URSS*. Vol. 39. 1943, pp. 13–16.

[35] Ray Reinhard. *Black Ant Tempts Fate on Nepenthes Rim*. 2015. URL: https://500px.com/photo/115165729/Black-Ant-Tempts-Fate-on-Nepenthes-Rim-by-Ray-Reinhard/?utm_medium=pinterest&utm_campaign=nativeshare&utm_content=web&utm_source=500px.

[36] AntsCanada. *Ants vs. Carnivorous Plants*. 2017. URL: https://www.youtube.com/watch?v=nEobGKAlGEU.

[37] T. S. Wong, S. H. Kang, S. K. Y. Tang, E. J. Smythe, B. D. Hatton, A. Grinthal, and J. Aizenberg. "Bioinspired self-repairing slippery surfaces with pressure-stable omniphobicity." In: *Nature* 477 (2011), pp. 443–447.

[38] A. Lafuma and D. Quéré. "Slippery pre-suffused surfaces." In: *Europhys. Lett.* 96 (2011), p. 56001.

[39] J. D. Smith, R. Dhiman, S. Anand, E. Reza-Garduno, R. E. Cohen, G. H. McKinley, and K. K. Varanasi. "Droplet mobility on lubricant-impregnated surfaces." In: *Soft Matter* 9 (2013), pp. 1772–1780.

[40] A. Keiser. "Dynamiques sur des surfaces texturées et imprégnées." In: (2018).

[41] J. H. Guan, E. Ruiz-Gutiérrez, B. B. Xu, D. Wood, G. McHale, R. Ledesma-Aguilar, and G. G. Wells. "Drop transport and positioning on lubricant-impregnated surfaces." In: *Soft Matter* 13.18 (2017), pp. 3404–3410.

[42] J. N. Israelachvili. *Intermolecular and surface forces*. Academic Press, 1990.

[43] P. Bourrianne. "Non-wetting and temp 'e rature: application to culinary coatings." PhD thesis. Paris 6, 2016.

[44] P. Kim, T. S. Wong, J. Alvarenga, M. J. Kreder, W. E. Adorno-Martinez, and J. Aizenberg. "Liquid-infused nanostructured surfaces with extreme anti-ice and anti-frost performance." In: *ACS Nano* 6 (2012), pp. 6569–6577.

[45] P. W. Wilson, W. Lu, H. Xu, P. Kim, M. J. Kreder, J. Alvarenga, and J. Aizenberg. "Inhibition of ice nucleation by slippery liquid-infused porous surfaces (SLIPS)." In: *Phys. Chem. Chem. Phys.* 15 (2013), pp. 581–585.

[46] L. Mishchenko, M. Khan, J. Aizenberg, and B. D. Hatton. "Spatial control of condensation and freezing on superhydrophobic surfaces with hydrophilic patches." In: *Adv. Funct. Mater.* 23 (2013), pp. 4577–4584.

[47] D. C. Leslie et al. "A bioinspired omniphobic surface coating on medical devices prevents thrombosis and biofouling." In: *Nat. Biotechnol.* 32 (2014), pp. 1134–1140.

[48] N. Vogel, R. A. Belisle, B. Hatton, T. S. Wong, and J. Aizenberg. "Transparency and damage tolerance of patternable omniphobic lubricated surfaces based on inverse colloidal monolayers." In: *Nat. Commun.* 4 (2013), p. 2176.

[49] K. C. Park, P. Kim, A. Grinthal, N. He, D. Fox, J. C. Weaver, and J. Aizenberg. "Condensation on slippery asymmetric bumps." In: *Nature* 531 (2016), pp. 78–82.

[50] X. Yao, Y. Hu, A. Grinthal, T. S. Wong, L. Mahadevan, and J. Aizenberg. "Adaptive fluid-infused porous films with tunable transparency and wettability." In: *Nat. Mater.* 12 (2013), pp. 529–534.

[51] D. Daniel, M. N. Mankin, R. A. Belisle, T. S. Wong, and J. Aizenberg. "Lubricant-infused micro/nano-structured surfaces with tunable dynamic omniphobicity at high temperatures." In: *Appl. Phys. Lett.* 102 (2013), p. 231603.

[52] J. Cui, D. Daniel, A. Grinthal, K. Lin, and J. Aizenberg. "Dynamic polymer systems with self-regulated secretion for the control of surface properties and material healing." In: *Nat. Mater.* 14 (2015), pp. 790–795.

[53] N. MacCallum et al. "Liquid-infused silicone as a biofouling-free medical material." In: *ACS Biomater. Sci. Eng.* 1 (2015), pp. 43–51.

[54] J. Cui, D. Daniel, A. Grinthal, K. Lin, and J. Aizenberg. "Dynamic polymer systems with self-regulated secretion for the control of surface properties and material healing." In: *Nature Mater.* 14 (2015), pp. 790–795.

[55] S. Anand, A. T. Paxson, R. Dhiman, J. D. Smith, and K. K. Varanasi. "Enhanced condensation on lubricant-impregnated nanotextured surfaces." In: *ACS Nano* 6 (2012), pp. 10122–10129.

[56] R. Xiao, N. Miljkovic, R. Enright, and E. N. Wang. "Immersion condensation on oil-infused heterogeneous surfaces for enhanced heat transfer." In: *Sci. Rep.* 3.1 (2013), pp. 1–6.

[57] P. B. Weisensee, Y. Wang, Q. Hongliang, D. Schultz, W. P. King, and N. Miljkovic. "Condensate droplet size distribution on lubricant-infused surfaces." In: *Int. J. Heat Mass Transfer* 109 (2017), pp. 187–199.

[58] J. Sun and P. B. Weisensee. "Microdroplet self-propulsion during dropwise condensation on lubricant-infused surfaces." In: *Soft Matter* 15.24 (2019), pp. 4808–4817.

[59] H. A. Stone. "Ice-phobic surfaces that are wet." In: *ACS Nano* 6 (2012), pp. 6536–6540.

[60] K. Rykaczewski, S. Anand, S. B. Subramanyam, and K. K. Varanasi. "Mechanism of frost formation on lubricant-impregnated surfaces." In: *Langmuir* 29 (2013), pp. 5230–5238.

[61] P. Irajizad, M. Hasnain, N. Farokhnia, S. M. Sajadi, and H. Ghasemi. "Magnetic slippery extreme icephobic surfaces." In: *Nat. Commun.* 7 (2016), p. 13395.

[62] M. Tress, S. Karpitschka, P. Papadopoulos, J. H. Snoeijer, D. Vollmer, and H.-J. Butt. "Shape of a sessile drop on a flat surface covered with a liquid film." In: *Soft matter* 13.20 (2017), pp. 3760–3767.

[63] C. Semprebon, G. McHale, and H. Kusumaatmaja. "Apparent contact angle and contact angle hysteresis on liquid infused surfaces." In: *Soft matter* 13.1 (2017), pp. 101–110.

[64] M. S. Sadullah, C. Semprebon, and H. Kusumaatmaja. "Drop dynamics on liquid-infused surfaces: the role of the lubricant ridge." In: *Langmuir* 34.27 (2018), pp. 8112–8118.

[65] C. Hao et al. "Superhydrophobic-like tunable droplet bouncing on slippery liquid interfaces." In: *Nat. Commun.* 6.1 (2015), pp. 1–7.

[66] J. H. Kim and J. P. Rothstein. "Droplet impact dynamics on lubricant-infused superhydrophobic surfaces: The role of viscosity ratio." In: *Langmuir* 32.40 (2016), pp. 10166–10176.

[67] C. Lee, H. Kim, and Y. Nam. "Drop impact dynamics on oil-infused nanostructured surfaces." In: *Langmuir* 30.28 (2014), pp. 8400–8407.

[68] Yi. Liu, J. S. Wexler, C. Schönecker, and H. A. Stone. "Effect of viscosity ratio on the shear-driven failure of liquid-infused surfaces." In: *Phys. Rev. Fluids* 1.7 (2016), p. 074003.

[69] I. Jacobi, J. S. Wexler, and H. A. Stone. "Overflow cascades in liquid-infused substrates." In: *Phys. Fluids* 27 (2015), p. 082101.

[70] J. S. Wexler, A. Grosskopf, M. Chow, Y. Fan, I. Jacobi, and H. A. Stone. "Robust liquid-infused surfaces through patterned wettability." In: *Soft Matter* 11 (2015), pp. 5023–5029.

[71] C. Howell et al. "Stability of surface-immobilized lubricant interfaces under flow." In: *Chem. Mater.* 27 (2015), pp. 1792–1800.

[72] P. Baumli, H. Teisala, H. Bauer, D. Garcia-Gonzalez, V. Damle, F. Geyer, M. D'Acunzi, A. Kaltbeitzel, H. J. Butt, and D. Vollmer. "Flow-Induced Long-Term Stable Slippery Surfaces." In: *Adv. Sci.* 6.11 (2019), p. 1900019.

[73] A. Keiser, L. Keiser, C. Clanet, and D. Quéré. "Drop friction on liquid-infused materials." In: *Soft Matter* 13 (2017), pp. 6981–6987.

[74] L. Keiser, H. Bense, P. Colinet, J. Bico, and E. Reyssat. "Marangoni bursting: evaporation-induced emulsification of binary mixtures on a liquid layer." In: *Phys. Rev. Lett.* 3 (2017), p. 074504.

[75] D. Daniel, J. V. I. Timonen, R. Li, S. J. Velling, and J. Aizenberg. "Oleoplaning droplets on lubricated surfaces." In: *Nat. Phys.* 13 (2017), pp. 1020–1025.

[76] A. Keiser, P. Baumli, D. Vollmer, and D. Quéré. "Universality of friction laws on liquid-infused materials." In: *Phys. Rev. F* 5.1 (2020), p. 014005.

[77] T. Mouterde, Gaélle Lehoucq, Stéphane Xavier, A. Checco, C. T. Black, A. Rahman, T. Midavaine, C. Clanet, and D. Quéré. "Antifogging abilities of model nanotextures." In: *Nat. Mater.* 16 (2017), pp. 658–663.

[78] P.-G. de Gennes. "Wetting: statics and dynamics." In: *Rev. Mod. Phys.* 57.3 (1985), p. 827.

[79] D. Bonn, J. Eggers, J. Indekeu, J. Meunier, and E. Rolley. "Wetting and spreading." In: *Rev. Mod. Phys.* 81.2 (2009), p. 739.

[80] J. H. Snoeijer and B. Andreotti. "Moving contact lines: scales, regimes, and dynamical transitions." In: *Annu. Rev. Fluid Mech.* 45 (2013), pp. 269–292.

[81] A-L. Biance, C. Clanet, and D. Quéré. "First steps in the spreading of a liquid droplet." In: *Phys. Rev. E* 69 (2004), p. 016301.

[82] J. C. Bird, S. Mandre, and H. Stone. "Short-Time Dynamics of Partial Wetting." In: *Phys. Rev. Lett.* 100 (2008), p. 234501.

[83] K. G. Winkels, J. H. Weijs, A. Eddi, and J. H. Snoeijer. "Initial spreading of low-viscosity drops on partially wetting surfaces." In: *Phys. Rev. E* 85.5 (2012), p. 055301.

[84] B.B.J. Stapelbroek, H.P. Jansen, E.S. Kooij, J.H. Snoeijer, and A. Eddi. "Universal spreading of water drops on complex surfaces." In: *Soft Matter* 10 (2014), pp. 2641–2648.

[85] L. H. Tanner. "The spreading of silicone oil drops on horizontal surfaces." In: *J. Phys. D: Appl. Phys.* 12.9 (1979), p. 1473.

[86] O. V. Voinov. "Hydrodynamics of wetting." In: *Fluid Dyn* 11.5 (1976), pp. 714–721.

[87] R. G. Cox. "The dynamics of the spreading of liquids on a solid surface. Part 1. Viscous flow." In: *J. Fluid Mech.* 168 (1986), pp. 169–194.

[88] J. J. Frenkel. "Viscous flow of crystalline bodies under the action of surface tension." In: *J. Phys. USSR* 9 (1945), p. 385.

[89] V. V. Skorokhod. "Development of the ideas of Ya. I. Frenkel'in the contemporary rheological theory of sintering." In: *Powder Metallurgy and Metal Ceramics* 34.9-10 (1996), pp. 521–527.

[90] R. W. Hopper. "Plane Stokes flow driven by capillarity on a free surface." In: *J. Fluid Mech.* 213 (1990), pp. 349–375.

[91] R. W. Hopper. "Plane Stokes flow driven by capillarity on a free surface. Part 2. Further developments." In: *J. Fluid Mech.* 230 (1991), pp. 355–364.

[92] R. W. Hopper. "Stokes flow of a cylinder and half-space driven by capillarity." In: *J. Fluid Mech.* 243 (1992), pp. 171–181.

[93] R. W. Hopper. "Coalescence of two viscous cylinders by capillarity: Part I, theory." In: *J. Am. Ceram. Soc.* 76.12 (1993), pp. 2947–2952.

[94] J. Eggers, J. R. Lister, and H. A. Stone. "Coalescence of liquid drops." In: *J. Fluid Mech.* 401 (1999), pp. 293–310.

[95] D. G. A. L. Aarts, H. N. W. Lekkerkerker, H. Guo, G. H. Wegdam, and D. Bonn. "Hydrodynamics of droplet coalescence." In: *Phys. Rev. Lett.* 95 (2005), p. 164503.

[96] S. T. Thoroddsen, K. Takehara, and T. G. Etoh. "The coalescence speed of a pendent and a sessile drop." In: *J. Fluid Mech.* 527 (2005), p. 85.

[97] S. C. Case and S. R. Nagel. "Coalescence in low-viscosity liquids." In: *Phys. Rev. Lett.* 100 (2008), p. 084503.

[98] J. D. Paulsen, J. C. Burton, and S. R. Nagel. "Viscous to inertial crossover in liquid drop coalescence." In: *Phys. Rev. Lett.* 106 (2011), p. 114501.

[99] M. Wu, T. Cubaud, and C.-M. Ho. "Scaling law in liquid drop coalescence driven by surface tension." In: *Phys. Fluids* 16.7 (2004), pp. L51–L54.

[100] L. Duchemin, J. Eggers, and C. Josserand. "Inviscid coalescence of drops." In: *J. Fluid Mech.* 487 (2003), pp. 167–178.

[101] C. R. Anthony, M. T. Harris, and O. A. Basaran. "Initial regime of drop coalescence." In: *Phys. Rev. F* 5.3 (2020), p. 033608.

[102] A. Eddi, K. G. Winkels, and J. H. Snoeijer. "Short time dynamics of viscous drop spreading." In: *Phys. Fluids* 25.1 (2013), p. 013102.

[103] D. D. Joseph, J. Nelson, M. Renardy, and Y. Renardy. "Two-dimensional cusped interfaces." In: *J. Fluid Mech.* 223 (1991), pp. 383–409.

[104] J.-T. Jeong and H. K. Moffatt. "Free-surface cusps associated with flow at low Reynolds number." In: *J. Fluid Mech.* 241 (1992), pp. 1–22.

[105] E. Lorenceau, D. Quéré, and J. Eggers. "Air entrainment by a viscous jet plunging into a bath." In: *Phys. Rev. Lett.* 93.25 (2004), p. 254501.

[106] T. J. Lin and H. G. Donnelly. "Gas bubble entrainment by plunging laminar liquid jets." In: *AIChE Journal* 12.3 (1966), pp. 563–571.

[107] E. Reyssat, E. Lorenceau, F. Restagno, and D. Quéré. "Viscous jet drawing air into a bath." In: *Phys. Fluids* 20.9 (2008), p. 091107.

[108] M. Tenjimbayashi, R. Togasawa, K. Manabe, T. Matsubayashi, T. Moriya, M. Komine, and S. Shiratori. "Liquid-Infused Smooth Coating with Transparency, Super-Durability, and Extraordinary Hydrophobicity." In: *Advanced Functional Materials* 26.37 (2016), pp. 6693–6702.

[109] C. Clanet and D. Quéré. "Onset of menisci." In: *J. Fluid Mech.* 460 (2002), p. 131.

[110] H. E. Huppert. "The propagation of two-dimensional and axisymmetric viscous gravity currents over a rigid horizontal surface." In: *J. Fluid Mech.* 121 (1982), pp. 43–58.

[111] H. E. Huppert. "Gravity currents: a personal perspective." In: *J. Fluid Mech.* 554 (2006), pp. 299–322.

[112] L. Duchemin and C. Josserand. "Dimple drainage before the coalescence of a droplet deposited on a smooth substrate." In: *Proc. Natl. Acad. Sci. U.S.A.* 117.34 (2020), pp. 20416–20422.

[113] A. Buguin, L. Vovelle, and F. Brochard-Wyart. "Shocks in inertial dewetting." In: *Phys. Rev. Lett.* 83.6 (1999), p. 1183.

[114] D. Bartolo, C. Josserand, and D. Bonn. "Retraction dynamics of aqueous drops upon impact on non-wetting surfaces." In: *J. Fluid Mech.* 545 (2005), pp. 329–338.

[115] F. E. C. Culick. "Comments on a ruptured soap film." In: *J. Appl. Phys.* 31.6 (1960), pp. 1128–1129.

[116] M. Sbragaglia, A. M. Peters, C. Pirat, B. M. Borkent, R. G. H. Lammertink, M. Wessling, and D. Lohse. "Spontaneous breakdown of superhydrophobicity." In: *Phys. Rev. Lett.* 99.15 (2007), p. 156001.

[117] A. M. Peters, C. Pirat, M. Sbragaglia, B. M. Borkent M. Wessling, D. Lohse, and R. G. H. Lammertink. "Cassie-Baxter to Wenzel state wetting transition: Scaling of the front velocity." In: *Eur. Phys. J. E* 29.4 (2009), pp. 391–397.

[118] P. A. Kralchevsky and K. Nagayama. *Particles at fluid interfaces and membranes: attachment of colloid particles and proteins to interfaces and formation of two-dimensional arrays*. Elsevier, 2001.

[119] V. Liimatainen, M. Vuckovac, V. Jokinen, V. Sariola, M. J. Hokkanen, Q. Zhou, and R. H. A. Ras. "Mapping microscale wetting variations on biological and synthetic water-repellent surfaces." In: *Nat. Commun.* 8.1 (2017), pp. 1–7.

[120] Etienne De Flacourt. *Histoire de la grande isle Madagascar*. KARTHALA Editions, 2007.

[121] Anthea Phillips and Anthony Lamb. "Pitcher-plants of Borneo." In: *Natural History Publications (Borneo)* 17.1 (1996), pp. 63–63.

[122] H. Chen, P. Zhang, L. Zhang, H. Liu, Y. Jiang, D. Zhang, Z. Han, and L. Jiang. "Continuous directional water transport on the peristome surface of Nepenthes alata." In: *Nature* 532.7597 (2016), pp. 85–89.

[123] J. Bico, J. Ashmore-Chakrabarty, G. H. McKinley, and H. A. Stone. "Rolling stones: The motion of a sphere down an inclined plane coated with a thin liquid film." In: *Phys. Fluids* 21.8 (2009), p. 082103.

[124] J. B. Boreyko and C. H. Chen. "Self-propelled dropwise condensate on superhydrophobic surfaces." In: *Phys. Rev. Lett.* 103 (2009), p. 184501.

[125] K. M. Wisdom, J. A. Watson, X. Qu, F. Liu, G. S. Watson, and C. H. Chen. "Self-cleaning of superhydrophobic surfaces by self-propelled jumping condensate." In: *Proc. Natl. Acad. Sci. U.S.A.* 110 (2013), pp. 7992–7997.

Part VII

ACKNOWLEDGEMENTS

I

None of this would have been possible
Without Fred and Claudette, who run the lab essentially!
So, the first thanks goes to them.

Thank you to my jury members:
The president of the jury – Lydéric Bocquet,
The referees – Cecile Cottin-Bizonne and Isabelle Cantat,
My examinors – Howard Stone and Jacco Snoeijer
And finally Christophe and David.
Thank you!

II

My days in Paris
(Especially Dec 2019 – Dec 2020)
Have created an epistemological rupture within me –
My unconscious.

It is truly hard to imagine a before.

I came to Paris for David.

All of this begins with a bunch of experiments I did in my kitchen in my undergrad days, which led me to discover David's book. I had always wanted to work with him since. And as life would have it, I found him as my advisor for my PhD.

And...
David has been much more than an advisor to me. Last year when I was devastated, lost, when my world came crashing - when I lost two of my friends in Paris – one to the Seine, and one to cancer, all during the pandemic – the way he stood by me was far beyond what could be expected of any advisor. And, he truly became, as the cliché goes - a friend, philosopher and guide. All my learnings and *unlearnings* have been through him – not just research,
But more – the way to be and beyond - so, I think
A simple thanks would not be enough.

III

José and Benoit are two of the most amazing people I have met in
my life – it seems as though no darkness ever touches them, they are
so bright and beautiful and full of child-like wonder!
So is Damien, who is full of empathy and care
And conversations with him have always been a delight!

IV

A bucketful of gratitude for the rest of the Quéréttes –
Armelle, who guided me in my initial days,
Pierre, Joachim and Daniel for all the joy they brought.
Thanks Aditya - my perpetual lunch companion and the only one
To be there - summer, winter, rain through the entirety of my PhD
(almost).
And, thanks to Marine and Benoit without whom
My life in Paris would have been very very different.
Marine, I have missed our procrastination routines since you left -
Our conversations were the sunshine during my cloud-covered grey
First years in Paris - they have been dangling in our new office room
Since you moved to Lorient.

And Benoit, how do I describe
Our beautiful ramblings that would have no beginning, no end –
From Hegel to Marx to modernity to capitalocene.

And thanks, Ambre for being there when I needed!

V

PMMH is family.
And, Les Arènes is home.

Blue and Magda's parties, beer-spilled discussions with Joseph, the
Renaud-Zhibo theory with Sebastian, the translations of Baptiste, the
jokes of Armand and Romeo, the heartfelt conversations with Lars,
the endless dancing of Martyna at Moulin d'Ande, the sewing
lessons of tall Manon, the late night conversations with Dheeraj, the
love beyond ideological differences of PH, the banter of Maika, the
alcoholisms of small Manon, and Hector and Gaby and Ceasar and
Lucas and Matthias and Gaspar and Jean –

My days in Paris would have been incomplete without all of you!

VI

The LubISS program
And Doris who headed it- took care of everyone,
Even through the pandemic!
And, Philipp – my first friend in the ITN!

VII

My first family - *the Waste Basket* – Akhil - the purest of the pure!
A cosmic pollen floating existentially in the universe...
Seray - the spirit, the healer! Martin - the silent shepherd!
Julie - the pragmatic, and Fouad - the steel!
And then Monica - the Snowy Owl!
And Hasan - he who knew all -
All the verses of the universe!

VIII

My comrades -
Manuj, Ritam, Madhuresh,
And especially
Abhishek
And
Indian Alliance Paris
The months from December 2019 to April 2020
Our making, our breaking, our reading rooms and so much more...

My friends –
Sanket, Disha, Sri, Dipanjana, Amulya,
And Amritansh and PintuDa and Ayush.
And Yash.
Always.

IX

Open mics in Paris
Au Chat Noir

Grafitting with *Titas*
The Anatomy of a Revolution
Rummaging through College Street.

X

Shantanab and Anish.

XI

My other family in Paris –
A Pigeon and an Oak tree
– *Irene* and *Mihir* –
Who Saved
My soul.

XII

S
.
a
.
.
a
.
.
.
g
.
.
.
.
n
.
.
.
.
.
i
.
.
.
.
.
.
k
.
.
.
.
.
.
.

.
.
.
.
.
.
.
.
.
.
.
.
.
.
.
.
.
.
.
.
.

XIII

b
a
b
a
Ma
Bon
BratoDa
And, as always
Namrata, *if not for you* . . .

Dedicated to Hassan

I don't know - when we leave
If we leave behind our words and spells
And syllables and souls -
Airborne - perhaps we susurrate
To eternity...

1989 – 2020

There are decades where nothing happens,
And there are weeks where decades happen.

— Lenin
(que l'on attendait pas ici)

RÉSUMÉ

Un solide texturé infusé est un matériau ambigu, sa surface étant mi-solide, mi-liquide. En conséquence, ces matériaux présentent généralement une adhérence extraordinairement faible qui les rend spécialement glissants pour des gouttes (d'un autre liquide) qu'on y dépose. Nous étudions dans cette thèse quelques comportements originaux de ces surfaces en termes de mouillage, d'adhésion et de friction – à la fois d'un point de vue expérimental et en loi d'échelle, quand c'est possible.

Dans la première section, nous montrons que les solides infusés, supposés ultra-glissants, ralentissent pourtant l'étalement d'une goutte d'eau par rapport aux solides classiques. La situation est opposée pour des gouttes visqueuses, dont l'étalement peut être nettement accéléré par le glissement à l'interface huile/goutte. Dans la deuxième section, nous montrons que, contrastant avec l'adhésion horizontale ultra-faible de ces matériaux, leur adhérence verticale peut être élevée et servir à capturer un liquide par viscosité (pince visqueuse). Dans la troisième section enfin, nous discutons des propriétés de friction de billes solides dévalant sur des surfaces infusées et décrivons en particulier comment ces sphères roulantes engendrent une traînée visqueuse derrière elles.

MOTS CLÉS

solides imprégnés de liquide, gouttes, mouillage, adhésion, friction

ABSTRACT

A textured solid infused with a liquid comprises a class of materials in between a liquid and a solid. Unlike classical solids, these materials typically exhibit extraordinarily little adhesion, due to the marginal role of pinning sites. In this thesis, we experimentally investigate the original spreading, adhesion and frictional behaviour of these special materials, the physics of which we capture with the construction of scaling laws, wherever possible.

In the first section, we show that infused solids, despite their celebrated slipperiness, slow down the spreading of a water drop in comparison to classical solids. The situation, however, is opposite for viscous drops, where spreading can be substantially enhanced by slip at the oil/drop interface. In the second section, we demonstrate that contrary to the vanishing lateral adhesion of these materials, their vertical adhesion is remarkably high. The dynamical adhesion of these solids can be utilized to create a viscous tweezer for water droplets. Finally in the third section, we discuss the friction properties of liquid-infused solids towards solid beads and describe in particular how these rolling spheres drag a tail behind them.

KEYWORDS

Liquid-infused Solids, Drops, Spreading, Adhesion, Friction